Semiconductor Materials and Devices for High Efficiency Broadband and Monochromatic Photovoltaic Energy Conversion

by

MEGHAN BEATTIE

A thesis submitted to the University of Ottawa
in partial fulfillment of the requirements for the
Doctorate in Philosophy degree in Physics

Department of Physics
Ottawa-Carleton Institute for Physics
University of Ottawa

© Meghan Beattie, Ottawa, Canada, 2021

Abstract

This thesis addresses barriers to the widespread adoption of high-efficiency photovoltaic devices through the use of innovative semiconductor materials and device design. The feasibility of various strategies is explored through experimental characterization and modeling of semiconductor materials and devices.

High-efficiency photovoltaic devices are made from epitaxially grown III-V semiconductor materials. Epitaxial devices are highly sensitive to lattice mismatch between the epi-layers and the substrate, requiring sophisticated substrate engineering or growth strategies to access materials outside of the lattice-matched regime. One promising strategy involves the electrochemical porosification of germanium on a lattice-mismatched silicon substrate to create a compliant interface for high-quality epitaxial growth of Ge, GaAs, and other equivalent-bandgap III-V semiconductors on silicon. This results in a threading dislocation density of $\sim 10^4$ cm^{-2}, a reduction of 4 to 6 orders of magnitude compared to direct epitaxy of germanium on silicon. This technology could enable the development of highly efficient III-V multi-junction photovoltaic devices on cost-effective silicon substrates that benefit from well-established commercial supply chains.

In the first part, I present characterization of the electrical properties of porous germanium. Experimental measurements revealed conductivities ranging from 0.6 to 33 $\left(\times 10^{-3}\right)$ Ω^{-1}cm^{-1}, depending on the morphology. The relationship between the electrical properties and the morphology is described using an electrostatic model that can be generalized to other porous semiconductors including silicon. For a compliant interface designed to integrate a standard triple-junction solar cell onto a silicon substrate, the porous Ge/Si layers are predicted to introduce < 0.01 $\Omega\,$cm^2 of series resistance to the device, which is sufficiently low for concentrated photovoltaic applications. Optoelectronic device modelling of the triple-junction solar cell on silicon demonstrates that III-V triple-junction solar cells fabricated on silicon using this compliant Ge/Si porous interface could achieve 93% of the efficiency of a comparable defect-free device.

The remainder of this thesis is concerned with the design and characterization of photovoltaic devices op-

timized for monochromatic illumination, known as photonic power converters. Most commercially available photonic power converters are based on GaAs and are suitable for short-range photonic power transmission through optical fiber (< 1 km). Extended reach power-over-fiber systems require the use of photonic power converters that are compatible with longer-wavelength light, which travels further in optical fiber. One candidate material for this application is the semiconductor quaternary alloy InAlGaAs lattice-matched to InP for photonic power converter operation in the telecommunications O-band, near 1310 nm. I describe the design and characterization of multi-junction InAlGaAs/InP photonic power converters grown by molecular beam epitaxy, including the analysis of material properties and characterization of single- and dual-junction devices under 1319-nm laser illumination. Optically thick devices are found to be diffusion-limited and device simulations suggest that non-radiative recombination is significant. The performance of InAlGaAs tunnel diodes, which act as interconnections for the absorbing junctions within a multi-junction device, is demonstrated to be highly dependent on the growth temperature, with peak tunneling current densities exceeding 1200 A/cm^2 in the best measured devices.

In addition to molecular beam epitaxy-grown InAlGaAs/InP devices, I also characterize single-junction O-band photonic power converters grown by metal-organic vapour phase epitaxy with two alternative absorber materials. A lattice-matched InGaAsP/InP device is compared to a more cost-effective lattice-mismatched GaInAs device grown on GaAs using a metamorphic buffer layer. Both devices are measured under 1319-nm laser illumination with a variety of beam sizes and peak efficiencies of 52.9% and 48.8% were measured for the InGaAsP/InP and the metamorphic-GaInAs/GaAs devices respectively. At illumination powers exceeding 100 mW, the performance begins to degrade with increasingly non-uniform illumination, indicating that illumination profiles should be as uniform as possible to maximize device performance.

Acknowledgements

First, I'd like to thank my supervisor, Prof. Karin Hinzer, for her guidance and support over the course of my graduate studies. Karin's enthusiasm for research is contagious and she helped me to navigate the ups and downs of the academic world with a positive attitude and a sense of humour. She encouraged me to step outside of my comfort zone and to pursue a variety of opportunities that have benefitted me both as a scientist and as a human. I am immensely grateful to Karin for her mentorship these past six years.

I am very grateful to Dr. Youcef Bioud at the Université de Sherbrooke for fabricating the porous germanium material. Further thanks to Youcef and to Prof. Abderraouf Boucherif and Prof. Richard Arès at the Université de Sherbrooke for their enthusiastic collaboration on the Engineered Substrates research project, which led to Chapter 3 of this thesis, and for graciously hosting me at the Institut interdisciplinaire d'innovation technologique (3IT) during my visit in 2016.

I would like to thank Prof. Zbigniew Wasilewski, Dr. Man Chun Alan Tam, and Dr. HoSung Kim at the University of Waterloo for the epitaxial growth of InAlGaAs materials and devices. Their keen collaboration on the PowerCom research project led to Chapter 4 of this thesis.

I would like to thank Dr. Henning Helmers, Dr. Oliver Höhn, and Dr. David Lackner at the Fraunhofer Institute for Solar Energy Systems (ISE) for sharing their photonic power converter samples and for a budding collaboration that led to Chapter 5 of this thesis.

Thank you to Dr. Chris Valdivia for his invaluable advice, for many hours spent editing my abstracts and papers (including those that appear in this thesis), and for countless fruitful discussions. Thank you to Dr. Matthew Wilkins for sharing his expertise and for his patience answering my many questions. Thank you to Dr. Marziyeh Zamiri for developing the contact mask fabrication process for the InAlGaAs photonic power converters, which was integral to my Ph.D. research, and for her support. Thank you to Prof. Jacob Krich for his constructive feedback and for his mentorship. Thank you to Daixi Xia for sharing her detailed-balance

calculations and for many valuable conversations. Additional thanks to Dr. Anna Trojnar, Dr. Ross Cheriton, Kayden Kaller, Trevor Coathup, Mandy Lewis, and the remaining members of the SUNLAB team, both past and present, for their collaboration and friendship.

A heartfelt thank you to Dylan Pierce for his unconditional love, patience, and encouragement, and for proof-reading at the last minute. Finally, I'd like to thank my family and friends for their love and support throughout my academic journey.

The research presented in this thesis was funded in part by the National Sciences and Engineering Research Council of Canada (NSERC) through the PGS-D Scholarship and other research programs, and by the Government of Ontario through the Ontario Graduate Scholarship (OGS) program. Much of the equipment used for the experimental work in this thesis was funded through the Canadian Foundation for Innovation. The simulation software TCAD Sentaurus and associated training was provided by CMC Microsystems.

Statement of Original Contributions

The work presented in this thesis was undertaken over the course of my Ph.D. research project, under the supervision of Prof. Karin Hinzer. Chapters 1 and 2 provide background information from the literature. Chapters 3, 4 and 5 are original contributions. Unless otherwise stated, the experiments and simulations therein were performed by me, as was the corresponding data analysis. There are four publications included in Chapters 3 and 4 of this thesis. In all cases, I was the main author of the text and generated all figures. A detailed breakdown of the specific contributions from each author precedes each publication.

The following is a brief summary of the work that was undertaken by me and key contributions from others for each of Chapters 3, 4 and 5:

Chapter 3:

- I performed the electrical characterization of mesoporous Ge and associated data analysis.
- I worked with undergraduate student David Hobson to develop the electrostatic model that predicts electrical properties of porous semiconductors.
- I performed optoelectronic simulations of triple-junction solar cells on voided Ge/Si engineered-substrates using the above-mentioned electrostatic model to predict the voided material electrical properties. The simulations were based on those developed by Matthew Wilkins for a standard triple-junction solar cell on a germanium substrate.
- All mesoporous Ge samples were fabricated by Youcef Bioud at the Université de Sherbrooke.
- Characterization of the mesoporous Ge morphology including electron microscopy, X-ray diffraction, and Fourier-transform infrared spectroscopy was performed by Youcef Bioud as well as associated data analysis.

Chapter 4:

- I designed the InAlGaAs photonic power converters with input from colleagues including Matthew Wilkins, Marziyeh Zamiri and Zbigniew Wasilewski.
- I designed and assembled the measurement station for laser-illuminated O-band photonic power converter measurements.
- I performed preliminary devices fabrication using the indium dot soldered contact method.
- I performed material and device characterization of InAlGaAs samples through experimental methods including spectroscopic ellipsometry, luminescence spectroscopy, quantum efficiency, and current-voltage measurements as well as associated data analysis.
- I assembled the material parameter database required for optoelectronic simulations of InAlGaAs photonic power converters and carried out simulations of single-junction devices using the TCAD Sentaurus commercial software.
- InAlGaAs material and device samples were grown by molecular beam epitaxy by Man Chun (Alan) Tam and HoSung Kim at the University of Waterloo.
- Device fabrication using contact mask metallization was performed by Marziyeh Zamiri, Kayden Kaller, and Trevor Coathup at the University of Ottawa.
- Contacts to p-type InP were evaporated at the National Research Council of Canada by Philip Waldron and Reza Dowlatshahi.
- Secondary ion mass spectrometry was performed on InAlGaAs tunnel diode samples by EAG Laboratories.
- Detailed-balance modelling of InAlGaAs PPCs was performed by Daixi Xia.

Chapter 5:

- I performed quantum efficiency and current-voltage measurements as well as associated data analysis.

- Photonic power converters discussed in this chapter were designed, grown, and fabricated at the Fraunhofer Institute for Solar Energy Systems (ISE) by Henning Helmers, Oliver Höhn, David Lackner, and team.

The work presented in this thesis lead to a number of publications and conference presentations, which are listed below.

Journal Articles

1. **M. N. Beattie**, C. E. Valdivia, M. M. Wilkins, M. Zamiri, K. L. C. Kaller, M. C. Tam, H. S. Kim, J. Krich, Z. R. Wasilewski, and K. Hinzer, "High current density tunnel diodes for multi-junction photovoltaic devices on InP substrates," *Applied Physics Letters* **118**(6), 062101, 2021.
2. **M. N. Beattie**, Y. A. Bioud, D. G. Hobson, A. Boucherif, C. E. Valdivia, D. Drouin, R. Arès, and K. Hinzer, "Tunable conductivity in mesoporous germanium," *Nanotechnology* **29**, 215701, 2018.

Trade Magazine Articles

1. **M. N. Beattie** and K. Hinzer, "Extending the reach of photonic power", *Compound Semiconductor*, **25**(7), 56–63, 2019.

Conference Proceedings

1. **M. N. Beattie**, D. Xia, M. M. Wilkins, C. E. Valdivia, M. Zamiri, M. C. Tam, H. S. Kim, K. L. C. Kaller, Z. R. Wasilewski, J. Krich, and K. Hinzer, "Two-junction III-V photonic power converter operating at monochromatic telecom wavelengths," in *2020 47th IEEE Photovoltaic Specialists Conference (PVSC)*, 1062–1066, Virtual Meeting, 2020. [Oral]
2. N. Nouri, C. E. Valdivia, **M. N. Beattie**, M. Zamiri, and K. Hinzer, "Thin photonic power converters designs with back reflector operating at a 1310 nm wavelength," in *2020 47th IEEE Photovoltaic Specialists Conference (PVSC)*, 2359–2362, Virtual Meeting, Jun. 2020. [Oral]
3. D. Xia, **M. N. Beattie**, M. C. Tam, M. M. Wilkins, C. E. Valdivia, Z. Wasilewski, K. Hinzer, and J. Krich, "Opportunities for high efficiency monochromatic photovoltaic power conversion at 1310 nm," in *2019 46th IEEE Photovoltaic Specialists Conference (PVSC)*, 2303–2306, Chicago, IL, 2019. [Oral; **Winner, Best Student Presentation Award, Area 1**]
4. Y. A. Bioud, **M. N. Beattie**, A. Boucherif, M. Jellit, R. Stricher, S. Ecoffey, G. Patriarche, D. Troadec, A. Soltani, N. Braidy, M. M. Wilkins, C. E. Valdivia, K. Hinzer, D. Drouin, and R. Arès, "A porous Ge/Si interface layer for defect-free III-V multi-junction solar cells on silicon," in *Proc. SPIE 10913,*

Physics, Simulation, and Photonic Engineering of Photovoltaic Devices VIII, 109130T, San Francisco, CA, 2019. [Oral]

5. **M. N. Beattie**, Y. A. Bioud, A. Boucherif, D. Drouin, R. Arès, C. E. Valdivia, and K. Hinzer, "III-V multi-junction solar cells on Si substrates with a voided Ge interface layer: A modeling study," in *2018 IEEE World Conference on Photovoltaic Energy Conversion (WCPEC) (A Joint Conference of 45th IEEE PVSC, 28th PVSEC & 34th EU PVSEC)*, 180–184, Waikoloa Village, HI, USA, 2018. [Poster]

Conference Presentations

1. **M. N. Beattie**, H. Helmers, C. E. Valdivia, H. Höhn, D. Lackner, and K. Hinzer, "Non-uniform illumination impacts on O-band InGaAsP and metamorphic GaInAs photonic power converters," in *3rd Optical Wireless and Fiber Power Transmission Conference (OWPT2021)*, Online, Japan, 2021. [Oral; **Winner, Best Paper Award**]

2. **M. N. Beattie**, D. Xia, M. M. Wilkins, C. E. Valdivia, M. Zamiri, M. C. Tam, H. S. Kim, K. L. C. Kaller, Z. R. Wasilewski, J. Krich, and K. Hinzer, "Designing a high voltage photonic power converter for extended reach power-over-fiber systems," in *SPIE 10913, Physics, Simulation, and Photonic Engineering of Photovoltaic Devices VIII*, San Francisco, CA, USA, 2020. [Oral]

3. M. Zamiri, N. Nouri, K. Kaller, **M. N. Beattie**, M. M. Wilkins, C. E. Valdivia, B. Lessard, Z. R. Wasilewski, and K. Hinzer, "Design for fabrication of high efficiency 1310 nm photonic power converter," in *19th International Conference on Numerical Simulation of Optoelectronic Devices*, Ottawa, ON, Canada, 2019. [Poster]

4. N. Nouri, C. E. Valdivia, **M. N. Beattie**, M. S. Zamiri, and K. Hinzer, "Simulation of thin high-efficiency photonic power converters under 1310 nm laser illumination," in *19th International Conference on Numerical Simulation of Optoelectronic Devices*, Ottawa, ON, Canada, 2019. [Poster]

5. D. Xia, **M. N. Beattie**, M. C. Tam, M. M. Wilkins, C. E. Valdivia, Z. R. Wasilewski, K. Hinzer, and J. J. Krich, "Detailed balance efficiency of 1310 nm multi-junction photonic power converters," in *19th International Conference on Numerical Simulation of Optoelectronic Devices*, Ottawa, ON, Canada, 2019. [Oral]

6. **M. N. Beattie**, M. M. Wilkins, M. C. Tam, C. E. Valdivia, Z. R. Wasilewski, and K. Hinzer, "Optical characterization of InAlGaAs on InP for monochromatic photonic power conversion," in *Photonics North Conference*, Québec, QC, Canada, 2019. [Oral]

7. M. M. Wilkins, **M. N. Beattie**, D. Xia, M. C. Tam, M. S. Zamiri, C. E. Valdivia, S. Fafard, D. P. Masson, J. J. Krich, Z. R. Wasilewski, and K. Hinzer, "Progress towards vertically stacked InAlGaAs photovoltaic power converters for fiber power transmission at 1310 nm," in *1st Optical Wireless and Fiber Power Transmission Conference (OWPT2019)*, Yokohama, Japan, 2019. [Oral]

8. **M. N. Beattie**, M. M. Wilkins, M. C. Tam, C. E. Valdivia, D. Masson, S. Fafard, Z. R. Wasilewski, and K. Hinzer, "Development of AlInGaAs-based photonic power converter for telecommunications O-band operation," in *SPIE 10913, Physics, Simulation, and Photonic Engineering of Photovoltaic Devices VIII*, San Francisco, CA, USA, 2019. [Oral]

9. C. E. Valdivia, **M. N. Beattie**, Y. A. Bioud, D. G. Hobson, A. Boucherif, D. Drouin, R. Arès, and K. Hinzer, "Mesoporous germanium for high-efficiency photovoltaic cells," in *42nd International Conference and Expo on Advanced Ceramics and Composites*, Daytona Beach, FL, USA, 2018. [**Invited Oral**]

10. **M. N. Beattie**, Y. A. Bioud, A. Boucherif, D. G. Hobson, D. Drouin, R. Arès, C. E. Valdivia, and K. Hinzer, "Quasi-monocrystalline Ge as an interface layer for multi-junction solar cells on si substrates: Electrical resistivity and device modelling," in *Photonics North Conference*, Ottawa, ON, Canada, 2017. [Oral]

11. **M. N. Beattie**, Y. A. Bioud, A. Boucherif, D. G. Hobson, D. Drouin, R. Arès, C. E. Valdivia, and K. Hinzer, "Quasi-monocrystalline germanium: Electrical resistivity characterization for multi-junction solar cell applications," in *13th International Conference on Concentrator Photovoltaic Systems (CPV-13)*, Ottawa, ON, Canada, 2017. [Poster]

12. **M. N. Beattie**, Y. A. Bioud, A. Boucherif, D. G. Hobson, D. Drouin, R. Arès, C. E. Valdivia, and K. Hinzer, "Electrical resistivity of mesoporous and quasi-monocrystalline germanium," in *Materials Research Society Spring Meeting*, Phoenix, AZ, USA, 2017. [Oral]

Table of Contents

Abstract ii

Acknowledgements iv

Statement of Original Contributions vi
- Journal Articles . . . viii
- Trade Magazine Articles . . . viii
- Conference Proceedings . . . viii
- Conference Presentations . . . ix

Table of Contents xi

List of Figures xiv

List of Tables xxiii

List of Acronyms xxv

List of Symbols xxvi

1 Introduction 1
- 1.1 Engineered Si substrates for III-V epitaxy . . . 3
- 1.2 Power-over-fiber . . . 5
- 1.3 Thesis outline . . . 9

2 Physics of semiconductor materials and photovoltaic devices 11
- 2.1 Semiconductor materials . . . 11
  - 2.1.1 Crystal structure and epitaxial growth . . . 12
  - 2.1.2 Energy band structure . . . 13
  - 2.1.3 Density of states and carrier density . . . 15
  - 2.1.4 Doping . . . 17
  - 2.1.5 Bias voltage . . . 18
  - 2.1.6 Conductivity and mobility . . . 18
  - 2.1.7 Drift and diffusion . . . 20
  - 2.1.8 Generation and recombination . . . 21
  - 2.1.9 Transport equations . . . 23
  - 2.1.10 Optical properties . . . 24
  - 2.1.11 Ternary and quaternary alloys . . . 25
- 2.2 Photovoltaic energy conversion . . . 26
  - 2.2.1 p-n junctions . . . 27

2.2.2 Photocurrent and quantum efficiency 28
2.2.3 Current-voltage characteristics 29
2.2.4 Multi-junction solar cells 31
2.2.5 Multi-junction photonic power converters 32
2.2.6 Tunnel diodes 33
2.3 Simulating PV devices in TCAD Sentaurus 35
2.3.1 Epi tool 36
2.3.2 Structure editor 36
2.3.3 MatPar tool 37
2.3.4 Sentaurus device simulator 37
2.3.5 Sentaurus visual 40

3 Voided Ge/Si substrate for III-V multi-junction solar cells 41
3.1 Electrical properties of mesoporous germanium 41
3.1.1 Introduction 44
3.1.2 Methods 46
3.1.2.1 Preparation of mesoporous Ge films 46
3.1.2.2 Thermal annealing 46
3.1.2.3 Material characterization 46
3.1.2.4 Current-voltage measurement 47
3.1.3 Results and discussion 47
3.1.3.1 Morphology of mesoporous germanium films 47
3.1.3.2 Electrical resistivity of mesoporous germanium 49
3.1.3.3 Structural analysis 53
3.1.3.4 Electrical transport modelling 57
3.1.4 Conclusion 62
3.1.A Supporting Information 64
3.1.A.1 Measuring porosity by infrared reflectance 64
3.1.A.2 Relationship between annealing temperature and surface crystallite size . . 65
3.1.A.3 Defining the space charge region and the Fermi level 66
3.1.A.4 Mobility contributions from lattice and charged impurity scattering 68
3.1.A.5 Effect of interface state density on transport model 69
3.2 Modelling of triple-junction solar cells on voided Ge/Si substrates 71
3.2.1 Introduction 73
3.2.2 Results and Discussion 74
3.2.2.1 Voided Germanium Interface Layer in MJSC 74
3.2.2.2 Electrostatic Models 75
3.2.2.3 Device Model 76
3.2.3 Conclusion 81
3.2.A Appendix 82
3.2.A.1 Equilibrium band diagrams 82
3.2.A.2 Simulated device structure and material parameters 82

4 InAlGaAs photonic power converters for O-band operation 94
4.1 Photonic power converter design and characterization 94
4.1.1 PPC device fabrication 94
4.1.1.1 Indium dot soldered contacts 95
4.1.1.2 Contact mask fabrication 96

4.1.2 Spectroscopic ellipsometry 101
4.1.3 Quantum efficiency 106
4.1.4 Optical absorption of p-InP substrate 112
4.1.5 Luminescence measurements 116
4.1.5.1 Electroluminescence 117
4.1.5.2 Photoluminescence 121
4.1.6 Single- and multi-junction PPC designs 122
4.1.7 Current-voltage characteristics 123
4.1.7.1 Dark 125
4.1.7.2 Illuminated 125
4.1.7.3 Limitations of the measurement apparatus 132
4.2 Single- and dual-junction InAlGaAs photonic power converters 132
4.2.1 Introduction 135
4.2.2 Results and discussion 136
4.2.2.1 Multi-junction detailed balance calculations 136
4.2.2.2 Single-junction photonic power converters 137
4.2.2.3 Tunnel diodes 141
4.2.2.4 Two-junction photonic power converter 142
4.2.3 Conclusion 144
4.3 Analysis of loss mechanisms 145
4.3.1 TCAD Sentaurus simulations 145
4.3.2 Material parameters used for PPC simulations 149
4.4 High current density tunnel diodes 153

5 InGaAsP and GaInAs PPCs for O-band operation 166
5.1 Quantum efficiency analysis 168
5.2 Current-voltage characteristics and beam size dependence 172

6 Summary and outlook 181

Bibliography 184

List of Figures

1.1 Bandgap as a function of lattice constant for group IV and binary III-V semiconductors. Dotted lines indicate the lattice constants of commonly used substrate materials (Si, Ge, GaAs, and InP). The AM1.5g solar spectrum [1] is plotted on the right and the visible and telecommunications photon energy ranges are indicated. . . . 2

1.2 Schematic of power-over-fiber system, adapted from Beattie and Hinzer [2]. . . . 5

1.3 Schematic of PPCs with (a) lateral and (b) vertical segmentation. ARC: anti-reflection coating, LCL: lateral conduction layer, TD: tunnel diode. Reprinted with permission from Beattie and Hinzer [2]. . . . 6

1.4 Attenuation in silica optical fiber as a function of wavelength (modified from Schubert [3]). The key telecommunications wavelength bands are highlighted. . . . 8

1.5 Transmission efficiency in optical fiber as a function of distance assuming attenuation coefficients of 2 dB/km for 850 nm, 0.4 dB/km for 1310 nm, and 0.2 dB/km for 1550 nm illumination. 9

2.1 (a) Diamond cubic and (b) zincblende cubic lattice structures. . . . 12

2.2 (a) First Brillouin zone for the FCC lattice. (b), (c) Energy band structure of GaAs and Si, respectively (modified using energy band structure from Ioffe Institute NSM archive [4]). . . . 14

2.3 (a) Energy band diagram as a function of position, x, (b) Fermi-Dirac distribution $f(E)$, (c) density of states functions $g_c(E)$ and $g_v(E)$, and (d) number densities of electrons and holes, $n(E)$ and $p(E)$. . . . 16

2.4 (a) Energy band diagram as a function of position, x, and (b) number densities of electrons and holes, $n(E)$ and $p(E)$, for an n-type semiconductor. (c) Energy band diagram and (b) number densities of electrons and holes for a p-type semiconductor. . . . 18

2.5 (a) Energy band diagram as a function of position, x, and (b) number densities of electrons and holes, $n(E)$ and $p(E)$, for an intrinsic semiconductor in equilibrium. (c) Energy band diagram and (b) number densities of electrons and holes for an intrinsic semiconductor under bias. . . . 19

2.6 Doping dependent electron and hole mobilities, μ_n and μ_p, for Ge. . . . 20

2.7 (a) Photogeneration and thermalization. (b) Radiative, (c) Auger, and (d) SRH recombination. . 22

2.8 (a) Bandgap and (b) DOS effective masses as a function of lattice constant for ternaries making up InAlGaAs. Parameters for the InAlGaAs compositions lattice-matched to InP are indicated. Binary and bowing parameters are taken from [5]. . . . 26

2.9 Sketch of p-n junction band diagrams in (a) equilibrium, (b) forward bias, and (c) reverse bias. . 28

2.10 Sketch of illuminated p-n junction band diagrams at (a) short-circuit, (b) forward bias, and (c) open-circuit. . . . 29

2.11 Sample *I-V* curve for an illuminated PV device. 30

2.12 Schematics depicting (a) an *N*-junction solar cell and (b) an *N*-junction PPC. The incident light is indicated and key PV cell components are labelled. TD: tunnel diode, ARC: anti-reflection coating. 32

2.13 Sketch of the band diagrams for a tunnel diode (a) at equilibrium, (b) when tunneling dominates, and (c) when thermal diffusion dominates. 34

2.14 Sample *I-V* curve for a tunnel diode. 34

2.15 TCAD Sentaurus tool flow. 36

2.16 Structure and meshing of GaAs n-p junction generated by the *Epi* tool and the *Structure Editor*. The virtual contacts are shown in pink. The black lines indicate the mesh. The full width of the structure is 60 μm of which only the central portion is shown. 37

2.17 Layer schematic showing electric field propagation as defined in TMM. 39

3.1 (a) Top view and (b) cross-sectional SEM image of as-prepared mesoporous Ge layer formed by BEE. (c) High-resolution SEM image of the Ge crystallites. Crystallite sizes and pore morphology at the substrate interface are indicated. (d) HRSTEM micrograph showing the interface between the Ge substrate and the mesoporous Ge interface. (e-j) Top view and (k-p) cross-sectional SEM images of mesoporous Ge layers annealed at 350 – 600°C under hydrogen flow. Scale bars are 200 nm in length unless otherwise indicated. The evolution of the morphology and crystallite size with annealing temperature is evident. 48

3.2 Variation of the surface crystallite size with annealing temperature. 50

3.3 Schematic of layer stack and four-wire sensing configuration for current-voltage measurements across the porous Ge (PGe) and Ge substrate layers indicating the area perpendicular to current flow A, the porous layer thickness t, and the total thickness of the PGe-Ge layer stack h. 50

3.4 (a) Current-voltage characteristics for as-prepared Ge (as-prep.) and after thermal annealing at 400, 450 and 550°C for 10 minutes. The thickness of the porous layer is between 1.4 and 1.45 μm for all samples shown in (a). (b) Product of average total resistance and area, $R_T A$, as a function of porous layer thickness, t, for as-prepared mesoporous Ge. Dashed line is the linear fit, which gives resistivity, and dotted lines are confidence interval bounds calculated using standard deviation on the fitting parameters. Error in A is 3%, in t is ±50 nm, and in R_T is determined from the standard deviation of multiple measurements for each sample. The resistivity of as-prepared porous Ge is found to be $1100 \pm 300\ \Omega\,\text{cm}$. 51

3.5 Porous Ge resistivity as a function of annealing temperature. The inset shows the resistivities between 450°C and 550°C on a smaller scale for clarity. The transition between porous and granular morphologies is indicated. The large uncertainty associated with the data point at 400°C is due to significant variability between samples that is presumed to be caused primarily by inconsistent contact resistance. Conductivity is given on the secondary y-axes. 52

3.6 X-ray diffraction signal of as-prepared mesoporous Ge (as-prep.) and after annealing at 350 – 650 °C. Note: single crystal samples were measured on a powder diffractometer and so relative peak intensity between samples is due to the orientation of the sample and is of no significance. For as-prepared mesoporous Ge, only the (400) diffraction peak is observed. At annealing temperatures exceeding 450 °C, polycrystallinity is observed as the appearance of new peaks including (111), (220), (311), (331), and (511). Inset shows the full peak for the as-prepared mesoporous Ge sample, scaled by a factor of 10-2 relative to the as-prepared peak shown in the main image. 54

3.7 GeH_x band in the transmission-FTIR spectrum of as-prepared mesoporous Ge and after thermal annealing at 250 – 550°C. The positions of mono-, di-, and tri-hydride stretch modes are indicated by vertical lines. Decreasing absorbance with annealing temperature indicates hydrogen desorption. 56

3.8 Integrated absorbance of the three GeH_x species as a function of annealing temperature. 57

3.9 Unit cells for (a) as-prepared and (b) annealed porous Ge electrical transport models. The dimension of the unit cell is given by 'd' and the radius of the pore/void is given by 'a'. (c-d) Schematic of carrier densities and band diagrams for unit cells that are (c) partially and (d) fully depleted of carriers under the depletion approximation. Ionized acceptor atoms are indicated by (−) and holes trapped by surface states are indicated by (+). The conduction E_c and valence E_v bands, the Fermi level E_F, the neutral level Φ_0, and the width of the space charge region W are shown. The energies of the bands are determined relative to the bottom of the valence band at the void-Ge interface. The band bending is determined by the electrostatic potential at the boundary of the space charge region, $(W + a)$. Spatial markers relate the band diagrams to the corresponding carrier density schematics. 58

3.10 (a, d) Average free carrier concentration, (b, e) carrier mobility, and (c, f) resistivity of (left) as-prepared and (right) annealed mesoporous Ge. Conductivity is shown on the secondary y-axis of (c) and (f). Electrical properties are shown for a variety of porosities as a function of pore/void size. A doping concentration of 3×10^{17} cm^{-3} and an interface state density of 4×10^{14} cm^{-2}eV^{-1} are assumed. Highlighted regions show the range of diameters over which the model can be compared with experimental results, for as-prepared mesoporous Ge (left) and after annealing at 550°C (right). Arrows indicate direction of increasing porosity. Values for bulk Ge (substrate) are shown. Simulated results are not shown for annealed mesoporous Ge with 70% porosity because porosities exceeding 52% are not permitted for the selected unit cell geometry. 61

3.11 Infrared reflectivity spectra of as-prepared mesoporous Ge layer with a thickness of 2.88 μm and a porosity of 72%. There are $m = 5$ clearly defined Fabry-Perot fringes between 2163 and 7254 cm^{-1} $(\delta v = 5061\text{cm}^{-1})$. 64

3.12 Arrhenius-like plot of the temperature-dependent crystallite size $(d_{\text{crystallite}})$ of annealed mesoporous Ge. 65

3.13 (a) Space charge region is contained within the unit cell. (b) When the baseline space charge width W_0 extends beyond the boundaries of the unit cell in some directions, the width is redefined so that it is fully contained. (c) When the baseline space charge width extends beyond the boundaries of the unit cell in all directions, the width is redefined to terminate at the boundaries of the unit cell and the Fermi level is adjusted accordingly. 68

3.14 (a) Modelled average free carrier concentration, (b) carrier mobility, and (c) resistivity of mesoporous Ge as a function of pore/void size for interface state densities ranging from 5×10^{12} to 5×10^{15} $cm^{-2}\,eV^{-1}$. Conductivity is shown on the secondary y-axis of (c). A doping concentration of 3×10^{17} cm^{-3} and a porosity of 50% are assumed. Arrows indicate direction of increasing interface state density. Values for bulk Ge are shown. 70

3.15 (a) Scanning electron microscopy (SEM) image of voided Ge. (b), (c) Transmission electron microscopy (TEM) images showing crystallinity of Ge near the surface and in the bulk of the voided material, respectively. The insets show the Fourier transforms of the TEM images. (d) Schematic of the proposed MJSC design. 75

3.16 Modelled resistivities for porous Ge (a) and porous Si (b) for p-type doping concentrations ranging from 10^{17} to 10^{19} cm^{-3}. Void fractions (VF) and void sizes are chosen to correspond to what has been observed experimentally: $VF = 0.4$ and 20 to 50 nm for Ge, 0.7 and 50 to 100 nm for Si. The surface state densities (N_s) on the void walls are taken to be $N_s = 5\times10^{14}$ $cm^{-2}\,eV^{-1}$ for Ge [6] and $N_s = 1\times10^{11}$ $cm^{-2}\,eV^{-1}$ for Si [7]. 76

3.17 (a) MJSC efficiency (η) under 1 sun for different p-type doping concentrations N_a in the voided Ge interface layer and the Si substrate. Cell designs with different doping combinations are numbered *i* – *ix*. (b), (c) Short-circuit band diagrams for low and high doping in Si (designs *i* and *iii*). Conduction and valence bands, CB and VB, and electron and hole quasi-Fermi levels, E_F(e) and E_F(h), are indicated. The potential step at the Si/Ge interface is outlined. 77

3.18 Current voltage curves of each subcell for Si doped at (a) 10^{18} cm^{-3} and (b) 10^{19} cm^{-3} (cell designs *v* and *vi*), under illumination of 1-sun AM1.5D. The Ge interface doping is 10^{18} cm^{-3} in both cases. Curves are shown for threading dislocation densities between 0 and 10^6 cm^{-2}. . . . 79

3.19 Current voltage curves in the Ge subcell for illumination at (a) 1 sun, (b) 10 suns, and (c) 100 suns. The Si doping concentrations are 10^{18} cm^{-3} (cell design *v*) and 10^{19} cm^{-3} (cell design *vi*). The Ge doping concentration is 10^{18} cm^{-3} for all cases. 79

3.20 (a), (b) MJSC efficiency for concentrations ranging from 1 to 1000 suns and threading dislocation densities between 0 and 10^6 cm^{-2}. The Si doping concentration is fixed at 10^{19} cm^{-3} and the Ge interface layer doping concentration is 10^{18} cm^{-3} and 10^{19} cm^{-3} for (a) and (b) respectively (cell designs *vi* and *ix*). The absolute difference in efficiency between (a) and (b) is shown in (c). 80

3.21 (a), (b) Equilibrium band diagrams for low and high doping in Si (designs *i* and *iii*). Conduction and valence bands, CB and VB, and the Fermi level, E_F, are indicated. The boxed regions in (a) and (b) are shown in more detail in (c) and (d) respectively. 82

4.1 Layer schematics for (a) a single-junction PPC, (b) a standalone TD, and (c) a dual-junction PPC. 95

4.2 (a) Photograph and (b) microscope image of PPCs prepared using indium dot soldered contacts. 96

4.3 Schematic depicting the fabrication process for PPC and TD samples. 98

4.4 (a) Microscope image of TLM contact pads. Important dimensions are given in microns. (b) Sample TLM measurements for ohmic contact to p-InGaAs. Both measured and corrected data are shown along with the fit to (4.1). 99

4.5 (a) Photograph and (b) microscope image of metallized and fabricated PPC wafer. The microscope image shows one of the mid-size cells in the 2×2 configuration. 100

4.6 (a) Ellipsometry data and corresponding fit to the Adachi new Forouhi dispersion formula for $In_{0.532}Al_{0.097}Ga_{0.371}As$. (b) Calculated n_r, κ values. 104

4.7 (a) Ellipsometry data and corresponding fit to the Lorentz single oscillator dispersion formula for $In_{0.527}Al_{0.356}Ga_{0.117}As$. (b) Calculated n_r, κ values. 105

4.8 Schematic of the quantum efficiency measurement system. 107

4.9 EQE, reflectance, and $EQE/(1-\mathcal{R})$ for an optically thin $In_{0.532}Al_{0.097}Ga_{0.371}As$ PPC with an absorber thickness of 0.7 μm. 108

4.10 $EQE/(1-\mathcal{R})$ for optically thin $(In_{0.52}Al_{0.48}As)_z\,(In_{0.53}Ga_{0.47}As)_{1-z}$ PPCs with a 0.7 μm absorber thickness. 108

4.11 Tauc plots for optically thin $(In_{0.52}Al_{0.48}As)_z\,(In_{0.53}Ga_{0.47}As)_{1-z}$ PPCs with a 0.7 μm absorber thickness. Each curve is fit to equation 4.16 using the marked data points that display a linear trend. The dashed lines represent the fits. The compositional parameter z and the calculated E_g are indicated for each PPC. The target laser energy for PPC operation (corresponding to 1310 nm wavelength) is indicated. 109

4.12 Comparison between quantum efficiency measurements for an optically thin $In_{0.532}Al_{0.097}Ga_{0.371}As$ PPC with an absorber thickness of 0.842 μm using indium dot soldered contacts (In dot) and mask-fabricated contacts (Fab), not including the cap etch. EQE, reflectance, and $EQE/(1-\mathcal{R})$ curves are shown. 110

4.13 Comparison between quantum efficiency measurements for a mask-fabricated, optically thin $In_{0.532}Al_{0.097}Ga_{0.371}As$ PPC with an absorber thickness of 0.842 μm before and after etching the cap layer. EQE, reflectance, and $EQE/(1-\mathcal{R})$ curves are shown. 111

4.14 (a) Transmittance and (b) absorption coefficient of the InGaAs cap layer determined from the PPC quantum efficiency data shown in Figure 4.13. The reference data comes from the reference optical properties for intrinsic $In_{0.53}Ga_{0.47}As$ stored in the Horiba DeltaPsi2 software. 112

4.15 (a) EQE measured from Ge photodiode, reference signal (EQE_{ref}) and for light transmitted through InP substrate (EQE_{InP}). (b) Relative intensities of light reflected from, absorbed within, and transmitted through the InP substrate. Regions are determined by plotting $\mathcal{T}$ and $1-\mathcal{R}$. Fit to the measured data is shown. 114

4.16 Absorption coefficient for p-InP substrate as a function wavelength on a log-log scale. α_{InP} data points were extracted point-by-point (p-b-p) from the data shown in Figure 4.15 using the TMM. Fits are shown for the band-to-band (BB) and FCA components as well as for the entire curve, fit according to equation 4.18. 115

4.17 Measurement system for electroluminescence (EL) and photoluminescence (PL). 116

4.18 (a) EL spectra for a PPC with active layer composition $In_{0.53}Al_{0.15}Ga_{0.32}As$ (z = 0.315) at 78 K for various current densities. Fits to equation 4.21 are shown by the dashed lines. (b) Shift in the EL peak energy as a function of current density, calculated relative to the peak for the largest current density (E_{ref}). (c) Full width at half maximum (FWHM) values as a function of current density. The dotted line gives the average. (d) Intensity of the EL peak as a function of current density. The dotted line is the power law fit. 118

4.19 (a) EL spectra for a PPC with active layer composition $In_{0.53}Al_{0.15}Ga_{0.32}As$ ($z = 0.315$) at 300 K for various current densities. Fits to equation 4.21 are shown by the dashed lines. (b) Shift in the EL peak energy as a function of current density, calculated relative to the peak for the largest current density (E_{ref}). (c) Full width at half maximum (FWHM) values as a function of current density. The dotted line gives the average. (d) Intensity of the EL peak as a function of current density. The dotted line is the power law fit. 118

4.20 (a) EL peak as a function of temperature, fit using equation 4.26. Trends for GaAs, InAs, and AlAs are shown for reference, shifted such the the curves overlap at 300 K. (b) Full width at half maximum for the EL peaks as a function of temperature. The dotted line shows the expect trend of FMWH ~ $1.8k_BT$. 120

4.21 Room temperature PL spectra for undoped (a) $In_{0.532}Al_{0.097}Ga_{0.371}As$ ($z = 0.205$) and (b) $In_{0.527}Al_{0.356}Ga_{0.117}As$ ($z = 0.748$) on InP with a 10 nm InGaAs cap layer. 121

4.22 Partitioned absorbance for a 4-junction InAlGaAs PPC with an active layer absorption coefficient of 7144 cm^{-1} at 1319 nm illumination targeting a total absorbance of 98%. The thickness of each subcell is indicated. 123

4.23 Dark *I*-*V* curve for InAlGaAs PPC. The low- and high-current measurement regimes are indicated as well as the resultant curve for which the currents are averaged in the overlapping region. 125

4.24 Dilas laser spectrum measured at 25°C with an output power of 14.0 W. 126

4.25 (a) Schematic of laser measurement setup showing beam path and optics. (b) Photograph of experimental setup with beam path overlaid in red. f denotes the lens focal length and $2w$ is the beam diameter. 126

4.26 Laser power as a function of laser current for (a) the ND2 filter, (b) the ND1 filter, and (c) full power. Measurements are shown for both the thermopile and the calibrated photodiode detectors. Calculations are based off of the fit to the ND2 photodiode measurement. 128

4.27 (a-c) Knife-edge beam profile measurements with the curve-fit shown in red for three spot sizes. (d-f) Super-Gaussian beam-shapes extracted from the fits. The $1/e^2$ diameter ($2w$) and the diameter containing 99% of the incident power ($2w_{99}$) are indicated. The profiles are normalized to a total power of 1. 130

4.28 Beam diameters $2w$ and $2w_{99}$ plotted against the z-position. Error bars correspond to the 95% confidence limits on the fitting parameters on the vertical axis and to the 0.2 mm uncertainty in the lens-to-sample distance on the horizontal axis. Quadratic fits are shown and the equations given. 131

4.29 *I*-*V* characteristics for InAlGaAs PPC samples with mesa dimensions of $3.85 \times 3.85\,mm^2$ and absorber thicknesses of (a) 4.1 μm and (b) 0.84 μm. The average irradiance is labelled and markers indicate the maximum power points for each curve. The beam diameter was $2w = 1.9$ mm. 131

4.30 Theoretical current-voltage characteristics for PPCs with 1 to 10 junctions. The inset shows the efficiency as a function of the number of junctions. Calculations are done using an extended detailed balance model in the radiative limit. Incident illumination is centered at 1319 nm with an intensity of 1 W/cm^2. The active layer bandgap is 0.867 eV. 136

4.31 Design schematic for one-junction PPC (not to scale). Materials and target bandgaps are indicated. 137

4.32 (a,b) Current-voltage characteristics for semi-transparent 1-junction PPCs under 1319 nm laser illumination at intensities between 0.05 and 0.33 W/cm^2. Absorber thicknesses are (a) 4.1 µm and (b) 0.84 µm. (c) Open-circuit voltage as a function of illumination intensity for the PPCs in (a) and (b). Solid lines show fits according to (1). See Table 4.9 for fit parameters. 138

4.33 Quantum efficiency and specular reflectance for semi-transparent 1-junction PPCs. The laser wavelength used for the J-V measurements is indicated. Absorber thicknesses are (a) 4.1 µm and (b) 0.84 µm. 139

4.34 Dark current-voltage characteristics for 1-junction PPC square diodes with 4.1 µm. absorber thickness. The side length for each square diode is shown in the legend. The inset shows the non-ideal diode equation 4.37 fit to the 125 µm. diode dark $J-V$ curve. See Table 4.11 for fit parameters. 140

4.35 Design schematic for two-junction PPC (not to scale). Materials and target bandgaps are indicated. The cap is not etched for this work. 142

4.36 J-V behaviour for InAlGaAs tunnel diode lattice-matched to InP, fully transparent up to 1.2 eV (including telecommunications O-band and C-band). The device operation range (currents up to 100 A/cm^2) is indicated. 142

4.37 (a) Measured EQE and $\mathcal{R}_{\text{spec}}$ for the 2-junction PPC. Adjusted QEs account for $\mathcal{R}_{\text{spec}}$ and for absorbance in the InGaAs cap $\left(\mathcal{A}_{\text{cap}}\right)$. (b) J-V characteristics for the 2-junction PPC under 1319 nm illumination (not current-matched). (c) W_{OC} for 1-junction PPCs and average W_{OC} for the 2-junction PPC. Intensities are adjusted for the 2-junction and 0.84 µm PPCs to account for 4% absorption in the cap. Solid lines show fits done using (1) and (4) for 1- and 2-junction PPCs respectively. 143

4.38 Comparison between experimentally measured and simulated QE and reflectivity for the 4.1 µm thick PPC. 145

4.39 Breakdown of simulated EQE and loss mechanisms for the 4.1 µm thick PPC. 146

4.40 Simulated and experimentally measured $J-V$ curves for PPC with 4.1 µm absorber thickness under 1319 nm illumination with an intensity of 100 mW/cm^2. 146

4.41 Simulated bandgap narrowing as a function of doping concentration for InAlGaAs according to equation 4.39. Values for GaAs are shown for comparison [8]. 147

4.42 Simulated and experimentally measured V_{OC} as a function of input intensity averaged over the entire PPC. 148

4.43 (a) TD target structure schematics (d represents the layer thickness). InGaAs and InAlAs layers, except for the etch stop, are lattice-matched to InP. (b) Top view microscope images of tunnel diode samples HT and LT respectively. Relative positions on InP quarter 3”-wafers are shown. The magnified image shows the square diode test pads used for measurements. Side lengths for each diode are given in microns. Note: The orientation of the test pads is upside-down for HT compared to LT. 157

4.44 (a) TD J-V curves are compared on a semi-logarithmic scale for diodes with a 200 µm side length. The position on the wafer is indicated for each curve. (b), (c) J-V curves on a linear scale for the LT-4 and HT-1 diodes respectively. All diodes shown are from the bottom row. Diodes with side lengths of up to 200 µm are shown for LT-4 in (b) and all sizes are shown for HT-1 in (c). See Figure 4.43b for diode locations. A marker indicates J_{pk} in all sub-figures. . . . 159

4.45 (a), (b) J_{pk} as a function of diode side length for HT and LT respectively. (c), (d) differential resistance R_0 as a function of diode side length for HT and LT respectively. The diode positions on each wafer are indicated. Solid symbols correspond to the top row of diodes and open symbols to the bottom row (see Figure 4.43b). 160

4.46 SIMS measurements of Be and Si concentrations in HT and LT. Position zero aligns with the centre of the tunnel diode. Doping concentrations are shown on a logarithmic scale across a 300 nm range surrounding the TD in (a), where the active TD and InAlAs cladding region is bounded by the solid black lines. In (b), the central TD region is shown with concentrations on a linear scale. Target doping concentrations are indicated by the shaded regions. Peak Be concentrations are indicated by the large markers in (b). 162

4.47 (a) PPC target structure schematic (d represents the layer thickness). InGaAs and InAlAs layers, except for the etch stop, are lattice-matched to InP. (b) 1- and 2-junction InAlGaAs operating J-V characteristics under 1319 nm laser illumination at an intensity of 0.22 W/cm^2. The inset shows the average W_{OC} per junction as a function of illumination intensity, up to 1.6 W/cm^2. The open symbols correspond to the J-V curves shown. 163

5.1 Bandgap as a function of lattice constant for ternaries making up InGaAsP. Binary and bowing parameters are taken from [5]. The absorber materials used for the InGaAsP/InP and MM-GaInAs/GaAs PPCs are indicated by the × and + symbols respectively. The O-band is highlighted for reference. 167

5.2 Layer schematics for (a) InGaAsP/InP and (b) MM-GaInAs/GaAs PPCs. 167

5.3 EQE, reflectance, and $EQE/(1-\mathcal{R})$ for InGaAsP/InP and MM-GaInAs/GaAs PPCs. The 1319 nm laser wavelength is highlighted for reference. 168

5.4 Tauc plots for InGaAsP/InP and MM-GaInAs/GaAs PPCs. Each curve is fit to equation 5.1 using the marked data points that display a linear trend. The dashed lines represent the fits and the calculated E_g is indicated for each PPC. 169

5.5 Absorption coefficient as a function of energy for InGaAsP/InP and MM-GaInAs/GaAs PPCs. Fits to equation 5.1 (Tauc) and equation 5.2 (Urbach) are shown as well as the point of closest approach between the fits (E_{CA}). 170

5.6 Fitting procedure to extract E_g for InGaAsP/InP and MM-GaInAs/GaAs PPCs according the method proposed by Helmers et al. [9]. Fits to equation 5.3 are represented by the dashed lines. The resultant value of E_g is indicated for each PPC. 171

5.7 Procedure to extract E_g for InGaAsP/InP and MM-GaInAs/GaAs PPCs according the method proposed by Rau et al. [10]. The EQE is shown as a function of energy near the band edge along with its derivative. The integration region for which $QE'(E) \geq \max[QE'(E)]/2$ is shaded and the resultant value of E_g is indicated for each PPC. 171

5.8 (a) Sample beam profile with $2w$ = 1.3 mm. (b) Schematic showing beam profile overlaid on PPC chip with diameters $2w$ and $2w_{99}$ indicated. (c) Relevant beam diameters and peak-to-average ratios (PAR). (d) Photograph of pointer laser illuminating PPC chip. 173

5.9 (a) I_{SC} as a function of incident 1319 nm laser power for InGaAsP/InP and MM-GaInAs/GaAs PPCs measured with a $1/e^2$ beam size of $2w = 1.3$ mm. Dashed lines are linear fits to equation 5.5. (b) Responsivity as a function of $1/e^2$ beam size. The PPC width (2.2 mm) is indicated and the hatched region shows where the $1/e^2$ beam size will begin to spill over the PPC edges. The dashed lines indicate the average responsivity, calculated for $2w < 2.2$ mm. Arrows indicate the required correction for $2w = 2.3$ mm. 173

5.10 $I-V$ characteristics measured at various incident powers under 1319 nm laser illumination for (a) InGaAsP/InP and (b) MM-GaInAs/GaAs PPCs. Curves are shown for $1/e^2$ beam diameters of 1.9 and 1.3 mm. The incident power is given in W for each curve. 174

5.11 $I-V$ characteristics measured at incident powers of (a) 0.169 W, (b) 0.232 W, and (c) 0.295 W under 1319 nm laser illumination for the MM-GaInAs/GaAs PPC. Curves are shown for $1/e^2$ beam diameters from 1.2 to 1.9 mm. The peak irradiance at the centre of the illumination profile is indicated for each curve. 175

5.12 Bandgap-voltage offset as a function of short-circuit current density for InGaAsP/InP and MM-GaInAs/GaAs PPCs measured under various illumination profiles. The $1/e^2$ beam diameters are indicated for each data set measured under 1319 laser light. The uniform illumination data was measured under the AM1.5d solar spectrum. Dashed lines are fits to equation 5.7. 177

5.13 Reduction in the V_{OC} relative to expected logarithmic trend as a function of $2w$ for InGaAsP/InP and MM-GaInAs/GaAs PPCs. Incident illumination power is 0.232 W, ... 178

5.14 Fill-factor as a function of short-circuit current density for InGaAsP/InP and MM-GaInAs/GaAs PPCs measured under various illumination profiles. The $1/e^2$ beam diameters are indicated for each data set. Dashed lines indicate the average fill-factor calculated for $I_{SC} < 0.1$ A. 179

5.15 Efficiency as a function of incident 1319 nm laser power for InGaAsP/InP and MM-GaInAs/GaAs PPCs measured under various illumination profiles. The $1/e^2$ beam diameters are indicated for each data set. 180

List of Tables

1.1 Selected approaches for heteroepitaxy of Ge and GaAs on Si substrates. 4

1.2 Overview of PPC devices from the literature. Entries in red are commercially available. 7

3.1 List of parameters used in determining the space charge region and the Fermi level.* 66

3.2 Parameters from Palankovski used for calculating the p-type carrier mobility of bulk germanium at room temperature. 68

3.3 Layer schematics for bottom Ge subcell, voided interface layer, and substrate. 75

3.4 Detailed epitaxial layer structure for triple-junction solar cell on voided Ge/Si. 84

3.5 Material parameters at 300 K used for $Ga_{0.5}In_{0.5}P$ in MJSC simulations. Values for electrons and holes are separated by a comma. 85

3.6 Material parameters at 300 K used for GaAs in MJSC simulations. Values for electrons and holes are separated by a comma. 86

3.7 Material parameters at 300 K used for Ge in MJSC simulations. Values for electrons and holes are separated by a comma. 87

3.8 Material parameters at 300 K used for $Al_{0.5}In_{0.5}P$ in MJSC simulations. Values for electrons and holes are separated by a comma. 88

3.9 Material parameters used for $Al_xGa_{1-x}As$ in MJSC simulations. Temperature is 300 K unless otherwise stated. Values apply to $In_{53}Ga_{47}As$ unless binary parameters are given, in which case interpolation is used. Values for electrons and holes are separated by a comma. 89

3.10 Material parameters at 300 K used for $Al_{0.25}Ga_{0.25}In_{0.5}P$ in MJSC simulations. Values for electrons and holes are separated by a comma. 90

3.11 Material parameters at 300 K used for Si in MJSC simulations. Values for electrons and holes are separated by a comma. 91

3.12 Electrical transport parameters for voided Ge and Si used in MJSC simulations. 92

3.13 Material parameters at 300 K used for MgF_2 and TiO_x in MJSC simulations. 92

3.14 Interface recombination parameters used for MJSC simulations. Values are the same for both electrons and holes. 92

3.15 Tunneling parameters used for MJSC simulations. Values for electrons and holes are separated by a comma. 93

4.1 Ohmic contact recipes and resistivities measured by TLM. 97

4.2 Starting thicknesses and refractive indices used for analysis of ellipsometry data. 102

4.3 Fitting parameters and goodness of fit for $In_{0.532}Al_{0.097}Ga_{0.371}As$ heterostructure in the range from 0.8 to 1.24 eV. 104

4.4 Fitting parameters and goodness of fit for $In_{0.527}Al_{0.356}Ga_{0.117}As$ heterostructure in the range from 0.8 to 1.24 eV. 106

4.5 Fitting parameters and goodness of fit for $In_{0.527}Al_{0.356}Ga_{0.117}As$ heterostructure in the range from 0.8 to 1.24 eV. 115

4.6 Varshni parameters for $In_{0.53}Al_{0.15}Ga_{0.32}As$ and for the component binaries. 120

4.7 Detailed InAlGaAs/InP two-junction PPC epitaxial layer structure. 124

4.8 Laser beam parameters. 130

4.9 Figures of merit for 1-junction PPCs in Figure 4.32. 138

4.10 Expected absorbance and $\mathcal{R}_{spec}$-adjusted QE at laser wavelength for 1-junction PPCs in Figure 4.33. 140

4.11 Fitting parameters for dark $J-V$ curves in Figure 4.34. 141

4.12 Figures of merit obtained from fitting V_{OC} for 4.1 μm PPC simulation and experiment. 148

4.13 Material parameters at 300 K used for InP in PPC simulations. Values for electrons and holes are separated by a comma. 149

4.14 Material parameters used for $In_xGa_{1-x}As$ in PPC simulations. Temperature is 300 K unless otherwise stated. Values apply to $In_{53}Ga_{47}As$ unless binary parameters are given, in which case interpolation is used. Values for electrons and holes are separated by a comma. 150

4.15 Material parameters used for $In_xAl_{1-x}As$ in PPC simulations. Temperature is 300 K unless otherwise stated. Values apply to $In_{52}Al_{48}As$ unless binary parameters are given, in which case interpolation is used. Values for electrons and holes are separated by a comma. 151

4.16 Material parameters at 300 K used for $(In_{0.52}Al_{0.48})_z(In_{0.53}Ga_{0.47})_{1-z}As$ in PPC simulations. Values for electrons and holes are separated by a comma. Interpolations are between $In_{0.53}Ga_{0.47}As$ and $In_{0.52}Al_{0.48}As$. 152

5.1 Tauc and Urbach fitting parameters for InGaAsP/InP and MM-GaInAs/GaAs PPCs. 170

5.2 Bandgaps obtained using Tauc, Helmers, and Rau methods for InGaAsP/InP and MM-GaInAs/GaAs PPCs. 172

5.3 Maximum illumination power and irradiance before TD peak tunneling current density was exceeded for MM-GaInAs/GaAs PPC. 176

5.4 Non-ideal diode equation parameters from fits to equation 5.7. 177

List of Acronyms

ARC	Anti-reflection coating
BEE	Bipolar electrochemical etching
BSF	Back surface field
DC	Direct current
D-HVPE	Dynamic hydride vapour phase epitaxy
DOS	Density of states
EL	Electroluminescence
EMI	Electromagnetic interference
EQE	External quantum efficiency
FCA	Free carrier absorption
FCC	Face-centred cubic
FF	Fill factor
FSF	Front surface field
FTIR	Fourier-transform infrared
FWHM	Full width at half maximum
HRSTEM	High-resolution scanning transmission electron microscopy
HT	High temperature
IQE	Internal quantum efficiency
LED	Light emitting diode
LT	Low temperature
MBE	Molecular beam epitaxy
MJ	Multi-junction
MJSC	Multi-junction solar cell
MM	Metamorphic
MOVPE	Metal-organic vapour phase epitaxy
MPP	Maximum power point
ND	Neutral density
PGe	Porous germanium
PL	Photoluminescence
PPC	Photonic power converter
PV	Photovoltaic
QE	Quantum efficiency
RTA	Rapid thermal annealing
RHEED	Reflection high-energy electron diffraction
SEM	Scanning electron microscopy
SIMS	Secondary ion mass spectrometry
SRH	Shockley-Read-Hall
TCAD	Technology computer aided design
TD	Tunnel diode
TDD	Threading dislocation density
TEM	Transmission electron microscopy
TLM	Transmission line method
TMM	Transfer matrix method
UV	Ultraviolet
VF	Void fraction

List of Symbols

Symbol	Description
A	Area
$\mathcal{A}$	Absorbance
a	Pore/void radius
A^*	Fitting parameter for Sotoodeh mobility model
A_0	Transition probability
A_{Aug}	Auger recombination coefficient
a_{lat}	Lattice constant
A_{void}	Void surface area
B_0	Fitting parameter
B_{rad}	Radiative recombination coefficient
C	Fitting parameter
c	Speed of light
C_{ex}	Excess current constant
C_{TLM}	Correction factor
d	Unit cell dimension
d_{cap}	Cap thickness
$d_{\mathrm{crystallite}}$	Average surface crystallite size
d_m	Thickness of mth layer
d_{ox}	Oxide thickness
d_{Q}	Quaternary thickness
d_{TLM}	Gap spacing for TLM
D	Minority carrier diffusion constant
D_{n}, D_{p}	Diffusion coefficient of electrons/holes
E	Energy
E_{a}	Activation energy
E_{c}	Conduction band edge
E_{CA}	Energy of closest approach
E_{F}	Fermi level
E_{Fn}, E_{Fp}	Quasi-Fermi level of electrons/holes
E_{g}	Bandgap energy
E_{i}	Fermi level, intrinsic semiconductor
E_m^+, E_m^-	Electric field of light propagating in + and − directions
E_{peak}	Luminescence peak energy
E_{ref}	Reference energy
E_{v}	Valence band edge
E_{vac}	Vacuum level
F	Electric field
$\mathcal{F}_{1/2}^{-1}$	Inverse Fermi-Dirac integral of order 1/2
f_j	Strength of jth oscillator
g_{c}, g_{v}	Density of states, conduction/valence band
G_{n}, G_{p}	Generation rate for electrons/holes
h	Planck's constant
$\hbar$	Reduced Planck's constantElectrical
I	Current
I_0	Dark saturation current
I_{avg}	Average light intensity

I_{laser}	Current diode current
I_{light}	Intensity of light
I_{lum}	Luminescence intensity
I_{MP}	Current at maximum power
I_{peak}	Peak light intensity
I_{ref}	Reference intensity
I_s, I_c	Ellipsometric parameters
I_{SC}	Short-circuit current
J	Current density
J_{diff}	Diffusion current density
J_{drift}	Drift current density
J_{pk}	Peak tunneling current density
J_{SC}	Short-circuit current density
J_{val}	Current density in tunnel diode valley
K	Bowing parameter
$\mathbf{k}$	Wavevector
k_B	Boltzmann constant
L	Radius of TLM contact pad
L_{mesa}	Mesa side length
L_T	Transfer length
$\mathbf{M}$	Transfer matrix
m_c^*, m_v^*	Density of states effective masses for conduction/valence band
n	Density of electrons
$\tilde{n}$	Complex index of refraction
N_0	Reference doping density
n_∞	High frequency refractive index
N_a	Density of ionized acceptors
N_c, N_v	Effective density of states for conduction/valence band
N_d	Density of ionized donors
n_i	Intrinsic carrier density
n_{ideal}	Ideality factor
N_{pts}	Number of data points
n_r	Real part of the refractive index
N_s	Density of surface states
n_{sum}	Sum of subcell ideality factors
N_{sv}	Surface states per unit volume
P	Power
$\mathcal{P}$	Porosity
p	Density of holes
p_{ave}	Average concentration of holes in porous Ge
P_{Full}	Full laser power
P_{in}	Power of incident light
$\mathbf{P}_m$	Propagation matrix
P_{max}	Maximum power
P_{NDi}	Laser power attenuated using an NDi filter where $i = 1$ or 2
P_{Tot}	Total beam power
q	Elementary electronic charge
Q_S	Surface charge
Q_V	Volume charge
R	Responsivity
$\mathcal{R}$	Reflectivity
$\mathcal{R}_s$	Reflectivity for s-polarized light
$\mathcal{R}_p$	Reflectivity for p-polarized light
R_0	Differential resistance
R_{Aug}	Rate of Auger recombination
R_c	Contact resistance
$r_{m-1,m}$	Fresnel reflection coefficient
R_n, R_p	Recombination rate for electrons/holes

R_{rad}	Rate of radiative recombination
R_{s}	Series resistance
R_{sh}	Shunt resistance
R_{sheet}	Sheet resistance
R_{SRH}	Rate of SRH recombination
R_{T}	Total resistance
s	Fitting parameter
$s_{\mathrm{Urb.}}$	Urbach tail steepness parameter
SR	Spectral response
T	Temperature
$\mathcal{T}$	Transmittance
t	Thickness
$\mathbf{T}_{m-1,m}$	Transmission matrix
$t_{m-1,m}$	Fresnel transmission coefficient
V	Bias voltage
V_{bi}	Built-in potential
v_{drift}	Drift velocity
V_{MP}	Voltage at maximum power
V_{OC}	Open-circuit voltage
V_{pk}	Voltage at peak tunneling current
$V_{\mathrm{S.C.}}$	Volume of the space charge region
V_{val}	Voltage in the tunnel diode valley
W	Width of the space-charge region
w	$1/e^2$ beam radius
w_0	Fitting parameter
w_{99}	Beam radius containing 99% of the incident power
W_{OC}	Bandgap-voltage offset
w_{n}, w_{p}	Depletion widths for n-/p-type material
z	Position of micrometer controlling lens-to-sample distance
α	Absorption coefficient
$\alpha_{E_{\mathrm{g}}}$	Absorption coefficient at the bandgap
α_{g}	Varshni fitting parameter
β	Beam shape parameter
β_{g}	Varshni fitting parameter
γ^*	Fitting parameter for doping dependent SRH lifetime
Γ_0	Spin-orbit broadening
Γ_j	Broadening of jth oscillator
Δ	Ellipsometric phase difference
Δ_0	Separation of transition energy by spin-orbit coupling
ΔE_{g}	Bandgap narrowing
$\tilde{\varepsilon}$	Complex dielectric function
ε_{r}, ε_{i}	Real and imaginary components of $\tilde{\varepsilon}$
ε_0	Permittivity of free space
$\varepsilon_{\mathrm{eff}}$	Effective relative dielectric function
ε_{s}	Static dielectric constant
η	Optical-to-electrical conversion efficiency
κ	Extinction coefficient
λ	Wavelength
μ	Mobility
μ_{n}, μ_{p}	Mobility of electrons/holes
μ_{min}	Fitting parameter for Sotoodeh mobility model
μ_{max}	Fitting parameter for Sotoodeh mobility model
ρ	Electrical resistivity
ρ_{c}	Contact resistivity
σ	Electrical conductivity

Symbol	Description
σ_{P_i}	Standard deviation of residuals for P_i where i = Full, ND1, or ND2
τ	Minority carrier lifetime
τ_{Aug}	Auger recombination lifetime
τ_{min}	Fitting parameter for doping dependent SRH lifetime
τ_{max}	Fitting parameter for doping and TDD dependent SRH lifetime
τ_{rad}	Radiative recombination lifetime
τ_{SRH}	SRH recombination lifetime
Φ	Work function
Φ_0	Neutral level
Φ_{p}	Incident photon flux
ϕ	Electrostatic potential
ϕ_{∞}	Electrostatic potential relative to infinity
χ	Electron affinity
χ^2	Goodness of fit
Ψ	Ellipsometric azimuth
ω_j	Frequency of jth oscillator
ω_{t}	Frequency of absorption peak oscillator

Chapter 1

Introduction

In our highly energy-dependent society, the need for reliable access to electricity has become paramount in even the most remote corners of the world. Using photovoltaic (PV) technology, electricity can be generated wherever there is light. In many cases, electricity can be harvested from sunlight using solar cells. For other applications, a monochromatic light source such as a laser can be used for targeted delivery of photonic energy, which is converted to electricity using a photonic power converter (PPC). Both solar cells and PPCs generate electricity from light through the photovoltaic effect.

Most PV devices are made from semiconductor materials, which absorb light with energy larger than their bandgap energies. Excess energy is lost to heat via thermalization and the overall output voltage of the device is limited by the bandgap. This means that the optical-to-electrical conversion efficiency of the device depends strongly on both the bandgap and the spectrum of incident light.

In solar energy conversion, the incident light spectrum is very broad, encompassing photon energies ranging from < 0.3 eV up to 4.2 eV [1]. The theoretical limiting efficiency for a basic solar cell is 33% with a bandgap near 1.4 eV under unconcentrated sunlight [11, 12]. Higher efficiencies can be obtained by stacking PV subcells with different bandgaps to improve the collection efficiency across the spectrum and mitigate thermalization losses [12, 13]. For PPCs illuminated by monochromatic light, the theoretical efficiency limit approaches 100% for very large input intensities when the bandgap and the photon energy are aligned [14].

The atomic structure of the semiconductor must also be taken into account when designing a PV device. Semiconductors are crystalline materials and their atomic spacing is characterized by the lattice constant. The most efficient PV devices are made using III-V semiconductors grown by epitaxy [13, 15, 16]. A sub-

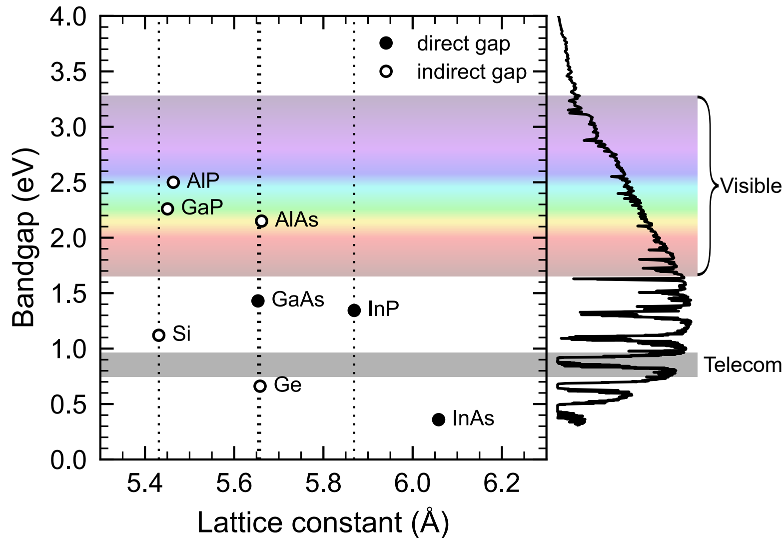

Figure 1.1: Bandgap as a function of lattice constant for group IV and binary III-V semiconductors. Dotted lines indicate the lattice constants of commonly used substrate materials (Si, Ge, GaAs, and InP). The AM1.5g solar spectrum [1] is plotted on the right and the visible and telecommunications photon energy ranges are indicated.

strate material is used as a template for the crystal structure of subsequent semiconductor layers. Excellent crystal quality can be obtained when the epi-layers have the same lattice constant as the substrate. Mismatch between the lattice constants results in defects that propagate through the lattice structure, negatively impacting the device performance. Commonly used substrate materials include Si, Ge, GaAs, and InP.

Figure 1.1 shows the bandgaps and lattice constants for a variety of common group IV and binary III-V semiconductor materials. The lattice constants of the commonly used substrate materials Si, Ge, GaAs, and InP are indicated for reference. Many of the semiconductors shown in Figure 1.1 can be alloyed to access a wider range of bandgap energies.

Despite producing record efficiencies up to 39.2% under unconcentrated AM1.5g and 47.1% under concentrated illumination [13], III-V multi-junction solar cells represent only a tiny fraction of terrestrial solar installations worldwide. Crystalline silicon PV has a more modest record efficiency of 26.7% under AM1.5g [16, 17], but as an inexpensive, earth-abundant material with a well-established supply chain for PV, it made up about 95% of global PV production in 2019 [18].

In 2018, Horowitz et al. proposed a “cost-reduction roadmap for III-V solar cells” to realize their potential and achieve greater market penetration [19]. They identify four key opportunities for improvement:

1. Scaling up production volume
2. Reducing the cost of epitaxy by transitioning to higher throughput metal-organic vapour phase epitaxy

(MOVPE) or dynamic hydride vapour phase epitaxy (D-HVPE) processes

3. Reducing the substrate costs through recycling or a change of material
4. Adoption of low-cost metallization processes such as electroplating or screen printing

In Chapter 3 of this thesis, I investigate a technique to enable high-quality epitaxy of III-V materials on Si substrates by engineering a voided-Ge compliant interface between the substrate and the epi-layers. This strategy helps to address two of the four opportunities described by Horowitz. Because Si dominates the PV industry, Si wafers are 100× less expensive than GaAs or Ge [19]. Furthermore, they are available in larger sizes and are compatible with well-established Si-PV manufacturing infrastructure [20], helping to increase throughput and scale up of production volume.

For PPCs, which are used in more niche applications, cost is less of an obstacle to market penetration. One of the primary opportunities for improvement lies in extending the transmission distance in optical fiber. Most commercially available PPCs are based on GaAs, which absorbs light with wavelengths around 850 nm (1.46 eV). This wavelength is unsuitable for long-distance transmission over optical fiber, limiting power-by-light systems to free-space power transmission or short distances in fiber ($< 1\,\mathrm{km}$). In Chapters 4 and 5 of this thesis, I explore novel PPC designs that rely on III-V semiconductor quaternary alloys to access longer wavelengths of light in the telecommunications band (see Figure 1.1) around 1310 nm, where practical transmission distances reach up to several kilometres.

1.1 Engineered Si substrates for III-V epitaxy

Lattice mismatch between the epitaxial layer and the substrate results in the formation of dislocations in the lattice structure that are detrimental to device performance. Misfit dislocations propagate along the the interface between the epi-layer and the substrate whereas threading dislocations propagate upwards through the epi-layers [21]. Threading dislocations are particularly problematic in PV devices when they penetrate the active layers, acting as recombination centres that can significantly reduce the minority carrier lifetimes and diffusion lengths [22]. The $\sim 4\%$ lattice mismatch between Ge or GaAs and Si results in threading dislocation densities (TDD) on the order of $10^8 - 10^{10}\,\mathrm{cm}^{-2}$ for direct epitaxy of Ge or GaAs on Si [20, 23], which is too large for PV devices that require TDD $< 10^6\,\mathrm{cm}^{-2}$ to achieve reasonable performance [22].

The pursuit of high quality epitaxial growth of lattice-mismatched III-V semiconductors on Si substrates has led to the development of many innovative fabrication techniques over the past four decades.

Table 1.1: Selected approaches for heteroepitaxy of Ge and GaAs on Si substrates.

Technique	Material system	Epi-layer quality	Ref.
Graded buffer layers	GaAs on Ge/GeSi/Si	TDD: 2×10^6 cm^{-2}	[24, 25]
		TDD: $0.8-1.5\times10^6$ cm^{-2}	[22]
Thermal cycle annealing	GaAs on Si	TDD: $2-3\times10^6$ cm^{-2}	[26]
	Ge on Si	TDD: 1.3×10^6 cm^{-2}	[27]
Epitaxial lateral overgrowth	GaAs on Si with patterned SiO_2 film	Defect-free width: 43 μm	[28]
Selective area growth	GaAs in SiO_2 trenches on Si	Defect-free width: 300 nm	[29]
	Ge in SiO_2 trenches on Si	Defect-free width: 400 nm	[30]
	Ge on Si pillars	Defect-free area: 3×3 μm^2	[31]
Electrochemical etching and annealing*	GaAs on voided Ge/Si	TDD: $\sim10^4$ cm^{-2}	[32]

*Approach explored in this thesis for III-V multi-junction solar cells on Si substrates.

An overview of various techniques is given in Table 1.1.

Though several of the techniques listed in Table 1.1 can be used to achieve TDD $\sim 10^6$ cm^{-2}, these methods typically require thick compositionally graded or cyclically annealed buffer layers that are resource intensive to grow. Methods including epitaxial lateral overgrowth and selective area growth can achieve regions that are entirely defect free, but are limited to small-scale applications.

In this thesis, the electrochemical etching and annealing method developed by Bioud et al. at the Université de Sherbrooke is explored, which has been demonstrated to achieve TDD as low as 10^4 cm^{-2} [32]. The process begins with a relaxed bulk Ge epitaxial film on a Si substrate with a TDD of $\sim 10^8$ cm^{-2}. Bipolar electrochemical etching [33, 34] is used to etch mesopores that preferentially follow the threading dislocations through the Ge layer into the Si substrate. After porosification, thermal annealing leads to a morphological transformation in which the mesopores coalesce into energetically favourable nano-voids near the Ge/Si interface that annihilate threading dislocations within the voided region, leaving the Ge surface nearly free from dislocations, enabling high-quality epitaxial growth. This two-step process relies on industry standard techniques that are efficient and easily scalable [32]. Applied to III-V PV technologies, the process could allow for significant cost-reductions and expansions in production volume.

A detailed understanding of the electrical properties of the voided Ge/Si material is required to develop III-V PV devices on voided-Ge/Si substrates. In Chapter 3 of this thesis, I investigate the conductivity of mesoporous and voided-Ge films and develop an electrostatic model to predict the carrier density and mobility of voided semiconductor materials. This model is then applied within a simulated III-V multi-junction solar cell on a voided Ge/Si substrate.

1.2 Power-over-fiber

Photonic power systems consist of a monochromatic light source, a transmission medium, and a photonic power converter (PPC) that generates electricity via the photovoltaic effect, as depicted in Figure 1.2. The transmission medium is typically either optical fiber for power-over-fiber systems or air for free-space power transmission. This thesis will focus specifically on PPCs for power-over-fiber applications, which is the more versatile option because it does not require line-of-site trajectories.

Unlike conventional power transmission via copper wire, photonic power transmission does not generate and is fully immune to electromagnetic interference (EMI). This advantage makes photonic power transmission ideal for isolating sensitive electronics in electrically noisy environments. Optical fiber is lighter, less expensive, and more tolerant of the environment than copper cabling, and there is no risk of sparking or electrical shock during photonic power transmission. Both power and high-bandwidth data can be transmitted simultaneously over a single optical fiber link [35, 36].

Well established applications for photonic power transmission include powering sensors for high voltage transmission line monitoring [37–39] and supplying power within magnetic resonance imaging machines [40]. Emerging applications exist within the automotive industry, aerospace, avionics, defence, medicine, telecommunications, and smart-grid infrastructures.

As with any PV device, the output voltage of a PPC is limited by the bandgap of the absorbing material.

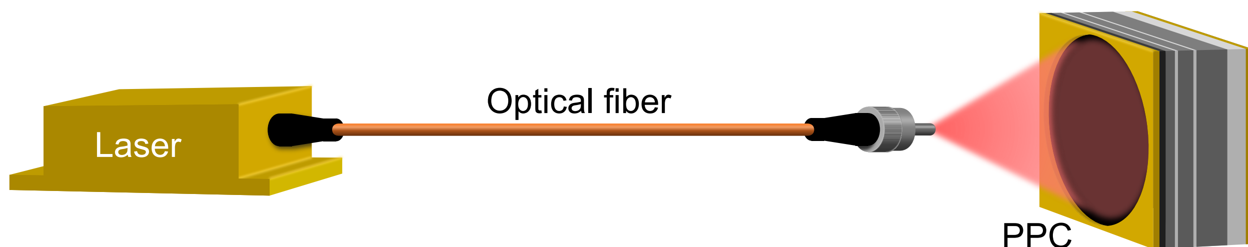

Figure 1.2: Schematic of power-over-fiber system, adapted from Beattie and Hinzer [2].

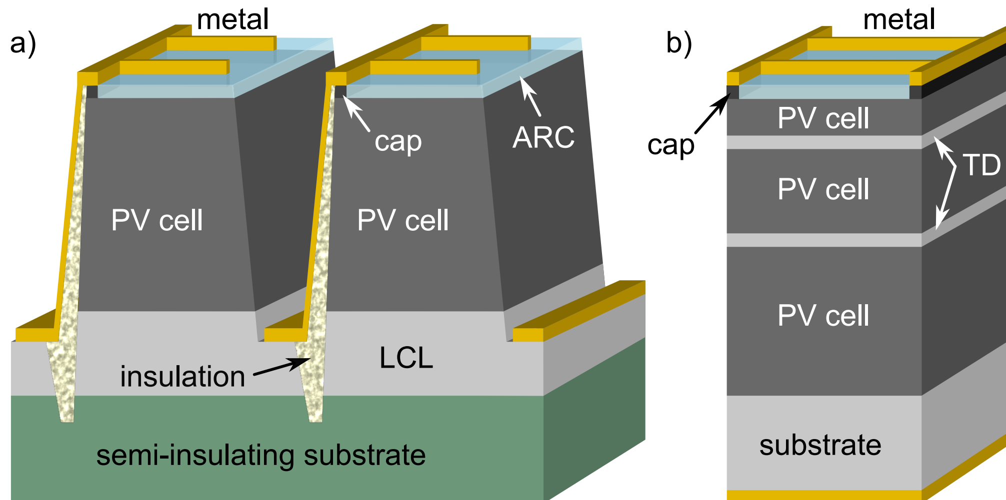

Figure 1.3: Schematic of PPCs with (a) lateral and (b) vertical segmentation. ARC: anti-reflection coating, LCL: lateral conduction layer, TD: tunnel diode. Reprinted with permission from Beattie and Hinzer [2].

Simple GaAs based PPCs are capable of generating about 1.2 V, which is too low for most power applications. Although conventional DC/DC converters could be used to increase the voltage, this approach is susceptible to EMI. A compact and integrated alternative involves scaling the voltage using series connections within the device itself.

One common approach involves lateral segmentation and interconnection of the device. Microfabrication techniques are used to laterally partition the device into series connected segments so that the output voltage scales with the number of serial interconnections. A schematic is shown in Figure 1.3a. This widely accepted technique can generate output voltages up to 30 V, allowing devices to be powered directly from the PPC. The main drawback of this approach is that it is highly sensitive to misalignment of the incident light [41, 42]. The photocurrent produced by each segment is proportional to the amount of illumination that it receives and the total device current is limited by the least productive segment.

State of the art PPCs are vertically segmented using a multi-junction architecture, as shown in Figure 1.3b. Rather than absorbing all of the input light within a single layer, the absorbing region is partitioned into semi-transparent PV sub-cells that are interconnected using tunnel diodes. The vertical segmentation technique, which is similar to multi-junction solar cell technology, greatly simplifies the fabrication and alignment requirements, improving the overall efficiency. Drawbacks of this method include more complex epitaxy and greater sensitivity to the wavelength of incident light, compared to the lateral segmentation technique [43]. An overview of select PPC devices from the literature is given in Table 1.2.

Table 1.2: Overview of PPC devices from the literature. Entries in red are commercially available.

Wavelength (nm)	Material	Segments (number)	Irradiance (W/cm^2)	V_{OC} (V)	Efficiency (%)	Ref.
805	GaAs	N/A	124	Unknown	57.4	[43]
808	GaAs	Vert. (3)	40	3.62	57	[44]
808	GaAs	Vert. (4)	40	4.83	58	[44]
808	GaAs	Vert. (6)	40	7.27	58	[44]
809	GaAs	Lat. (4)	2.4	4.7	56.3	[45]
810	GaAs	Vert. (2)	34	2.33	53.6	[46]
810	GaAs	Vert. (2) × Lat. (3)	10.6	6.67	34	[46]
820	GaAs	Lat. (6)	0.25 W*	6.7	55	[47]
820	GaAs	N/A	0.48	1.1	57	[48]
820	GaAs	N/A	61.5	1.2	56	[49]
820	GaAs	Lat. (8)	3.9	8.8	46	[49]
837	GaAs	Vert. (5)	10.2	5.9	66.3	[50]
850	GaAs	Vert. (20)	36.5	23.29	60.3	[50]
915	Si	Lat.**	1.3	> 2.8	41.2	[51]
915	Si	Lat.**	1.4	> 8.7	40.7	[51]
915	Si	Lat.**	1.5	> 29.2	40.5	[51]
1064	Si	Lat.**	1.4	> 26.7	25.4	[51]
1064	InGaAsP/InP	N/A	9.8	0.8	34.5	[52]
1064	InGaAs/GaAs	N/A	7	0.76	41.4	[53]
1070	InAlGaAs/InP	N/A	0.16	0.79	40.7	[54]
1310***	InGaAsP/InP	N/A	9.3	Unknown	51.1**	[55]
1310***	GaInAs/GaAs	N/A	5.2	Unknown	44.5**	[55]
1550	GaSb	N/A	11.4	~ 0.5	38.7	[56]
1550	InGaAsP/InP	N/A	0.1	Unknown	44.6	[57]
1550	InGaAs/InP	N/A	5.41	0.48	34	[48]
1680	GaSb	N/A	76.3	> 0.57	49	[49]
2100	InGaAs/InP	N/A	3.78	0.29	22	[48]

*Unknown sample area.
**Multi-junction architecture illuminated from the side, requires uniform illumination.
***Measured under AM1.5d illumination, reporting "equivalent monochromatic efficiency" at 1310 nm. Monochromatic measurements are reported in Chapter 5.

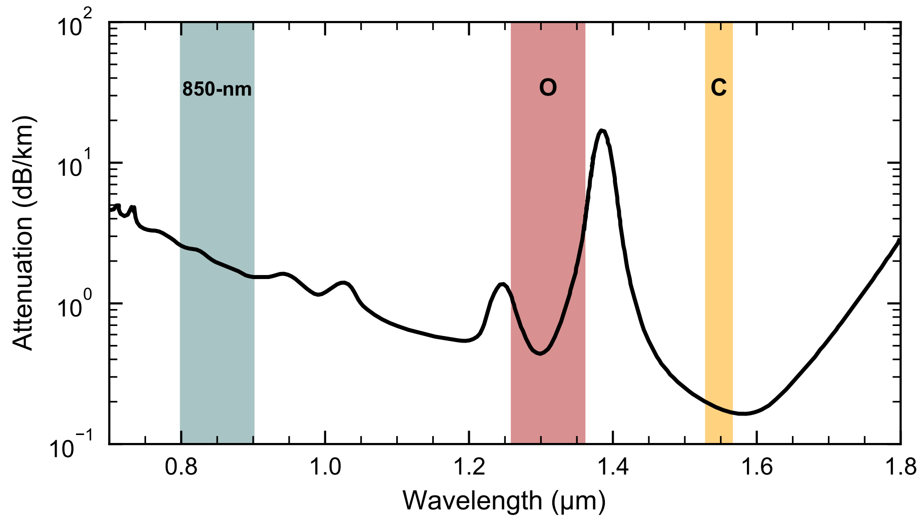

Figure 1.4: Attenuation in silica optical fiber as a function of wavelength (modified from Schubert [3]). The key telecommunications wavelength bands are highlighted.

The majority of PPCs that have been developed to date are based on GaAs and absorb light in the 800-850 nm wavelength range. These devices are well-suited to free-space power transmission, but are strongly attenuated in optical fiber. The attenuation in standard silica optical fiber is shown as a function of wavelength in Figure 1.4. Attenuation up to ~ 1.2 μm is dominated by Rayleigh scattering and above ~ 1.6 μm, the fiber is absorbent. The absorption peaks in the spectrum are primarily caused by moisture content within the silica. The original (O) telecommunications band, near 1310 nm, and the conventional (C) band, near 1550 nm, are much better suited to longer-distance power-over-fiber applications than the 850-nm band due to their much smaller attenuation coefficients.

The transmission efficiency at three key wavelengths used for telecommunications applications is shown in Figure 1.5, where we have used attenuation coefficients of 2 dB/km for 850 nm, 0.4 dB/km for 1310 nm, and 0.2 dB/km for 1550 nm [3]. After 1 km of transmission, the 850 nm light retains only 63% of its incident intensity whereas the 1310 nm and 1550 nm wavelengths retain 91% and 95% respectively. After 10 km, the 1310 nm and 1550 nm wavelengths retain 40% and 63% respectively while the 850 nm light is almost entirely lost.

To date, only a handful of PPCs have been designed for O- and C-band operation. Operation in these bands demands a shift away from GaAs-based devices to alternative materials with smaller bandgaps that can absorb the longer wavelengths. Smaller bandgaps are associated with comparatively smaller operating voltages, making segmentation strategies to boost the voltage even more important. For transmission dis-

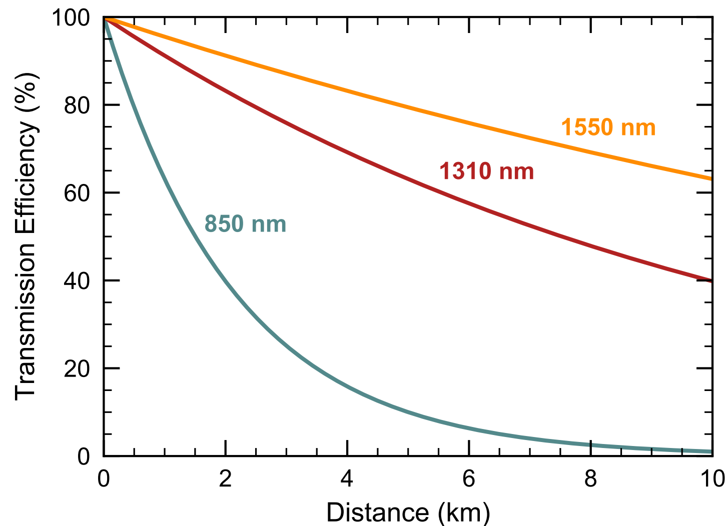

Figure 1.5: Transmission efficiency in optical fiber as a function of distance assuming attenuation coefficients of 2 dB/km for 850 nm, 0.4 dB/km for 1310 nm, and 0.2 dB/km for 1550 nm illumination.

tances ranging from a few-hundred meters to several kilometres, 1310-nm O-band devices are likely to be more practical than their C-band counterparts due to the larger base-voltage that they can achieve, meaning that fewer segments would be required to increase the voltage.

In Chapter 4 of this thesis, I introduce a PPC design targeting O-band absorption using the quaternary InAlGaAs lattice-matched to InP. In addition to the design and characterization of single-junction devices, compatible tunnel diodes are developed, enabling the realization of a two-junction PPC that is measured under 1319-nm laser illumination.

In Chapter 5, I characterize single-junction O-band PPCs developed at Fraunhofer ISE [55] with two different absorber materials: InGaAsP lattice-matched to InP and metamorphic GaInAs on a GaAs substrate. The impact of non-uniform illumination on the device performance is investigated.

1.3 Thesis outline

This thesis is comprised of six chapters, with Chapters 3, 4, and 5 each focusing on different devices and material systems related to III-V semiconductor photovoltaic devices. Several sections are written in a traditional manuscript format, while a total of two journal papers and two conference proceedings are included in the remaining sections. My own contributions and those of each co-author are clearly stated at the beginning of each publication.

Chapter 2 introduces the background material, detailing important concepts relating to the physics of semiconductors, the physics of photovoltaic devices, and an overview of the simulation techniques used to model these devices.

Chapter 3 presents an investigation of the electrical properties of voided Ge films and the implications for the development of III-V multi-junction solar cells on voided-Ge/Si substrates. Electrical characterization of mesoporous and voided Ge samples prepared at the Université de Sherbrooke is outlined in a journal paper that was published in *Nanotechnology* and an electrostatic model is proposed to predict the electrical properties of voided semiconductor materials (Section 3.1). A conference proceeding presented at the 7th World Conference On Photovoltaic Energy Conversion (WCPEC-7) is then included, which applies the electrostatic model to simulations of a triple-junction solar cell (Section 3.2).

Chapter 4 details the development of multi-junction InAlGaAs/InP PPCs targeting absorbance in the telecommunications O-band. Experimental characterization of bulk semiconductor layers and single-junction PV devices grown by molecular beam epitaxy at the University of Waterloo is detailed in the first section of this chapter (Section 4.1). Section 4.2 is a conference proceeding presented at the 47th IEEE Photovoltaic Specialists Conference (PVSC-47) that presents experimental characterization of 1- and 2-junction O-band PPCs. Section 4.3 consists of a brief analysis of the loss mechanisms within a single-junction InAlGaAs/InP PPC through device modelling. The chapter concludes with a journal paper that was published in *Applied Physics Letters* that presents detailed experimental characterization of InAlGaAs/InP tunnel diodes that are designed to be transparent in the O-band for the development of multi-junction PPC devices. (Section 4.4).

Chapter 5 contains experimental analysis of InGaAsP/InP and metamorphic GaInAs/GaAs O-band PPCs designed and fabricated at Fraunhofer ISE. Quantum efficiency measurements are analyzed for both PPC designs in Section 5.1. In Section 5.2, the impact of non-uniform illumination profiles on PPC performance is investigated.

The thesis concludes with Chapter 6, which summarizes the work as a whole and discusses the future outlook for each of the technologies discussed in this thesis.

Chapter 2

Physics of semiconductor materials and photovoltaic devices

This thesis lies at the intersection of materials science and semiconductor device engineering. An understanding of the physics of semiconductor materials and photovoltaic devices is essential to the research presented here. A brief overview of these topics is provided in this chapter.

2.1 Semiconductor materials

Semiconductors are a class of materials that exhibit electrical conductivities between those of conductors and insulators. By manipulating the number of electrons that are available to conduct current in the material, the conductivity itself can be modified. This is typically done by introducing impurity atoms called dopants into the crystalline structure of the semiconductor. The tunable nature of semiconductor conductivity means that these materials are highly suited to electronics applications, which use external circuitry to manipulate the flow of electric current within the semiconductor device.

Semiconductors can be either elemental or compound and are classified by periodic table group according to the number of valence electrons. Elemental semiconductors are formed from a single atomic species. Common examples include the group IV elements silicon (Si) and germanium (Ge). Compound semiconductors are formed of two or more atomic species. Common examples are the III-V binary semiconductors gallium arsenide (GaAs) and indium phosphide (InP). Compound semiconductors comprising three or more atomic species are referred to as semiconductor alloys and posses properties that are highly dependent on

composition.

The basic properties of semiconductors are described in this section.

2.1.1 Crystal structure and epitaxial growth

The atoms that comprise a semiconductor material are held together by covalent bonds in a crystal lattice. When formed under ideal conditions, bulk semiconductor crystals are highly uniform, possessing long-range order and symmetry. Sub-optimal conditions result in the formation of poly-crystalline semiconductors, which have randomly oriented crystalline grains without long-range order, or amorphous semiconductors, in which the atoms are arranged with approximate short-range order in the absence of long-range order.

The group IV semiconductors Si and Ge have diamond cubic lattice structures in which each group IV atom is bonded to its four nearest neighbours in a tetrahedral configuration. Most III-V semiconductors have zincblende cubic lattice structures that rely on tetrahedral bonding between the group III and the group V atoms. Both diamond and zincblende lattices can be though of as two intersecting face-centred cubic (FCC) lattice structures. The spacing between the atoms at the corners of the cube is known as the lattice constant, a_{lat}. The lattice structures are shown in Figure 2.1.

Crystalline materials can be obtained via epitaxial growth, a process in which material is deposited one atomic layer at a time on a crystalline substrate. The substrate acts as a template for the lattice of the epi-layer. When the lattice constant of the epitaxial material matches that of the substrate, high quality epitaxial layers can be achieved. On the other hand, lattice mismatch results in the formation of strained epitaxial

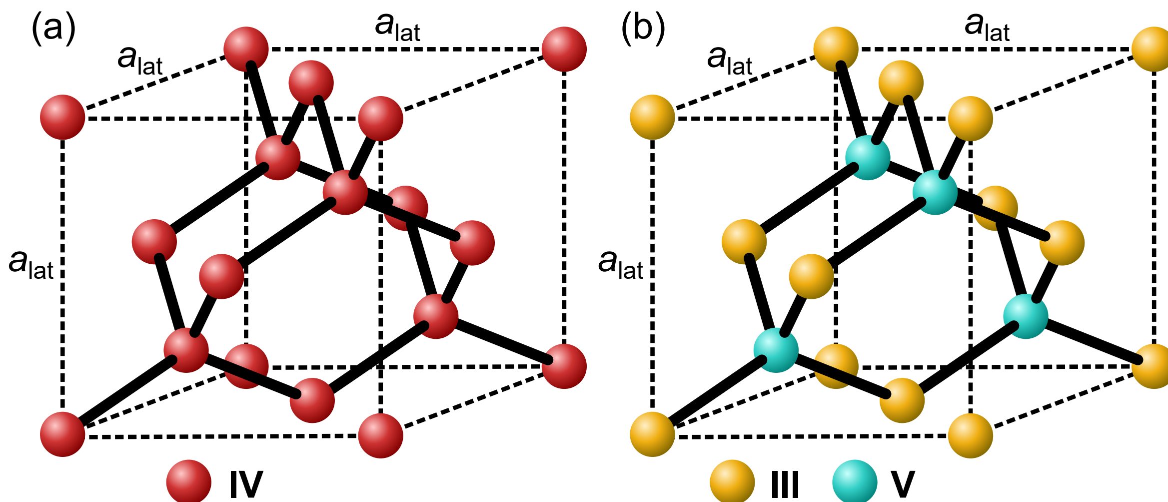

Figure 2.1: (a) Diamond cubic and (b) zincblende cubic lattice structures.

layers. When strained layers reach a critical thickness, strain relaxation occurs resulting in the formation of defects within the lattice structure. Defects that propagate vertically through the lattice are called threading dislocations and have an adverse effect on the material properties within the affected layers. Metamorphic (MM) epitaxy refers to lattice-mismatched epitaxy with epi-layer thickness exceeding the critical thickness. The goal of MM epitaxy is to accommodate strain with misfit dislocations while minimizing the formation of threading dislocations [58].

Two widely used forms of epitaxy are molecular beam epitaxy (MBE) and metal-organic vapour phase epitaxy (MOVPE). In MBE, elements required to form the epitaxial material are heated to high temperatures in effusion cells. Vaporized atoms are ejected from the cells through a narrow opening and directed towards the substrate where they deposit and form bonds with each other, generating the crystalline epi-layers. The thickness of the epi-layers is monitored by reflection high-energy electron diffraction (RHEED), in which a high-energy electron beam is deflected from the sample at a steep angle and the resulting diffraction pattern gives information about the film growth rate as well as surface morphology and geometry [59]. MBE is performed in an ultra-high vacuum environment $\left(10^{-9}\text{ Torr}\right)$, which is required for RHEED measurements and prevents contamination of the epi-material. The substrate is positioned on a rotating, temperature-controlled sample holder [60].

MOVPE is a form of chemical vapour deposition in which gaseous metal-organic precursors containing the elements required for epitaxy react with each other at the substrate, which is positioned on a temperature-controlled holder. Semiconductor compounds that are produced in the reaction adhere to the substrate, forming the crystalline epi-layers [59]. MOVPE operates at much higher pressures than MBE ($15-750$ Torr) [61]. The MOVPE growth rate is much higher than that of MBE, an important consideration for commercial applications in which high throughput is essential. For research applications, MBE is often preferred over MOVPE because it offers greater control over layer composition, uniformity, and interfaces [61].

2.1.2 Energy band structure

The electrons belonging to an isolated atom are restricted to atomic orbitals with quantized energy, where the occupation of an orbital is determined by the energy state of the atom. In the ground state, only the lowest energy orbitals are occupied.

Covalent bonding between atoms results in splitting of the orbital energy levels. When many covalent bonds are formed, as in a crystalline solid, repeated splitting results in the formation of continuous energy

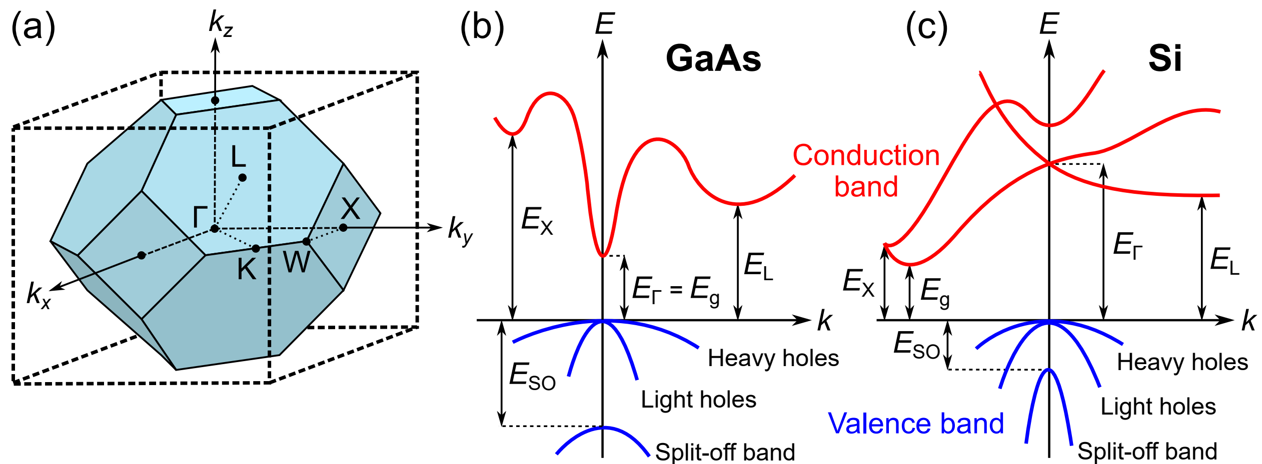

Figure 2.2: (a) First Brillouin zone for the FCC lattice. (b), (c) Energy band structure of GaAs and Si, respectively (modified using energy band structure from Ioffe Institute NSM archive [4]).

bands. When the band of ground state occupied energy levels overlaps with the band of ground state unoccupied energy levels to form a continuum, the material is a metal. When a gap exists between the ground state occupied and unoccupied energy bands, the material is a semiconductor. The band of occupied levels is called the valence band while the band of unoccupied levels is called the conduction band. In general, the vast majority of energy states within the valence band are occupied and electrons in the valence band are extremely limited in their mobility. When an electron gains enough energy, through photon absorption for example, it can be promoted into the conduction band where it can move around freely through the mostly unoccupied states. The width of the energy gap, know as the bandgap energy, is one of the key defining material properties of a semiconductor.

Due to the periodic nature of a crystal lattice, electrons occupy energy bands that extend throughout the crystal rather than being bound to a given atom. The energy band structure is described in momentum space (**k**-space), which is related to the crystal's reciprocal lattice. The reciprocal lattice can be calculated by taking the Fourier transform of the lattice in real space. The central primitive unit cell of the reciprocal lattice, which contains a single reciprocal lattice point at its centre, is known as the first Brillouin zone. Figure 2.2a shows the first Brillouin zone of the FCC lattice with high-symmetry points indicated. Figure 2.2b and c show the energy band structures for GaAs and Si respectively.

In a direct gap semiconductor, the minimum energy in the conduction band and the maximum energy in the valence band align at the Γ-point where $\mathbf{k} = 0$. An electron can be promoted from the valence band directly into the conduction band by absorbing a photon with energy equal to the bandgap energy, E_g. When

the conduction band minimum does not align with the valence band maximum, the energy gap is indirect and an electron must undergo a change in momentum (wavevector $\mathbf{k}$) to absorb a photon with energy E_g.

2.1.3 Density of states and carrier density

It is often convenient to depict the energy band structure as a function of position, with the valence band edge, E_v, and the conduction band edge, E_c, separated by the bandgap, as shown in Figure 2.3a. We assume that a continuum of state exists within each band. This is how the band structure will be illustrated for the remainder of this thesis. The minimum energy required to remove an electron from the semiconductor crystal altogether is called the electron affinity, χ. Electron affinity is defined as the difference between the conduction band edge and the vacuum level, E_{vac}, as shown in Figure 2.3a.

Between the valence band and the conduction band lies the Fermi level (E_F), which is represented by a dotted line in Figure 2.3a. The Fermi level represents the energy at which an energy level would have a 50% probability of being occupied under equilibrium conditions. The occupation probability of an energy level, E, can be calculated according to the Fermi-Dirac distribution:

$$f(E) = \frac{1}{1 + \exp\left(\frac{E - E_F}{k_B T}\right)} \quad (2.1)$$

where k_B is the Boltzmann constant and T is the temperature. Given that the Fermi level lies within the bandgap, it does not correspond to a real energy state that could be occupied by an electron. At absolute zero, every state below E_F (the valence band) is occupied and every state above E_F (the conduction band) is vacant. At $T > 0$, thermal excitation of electrons from the valence band into the conduction band results in a non-zero probability that some of the conduction band states will be occupied. The Fermi-Dirac distribution is shown for T = 1500 K in Figure 2.3b.

To determine the concentration of electrons within a material, it is necessary to consider the density of states (DOS) in addition to the occupation probability. The product of the DOS and the Fermi-Dirac distribution gives the number density of electrons at equilibrium as a function of energy, $n(E)$. Integrating over the conduction band yields the total concentration of electrons in the conduction band

$$n = \int_{E_c}^{\infty} n(E)\, dE = \int_{E_c}^{\infty} g_c(E) f(E)\, dE \quad (2.2)$$

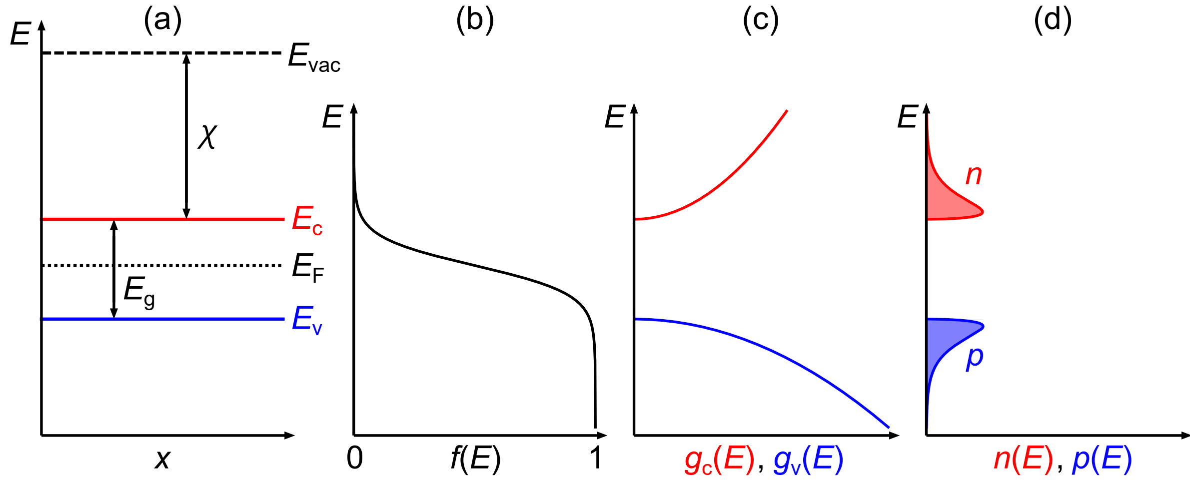

Figure 2.3: (a) Energy band diagram as a function of position, x, (b) Fermi-Dirac distribution $f(E)$, (c) density of states functions $g_c(E)$ and $g_v(E)$, and (d) number densities of electrons and holes, $n(E)$ and $p(E)$.

where g_c is the conduction band DOS. In the valence band where the vast majority of electronic states are occupied by electrons, it's customary to instead count the vacancies or "holes" left behind by electrons in the conduction band. The corresponding expression for the total concentration of holes is then

$$p = \int_{-\infty}^{E_v} p(E)\,dE = \int_{-\infty}^{E_v} g_v(E)\left[1 - f(E)\right] dE \tag{2.3}$$

where g_v is the valence band DOS. Using the Pauli exclusion principle and assuming that the band structure is parabolic in nature, which holds close to the band edge, the densities of states for the conduction and valence bands are

$$g_c(E) = \frac{1}{2\pi^2}\left(\frac{2m_c^*}{\hbar^2}\right)^{\frac{3}{2}}\sqrt{E - E_c}, \qquad g_v(E) = \frac{1}{2\pi^2}\left(\frac{2m_v^*}{\hbar^2}\right)^{\frac{3}{2}}\sqrt{E_v - E} \tag{2.4}$$

where $\hbar$ is the reduced Planck constant and m_c^* and m_v^* are the DOS effective masses for the conduction and valence bands respectively. The DOS functions and the number density of electrons and holes are plotted against energy in Figure 2.3c and d.

When the Fermi level is far from the band edges, the Boltzmann approximation can be used to simplify the calculation of electron and hole concentrations. Under the Boltzmann approximation,

$$f(E) \approx \exp\left(\frac{E_F - E}{k_B T}\right) \tag{2.5}$$

and the integrals in equations 2.2 and 2.3 can be evaluated exactly. The resulting expressions for electron and hole concentrations are

$$n = N_\mathrm{c} \exp\left(\frac{E_\mathrm{F} - E_\mathrm{c}}{k_\mathrm{B}T}\right), \qquad p = N_\mathrm{v} \exp\left(\frac{E_\mathrm{v} - E_\mathrm{F}}{k_\mathrm{B}T}\right) \tag{2.6}$$

where N_c and N_v are the effective DOS for the conduction and valence bands respectively, given by

$$N_\mathrm{c} = 2\left(\frac{m_\mathrm{c}^* k_\mathrm{B}T}{2\pi\hbar^2}\right)^{\frac{3}{2}}, \qquad N_\mathrm{v} = 2\left(\frac{m_\mathrm{v}^* k_\mathrm{B}T}{2\pi\hbar^2}\right)^{\frac{3}{2}} \tag{2.7}$$

For an intrinsic semiconductor, the concentration of electrons is perfectly balanced by the concentration of holes such that $n = p = n_\mathrm{i}$ where n_i is the intrinsic carrier density defined by the expression

$$n_\mathrm{i}^2 = np = N_\mathrm{c}N_\mathrm{v} \exp\left(-\frac{E_\mathrm{g}}{k_\mathrm{B}T}\right) \tag{2.8}$$

The Fermi level of an intrinsic semiconductor, E_i, lies close to the centre of the bandgap and can be calculated using the effective DOS

$$E_\mathrm{i} = \frac{E_\mathrm{c} - E_\mathrm{v}}{2} - \frac{k_\mathrm{B}T}{2} \ln\left(\frac{N_\mathrm{c}}{N_\mathrm{v}}\right) \tag{2.9}$$

2.1.4 Doping

Donor impurities “donate” extra valence electrons to the semiconductor, increasing the concentration of free electrons and shifting the Fermi level upwards toward the conduction band. This works because the donor atoms introduce an occupied energy level close to the conduction band edge, allowing electrons existing in that state to easily thermalize into the conduction band, ionizing the donor atoms. When the density of ionized donors $N_\mathrm{d} \gg n_\mathrm{i}$, $n \approx N_\mathrm{d}$ and correspondingly $p = n_\mathrm{i}^2/N_\mathrm{d}$. An energy band diagram and the computed number densities for electrons and holes are shown in Figure 2.4a and b for an n-type semiconductor.

Similarly, acceptor impurities increase the concentration of holes in the valence band by “accepting” valence electrons from the semiconductor, moving the Fermi level down toward the valence band. The acceptor introduces an unoccupied energy state close to the valence band edge that is easily filled by electrons thermalizing from the valence band, ionizing the acceptor atoms. When the density of ionized acceptors $N_\mathrm{a} \gg n_\mathrm{i}$, then $p \approx N_\mathrm{a}$ and correspondingly $n = n_\mathrm{i}^2/N_\mathrm{a}$. An energy band diagram and the computed number densities for electrons and holes are shown in Figure 2.4c and d for a p-type semiconductor.

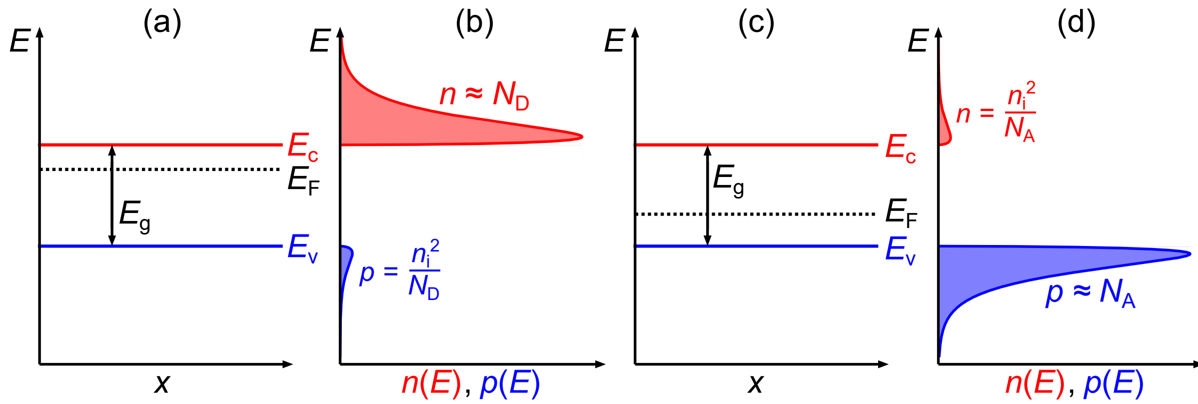

Figure 2.4: (a) Energy band diagram as a function of position, x, and (b) number densities of electrons and holes, $n(E)$ and $p(E)$, for an n-type semiconductor. (c) Energy band diagram and (b) number densities of electrons and holes for a p-type semiconductor.

2.1.5 Bias voltage

It's also possible to influence the carrier concentrations within a semiconductor by applying a bias voltage, V, that induces splitting of the Fermi level. Relaxation of the perturbed free electron and hole populations within their respective bands is orders of magnitude faster than relaxation between the bands. As such, the free electron and hole populations each relax to quasi-thermal equilibrium, associated with distinct quasi-Fermi levels, E_{Fn} and E_{Fp}. The difference between the quasi-Fermi levels is given by

$$\Delta\mu = E_{\mathrm{Fn}} - E_{\mathrm{Fp}} \tag{2.10}$$

where $\Delta\mu = qV$ for an ideal semiconductor with lossless transport.

The carrier concentrations under bias are then

$$n = N_{\mathrm{c}} \exp\left(\frac{E_{\mathrm{Fn}} - E_{\mathrm{c}}}{k_{\mathrm{B}}T}\right), \qquad p = N_{\mathrm{v}} \exp\left(\frac{E_{\mathrm{v}} - E_{\mathrm{Fp}}}{k_{\mathrm{B}}T}\right) \tag{2.11}$$

The impact of an applied bias voltage on the band diagram and the carrier densities is shown in Figure 2.5.

2.1.6 Conductivity and mobility

The conductivity of a semiconductor is directly related to the free carrier densities and is given by

$$\sigma = q\left(\mu_{\mathrm{n}} n + \mu_{\mathrm{p}} p\right) \tag{2.12}$$

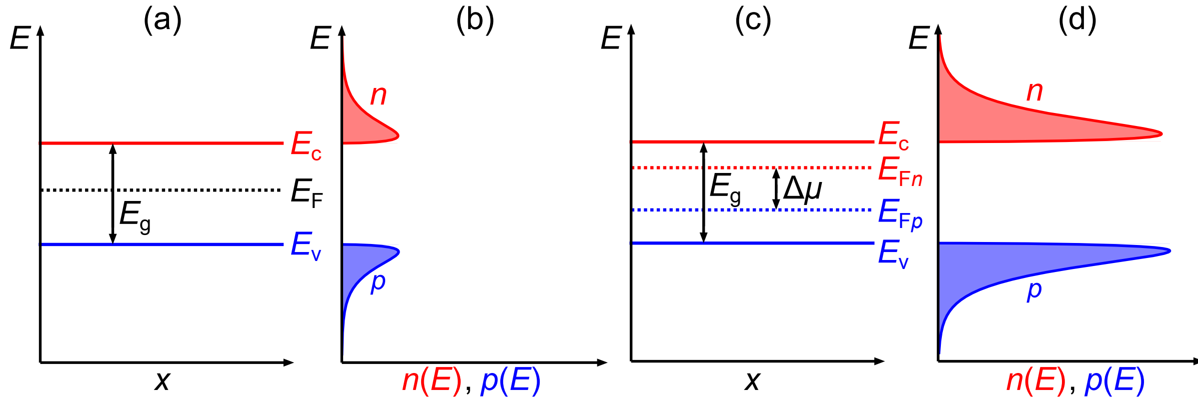

Figure 2.5: (a) Energy band diagram as a function of position, x, and (b) number densities of electrons and holes, $n(E)$ and $p(E)$, for an intrinsic semiconductor in equilibrium. (c) Energy band diagram and (b) number densities of electrons and holes for an intrinsic semiconductor under bias.

where μ_n and μ_p are the electron and hole mobilities and q is the electronic charge. In the context of semiconductors, we frequently discuss the resistivity, ρ, rather than conductivity where $\rho = 1/\sigma$. The carrier concentrations, and therefore conductivity, can be modified by introducing dopants to the crystal lattice.

The electrical mobility of a charged particle relates the magnitude of the drift velocity, v_drift, to electric field F

$$|v_\mathrm{drift}| = \mu F \tag{2.13}$$

The mobility is usually expressed in units of $\mathrm{cm}^2/(\mathrm{V\cdot s})$ and is limited by various scattering processes including phonon scattering and ionized impurity scattering, carrier-carrier scattering, and defect scattering. The contributions for each process can be summed according to Matthiessen's rule

$$\frac{1}{\mu} = \frac{1}{\mu_\mathrm{phonon}} + \frac{1}{\mu_\mathrm{doping}} + \frac{1}{\mu_\mathrm{carrier}} + \frac{1}{\mu_\mathrm{defect}} \tag{2.14}$$

The doping-dependent mobility of a bulk semiconductor can be described by empirical models such as the Sotoodeh model [62]:

$$\mu(N_\mathrm{d}, N_\mathrm{a}) = \mu_\mathrm{min} + \frac{\mu_\mathrm{max} - \mu_\mathrm{min}}{1 + \left(\frac{N_\mathrm{d}+N_\mathrm{a}}{N_0}\right)^{A^*}} \tag{2.15}$$

where μ_min, μ_max, N_0 and A^* are fitting parameters. This model accounts for both the phonon scattering and ionized impurity in accordance with Matthiessen's rule. With increasing doping density N_d and N_a, scattering through the Coulomb interaction results in a reduction in the mobility. Screening of the charged impurities by free carriers results in a levelling off of the mobility at higher doping densities. The model is

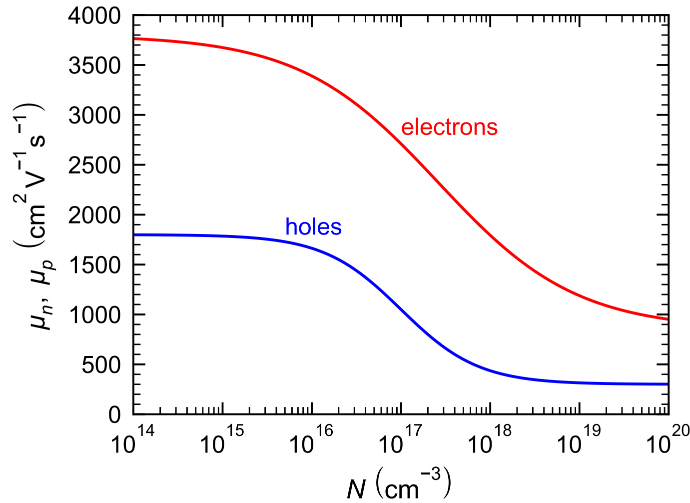

Figure 2.6: Doping dependent electron and hole mobilities, μ_n and μ_p, for Ge.

valid up to a doping density of $\sim 10^{20}$ cm^{-3}. The electron and hole mobilities for Ge are shown as a function of doping density in Figure 2.6.

2.1.7 Drift and diffusion

In general, current density in a semiconductor can be described as the sum of the drift current density and the diffusion current density

$$J = J_{\text{drift}} + J_{\text{diff}} \tag{2.16}$$

The drift current is induced by the presence of an electrostatic field F and follows the relation

$$J_{\text{drift}} = \sigma F = q\left(\mu_{\text{n}} n + \mu_{\text{p}} p\right) F = J_{\text{drift,n}} + J_{\text{drift,p}} \tag{2.17}$$

The presence of an electric field is associated with a gradient in the vaccum level and corresponding gradients in the conduction and valence bands. seThe free carriers move to minimize their electrostatic potential. Electrons are driven down the conduction band opposite to the direction of the electric field while holes migrate up the valence band in the direction of the field such that the current density and the field point in the same direction.

The diffusion current is induced by a gradient in the electron and hole concentrations and is given by

$$J_{\text{diff}} = q\left(D_{\text{n}}\nabla n - D_{\text{p}}\nabla p\right) = J_{\text{diff,n}} + J_{\text{diff,p}} \tag{2.18}$$

where D_{n} and D_{p} are the diffusion coefficients of electrons and holes, which are related to their corresponding mobilities by the Einstein relation, $D = \mu k_{\text{B}}T/q$. In a diffusion process, the carriers migrate from regions of high density to low density.

2.1.8 Generation and recombination

Aside from thermal generation, where electrons are promoted into the conduction band after gaining energy from lattice vibrations, photogeneration is the most important process for generating free carriers in a semiconductor. In photogeneration, an electron is promoted into the conduction band when it absorbs a photon with energy $E \geq E_{\text{g}}$. Whenever an electron is promoted from the valence to the conduction band, a hole is left behind in the valence band such that the generation rates of electrons and holes are identical. After absorbing a photon with energy $E > E_{\text{g}}$, the generated carriers lose energy through lattice interactions until they reach the band edge, a process called thermalization. The photogeneration and thermalization processes are shown in Figure 2.7a.

There are several methods by which carriers can recombine from band to band, including radiative, Auger, and Shockley-Read-Hall (SRH) recombination. Radiative recombination occurs when an electron and hole recombine through the emission of a photon, as shown in Figure 2.7b. The radiative recombination rate depends on carrier concentration as in the following equation

$$R_{\text{rad}}(n,p) = B_{\text{rad}}\left(np - \gamma_{\text{n}}\gamma_{\text{p}}n_{\text{i}}^{2}\right) \tag{2.19}$$

where B_{rad} is the radiative recombination coefficient with units of cm^3/s. γ_{n} and γ_{p} account for the difference in free carrier concentration when using Fermi-Dirac statistics compared to the Boltzmann approximation [63, 64]

$$\gamma_{\text{n}} = \frac{n}{n_{\text{Boltzmann}}} = \frac{n}{N_{\text{c}}}\exp\left(\frac{E_{\text{c}} - E_{\text{Fn}}}{k_{\text{B}}T}\right), \qquad \gamma_{\text{p}} = \frac{p}{p_{\text{Boltzmann}}} = \frac{p}{N_{\text{v}}}\exp\left(\frac{E_{\text{Fp}} - E_{\text{v}}}{k_{\text{B}}T}\right) \tag{2.20}$$

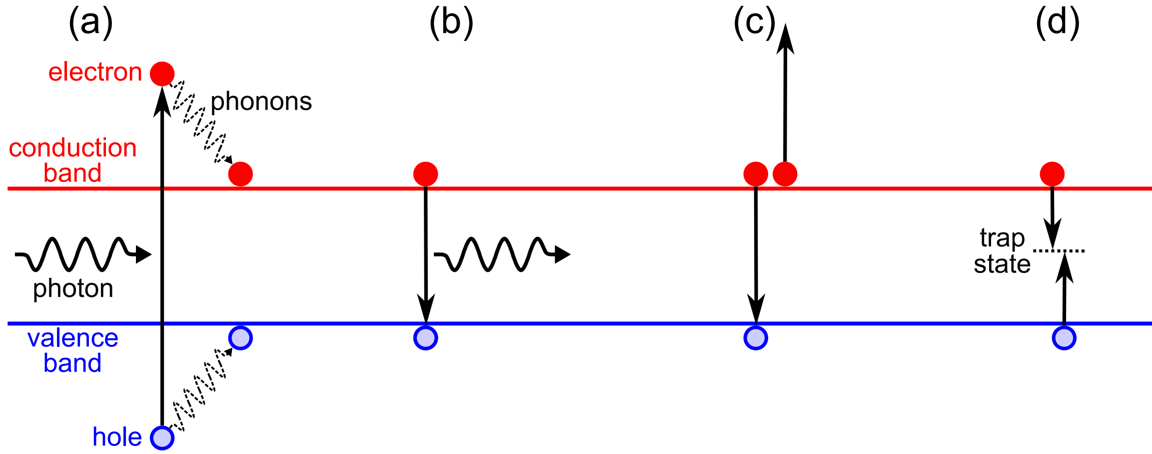

Figure 2.7: (a) Photogeneration and thermalization. (b) Radiative, (c) Auger, and (d) SRH recombination.

In doped semiconductors, the minority carrier radiative lifetimes are

$$\tau_{\mathrm{n,rad}} = \frac{1}{B_{\mathrm{rad}} N_{\mathrm{a}}}, \qquad \tau_{\mathrm{p,rad}} = \frac{1}{B_{\mathrm{rad}} N_{\mathrm{d}}} \tag{2.21}$$

for electrons and holes respectively.

Auger recombination is a non-radiative process in which an electron and a hole recombine in the presence of a third carrier. The energy from the recombination process is transferred to the third carrier, which is promoted to a higher energy state. The process is depicted in Figure 2.7c. The rate of Auger recombination varies with carrier concentration according to

$$R_{\mathrm{Aug}}(n,p) = \left(A_{\mathrm{Aug,n}} n + A_{\mathrm{Aug,p}} p\right)\left(np - n_i^2\right) \tag{2.22}$$

where $A_{\mathrm{Aug,n}}$ and $A_{\mathrm{Aug,p}}$ are the Auger recombination coefficients with units of cm^6/s. For a doped semiconductor, the corresponding minority carrier Auger lifetimes are

$$\tau_{\mathrm{Aug,n}} = \frac{1}{A_{\mathrm{Aug,n}} N_{\mathrm{a}}^2}, \qquad \tau_{\mathrm{Aug,p}} = \frac{1}{A_{\mathrm{Aug,p}} N_{\mathrm{d}}^2} \tag{2.23}$$

for electrons and holes respectively.

SRH recombination occurs when carriers recombine via trap states within the bandgap, as in Figure 2.7d. These trap states are often associated with lattice impurities such as dopants. The minority carrier lifetime

can be modelled empirically as a function of the doping density according the the following equation

$$\tau_{\mathrm{SRH}}(N_{\mathrm{d}}, N_{\mathrm{a}}) = \tau_{\min} + \frac{\tau_{\max} - \tau_{\min}}{1 + \left(\frac{N_{\mathrm{d}} + N_{\mathrm{a}}}{N_0}\right)^{\gamma^*}} \tag{2.24}$$

where $\tau_{\min}$, $\tau_{\max}$, N_0 and γ^* are fitting parameters associated with the material. Carrier lifetime goes down for higher doping concentration. This is because the high density of impurities is associated with a higher density of recombination centres. Trap states may also be induced by lattice defects such as threading dislocations, which will be discussed further in Section 3.2. The rate of SRH recombination can be calculated from the lifetimes and the carrier densities as

$$R_{\mathrm{SRH}}(n, p) = \frac{np - \gamma_{\mathrm{n}}\gamma_{\mathrm{p}} n_{\mathrm{i}}^2}{\tau_{\mathrm{SRH,n}}\left(p + \gamma_{\mathrm{p}} p_{\mathrm{t}}\right) + \tau_{\mathrm{SRH,p}}\left(n + \gamma_{\mathrm{n}} n_{\mathrm{t}}\right)} \tag{2.25}$$

where p_{t} and n_{t} are the carrier densities when E_{Fp} and E_{Fn} are equal to the energy of the trap state.

The effective minority carrier lifetimes combine all of the recombination mechanisms according to Matthiessen's rule

$$\frac{1}{\tau} = \frac{1}{\tau_{\mathrm{rad}}} + \frac{1}{\tau_{\mathrm{Aug}}} + \frac{1}{\tau_{\mathrm{SRH}}} \tag{2.26}$$

Radiative recombination is the dominant recombination processor for high-quality direct-gap semiconductors, whereas for high-quality indirect-gap semiconductors, the Auger process dominates. When the density of defects and impurities is sufficiently large, SRH recombination may become dominant in either direct- or indirect-gap semiconductors.

2.1.9 Transport equations

The key equations that describe carrier transport in semiconductor materials are Poisson's equation and the continuity equations. Poisson's equation relates the charge density to the electric field, $\mathbf{F}$, and therefore to the electrostatic potential, ϕ

$$\nabla \cdot \mathbf{F} = \nabla \cdot (-\nabla\phi) = \frac{q}{\varepsilon_{\mathrm{s}}}\left(p - n + N_{\mathrm{d}} - N_{\mathrm{a}}\right) \tag{2.27}$$

where ε_s is the static dielectric constant. The continuity equations ensure that the number of electrons is conserved at all times

$$-\frac{1}{q}\nabla \cdot \mathbf{J}_n = G_n - R_n - \frac{\partial n}{\partial t} \quad (2.28)$$

$$\frac{1}{q}\nabla \cdot \mathbf{J}_p = G_p - R_p - \frac{\partial p}{\partial t} \quad (2.29)$$

where G_n and G_p are the generation rates for electrons and holes and R_n and R_p are the corresponding recombination rates. In steady state, the carrier densities are constant over time such that $\frac{\partial n}{\partial t} = \frac{\partial p}{\partial t} = 0$. In this way, Poisson's equation and the continuity equations form a set of coupled partial differential equations.

2.1.10 Optical properties

The interaction between light and matter for a bulk semiconductor is described by the complex index of refraction

$$\tilde{n} = n_r + i\kappa \quad (2.30)$$

where n_r is the real part and κ is the imaginary part, called the extinction coefficient.

The fraction of normally incident light reflected at the interface between two materials with different refractive index, called the reflectivity, is given by

$$\mathcal{R} = \left|\frac{\tilde{n}_1 - \tilde{n}_2}{\tilde{n}_1 + \tilde{n}_2}\right|^2 \quad (2.31)$$

For a typical semiconductor, $n_r \sim 3$ to 4 for visible and near infrared wavelengths such that $\sim 30\%$ of light is reflected at an interface with air $\left(n_{r,air} = 1\right)$.

The absorption of light is described by the absorption coefficient, α, which is related to the extinction coefficient by the relation

$$\alpha = \frac{4\pi\kappa}{\lambda} \quad (2.32)$$

where λ is the wavelength of light. For a direct-gap semiconductor, the absorption coefficient varies according to

$$\alpha(E) \propto \frac{\sqrt{E - E_g}}{E} \quad (2.33)$$

The absorbance of a bulk semiconductor material with thickness t follows the Beer-Lambert law and is

given by

$$\mathcal{A} = 1 - e^{-\alpha t} \tag{2.34}$$

Following this relation, the intensity of light decays exponentially with depth as it penetrates into a semiconductor, provided that its photon energy is larger than E_{g}.

2.1.11 Ternary and quaternary alloys

Compound semiconductors possess material properties that are highly dependent on the material composition. By alloying binary semiconductors to create ternary or quaternary compounds, its possible to access a range of materials parameters, including bandgaps and lattice constants, that would otherwise be inaccessible. There are several ternary and quaternary alloys discussed in this thesis, with a particular emphasis on the quaternary InAlGaAs, which is discussed at length in Chapter 4.

The majority of the material parameters for a ternary compound with the form $\mathrm{A}_x\mathrm{B}_{1-x}\mathrm{C}$ are empirically found to obey the following relation, which depends on the binary parameters and the composition x according to [5, 65]

$$Par_{ABC}(x) = Par_{\mathrm{AC}}x + Par_{\mathrm{BC}}(1-x) - K_{Par}x(1-x) \tag{2.35}$$

where Par is an arbitrary material parameter, Par_{AC} and Par_{BC} are the values of that parameter corresponding to the binaries AC and BC, and K_{Par} is the bowing parameter associated with Par. For most parameters, the K_{Par} is negligible and equation 2.35 reduces to a simple linear interpolation. One parameter for which K_{Par} is usually significant is the bandgap.

There are two types of quaternary alloys. The first type is a combination of the four binaries, AC, AD, BC, and BD, with the form $\mathrm{A}_x\mathrm{B}_{1-x}\mathrm{C}_y\mathrm{D}_{1-y}$. The material parameters for quaternaries of this type can be calculated using the parameters for the ternary compounds ABC, ABD, ACD, and BCD according to [5, 65]

$$\begin{aligned} Par_{ABCD}(x,y) = &\frac{x(1-x)[yPar_{ABC}(x) + (1-y)Par_{ABD}(x)]}{x(1-x)+y(1-y)} \\ &+ \frac{y(1-y)[xPar_{ACD}(y) + (1-x)Par_{BCD}(y)]}{x(1-x)+y(1-y)} \end{aligned} \tag{2.36}$$

The second type is a combination of the three binaries AD, BD, and CD with the form $\mathrm{A}_x\mathrm{B}_y\mathrm{C}_{1-x-y}\mathrm{D}$. This thesis is extensively concerned with InAlGaAs, a quaternary of the second type with binaries InAs, AlAs, and GaAs. The material parameters for quaternaries of this type can be calculated using the parameters

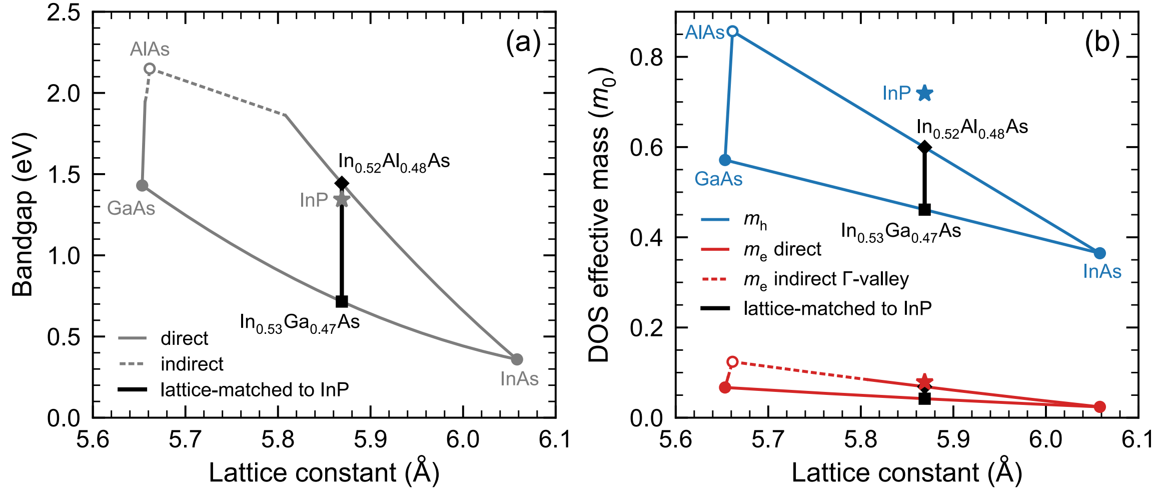

Figure 2.8: (a) Bandgap and (b) DOS effective masses as a function of lattice constant for ternaries making up InAlGaAs. Parameters for the InAlGaAs compositions lattice-matched to InP are indicated. Binary and bowing parameters are taken from [5].

for the ternary compounds ABD, BCD, and ACD according to [5, 65]

$$Par_{ABCD}(x,y) = \frac{xyPar_{ABD}(u) + y(1-x-y)Par_{BCD}(v) + x(1-x-y)Par_{ACD}(w)}{xy + y(1-x-y) + x(1-x-y)} \tag{2.37}$$

$$u = \frac{1-x-y}{2}, \qquad v = \frac{2-x-2y}{2}, \qquad w = \frac{2-2x-y}{2}$$

Alternatively, quaternaries can sometimes be described as a combination of two ternary semiconductors. In this case, the material parameters could be calculated according to equation 2.35 where the binary parameters are replaced by the relevant ternary parameters.

The bandgap is plotted as a function of lattice constant for the ternary alloys that make up the quaternary InAlGaAs in Figure 2.8a. The bandgap range for InAlGaAs lattice matched to InP, a mixture of $In_{0.52}Al_{0.48}As$ and $In_{0.53}Ga_{0.47}As$, is indicated. Figure 2.8b shows the corresponding DOS effective masses for the ternaries making up InAlGaAs.

2.2 Photovoltaic energy conversion

PV devices are made from layers of doped semiconductor materials arranged to form a p-n junction. When light is incident on a PV device, photons are absorbed in the semiconductor material and electrons are promoted from the valence band into the conduction band creating free carriers. The built-in asymmetry

of the p-n junction sweeps free carriers of opposite polarities in opposite directions, separating them before they recombine. The free carriers are then fed into an external circuit, generating electricity. This process is called the photovoltaic effect. The basic operation of PV devices is described in this section along with the standard metrics that are used to evaluate and characterize PV device performance.

2.2.1 p-n junctions

The foundation of a photovoltaic cell is the p-n junction, which exists at the intersection between adjacent p- and n-type semiconductor regions. The junction is characterized by a built-in electrostatic field generated by the diffusion of majority carriers across the interface, leaving behind charged impurities on either side. The presence of the field induces a minority carrier drift current that balances the majority carrier diffusion under equilibrium conditions. In equilibrium, the Fermi level is constant throughout the device. The built-in potential is given by the difference in work function between the p-side and the n-side, where the work function $\Phi = (E_{\mathrm{vac}} - E_{\mathrm{F}})/q$. For a homojunction where the same semiconductor material is used on either side of the junction, the built-in potential reduces to

$$V_{\mathrm{bi}} = \frac{k_{\mathrm{B}}T}{q} \ln\left(\frac{N_{\mathrm{d}}N_{\mathrm{a}}}{n_{\mathrm{i}}^2}\right) \tag{2.38}$$

A sketch of the equilibrium band-diagram for a p-n junction with $N_{\mathrm{d}} = N_{\mathrm{a}}$ is shown in Figure 2.9a.

The interfacial region occupied by the ionized impurity atoms is known as the depletion or space-charge region. Under the depletion approximation, we estimate the width of the space-charge region by assuming that the carriers in this region are fully depleted. The potential is taken to be constant in the quasi-neutral regions outside of the space charge region. The boundaries of the space charge region, known as the depletion widths, can be found using Poisson's equation [12]. They are

$$w_{\mathrm{p}} = \frac{1}{N_{\mathrm{a}}}\sqrt{\frac{2\varepsilon_{\mathrm{s}}V_{\mathrm{bi}}}{q\left(\frac{1}{N_{\mathrm{a}}}+\frac{1}{N_{\mathrm{d}}}\right)}}, \qquad w_{\mathrm{n}} = \frac{1}{N_{\mathrm{d}}}\sqrt{\frac{2\varepsilon_{\mathrm{s}}V_{\mathrm{bi}}}{q\left(\frac{1}{N_{\mathrm{a}}}+\frac{1}{N_{\mathrm{d}}}\right)}} \tag{2.39}$$

Under an applied bias voltage V, the total potential difference across the space-charge region is given by $V_{\mathrm{j}} = V_{\mathrm{bi}} - V$. Consequently, in the case of forward bias where $V_{\mathrm{j}} < V_{\mathrm{bi}}$, the barrier to majority carrier diffusion across the junction is reduced. This leads to a net current flow that is dominated by majority carrier diffusion, injecting minority carriers into the quasi-neutral regions. Under reverse bias, $V_{\mathrm{j}} > V_{\mathrm{bi}}$ and the

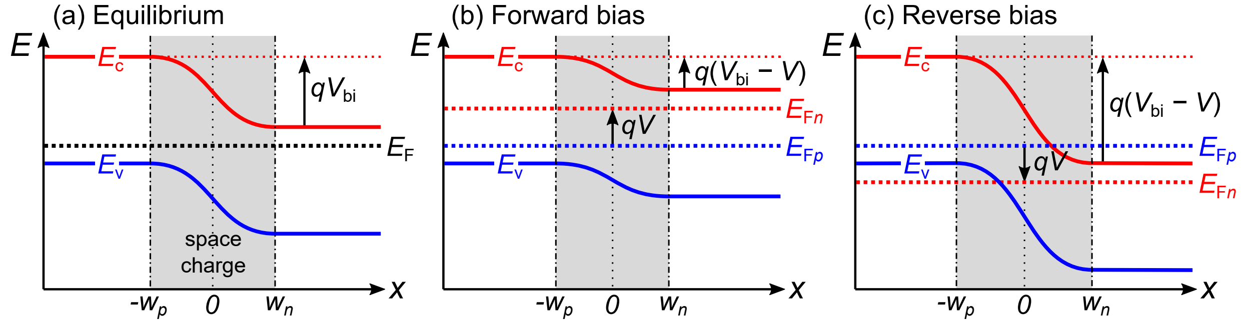

Figure 2.9: Sketch of p-n junction band diagrams in (a) equilibrium, (b) forward bias, and (c) reverse bias.

barrier to majority carrier diffusion increases, leading to a net current flow dominated by the minority carrier drift current, which extracts minority carriers from the quasi-neutral regions. In both cases, the potential drop is restricted to the space-charge region, wherein $qV = E_{\mathrm{Fn}} - E_{\mathrm{Fp}}$ such that [12]

$$np = n_{\mathrm{i}}^2 \exp\left(\frac{qV}{k_{\mathrm{B}}T}\right) \quad \text{for} \quad -w_{\mathrm{p}} < x < w_{\mathrm{n}} \tag{2.40}$$

Band diagrams depicting the junction in forward and reverse bias are shown in Figure 2.9b and c.

2.2.2 Photocurrent and quantum efficiency

Under illumination, splitting of the electron and hole quasi-Fermi levels gives rise to minority carrier densities that exceed the equilibrium concentrations. The elevated concentration of minority carriers in the depletion region results in a significant drift current known as the photocurrent or the short-circuit current density (J_{SC}). The band diagram for the illuminated p-n junction at short-circuit, where the net current density is equal to J_{SC}, is shown in Figure 2.10a.

The magnitude of the photocurrent is related to the incident photon flux (Φ_{p}) by the external quantum efficiency (EQE), which is the ratio of the number of carriers collected by the external circuit to the number of incident photons. Both the photon flux and the external quantum efficiency are functions of photon energy, and so the total photocurrent density is given by

$$J_{\mathrm{SC}} = q \int_0^{\infty} \Phi_{\mathrm{p}}(E)\, EQE(E)\, dE \tag{2.41}$$

In the ideal case, $EQE = 1$ for all photon energies $E \geq E_{\mathrm{g}}$ and $EQE = 0$ for $E < E_{\mathrm{g}}$. In reality, a variety of factors limit the EQE for $E \geq E_{\mathrm{g}}$. These factors include reflection from surfaces and interfaces,

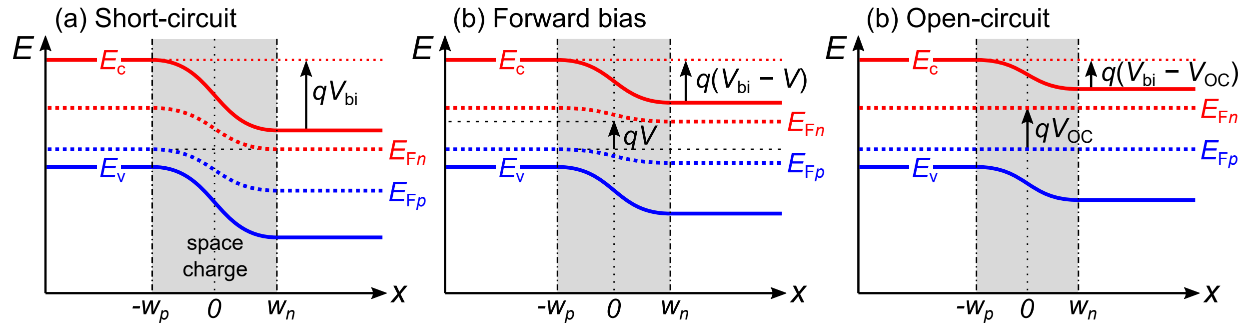

Figure 2.10: Sketch of illuminated p-n junction band diagrams at (a) short-circuit, (b) forward bias, and (c) open-circuit.

transmission through the absorbing material, recombination of free carriers before they are collected, and parasitic absorption in regions of the PV device other than the active layers. Furthermore, phonon interactions and impurity states enable small amounts of sub-gap absorption, leading to formation of an Urbach tail with $EQE > 0$ below the bandgap[66, 67].

When assessing the loss mechanisms in a PV device, another useful metric is the internal quantum efficiency (IQE). IQE is defined as the ratio of the the number of carriers collected by the external circuit to the number of absorbed photons, given by

$$IQE(\lambda) = \frac{EQE(\lambda)}{1 - \mathcal{R}(\lambda) - \mathcal{T}(\lambda)} \tag{2.42}$$

where $\mathcal{R}(\lambda)$ is the reflectivity and $\mathcal{T}(\lambda)$ is the transmittance.

2.2.3 Current-voltage characteristics

The impact of an applied forward bias on the band diagram of an illuminated PV device is shown in Figure 2.10b. The forward bias reduces the potential barrier across the junction, resulting in a majority carrier diffusion current that injects minority carriers into the quasi-neutral regions, opposing the photocurrent. The net current flow within a PV device can be expressed in terms of the non-ideal diode equation

$$I(V) = I_0 \left[\exp\left(\frac{qV}{n_{\mathrm{ideal}} k_{\mathrm{B}} T} \right) - 1 \right] - I_{\mathrm{SC}} \tag{2.43}$$

where I_0 is that dark saturation current, n_{ideal} is the ideality factor, and $I_{\mathrm{SC}} = J_{\mathrm{SC}} A$ for a PV device of active area A. In an ideal diode where there is very little recombination in the space-charge region, the dark current

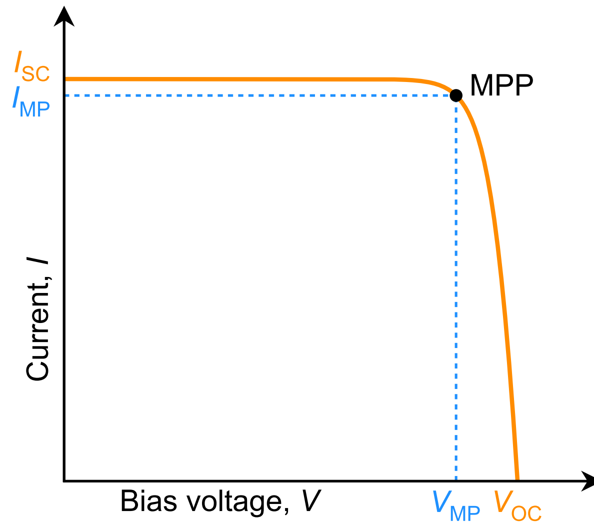

Figure 2.11: Sample I-V curve for an illuminated PV device.

flow is dominated by diffusion and $n_{\text{ideal}} = 1$. In the other extreme, a significant amount of recombination within the space-charge region can sometimes dominate the dark current such that $n_{\text{ideal}} = 2$.

The inclusion of parasitic series and shunt resistances in equation 2.43 results in the modified expression

$$I(V) = I_0 \left[\exp\left(\frac{q(V - IR_s)}{n_{\text{ideal}} k_B T} \right) - 1 \right] + \frac{V - IR_s}{R_{sh}} - I_{SC} \tag{2.44}$$

where R_s is series resistance and R_{sh} is shunt resistance. In the ideal case, $R_s = 0$ to and $R_{sh} \rightarrow \infty$.

When plotting the current-voltage characteristics of an illuminated PV device, the sign of the current is often swapped so that the photocurrent is positive and the dark current is negative. A sample I-V curve is shown in Figure 2.11 with the important points highlighted. In addition to the short-circuit current, there are several key figures of merit to be considered.

The open-circuit voltage (V_{OC}) represents the bias voltage at which the current through the illuminated PV device goes to zero. The band diagram for an illuminated PV device at open circuit is shown in Figure 2.10c. The open-circuit condition is satisfied when the light induced current (J_{SC}) is perfectly balanced by the dark current of the diode. Noting that J_{SC} scales linearly with illumination intensity and the dark current increases exponentially with temperature, the V_{OC} is found to increase logarithmically with illumination intensity. The V_{OC} cannot be larger than the bandgap of the absorbing semiconductor (i.e. $V_{OC} < E_g/q$). For a very good solar cell illuminated at 1-sun $\left(0.1\ \text{W/cm}^2\right)$ we can expect $V_{OC} \sim E_g/q - 0.4$ V [68].

The maximum power point (MPP) is the point on the *I-V* curve at which the maximum output power $P_{\max}$ is achieved. In short, $P_{\max} = I_{\mathrm{MP}} V_{\mathrm{MP}}$, where I_{MP} and V_{MP} are respectively the current density and voltage at maximum power. The "squareness" of the *I-V* curve is quantified by the fill factor (FF) where

$$FF = \frac{P_{\max}}{I_{\mathrm{SC}} V_{\mathrm{OC}}} = \frac{I_{\mathrm{MP}} V_{\mathrm{MP}}}{I_{\mathrm{SC}} V_{\mathrm{OC}}} \tag{2.45}$$

The final figure of merit is the optical-to-electrical conversion efficiency (η), which is defined by

$$\eta = \frac{P_{\max}}{P_{\mathrm{in}}} = \frac{I_{\mathrm{SC}} V_{\mathrm{OC}} FF}{P_{\mathrm{in}}} \tag{2.46}$$

where P_{in} is the power of the incident light.

The relationship between I_{SC} and P_{in} is dictated by the responsivity, R, where

$$I_{\mathrm{SC}} = R P_{\mathrm{in}} \tag{2.47}$$

The responsivity is heavily dependent on the incident spectrum and it is sometimes more convenient to discuss the spectral response SR which is a function of wavelength

$$SR(\lambda) = \frac{\lambda q}{hc} EQE(\lambda) \tag{2.48}$$

Both R and SR have units of A/W.

2.2.4 Multi-junction solar cells

One of the critical limitations of PV devices is their inability to absorb photons with $E < E_{\mathrm{g}}$. A significant portion of the solar energy spectrum may be inaccessible to a given solar cell depending on the bandgap energy of its absorber material. Furthermore, for photons with $E > E_{\mathrm{g}}$, the excess energy is lost to lattice vibrations in the thermalization process and is not collected by the external circuit. Multi-junction solar cells (MJSC) employ vertically stacked PV subcells, each with a different bandgap, to absorb a greater portion of the solar spectrum and minimize thermalization losses.

MJSCs are grown by epitaxy, with adjacent subcells interconnected by tunnel diodes that act as low-resistance ohmic interfaces. The epitaxial nature of the multi-junction architecture requires lattice-matching

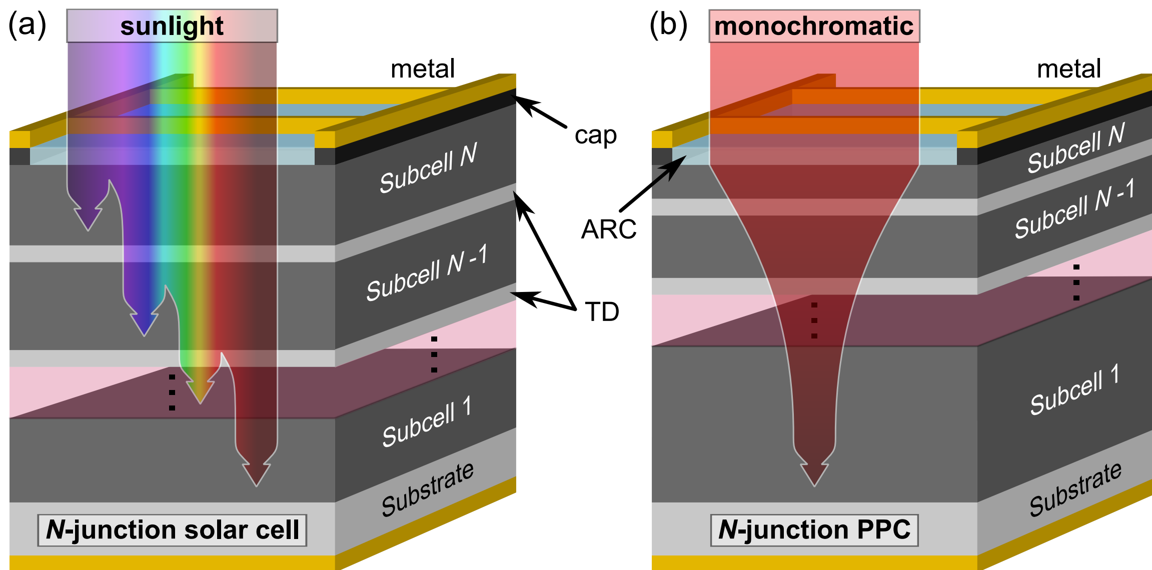

Figure 2.12: Schematics depicting (a) an N-junction solar cell and (b) an N-junction PPC. The incident light is indicated and key PV cell components are labelled. TD: tunnel diode, ARC: anti-reflection coating.

of the semiconductor materials throughout the layer stack to prevent the formation of threading dislocations in the crystal lattice. This limits the available bandgaps to those of semiconductors that are lattice-matched to readily available crystalline substrates such as Ge or GaAs. Alternatively, several methods exist to relax the requirement for lattice matching through the use of engineered substrates [28–32] (to be discussed in Chapter 3) or metamorphic buffer layers [20, 55, 69] (to be discussed in Chapter 5).

The subcells of the N-junction MJSC are arranged with the largest bandgap, $E_{g,N}$ at the top and the smallest bandgap, $E_{g,1}$, at the bottom. In this way, light with $E \geq E_{g,N}$ is absorbed in the top subcell while light with $E < E_{g,N}$ passes through to be absorbed in subsequent subcells. Only light with $E < E_{g,1}$ will be lost. A schematic of an N-junction solar cell is shown in Figure 2.12a.

Given the series-connected nature of the subcells, the current flow through the entire stack is limited by the lowest producing subcell. To prevent current-limiting, the bandgaps and thicknesses of each subcell are selected so that each subcell produces the same current. This is referred to as current-matching. The total output voltage is the sum of the voltages of each subcell.

2.2.5 Multi-junction photonic power converters

Optimized for monochromatic illumination, PPCs do not suffer from the transparency and thermalization losses that affect solar cells. As such, multi-junction designs are not required to achieve high PPC efficiencies

> 50% [70].

One particular challenge with PPCs is that the output voltage is limited by the bandgap of the absorber material. The voltage produced by a single cell is often insufficient to power the desired load. This problem can be rectified by adopting a multi-junction architecture, portioning the absorber material into optically thin subcells that are connected in series by tunnel diodes. The subcells are made from the same absorber material and each have the same bandgap. Their thicknesses are chosen to absorb equal portions of the monochromatic light and produce the same current to achieve current-matching. When current-matching is achieved, the operating current density of the N-junction PPC will be $J = J_{1J}/N$, where J_{1J} is the current of an equivalent single-junction PPC. The total output voltage scales with the number of junctions and can be tailored to the target application.

A schematic of an N-junction PPC is shown in Figure 2.12b. Following Beer-Lambert absorption as in equation 2.34, where absorption is strongest near the surface and decays exponentially with depth, the subcells are arranged from thinnest at the top to thickest at the bottom.

The wavelength-dependent nature of the optical absorption means that multi-junction PPCs are optimized for a specific wavelength of light. Deviations from the target wavelength $\lambda_{\mathrm{target}}$ result in performance losses when the current is limited by either the bottom subcell for $\lambda < \lambda_{\mathrm{target}}$ or by the top subcell for $\lambda > \lambda_{\mathrm{target}}$. The tolerance for wavelength deviations without significant current loss depends on the strength of the luminescent coupling, in which the photons emitted in a given junction by radiative recombination processes are reabsorbed in other junctions, helping to balance the current. Luminescent coupling is very strong in materials where radiative recombination is the dominant recombination process, leading to wavelength tolerances on the order of 100 nm [71]. In materials that have significant non-radiative recombination, luminescent coupling is much weaker.

2.2.6 Tunnel diodes

Multi-junction PV devices rely on tunnel diodes (TD) to connect the junctions. The TDs act as low-resistance series connections, allowing current to flow from one subcell to the next with minimal resistive losses. The TD structure consists of a very highly doped p-n junction with opposite orientation compared to the n-p junctions that comprise the absorbing subcells. The high doping creates a very abrupt junction, allowing majority carriers on either side of the junction to recombine by tunneling through the potential barrier.

An example of the equilibrium band-structure for a basic TD is shown in Figure 2.13a. Under an applied

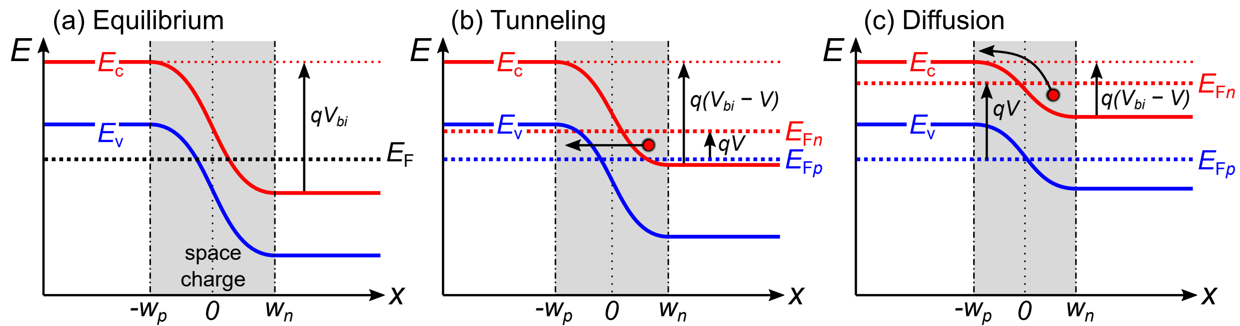

Figure 2.13: Sketch of the band diagrams for a tunnel diode (a) at equilibrium, (b) when tunneling dominates, and (c) when thermal diffusion dominates.

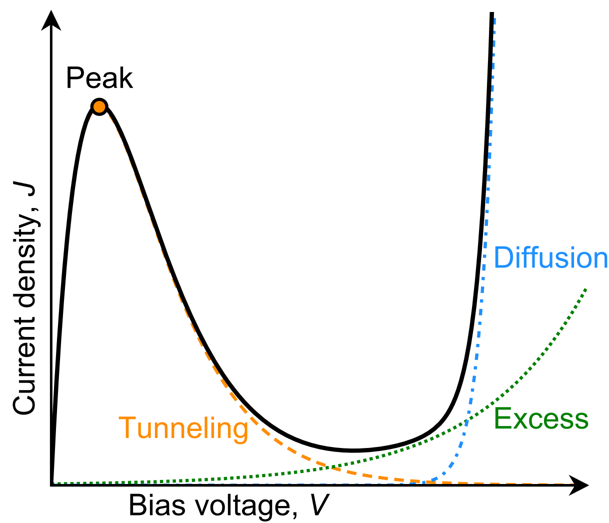

Figure 2.14: Sample *I*-*V* curve for a tunnel diode.

bias, the total current of the tunnel diode has three components: the tunneling current, the excess current, and the diffusion current. Sample *J*-*V* characteristics for a TD are shown in Figure 2.14.

When a small forward bias is applied, electrons in the conduction band on the n-side of the junction tunnel through the barrier to the vacant electronic states in the valence band on the p-side. The tunneling current density reaches its peak when the overlap between the occupied conduction band states on the n-side and the vacant valence band states on the p-side is maximized. The band diagram for the tunneling process is shown in Figure 2.13b.

As the voltage continues to increase, the overlap between occupied conduction band states on the n-side and vacant valence band states on the p-side becomes smaller and the tunneling current is reduced. This region of the *J*-*V* curve is characterized by a negative differential resistance. The depth of the *J*-*V* curve

valley is usually determined by the excess current, which corresponds to tunneling via energy states within the bandgap. In an ideal TD, there are no states in the bandgap and the excess current is zero.

Further increase in the applied bias allows thermal diffusion to become dominant with a corresponding increase in the current flow, as in a standard diode. The associated band diagram is shown in Figure 2.13c.

The *J*-*V* characteristics for a TD, depicted in Figure 2.14, are well approximated by the following equation [70]:

$$J(V) = \frac{J_{\text{pk}} V}{V_{\text{pk}}} \exp\left(1 - \frac{V}{V_{\text{pk}}}\right) + J_{\text{val}} \exp\left(C_{\text{ex}}\left(V - V_{\text{val}}\right)\right) + J_0 \left[\exp\left(\frac{qV}{n_{\text{ideal}} k_{\text{B}} T}\right) - 1\right] \tag{2.49}$$

where J_{pk} and V_{pk} are the current density and voltage of the the tunneling peak, J_{val} and V_{val} are the current density and voltage of the valley, and C_{ex} is a constant.

When embedded within a multi-junction PV device, the tunnel diode is intended to operate only in the region of the *J*-*V* curve to the left of the peak, where the differential resistance (R_0) is low. To ensure that this condition is met, it is essential that J_{pk} exceeds the maximum operating current density of the PV device. In the case where $J > J_{\text{pk}}$, the TD will be forced to operate in the diffusion current regime and the corresponding voltage drop across the TD will be large.

To avoid parasitic absorption losses, the semiconductor materials comprising the TDs must have bandgaps that are larger than those of the absorbing junctions below. Given the epitaxial nature of multi-junction PV devices, the TD materials must also be lattice matched to the substrate to prevent the formation of lattice defects and threading dislocations. Further discussion of TDs designed for InP-based PPCs can be found in Section 4.4.

2.3 Simulating PV devices in TCAD Sentaurus

The technology computer aided design (TCAD) Sentaurus software is a simulation package from Synopsys Inc. designed specifically for optoelectronic modelling of semiconductor devices. The package uses a series of individual programs called “tools” that run sequentially to generate a comprehensive simulation of an optoelectronic device in various conditions. Each tool has its own command file, inputs, and outputs. The tool flow is described in Figure 2.15. This section will discuss the functionality of each tool and briefly explain how a simple one-dimensional simulation of a III-V semiconductor PV device is generated in TCAD Sentaurus. The one-dimensional geometry is less computationally intensive than two- and three-dimensional simulations and is suitable for many applications, but does not account for effects such as perimeter recom-

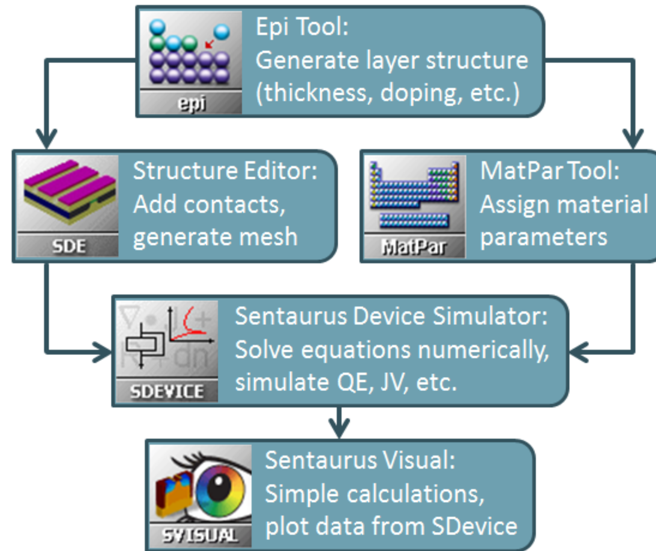

Figure 2.15: TCAD Sentaurus tool flow.

bination, gridline shading, or lateral current flow. A more detailed description of the simulation process for III-V multi-junction photovoltaics is given by Wilkins and Hinzer [63] and by Walker [72].

2.3.1 Epi tool

The *Epi* tool generates the layer structure of a simple epitaxial device. The materials making up each layer are specified in the *Epi* tool command file along with the layer thickness, doping concentration, and molar fraction for compound semiconductor alloys. A preliminary mesh is also generated at this point, to be further refined in the *Structure Editor*.

2.3.2 Structure editor

Preliminary information about the structure and mesh generated in the *Epi* tool is passed into the *Structure Editor*, which creates “virtual” contacts for current collection and generates the final mesh.

Virtual contacts can be positioned at any surface or interface within the device. They exhibit ideal ohmic behaviour and are fully transparent to light, meaning that they do not shade the structure from incident illumination as real contacts would. For a one-dimensional simulation of a single-junction PV device, the contacts are positioned across the entire top and bottom surfaces.

The mesh generated by the *Structure Editor* divides the heterostructure into discretized regions. The mesh density varies throughout the structure to resolve potential gradients and optical generation. The finest

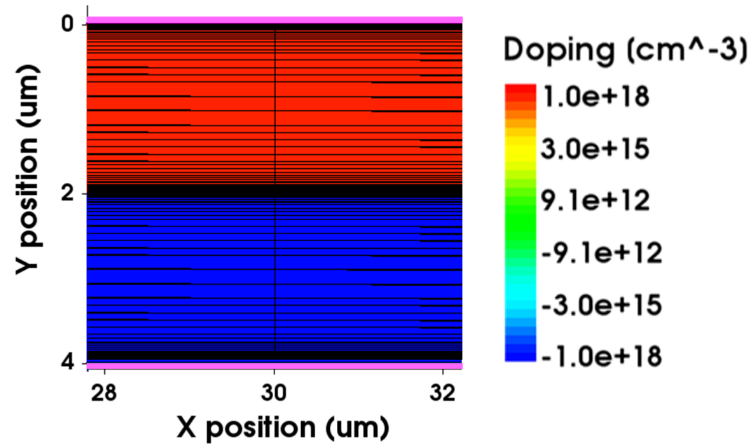

Figure 2.16: Structure and meshing of GaAs n-p junction generated by the *Epi* tool and the *Structure Editor*. The virtual contacts are shown in pink. The black lines indicate the mesh. The full width of the structure is 60 μm of which only the central portion is shown.

mesh spacing is found near interfaces where the most extreme potential gradients are found, requiring the best resolution. Figure 2.16 shows the structure and meshing of a GaAs n-p junction with a total thickness of 4 μm generated using the *Epi* tool and the *Structure Editor*. The n- and p-layers are both doped at 10^{18} cm^{-3}.

2.3.3 MatPar tool

Information about the materials in the layer structure generated in the *Epi* tool is imported into the *MatPar* tool. The *MatPar* tool then calls on a user-defined library of material parameter files to assign the appropriate parameters to each layer within the heterostructure including band gap, density of states, carrier effective masses, carrier mobilities, dielectric permittivities, complex refractive indices, and recombination rates.

2.3.4 Sentaurus device simulator

All structural, meshing, and material information generated by the *Structure Editor* and *MatPar* tools are passed to the Sentaurus Device Simulator (*SDevice*), which is the computational engine used to simulate *J-V* and QE curves. In both cases, the first step is to solve the Poisson equation (equation 2.27) to determine the carrier densities under equilibrium conditions. Following the equilibrium calculation, the optical generation profile is calculated along with the steady state current density. In the case of *J-V* simulations, the optical generation profile is computed for the entire incident spectrum and then the current density is computed as a function of the applied bias. For QE simulations, the optical generation profile is computed for monochromatic light one wavelength at a time. The applied bias is fixed at 0 V and the current density is computed as

a function of wavelength.

The transfer matrix method (TMM) is used to calculate the optical generation using the optical properties of each layer assigned by the *MatPar* tool. It calculates the incident light's propagation through the layer stack, determining transmission and reflection at each interface as well as optical absorption and carrier generation in each layer under the assumption that the ratio of absorbed photons to generated carriers is 1:1. The TMM calculation is performed one wavelength at a time. For *J-V* simulations, the optical generation profile is then summed over the incident spectrum.

The transfer matrix itself is the matrix product of the transmission matrices $\mathbf{T}_{m-1,m}$ for each interface and the propagation matrices $\mathbf{P}_m$ for each layer, given by [63, 73]

$$\begin{bmatrix} E^+_{m-1,\mathrm{bot}} \\ E^-_{m-1,\mathrm{bot}} \end{bmatrix} = \mathbf{T}_{m-1,m} \begin{bmatrix} E^+_{m,\mathrm{top}} \\ E^-_{m,\mathrm{top}} \end{bmatrix}, \qquad \mathbf{T}_{m-1,m} = \frac{1}{t_{m-1,m}} \begin{bmatrix} 1 & r_{m-1,m} \\ r_{m-1,m} & 1 \end{bmatrix} \tag{2.50}$$

$$\begin{bmatrix} E^+_{m,\mathrm{top}} \\ E^-_{m,\mathrm{top}} \end{bmatrix} = \mathbf{P}_m \begin{bmatrix} E^+_{m,\mathrm{bot}} \\ E^-_{m,\mathrm{bot}} \end{bmatrix}, \qquad \mathbf{P}_m = \begin{bmatrix} e^{-ik_m d_m} & 0 \\ 0 & e^{+ik_m d_m} \end{bmatrix} \tag{2.51}$$

where $t_{m-1,m}$ and $r_{m-1,m}$ are the Fresnel transmission and reflection coefficients, $k_m = 2\pi\tilde{n}_m/\lambda$ is the wavevector, and d_m is the layer thickness. The electric field propagation through the layer stack is shown in Figure 2.17. The transfer matrix for the entire stack with N layers is given by

$$\begin{bmatrix} E^+_{0,\mathrm{bot}} \\ E^-_{0,\mathrm{bot}} \end{bmatrix} = \mathbf{M} \begin{bmatrix} E^+_{N+1,\mathrm{top}} \\ 0 \end{bmatrix}, \qquad \mathbf{M} = \prod_{m=1}^{N} \left(\mathbf{T}_{m-1,m}\mathbf{P}_m\right) \mathbf{T}_{N,N+1} \tag{2.52}$$

Following the calculation of optical generation, the steady state electrostatic potential and the carrier concentrations are calculated by solving the Poisson and electron and hole continuity equations (equations 2.27, 2.28, and 2.29), which comprise a set of coupled partial differential equations. *SDevice* solves this set of partial differential equations numerically using the box discretization method [74, 75]. The nonlinear partial differential equations are approximated as linear difference equations and solved over small regions of the total structure as determined by the mesh generated in the *Structure Editor*. At contact interfaces,

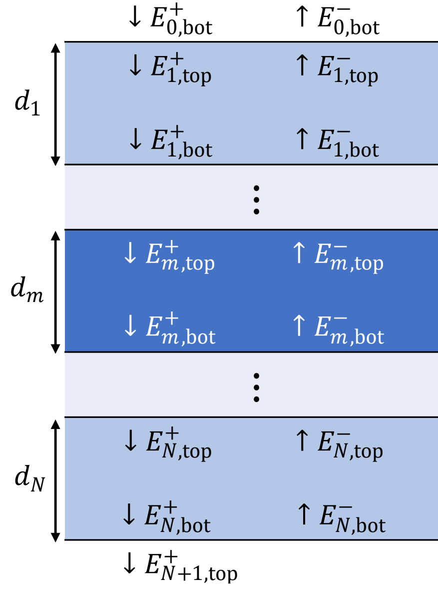

Figure 2.17: Layer schematic showing electric field propagation as defined in TMM.

equilibrium carrier concentrations are assumed. The electrostatic potential ϕ and the carrier densities n and p are calculated numerically at each element of the mesh.

The one-dimensional current densities can be described in terms of the electron and hole densities (n, p), mobilities $(\mu_\text{n}, \mu_\text{p})$ and quasi Fermi levels $(E_{F\text{n}}, E_{F\text{p}})$ as

$$J_\text{n} = \mu_\text{n} n \frac{d}{dy} E_\text{Fn} \tag{2.53}$$

$$J_\text{p} = \mu_\text{p} p \frac{d}{dy} E_\text{Fp} \tag{2.54}$$

The quasi Fermi levels are calculated assuming a fixed temperature T throughout the layer stack according to Fermi-Dirac statistics such that [63]

$$E_\text{Fn} = k_\text{B} T \mathcal{F}^{-1}_{1/2}\left(\frac{n}{N_\text{c}}\right) + E_\text{c} \tag{2.55}$$

$$E_\text{Fp} = -k_\text{B} T \mathcal{F}^{-1}_{1/2}\left(\frac{p}{N_\text{v}}\right) + E_\text{v} \tag{2.56}$$

where $\mathcal{F}^{-1}_{1/2}$ is the inverse Fermi-Dirac integral of order 1/2. We can relate the expressions for current given in equations 2.53 and 2.54 back to the drift and diffusion expressions from Section 2.1.7 by observing that the first term in equations 2.55 and 2.56 will give rise to the diffusion current and the second term will give

rise to drift.

A complete discussion of the functionality of the *SDevice* tool including both the TMM and the box discretization method can be found in the Sentaurus user guide [76] and in the PhD theses of Matthew Wilkins [64] and Alex Walker [72].

2.3.5 Sentaurus visual

The final tool in the simulation flow is *Sentaurus Visual*. This tool is used to visualize the outputs of the *SDevice* tool by generating plots. It is also capable of performing simple calculations such as computing the fill factor and the efficiency from a *J-V* curve or computing the external and internal quantum efficiencies.

Chapter 3

Voided Ge/Si substrate for III-V multi-junction solar cells

3.1 Electrical properties of mesoporous germanium

MEGHAN N. BEATTIE, YOUCEF A. BIOUD, DAVID G. HOBSON, ABDERRAOUF BOUCHERIF, CHRISTOPHER E. VALDIVIA, DOMINIQUE DROUIN, RICHARD ARÈS, AND KARIN HINZER

Scope and impact

The following is a reproduction of an article that was published in *Nanotechnology* in 2018, with the original title: "Tunable conductivity in mesoporous germanium" [6]. The article describes my work characterizing the conductivity of mesoporous Ge films and the impact of thermal annealing on the morphology and electrical properties. Research endeavours across a variety of fields will benefit from a detailed understanding of the electrical properties of mesoporous Ge. Within the scope of this thesis, understanding the electrical properties of mesoporous Ge that has undergone thermal annealing is critical to the development of III-V PV devices on Si substrates engineered with a voided Ge compliance layer to accommodate lattice mismatch.

We have experimentally demonstrated mesoporous Ge conductivity that is tunable over at least two orders of magnitude by varying the size of the nanostructures using thermal annealing, with theoretical calculations suggesting that tuning is possible over four orders of magnitude. We provide a detailed account of our experiments including extensive work that we have done to characterize the nanostructure morphology as well as the electrical resistivity. To support our experimental results, we present an electrostatic model to re-

late nanostructure size to the electrical properties of mesoporous Ge. To our knowledge, this manuscript was the first comprehensive study of the electrical conductivity of mesoporous Ge prepared by electrochemical etching.

Author contributions

MEGHAN N. BEATTIE As the lead University of Ottawa-based graduate student associated with the project, I proposed the experimental technique used to measure the conductivity of the mesoporous Ge films and performed the electrical characterization and accompanying data analysis presented in this paper (see Section 3.1.3.2). I worked with undergraduate student David Hobson to develop the electrostatic model (see Section 3.1.3.4 and Supporting Information Sections 3.1.A.3, 3.1.A.4, and 3.1.A.5). As first author, I wrote the manuscript and prepared final versions of all of the figures.

DR. YOUCEF A. BIOUD As the lead Université de Sherbrooke graduate student associated with the project, Youcef fabricated the mesoporous Ge films using bipolar electrochemical etching and rapid thermal annealing. He performed the electron microscopy (Figure 3.1), accompanying analysis of crystallite size (Figure 3.2), and detailed structural analysis presented in Section 3.1.3.3 and Supporting Information Sections 3.1.A.1 and 3.1.A.2 including X-ray diffraction, Fourier-transform infrared spectroscopy, and infrared reflectivity measurements. Youcef drafted text and figures for the structural analysis sections named above. He provided detailed feedback throughout the research process and assisted in editing the manuscript as a whole.

DAVID G. HOBSON As an undergraduate research assistant within the University of Ottawa's SUNLAB research group, David assisted with developing the electrostatic model presented in Section 3.1.3.4 and Supporting Information Sections 3.1.A.3, 3.1.A.4, and 3.1.A.5.

PROF. ABDERRAOUF BOUCHERIF As a research associate with the Institut interdisciplinaire d'innovation technologique (3IT) at the Université de Sherbrooke, Abderraouf guided Youcef in the mesoporous germanium fabrication and structural analysis. He also helped to guide my research related to electrical characterization and modelling, provided detailed feedback during data analysis, and assisted in editing the manuscript.

Dr. Christopher E. Valdivia As a senior research scientist within the University of Ottawa's SUNLAB research group, Chris helped to guide my research, provided detailed feedback during data analysis, and assisted in editing the manuscript.

Prof. Dominique Drouin As a professor at the Université de Sherbrooke and one of Youcef's co-supervisors, Dominique oversaw Youcef's work in mesoporous germanium fabrication and structural analysis, provided detailed feedback during data analysis, and assisted in editing the manuscript.

Prof. Richard Arès As a professor at the Université de Sherbrooke and one of Youcef's co-supervisors, Richard oversaw Youcef's work in mesoporous germanium fabrication and structural analysis, provided detailed feedback during data analysis, and assisted in editing the manuscript.

Prof. Karin Hinzer As the director of the University of Ottawa's SUNLAB research group, Karin oversaw my research, provided detailed feedback during data analysis, and assisted in editing the manuscript.

Copyright

This is the Accepted Manuscript version of an article accepted for publication in Nanotechnology. IOP Publishing Ltd is not responsible for any errors or omissions in this version of the manuscript or any version derived from it. The Version of Record is available online at:

M. N. Beattie, Y. A. Bioud, D. G. Hobson, A. Boucherif, C. E. Valdivia, D. Drouin, R. Arès, and K. Hinzer, "Tunable conductivity in mesoporous germanium," *Nanotechnology* **29**, 215701, 2018.
DOI: 10.1088/1361-6528/aab3f7

Abstract

Germanium-based nanostructures have attracted increasing attention due to favorable electrical and optical properties, which are tunable on the nanoscale. High densities of germanium nanocrystals are synthesized via electrochemical etching, making porous germanium an appealing nanostructured material for a variety of applications. In this work, we have demonstrated highly tunable electrical conductivity in mesoporous germanium layers by conducting a systematic study varying crystallite size using thermal annealing, with experimental conductivities ranging from 0.6 to 33 ($\times10^{-3}$) $\Omega^{-1}\,\text{cm}^{-1}$. The conductivity of as-

prepared mesoporous germanium with 70% porosity and crystallite size between 4 and 10 nm is shown to be $\sim 0.9 \times 10^{-3}\ \Omega^{-1}\,\mathrm{cm}^{-1}$, 5 orders of magnitude smaller than that of bulk p-type germanium. Thermal annealing for 10 minutes at 400°C further reduced the conductivity; however, annealing at 450°C caused a morphological transformation from columnar crystallites to interconnecting granular crystallites and an increase in conductivity by two orders of magnitude relative to as-prepared mesoporous germanium caused by reduced influence of surface states. We developed an electrostatic model relating the carrier concentration and mobility of p-type mesoporous germanium to the nanoscale morphology. Correlation within an order of magnitude was found between modelled and experimental conductivities, limited by variation in sample uniformity and uncertainty in void size and fraction after annealing. Furthermore, theoretical results suggest that mesoporous germanium conductivity could be tuned over four orders of magnitude, leading to optimized hybrid devices.

3.1.1 Introduction

Germanium (Ge) nanostructures have received significant attention in recent years due to their remarkable optical and electrical properties. Strong quantum confinement has been observed in these materials allowing the optical and electrical properties of Ge to be precisely tuned by varying the nanostructure size and shape [77–82]. Furthermore, the lack of a stable oxide in Ge allows straightforward functionalization of nanostructures and can be used for surface passivation, for improving compatibility with solvents, and for triggering responses in the material to external stimuli [83–85]. Ge nanostructures are also being investigated as anodes for next generation lithium-ion rechargeable batteries because of the outstanding volumetric lithium storage capacity of Ge as well as much improved cycling stability relative to bulk Ge due to the high surface to volume ratio and the space separation between nanostructures [85–93].

In the fabrication of nanostructures, it is often desirable to achieve a high-density film rather than small quantities of singular nanocrystals. Additionally, for lithium-ion batteries, it is essential to have sufficient space between nanostructures to allow for volumetric expansion over lithiation/delithiation cycles [89]. Both of these preceding criteria can be achieved by bipolar electrochemical etching of bulk Ge to make porous Ge films up to several microns in thickness [33, 34, 94–97]. Though other techniques including redox-transmetalation reactions [85], surfactant templating [98–100], and nanoparticle assisted growth [101] have been used to synthesize porous Ge, bipolar electrochemical etching has become a leading fabrication choice because it is simple and offers a high degree of flexibility and control. This technique generates high densities

of columnar Ge nanocrystals separated by pores with diameters on the order of 10 nm (mesoporous Ge). Structural properties such as porosity and crystallite size are varied by changing the etching conditions such as etching current and pulse duration [33, 95]. Recent studies characterizing the optical properties of porous Ge demonstrate tunable photoluminescence and bandgap [77, 102–104]. Previous work by Jing et al. reported lateral conductivities on the order of 0.1 to 1 $\Omega^{-1}\,\mathrm{cm}^{-1}$ for mesoporous Ge fabricated by annealing of GeO_2 ceramic films [105]; however, little information is available regarding the electrical properties of mesoporous germanium fabricated by electrochemical etching. Knowledge of these electrical properties is crucial for optimal implementation in applications such as lithium-ion batteries, thin-film multi-junction solar cells [106], near-infrared light emitting diodes [102], and optical sensors [34].

Electrical properties in the most extensively studied porous semiconductor, porous silicon, made by electrochemical etching [107, 108] have been shown to vary significantly with crystallite size, porosity, and fabrication conditions. Conductivities ranging from 10^{-11} to 10^{-3} $\Omega^{-1}\,\mathrm{cm}^{-1}$ have been reported for meso- and nanoporous silicon [109–114] with crystallite sizes typically in the range of 5 to 10 nm. Changes in electrical behaviour have been observed with thermal treatment [112], gas adsorption [115, 116], and exposure to polar liquids [117]. Similar studies have not been performed in mesoporous Ge due to historical challenges associated with reproducibility and control in the fabrication process [33, 118, 119]; however, recent advances in the electrochemical etching procedures have vastly improved the viability of this technique [33, 34, 95] and systematic studies are now possible.

In this work, we show that mesoporous Ge films have conductivity several orders of magnitude smaller than the Ge substrate on which they are fabricated. We investigate the effect of thermal annealing on the morphology of mesoporous Ge and correlate changes in the electrical behaviour with morphological and structural changes produced by thermal treatment. The results show that this annealing procedure allows controllable tuning of the nanostructure size over more than two orders of magnitude. Furthermore, the conductivity increases by at least two orders of magnitude with annealing temperature as the crystallites become larger, indicating that there is potential to achieve reasonable conductivities for applications such as energy conversion and storage while still maintaining the benefits of the nanostructures introduced by porosification. Finally, we propose an electrostatic model that predicts the evolution of average free carrier concentration and mobility with changing morphology in mesoporous Ge. This model considers the void shape and size, the porosity, the Ge doping concentration, and the expected density of surface states on the pore walls, which act as traps for the free carriers. The calculations assume that a depletion region exists at

the interface between Ge and the void and that the void-dependent mobility is inversely proportional to the density of surface states. This model makes a direct link between morphology and electrical conductivity in porous Ge, and could equally be applied to any porous semiconductor.

3.1.2 Methods

3.1.2.1 Preparation of mesoporous Ge films

Mesoporous Ge layers were fabricated on p+ type Ge wafers by bipolar electrochemical etching (BEE) [33, 34] in a two-electrode electrochemical cell with a platinum wire counter electrode manufactured by Kymosis using an electrolyte consisting of 5:1 hydrofluoric acid (49%) and anhydrous ethanol. The p+ type Ge wafers were (100) oriented with a 6° miscut and had a nominal resistivity of 0.025 $\Omega\,\mathrm{cm}$. Electrical contact was established by pressing the backside of the wafer onto a gold-coated copper electrode. To ensure the formation of a uniform mesoporous layer, a DC initiation step was used during which a anodic etching current of +1.5 $\mathrm{mA/cm^2}$ was applied for 10 s prior to beginning the BEE step [34]. After initiation, anodic and cathodic currents with densities of 1.5 $\mathrm{mA/cm^2}$ were applied alternately with pulse durations of 1 s. The etching rate was approximately 15 nm/min and etching times were varied to fabricate mesoporous Ge layers with thicknesses ranging from 0.1-3 μm.

3.1.2.2 Thermal annealing

Annealing of mesoporous Ge samples was performed in a forming gas (N2:H2 90:10) ambient using a J.I.P. ELEC JetFirst rapid thermal annealing (RTA) system with a ramp rate of 25°C/s. Annealing temperatures ranged from 250°C to 650°C. The duration was fixed at 10 minutes for all temperatures.

3.1.2.3 Material characterization

The structural morphologies and thicknesses of as-prepared and annealed mesoporous Ge films were characterized by scanning electron microscopy (SEM) using a Zeiss 1540XB CrossBeam Workstation. Quantitative nanostructural analysis of the crystallite size distribution was performed by Fourier analysis of the SEM images using the ImageJ software. The crystal structure of as-prepared mesoporous Ge was further examined by high-resolution scanning transmission electron microscopy (HRSTEM) using a FEI Titan Cubed electron microscope equipped with a CEOS image and probe corrector operated at 300 kV. X-ray diffractograms of

as-prepared and annealed mesoporous Ge samples were measured using a Philips X'Pert powder diffractometer immediately after preparation. Transport of porous Ge samples was performed under propanol. Fourier-transform infrared (FTIR) spectroscopy was performed on as-prepared and annealed mesoporous Ge samples using a VERTEX 80/70v FTIR spectrometer using a Globar source, a KBr beam splitter, and a MCT D15 detector. Hydrogen absorbance was determined by transmission FTIR spectroscopy with a spectral resolution of 2.0 cm^{-1} and a scanning time of 5 minutes for as-prepared mesoporous Ge and after annealing at various temperatures. Microscopic FTIR reflectance analysis was used to determine the porosity of as-prepared mesoporous Ge using a standard 15$\times$ objective with a gold surface as reference.

3.1.2.4 Current-voltage measurement

Ohmic contacts were realized by direct deposition of nickel (30 nm) and gold (450 nm) on the top side and nickel (30 nm) and gold (150 nm) on the back side. Preliminary samples were fabricated with equal thickness of gold (150 nm) on both faces, however the thickness of the top gold layer was increased to ensure a singly connected contact after non-ohmic behaviour was observed in some samples. The specific contact resistivity ρ_c ranges from about 5×10^{-3} to 5×10^{-2} Ωcm^2 depending on the annealing condition (ρ_c decreases with increasing annealing temperature). Metallization of annealed samples was performed after the thermal treatment. Samples were cleaved after metallization. Current-voltage ($I - V$) characteristics were measured by four-wire sensing. Samples were fixed to a gold-plated stage using a vacuum connection. Electrical contact was made to the top of the samples using tungsten tipped probes and to the bottom via connection to the stage. The $I - V$ characteristic was measured for each sample by ramping the applied voltage from -200 mV to 200 mV in steps of 1 mV, using a limit of ± 150 mA for the current. A Keithley 2420 source meter was used as the power source and to perform measurements of current and voltage.

3.1.3 Results and discussion

3.1.3.1 Morphology of mesoporous germanium films

Mesoporous Ge layers were fabricated on p+ type Ge wafers by bipolar electrochemical etching (BEE), as described in the Methods section. Top view and cross-sectional scanning electron microscope (SEM) images of as-prepared mesoporous Ge are shown in Figure 3.1a-c. A uniform distribution of nano-sized columnar pores extends down from the surface with some branchial pore channels. The pores terminate abruptly at

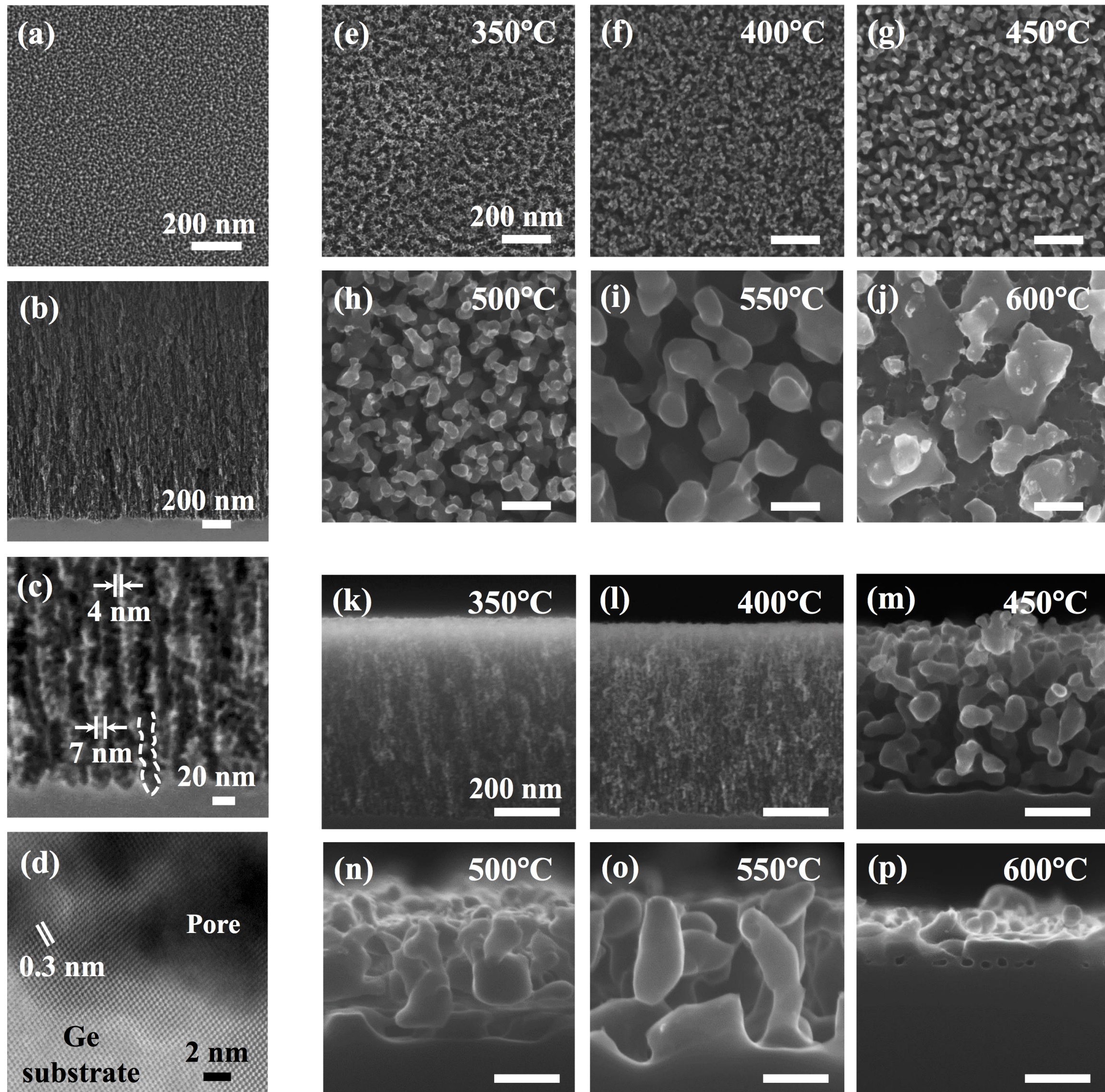

Figure 3.1: (a) Top view and (b) cross-sectional SEM image of as-prepared mesoporous Ge layer formed by BEE. (c) High-resolution SEM image of the Ge crystallites. Crystallite sizes and pore morphology at the substrate interface are indicated. (d) HRSTEM micrograph showing the interface between the Ge substrate and the mesoporous Ge interface. (e-j) Top view and (k-p) cross-sectional SEM images of mesoporous Ge layers annealed at 350 – 600°C under hydrogen flow. Scale bars are 200 nm in length unless otherwise indicated. The evolution of the morphology and crystallite size with annealing temperature is evident.

the interface between the mesoporous layer and the parent substrate. The size of the Ge nanocrystallites is estimated to be in the range of 4-10 nm (see Figure 3.1c). The high-resolution scanning transmission electron microscopy (HRSTEM) micrograph shown in Figure 3.1d reveals that the Ge nanostructures retain the same crystallographic orientation as the Ge substrate with diamond lattice structure and an inter-planar spacing of ~ 0.3 nm, which is consistent with previous findings [102].

Porosities were measured by analyzing Fabry-Perot fringes observed in the infrared reflectance spectrum [34] (see Supporting Information, Section 3.1.A.1). We observed an average porosity of 72% in as-prepared mesoporous Ge samples.

Top view and cross-sectional SEM images of mesoporous Ge after annealing for 10 minutes at temperatures ranging from 350°C to 600°C are shown in Figure 3.1e-p. As the annealing temperature was increased, the Ge nanocrystallites grew larger in size. At an annealing temperature of 450°C, a significant morphological transformation occurred in which the porous structure self-organized into a network of elongated granular crystallites. After annealing at 600°C, the upper crystallites became interconnected forming nano-voids [120, 121] with average sizes in the range of 20-50 nm. For some samples, the creation of a layer of nano-voids was observed after annealing at 550°C rather than 600°C. This was likely due to minute changes in substrate resistivity and etching current between samples.

The sizes of the Ge nanocrystallites at the surface of the annealed samples were extracted from top view SEM observations using the Fourier transform of the images (see Figure 3.1e-j). The average crystallite size was determined by fitting the size distribution with a log-normal function. The reorganization of the structure to form larger crystallites is induced by Ostwald ripening [121], in which the Ge atoms on the surface jump to more favorable energy positions during thermal annealing below the Ge melting point (938°C). The average surface crystallite size $\left(d_{\text{crystallite}}\right)$ increased exponentially with annealing temperature (T), as shown in Figure 3.2, indicating strong Boltzmann-like temperature dependence, which is consistent with sintering theory developed for porous materials [122]. This relationship indicates that the average crystallite size can be precisely tuned through annealing temperature and duration. Further details are given in the Supporting Information, Section 3.1.A.2.

3.1.3.2 Electrical resistivity of mesoporous germanium

Surface effects caused by the high density of mesoscopic pores have a significant impact on electrical transport. Due to the nature of the samples (highly resistive film bonded to a comparatively low resistance

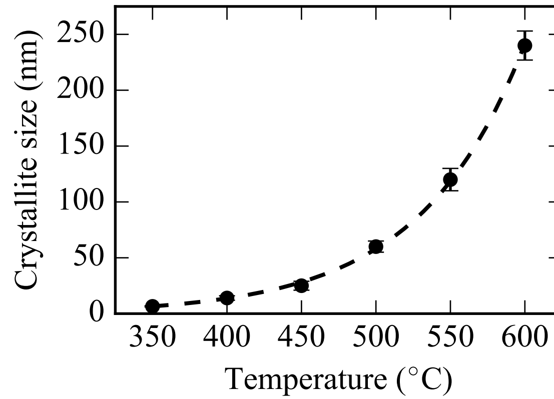

Figure 3.2: Variation of the surface crystallite size with annealing temperature.

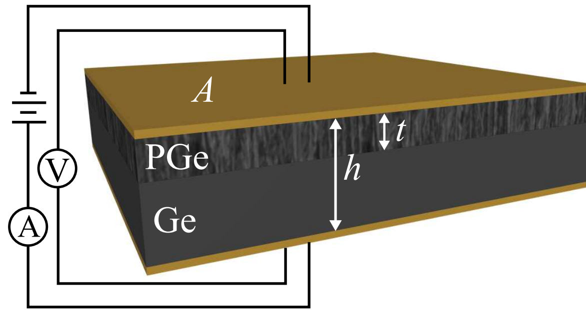

Figure 3.3: Schematic of layer stack and four-wire sensing configuration for current-voltage measurements across the porous Ge (PGe) and Ge substrate layers indicating the area perpendicular to current flow A, the porous layer thickness t, and the total thickness of the PGe-Ge layer stack h.

substrate), conventional methods for measuring conductivity such as Hall effect measurements were not appropriate. For this reason, a simple thickness-dependent experimental technique was devised.

Blanket contacts of nickel and gold were applied to the top and bottom surfaces of as-prepared and annealed mesoporous Ge samples on the parent substrate in preparation for current-voltage measurements. After metallization, the sample edges were cleaved, creating a sandwich-type structure (see Figure 3.3).

Linear current-voltage characteristics observed using the four-wire sensing technique for both as-prepared and annealed samples indicated the formation of ohmic contacts (see Figures 3.3 and 3.4a). Total resistance R_T was determined from current-voltage measurements and the average value for each sample was plotted as a function of porous layer thickness (see Figure 3.4b). The resistivity of the porous layer ρ_{PGe} was determined by assuming the following relationship between total resistance and porous layer thickness:

$$R_T = \frac{\rho_{PGe}}{A} t + \frac{\rho_{Ge}(h-t)}{A} + R_c \approx \frac{\rho_{PGe}}{A} t + R_0 \qquad (3.1)$$

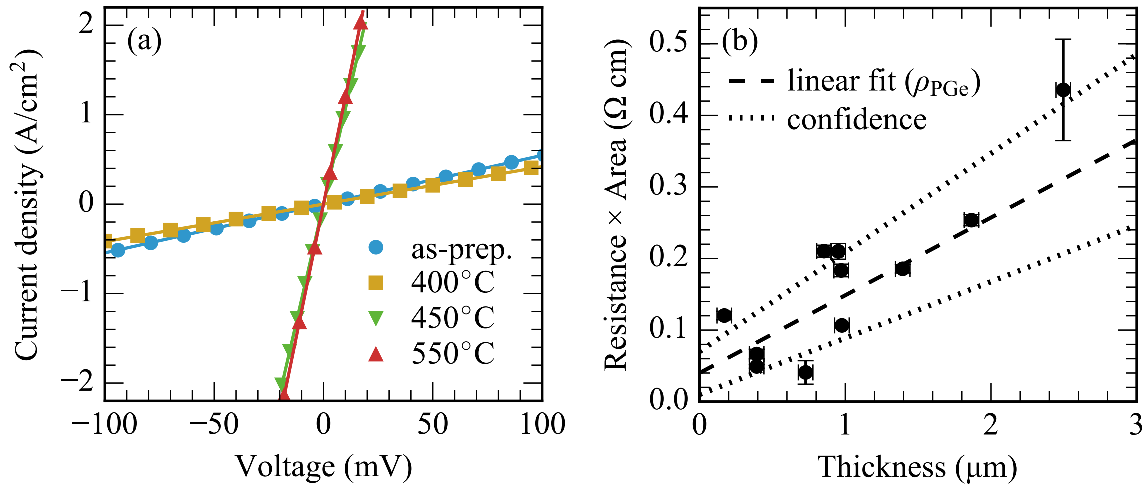

Figure 3.4: (a) Current-voltage characteristics for as-prepared Ge (as-prep.) and after thermal annealing at 400, 450 and 550°C for 10 minutes. The thickness of the porous layer is between 1.4 and 1.45 µm for all samples shown in (a). (b) Product of average total resistance and area, $R_T A$, as a function of porous layer thickness, t, for as-prepared mesoporous Ge. Dashed line is the linear fit, which gives resistivity, and dotted lines are confidence interval bounds calculated using standard deviation on the fitting parameters. Error in A is 3%, in t is ±50 nm, and in R_T is determined from the standard deviation of multiple measurements for each sample. The resistivity of as-prepared porous Ge is found to be $1100 \pm 300\ \Omega\,\text{cm}$.

where A, t, and h are indicated in Figure 3.3. R_c is the contact resistance, which is grouped along with the initial substrate resistance into the thickness-independent term R_0. Contact resistance was assumed to be similar for all samples at each annealing condition because surface porosity variation between samples annealed at the same temperature is small. In the final expression, we have used the fact that the Ge substrate resistivity ($\rho_{Ge} \sim 0.025\ \Omega\,\text{cm}$) is negligible compared to the resistivity of the porous layer. Conductivity is simply the inverse of resistivity.

Figure 3.4b shows the total resistance (averaged over multiple measurements) as a function of porous layer thickness for as-prepared mesoporous Ge. A linear fit was performed by weighted least squares and the resistivity of the mesoporous Ge was found to be $1100 \pm 300\ \Omega\,\text{cm}$, five orders of magnitude larger than that of the original Ge substrate. The uncertainty corresponds to the standard deviation of the fitting parameters.

The large increase in resistivity after porosification can be explained by the high surface to volume ratio of mesoporous Ge films, on the order of 10^7 cm^{-1}, and the high density of surface states generated on the pore walls. Although the surface state density has yet to be measured in mesoporous Ge, total surface state densities of at least 10^{13} cm^{-2} and possibly exceeding 10^{14} cm^{-2} are expected for Ge with native oxide [123–126]. For clean Ge surfaces, surface state densities may be on the order of 4×10^{14} cm^{-2}eV^{-1}, assuming (as in section 3.1.3.4) that the states are evenly distributed throughout the band gap [123, 126]. The impact of

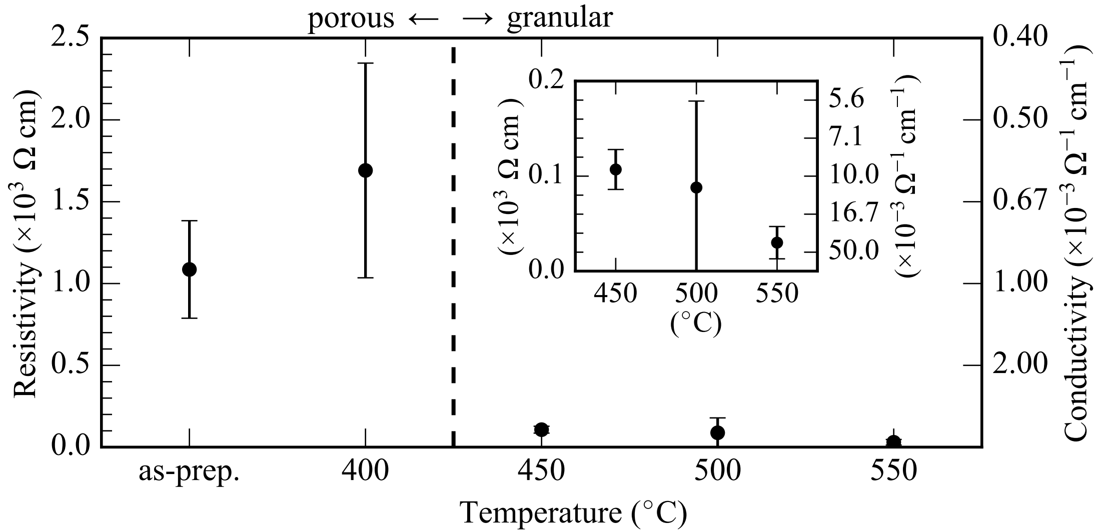

Figure 3.5: Porous Ge resistivity as a function of annealing temperature. The inset shows the resistivities between 450°C and 550°C on a smaller scale for clarity. The transition between porous and granular morphologies is indicated. The large uncertainty associated with the data point at 400°C is due to significant variability between samples that is presumed to be caused primarily by inconsistent contact resistance. Conductivity is given on the secondary y-axes.

surface states on carrier transport has previously been observed in Ge nanowires [124, 125] as well as in porous silicon layers [110, 127]. Surface states trap carriers, creating a space charge region and depleting the free carrier concentration in the material [110, 124, 125, 127, 128] while simultaneously reducing carrier mobility [129]. This results in the high resistivity (low conductivity) that we have observed in the porous material.

These assumptions are further supported by relating changes in electrical behaviour to morphological changes induced by annealing. After annealing at 450°C, the transition from a porous structure to a granular-type structure caused the resistivity to decrease by two orders of magnitude relative to that of the as-prepared mesoporous Ge. The dependence of resistivity and conductivity on annealing temperature is shown in Figure 3.5.

When the Ge nanocrystallites are small, surface state interactions dominate the electrical transport properties. With increasing nanocrystallite size, the specific surface area of the material goes down and surface states become less important. The most significant change in resistivity occurred at the transition to granular morphology after annealing at 450°C; however, the resistivity continued to decrease at higher annealing temperatures as the crystallites continued to grow. At temperatures exceeding 550°C, variations between

samples became dominant relative to the trend of increasing resistance with porous layer thickness and so it was not possible to extract reliable estimates of resistivity.

3.1.3.3 Structural analysis

To investigate the processes behind the morphological and electrical transformations that occurred with thermal annealing, further analysis of crystallographic properties and surface chemistry was performed.

X-ray diffraction measurements were performed to investigate the crystal structure before and after annealing. The diffraction signal between 20° and 100° for as-prepared mesoporous Ge with a layer thickness of 2 μm on the parent substrate wafer is shown in Figure 3.6 together with those of porous layers annealed at temperatures from 350 to 650°C. The samples were measured immediately after preparation and transported in propanol to prevent the formation of an oxide. All the diffraction peaks are identified and correspond to the diamond lattice structure of Ge with a lattice constant of 5.65 Å. No peaks from oxides such as GeO_2 (hexagonal or tetragonal) were observed within the detection limit of our equipment. For as-prepared mesoporous Ge, only one significant diffraction peak was observed, originating from the (400) plane family. X-ray diffraction measurements were performed on single crystal samples using a powder diffractometer, and therefore the intensity of the (400) peak varied between samples depending on the orientation. The relative intensity of the peaks between samples is not important.

After annealing at temperatures exceeding 450°C, diffraction peaks were observed from several additional crystallographic directions suggesting that randomly oriented crystallites were formed. The peaks from mesoporous Ge samples annealed at 550°C and 650°C coincide with the diffraction signature that can be observed in poly-Ge [130], confirming the polycrystalline nature of the nanostructures for this range of annealing temperatures. Atom migration and Ostwald ripening led to the formation of misoriented nanocrystallites that had lost crystallographic coherence with the substrate during annealing at high temperatures. The appearance of polycrystalline Ge signified the presence of trap states at grain boundaries that have a similar effect to the surface states on void walls, reducing majority carrier concentration and mobility and limiting the conductivity of the material [131]. The observed increase in conductivity after annealing would likely be even more significant if crystallographic order was maintained throughout the process.

The wide diffraction peak observed near 66° at all temperatures in Figure 3.6 is amorphous-like in shape. A similar effect has been observed by X-ray diffraction in porous Si [132] and by Raman spectroscopy in porous Ge [133]. No disordered region was observed in the TEM image corresponding to the amorphous

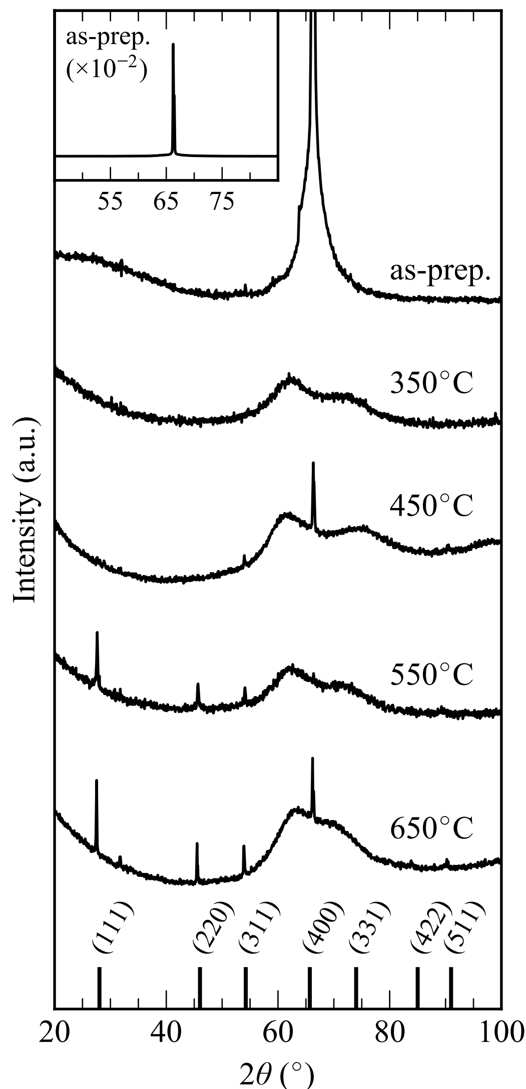

Figure 3.6: X-ray diffraction signal of as-prepared mesoporous Ge (as-prep.) and after annealing at 350 – 650 °C. Note: single crystal samples were measured on a powder diffractometer and so relative peak intensity between samples is due to the orientation of the sample and is of no significance. For as-prepared mesoporous Ge, only the (400) diffraction peak is observed. At annealing temperatures exceeding 450 °C, polycrystallinity is observed as the appearance of new peaks including (111), (220), (311), (331), and (511). Inset shows the full peak for the as-prepared mesoporous Ge sample, scaled by a factor of 10-2 relative to the as-prepared peak shown in the main image.

phase for as-prepared mesoporous Ge near the interface with the bulk substrate (see Figure 3.1d).

As-prepared mesoporous Ge is coated with covalently bonded hydrogen [94, 134], providing electronic passivation [135] of the surface. We investigate the stability of this coating by studying hydrogen desorption with thermal annealing to clarify the surface diffusion mechanism that results in a reorganization of the structure in mesoporous germanium and to see its influence on electrical properties.

Fourier transform infrared (FTIR) spectra were recorded for mesoporous Ge layers at a series of annealing temperatures to monitor the hydrogen desorption. The transmission FTIR spectrum of as-prepared mesoporous Ge (Figure 3.7) reveals an absorbance band in the range of $1900-2100$ cm^{-1} attributed to germanium hydride GeH_x stretch mode vibrations. This asymmetric stretching band is dominated by two components at 1982 and 2024 cm^{-1}, corresponding to germanium mono- and di-hydride species, with a smaller component at 2063 cm^{-1} associated with the tri-hydride [135, 136]. Due to the high surface area of mesoporous Ge compared to a 2D bulk Ge surface [94], the mono-, di-, and tri-hydride stretch modes can be clearly distinguished and their positions are indicated in the spectrum. Such varied H-termination is typical of an atomically rough or porous material, such as porous Si [137].

Figure 3.7 shows the evolution of the GeH_x absorbance band after annealing at temperatures ranging from 250°C to 550°C for 10 minutes. The annealing process is identical to that carried out to induce morphological changes (see Section 3.1.2.2). The band was modelled as the sum of three Gaussians corresponding to the three stretch modes [34]. The amount of GeH_x absorbance decreased with annealing temperature. This is attributed to the surface diffusion of germanium atoms along the pore walls, which tends to minimize the high surface energy [138].

Figure 3.8 illustrates the strong non-linear dependence of the integrated absorbance on annealing temperature. In the range of 250°C to 350°C, the infrared absorbance decreased abruptly due to hydrogen desorption [137], causing the formation of dangling bonds, which facilitated the surface diffusion of germanium atoms and the changes in morphology observed with thermal annealing. The most significant desorption (between 250°C and 350°C), preceded the abrupt morphological transformation that occurred at 450°C (see Figure 3.1). This suggests that hydrogen desorption and Ostwald ripening may not be simultaneous processes. In this case, there may have been an increase in the surface state density prior to the onset of significant Ostwald ripening, which would explain the observed increase in resistivity of the samples annealed at 400°C. The hydrogen is almost fully desorbed after annealing at 550°C.

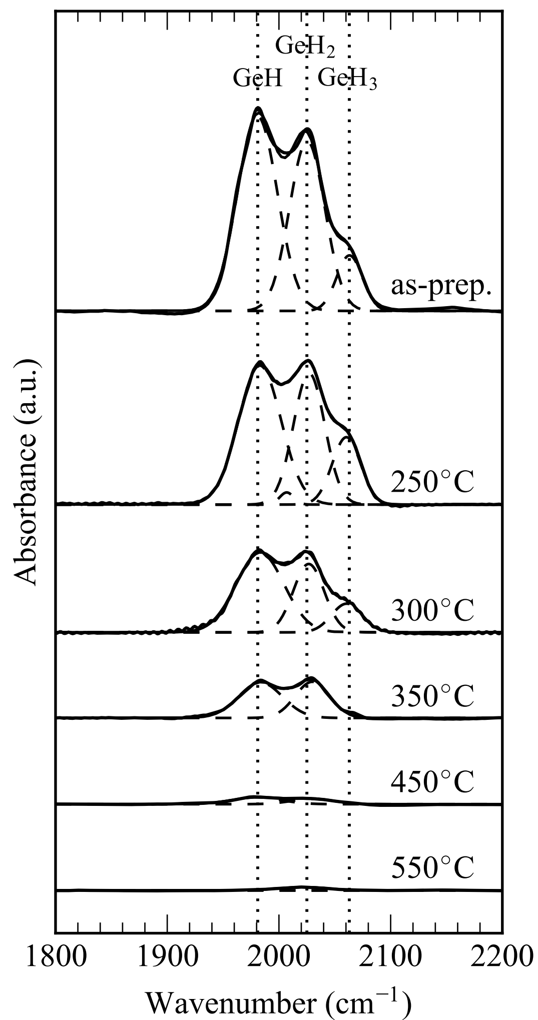

Figure 3.7: GeH_x band in the transmission-FTIR spectrum of as-prepared mesoporous Ge and after thermal annealing at 250 – 550°C. The positions of mono-, di-, and tri-hydride stretch modes are indicated by vertical lines. Decreasing absorbance with annealing temperature indicates hydrogen desorption.

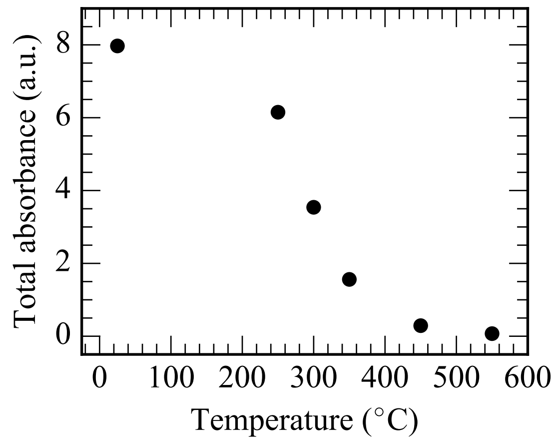

Figure 3.8: Integrated absorbance of the three GeH_x species as a function of annealing temperature.

3.1.3.4 Electrical transport modelling

Banerjee et al. proposed simple electrostatic models for the free carrier concentration and mobility in annealed porous Si [128, 129]. Starting from this framework, we have developed new models specifically for as-prepared and annealed porous Ge. Key differences in these models relative to those introduced by Banerjee et al. include the calculation of the electric potential in three dimensions rather than one, the expansion of the mobility model into multiple terms combined according to Matthiessen's rule, and the choice of cylindrical pore as well as spherical void unit cell geometries to represent mesoporous and voided materials, respectively. This model is intended to be indicative, and more detailed experimental characterization of key material parameters (such as surface state density and internal surface area) will improve its accuracy.

The columnar pores of as-prepared mesoporous Ge were modelled as cylindrical pores within cubic unit cells, shown in Figure 3.9a, assuming periodic repetition of the unit cells through all space. This periodic array of identical pores is meant to represent the average pore shape, size, and distribution over a large area.

We do not attempt to model the complex granular morphology produced by annealing at lower temperatures, and rather turn our attention to the voided Ge material that begins to form in some samples after annealing for 10 minutes at temperatures exceeding 550°C (see Figure 3.1p). We have chosen to represent this system as a network of Ge nanocrystallites divided by spherical voids, shown in Figure 3.9b. As with the columnar pores, this model applies a periodic array of identical voids to represent an average geometry over a large area, rather than attempting to incorporate the non-uniformity in void shape, size, and distribution that is characteristic of voided Ge materials [106, 121]. This spherical void model would best be applied to

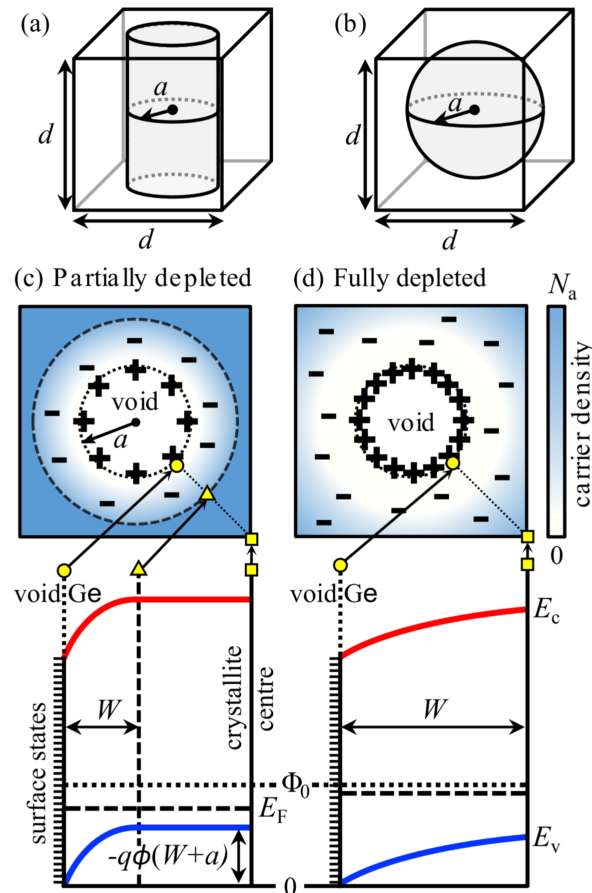

Figure 3.9: Unit cells for (a) as-prepared and (b) annealed porous Ge electrical transport models. The dimension of the unit cell is given by 'd' and the radius of the pore/void is given by 'a'. (c-d) Schematic of carrier densities and band diagrams for unit cells that are (c) partially and (d) fully depleted of carriers under the depletion approximation. Ionized acceptor atoms are indicated by (−) and holes trapped by surface states are indicated by (+). The conduction E_c and valence E_v bands, the Fermi level E_F, the neutral level Φ_0, and the width of the space charge region W are shown. The energies of the bands are determined relative to the bottom of the valence band at the void-Ge interface. The band bending is determined by the electrostatic potential at the boundary of the space charge region, $(W+a)$. Spatial markers relate the band diagrams to the corresponding carrier density schematics.

Ge layers with a high density of spherical cavities, which can be synthesized by annealing of mesoporous Ge under certain conditions, as shown in previous studies [106, 121].

Schematics of the band diagrams are shown in Figure 3.9c-d where the effect of the surface states on the bands is illustrated near the void-Ge interface. Surface state energies are assumed to be distributed uniformly throughout the band gap [123, 139]. The neutral level Φ_0 represents the level at which the surface would be charge neutral if all surface states below were occupied and all surface states above were vacant. In p-type Ge, the Fermi level is below the neutral level and so the surface states act as donors, trapping p-type carriers

and creating a buildup of positive charge on the surface. This separation of charge creates a space-charge region surrounding the void, inducing band bending at the interface. Assuming a density of surface states N_s, a doping concentration N_a, and taking the unit cell to be charge neutral, the width of the space charge region W was calculated using Gauss' law to solve for the electric potential ϕ under the depletion approximation where it was assumed that the space charge region was depleted of carriers and that the electric field was confined to this region (see Supporting Information, section 3.1.A.3).

Once the space charge region was defined, the depletion approximation was relaxed. The spatial density of carriers is given by

$$p(r) = \begin{cases} 0 & 0 \leq r < a \\ N_a \exp\left[-\frac{q\phi_\infty(r)}{k_B T}\right] & a \leq r < W + a \\ N_a & r \geq W + a \end{cases} \tag{3.2}$$

where ϕ_∞ is the electric potential defined relative to infinity. The approximate spatial carrier density is shown in figure 3.9c-d for the cases where the unit cell is partially and fully depleted of carriers under the depletion approximation. The average carrier concentration p_{ave} in porous Ge was found by integrating the spatial density over the volume of Ge in the unit cell.

The mobility μ was calculated using Matthiessen's rule with a correction factor $(1–\mathcal{P})$, where $\mathcal{P}$ is porosity, to account for the fact that no carriers can travel in the void.

$$\mu = \left(\frac{1}{\mu_{Ge}} + \frac{1}{\mu_{void}}\right)^{-1} (1 - \mathcal{P}) \tag{3.3}$$

where μ_{Ge} is the mobility of bulk Ge calculated according to Klassen's unified mobility model [140] based on parameters from Palankovski [141] (see Supporting Information, section 3.1.A.4). The mobility contribution due to the voids is given by

$$\mu_{void} = C \frac{1}{N_{sv}} \tag{3.4}$$

where $N_{sv} = N_s E_g \left(A_{void}/d^3\right)$ is the number of surface states per unit volume (A_{void} is the surface area of the void) and C is a fitting parameter.

Having calculated the average carrier concentration and mobility, it is straightforward to calculate the resistivity:

$$\rho = \frac{1}{q p_{ave} \mu} = \frac{1}{\sigma} \tag{3.5}$$

where σ is conductivity.

The fitting parameter C was found by comparing to the experimental resistivity for as-prepared porous Ge. We assumed a pore diameter $2a = 7$ nm, a porosity $\mathcal{P} = 70\%$, and a doping concentration $N_\mathrm{a} = 3 \times 10^{17}\ \mathrm{cm}^{-3}$ assuming uniform spacing and 100% activation. A surface state density $N_\mathrm{s} = 4 \times 10^{14}\ \mathrm{cm}^{-2}\,\mathrm{eV}^{-1}$ is chosen to agree with expectations for clean Ge surfaces [123, 126]. The neutral level Φ_0 was taken to be one third of the bandgap [139] (0.22 eV). Based on these assumptions and setting $\rho = 1100\ \Omega\,\mathrm{cm}$, a value of $C \sim 320{,}000\ \mathrm{cm}^{-1}\,\mathrm{V}^{-1}\,\mathrm{s}^{-1}$ was obtained.

The modelled free carrier concentration, carrier mobility, and resistivity for as-prepared mesoporous Ge are shown as a function of pore size in Figure 3.10a-c. For a void diameter of 7 nm and a porosity of 70%, the average free carrier concentration is reduced by three orders of magnitude relative to the substrate doping density and the mobility is reduced by two orders of magnitude. These reductions are caused by the strong influence of surface states near the void-Ge interface. As anticipated, both carrier concentration and mobility increase as the pores become larger and further apart, resulting in increased conductivity. Similar trends are observed for the spherical void model. The cusp-like features observed in the carrier concentration and resistivity curves correspond to the transition from the fully depleted case to the partially depleted case (see Supporting Information, section 3.1.A.3). As the porosity increases, the fully depleted case applies over a wider range of void sizes. In the partially depleted case for large void size, both carrier concentration and mobility scale with $(1 - \mathcal{P})$. This is also the limiting case when the surface state density goes to zero. Reducing the surface state density could increase the conductivity by up to five orders of magnitude for highly porous materials with small pore size.

Figure 3.10c and f show a comparison between the modelled and experimental conductivities for as-prepared porous Ge and after annealing at 550°C. We did not directly compare the experimental data at other annealing temperatures to the model because of the substantial difference between the modelled geometry (spherical voids) and the true morphology of the material (interconnected granular crystallites). Although the morphology of the sample shown in Figure 3.1 after annealing at 550°C also has granular form, at this temperature we started to see the formation of spherical voids in some samples. The margins of average void size indicated in Figure 3.10f are determined by assuming the void size is equivalent to the average spacing between crystallites for samples with granular morphology.

The continuously decreasing resistivity shown in Figure 3.10 as a function of void size does not strictly agree with what was observed in experiment, where we first saw an increase after annealing at 400°C before

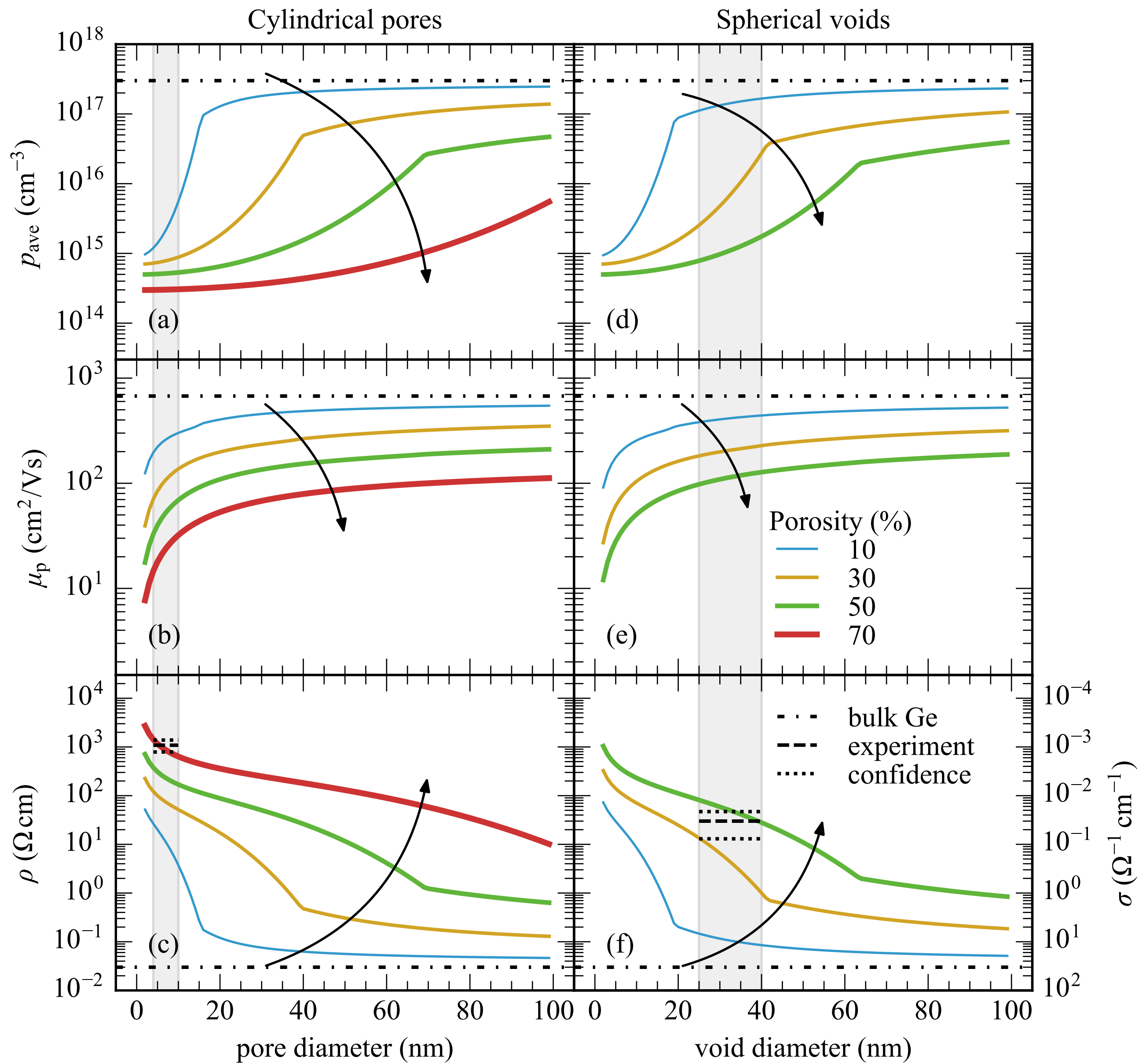

Figure 3.10: (a, d) Average free carrier concentration, (b, e) carrier mobility, and (c, f) resistivity of (left) as-prepared and (right) annealed mesoporous Ge. Conductivity is shown on the secondary y-axis of (c) and (f). Electrical properties are shown for a variety of porosities as a function of pore/void size. A doping concentration of 3×10^{17} cm^{-3} and an interface state density of 4×10^{14} cm^{-2} eV^{-1} are assumed. Highlighted regions show the range of diameters over which the model can be compared with experimental results, for as-prepared mesoporous Ge (left) and after annealing at 550°C (right). Arrows indicate direction of increasing porosity. Values for bulk Ge (substrate) are shown. Simulated results are not shown for annealed mesoporous Ge with 70% porosity because porosities exceeding 52% are not permitted for the selected unit cell geometry.

the expected decrease was observed. The reason for this discrepancy is that the model assumes the density of surface states is unchanged for all void sizes. This does not account for the variation in hydrogen coverage observed in experiment, where we expect that significant hydrogen desorption first results in an increased surface state density prior to the onset of significant Ostwald ripening.

Given that the porosity of mesoporous Ge is expected to decrease with annealing due to thinning of the porous layer that was observed experimentally (see Figure 3.1k-p), the estimation of porosity in the range of 30-50% after annealing at 550°C for 10 minutes, obtained by comparing the experimental and theoretical results in Figure 3.10f, is reasonable. This implies that surface state densities are similar for as-prepared mesoporous Ge and for annealed mesoporous Ge after the onset of Ostwald ripening, indicating that any initial increase in surface states density is countered by the rearrangement of the Ge atoms at sufficiently high temperature. Decreasing the surface state density by optimizing the surface passivation would allow for significant enhancement of the mesoporous Ge conductivity.

For smaller crystallite sizes, quantum confinement effects are expected to change the band-gap [77, 102]. This effect was not included in this model because it has yet to be well characterized for mesoporous Ge materials. Inclusion of this effect will improve the accuracy of this model, particularly for high porosities and small pore or void sizes [128].

Values used for the neutral level and the density of surface states are estimated and assumed to be unchanged by thermal annealing. Experimental measurements of these values for the material systems being studied (before and after thermal treatment) would improve the accuracy of the model. Additionally, experimental determination of the internal surface area of mesoporous Ge would be highly beneficial, given that the pores are not smooth cylinders as was assumed in the model, and this may increase the effective interface state density that should be used. Further discussion of the impact of interface state density on the simulated transport properties is included in the Supporting Information, section 3.1.A.5.

3.1.4 Conclusion

The resistivity of as-prepared mesoporous Ge with an average porosity of 72% and crystallite sizes ranging from 4-10 nm was found to be $\sim 1100\ \Omega$cm, five orders of magnitude higher than that of the p-type Ge substrate (0.025 Ωcm). This high resistivity is due to the high density of surface states on the pore walls, which trap free carriers, significantly reducing average carrier concentration and mobility, and could be useful for electrical isolation in Ge circuits. This is supported by modelling results, which suggest that there

is a depletion of carriers by several orders of magnitude for mesoporous samples with high porosity.

Thermal annealing initiated hydrogen desorption from the pore walls and surface diffusion of Ge atoms via Ostwald ripening, allowing the size of the Ge nano-crystallites to be predictably controlled by varying the annealing temperature and duration. At low annealing temperatures (< 450°C), considerable hydrogen desorption was observed without significant changes in the morphology of the material. We predict that this imbalance results in an increased surface state density, which would explain the increased resistivity observed after annealing for 10 minutes at 400°C relative to the resistivity of as-prepared mesoporous Ge. A morphological transformation was observed after annealing for 10 minutes at 450°C from porous-type material to a granular crystallite structure. Long range crystalline order, which was observed after the etching process, was slowly lost during annealing as the Ge atoms reorganized. The average size of the crystallites increased exponentially with annealing temperature until they connected to each other, creating a layer of nano-voids beneath the surface after annealing at 550 - 600°C. Increasing crystallite size reduced the influence of surface states on the electrical properties of the material, and our electrostatic model predicted rapidly decreasing resistivity with increasing void size. This was clearly observed in experiment after annealing at 450°C where an abrupt drop in resistivity by two orders of magnitude relative to the as-prepared mesoporous Ge occurred.

The high resistivity of mesoporous Ge after initial preparation and the variability with annealing demonstrates the potential for mesoporous Ge materials to be used as tunable resistors or insulating layers in a variety of applications. Furthermore, we believe that the resistivity can be sufficiently reduced to allow for annealed mesoporous Ge to be used in energy conversion and storage applications.

Acknowledgements

This work is supported by the Natural Sciences and Engineering Research Council of Canada (NSERC), the Canada Research Chair program, the Canadian Foundation for Innovation, the Fonds de recherche du Québec – Nature et technologies (FQRNT), the Ontario Research Fund, and the Ontario Graduate Scholarship program. The authors would like to thank G. Beaudin and C. Roy for the technical help and J. Krich for useful discussions. The EM research described in this paper was performed at the Canadian Centre for Electron Microscopy at McMaster University, which is supported by NSERC and other government agencies.

3.1.A Supporting Information

3.1.A.1 Measuring porosity by infrared reflectance

Infrared light incident on the surface of as-prepared mesoporous Ge samples is reflected from both the top interface (air to porous Ge) and the bottom interface (porous Ge to Ge substrate). Interference between reflections from the two interfaces generates Fabry-Perot fringes in the reflectance spectrum shown in Figure 3.11. The interference pattern is used to determine the refractive index of the film using the following expression:

$$n_{\mathrm{r,PGe}} = \frac{m}{2\,\delta\nu\,t} \tag{3.6}$$

where m is the number of fringes within wavenumber region $\delta\nu$ and t is the film thickness, estimated from SEM images.

In the approximation of an isotropic medium, the Landau-Lifshitz-Looyenga model [142] is well suited for determining the porosity of the mesoporous Ge layer. In the case of freshly prepared porous Ge, the refractive index is a weighted average of the refractive indices of Ge and air

$$\mathcal{P} = \frac{n_{\mathrm{r,PGe}}^{2/3} - n_{\mathrm{r,Ge}}^{2/3}}{1 - n_{\mathrm{r,Ge}}^{2/3}} \tag{3.7}$$

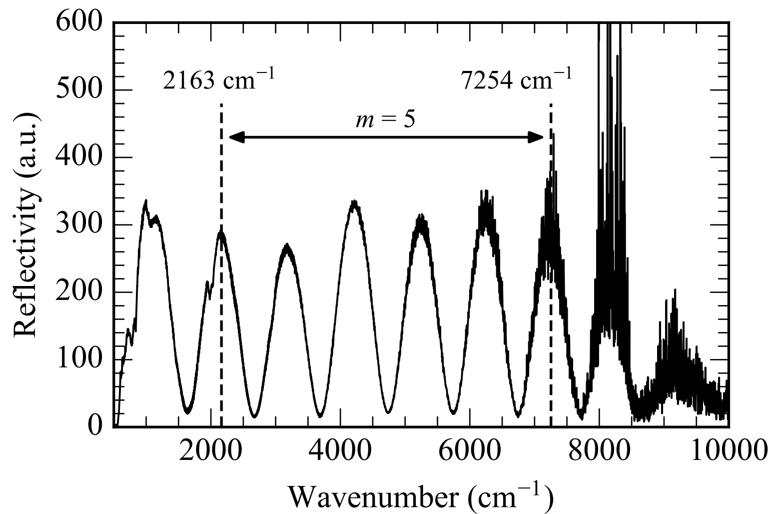

Figure 3.11: Infrared reflectivity spectra of as-prepared mesoporous Ge layer with a thickness of 2.88 μm and a porosity of 72%. There are $m = 5$ clearly defined Fabry-Perot fringes between 2163 and 7254 cm^{-1} $\left(\delta\nu = 5061\mathrm{cm}^{-1}\right)$.

where we have taken the refractive index of air to be unity. The refractive index of Ge is reasonably stable around $n_{\mathrm{Ge}} \approx 4$ in the range of interest.

The porous layer thickness for the sample corresponding to the data in Figure 3.11 is 2.88 μm, and so the calculated porosity is 72%.

3.1.A.2 Relationship between annealing temperature and surface crystallite size

Figure 3.12 shows the average crystallite size of mesoporous Ge for various annealing temperatures, depicted as an Arrhenius plot. The activation energy (E_{a}) for this mass-diffusion process is found to be 0.69 eV, larger than the activation energies found for sintering of porous Si (0.16 – 0.23 eV) [122, 143]. The crystallite size varies strongly with temperature and obeys the Arrhenius-like relation:

$$d_{\mathrm{crystallite}} \propto \exp\left(-\frac{E_{\mathrm{a}}}{k_{\mathrm{B}}T}\right) \tag{3.8}$$

where k is the Boltzmann constant.

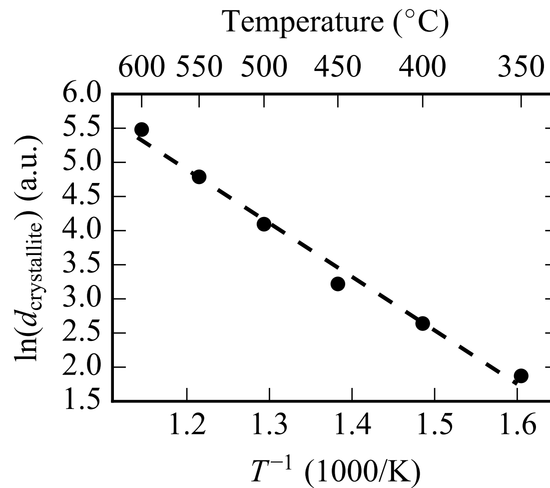

Figure 3.12: Arrhenius-like plot of the temperature-dependent crystallite size $(d_{\mathrm{crystallite}})$ of annealed mesoporous Ge.

Table 3.1: List of parameters used in determining the space charge region and the Fermi level.*

Parameter	**Description**	**Value/Units**
q	Elementary charge on an electron	C (f.c.)
ε_r	Relative permittivity (Ge)	16.2
ε_0	Vacuum permittivity	F/m (f.c.)
N_a	Doping concentration	cm^{-3}
N_s	Surface state density	$cm^{-2}\,eV^{-1}$
N_v	Effective density of states in the valence band (Ge)	5×10^{18} cm^{-3}
E_v	Valence band edge	eV
A_{void}	Surface area of a void	cm^2
$V_{S.C.}$	Volume of the space charge region	cm^3

*Fixed values are given, fundamental constants are indicated by (f.c.).

3.1.A.3 Defining the space charge region and the Fermi level

By Gauss' law under the depletion approximation, the electric potential in the cylindrical pore unit cell, calculated relative to the center of the void, is

$$\phi_{cyl}(r) = \begin{cases} 0 & 0 \le r < a \\ \frac{qN_a}{2\varepsilon_s\varepsilon_0}\left[\frac{r^2-a^2}{2} - (W+a)^2 \ln\left(\frac{r}{a}\right)\right] & a \le r < W+a \\ \frac{qN_a}{2\varepsilon_s\varepsilon_0}\left[\frac{(W+a)^2-a^2}{2} - (W+a)^2 \ln\left(\frac{W+a}{a}\right)\right] & r \ge W+a \end{cases} \tag{3.9}$$

Similarly, for the spherical void unit cell, the potential is given by

$$\phi_{sph}(r) = \begin{cases} 0 & 0 \le r < a \\ \frac{qN_a}{3\varepsilon_s\varepsilon_0}\left[\frac{r^2-a^2}{2} - (W+a)^3 \left(\frac{1}{r} - \frac{1}{a}\right)\right] & a \le r < W+a \\ \frac{qN_a}{3\varepsilon_s\varepsilon_0}\left[\frac{3(W+a)^2-a^2}{2} - \frac{(W+a)^3}{a}\right] & r \ge W+a \end{cases} \tag{3.10}$$

All parameters are defined in Table 3.1.

The space charge width W is calculated using the charge neutrality condition where it is assumed that the charges contributed by the positively charged surface states (Q_S) and by the ionized acceptor atoms (Q_V)

sum to zero.

$$Q_S + Q_V = 0 \tag{3.11}$$

$$Q_S = qN_s A_{void}(\Phi_0 - E_F) \tag{3.12}$$

$$Q_V = -qN_a V_{S.C.}(W) \tag{3.13}$$

where $V_{S.C.}$ is the volume of the space charge region.

We first assume that the space charge region has the same symmetry as the void (either cylindrical or spherical). Assuming all acceptor atoms are fully ionized, the Fermi level E_F is found using the standard expression for the carrier concentration in a bulk semiconductor

$$p_0 = N_v e^{-\frac{E_F - E_v}{k_B T}} \cong N_a \tag{3.14}$$

The valence band edge E_v, indicated in Figure 3.9c, is given by

$$E_v = -q\phi(W_0 + a) \tag{3.15}$$

using ϕ_{cyl} or ϕ_{sph}, as appropriate. The baseline width of the space charge region (W_0) is found by numerically solving the transcendental equation (3.11). There are three scenarios that arise, depicted in Figure 3.13.

a) The space charge region is fully contained within the unit cell. In this case, the Fermi level is appropriate and we can proceed with $W \equiv W_0$.

b) The baseline space charge width W_0 extends beyond the boundaries of the unit cell in some directions but not in others. In this case, we define a space charge region that is no longer symmetrical about the void and is instead bounded by the unit cell wherever W_0 extends beyond its boundaries. W_0 is incremented in steps of 0.01 nm until either the charge neutrality condition is satisfied or the space charge region reaches the boundaries of the unit cell in all directions (see case c).

c) The baseline space charge width W_0 extends beyond the boundaries of the unit cell in all directions. In this case, we assume the entire unit cell is depleted of carriers and adjust the Fermi level to satisfy the charge neutrality condition (equation 3.11). The final space charge width is maximized such that $W = d\frac{\sqrt{3}}{2} - a$.

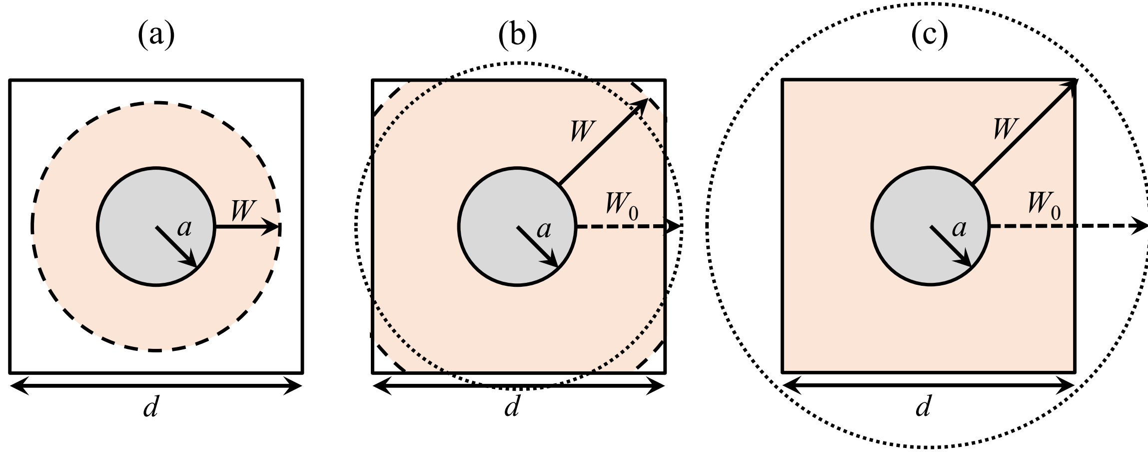

Figure 3.13: (a) Space charge region is contained within the unit cell. (b) When the baseline space charge width W_0 extends beyond the boundaries of the unit cell in some directions, the width is redefined so that it is fully contained. (c) When the baseline space charge width extends beyond the boundaries of the unit cell in all directions, the width is redefined to terminate at the boundaries of the unit cell and the Fermi level is adjusted accordingly.

Table 3.2: Parameters from Palankovski used for calculating the p-type carrier mobility of bulk germanium at room temperature.

Parameter	**Value**
μ_{max}	$1800\ \text{cm}^2/\text{V s}$
μ_{min}	$300\ \text{cm}^2/\text{V s}$
N_{ref}	$10^{17}\ \text{cm}^{-3}$

3.1.A.4 Mobility contributions from lattice and charged impurity scattering

The Ge p-type mobility comprises components due to lattice scattering and due to scattering of charged impurities. This is calculated according to Klaasen's unified mobility model [140]

$$\mu_{\text{Ge}} = \left(\frac{1}{\mu_{\text{lattice}}} + \frac{1}{\mu_{\text{impurities}}} \right)^{-1} \tag{3.16}$$

$$\mu_{\text{lattice}} = \mu_{\text{max}} \tag{3.17}$$

$$\mu_{\text{impurities}} = \frac{\mu_{\text{max}}^2}{\mu_{\text{max}} - \mu_{\text{min}}} \left(\frac{N_{\text{ref}}}{N_{\text{a}}} \right) + \frac{\mu_{\text{max}}\mu_{\text{min}}}{\mu_{\text{max}} - \mu_{\text{min}}} \left(\frac{p_{\text{ave}}}{N_{\text{a}}} \right) \tag{3.18}$$

with parameters from Palankovski [141] given in Table 3.2.

For bulk Ge, the average carrier concentration is roughly equal to the doping density ($p_{\text{ave}} \approx N_{\text{a}}$) and

Klaasen's model gives identical results to Palankovski. In mesoporous germanium, $p_{\mathrm{ave}} < N_{\mathrm{a}}$ and so the resulting mobility calculated using Klaasen's model is lower than results computed according to Palankovski.

Note that this model is only valid at room temperature and does not include minority impurity scattering or electron-hole scattering as these effects are assumed to be negligible for this system.

3.1.A.5 Effect of interface state density on transport model

The interface state density for mesoporous Ge has not yet been measured, and so estimated values from the literature are used in the electrostatic model that has been described. Here, the impact of the surface state density on simulated transport properties is explored for densities ranging from 5×10^{12} to 5×10^{15} $\mathrm{cm^{-2}\,eV^{-1}}$ (see Figure 3.14).

As the interface state concentration increases, we first see a large drop in average carrier concentration (Figure 3.14a); however, for interface state densities exceeding 5×10^{13} $\mathrm{cm^{-2}\,eV^{-1}}$, the number of surface states is so large that enlarging the interface state density further has minimal impact. Conversely, the impact of the interface states on mobility becomes dominant as the interface state density increases (Figure 3.14b). Overall, the resistivity increases considerably with increasing surface state density, as shown in Figure 3.14c. It should be noted that the calculations shown in Figure 3.14 were done using the fitting parameter $C\sim$ 320,000 $\mathrm{cm^{-1}\,V^{-1}\,s^{-1}}$, which was obtained by comparison to experiment assuming an interface state density of 4×10^{14} $\mathrm{cm^{-2}\,eV^{-1}}$. If the true interface state density of the material differs from this value, the fitting parameter C must differ as well, and so the mobilities and resistivities shown in Figures 3.14b and c would change accordingly; however, the general trends shown in figure 3.14 would be the same.

Ultimately, obtaining an accurate measurement of the interface state density for mesoporous Ge and establishing the effect of annealing on this value will greatly improve the accuracy of this model for the material systems under investigation. Furthermore, the preliminary simulation results shown in Figure 3.14 suggest that surface treatment in order to reduce the interface state density (see for example [144, 145]) in addition to varying the morphology may prove to be highly effective in tuning the conductivity of mesoporous Ge films.

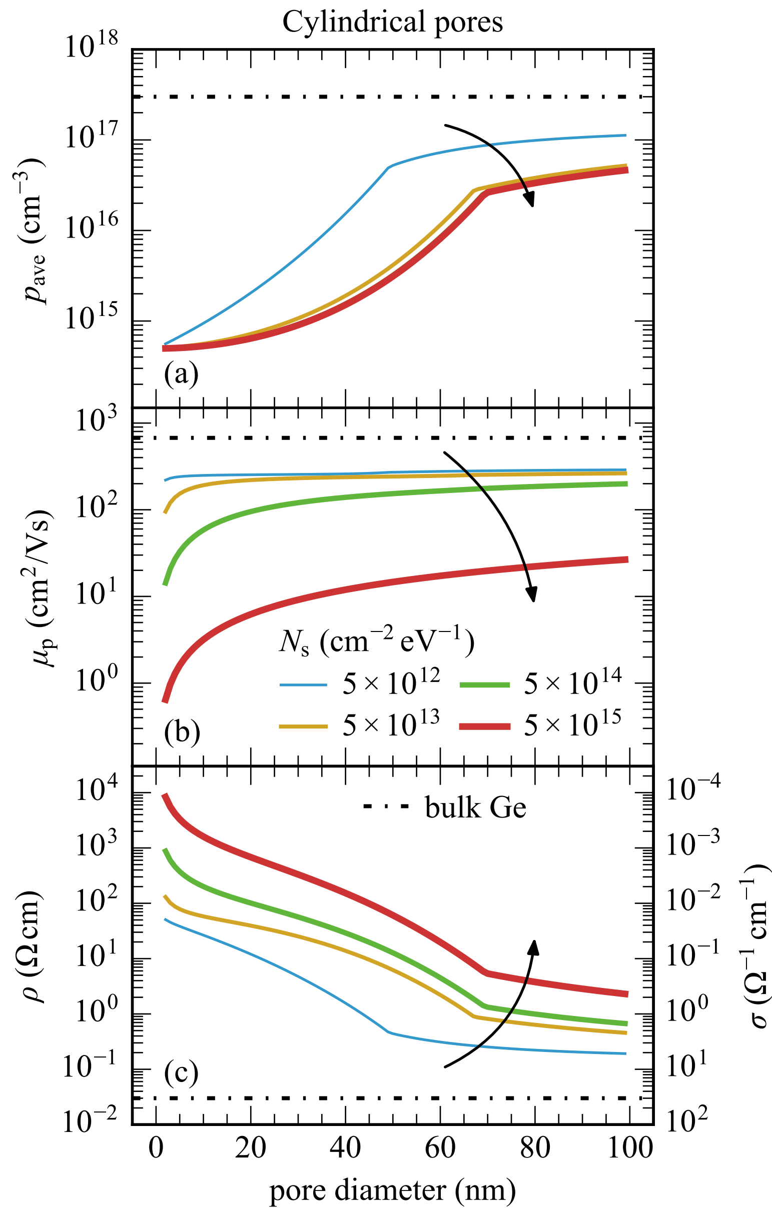

Figure 3.14: (a) Modelled average free carrier concentration, (b) carrier mobility, and (c) resistivity of mesoporous Ge as a function of pore/void size for interface state densities ranging from 5×10^{12} to 5×10^{15} cm^{-2}eV^{-1}. Conductivity is shown on the secondary y-axis of (c). A doping concentration of 3×10^{17} cm^{-3} and a porosity of 50% are assumed. Arrows indicate direction of increasing interface state density. Values for bulk Ge are shown.

3.2 Modelling of triple-junction solar cells on voided Ge/Si substrates

MEGHAN N. BEATTIE, YOUCEF A. BIOUD, ABDERRAOUF BOUCHERIF, DOMINIQUE DROUIN, RICHARD ARÈS, CHRISTOPHER E. VALDIVIA, AND KARIN HINZER

Scope and impact

The following is a reproduction of a conference proceeding that was presented at the 7th World Conference On Photovoltaic Energy Conversion, June 2018, Waikoloa, Hawaii, with the original title: “III-V Multi-Junction Solar Cells on Si Substrates with a Voided Ge Interface Layer: A Modeling Study” [146]. The publication describes my work simulating III-V multi-junction solar cells on Si substrates engineered using a voided germanium compliance layer to accommodate the lattice mismatch. The simulations make use of the electrostatic model described in Section 3.1 and consider the impact of threading dislocations on the PV device performance. Our results indicate that for a triple-junction solar cell (InGaP/GaAs/Ge) grown on a silicon substrate, devices with threading dislocation densities on the order of $10^6\,\mathrm{cm}^{-2}$ and $10^4\,\mathrm{cm}^{-2}$ could respectively attain ~ 76% and ~ 93% of the efficiency of a comparable defect-free device. Furthermore, the majority of the losses come from the Ge subcell, indicating that alternative designs that neglect the Ge cell may yield improved efficiencies.

The simulations imply that voided Ge/Si engineered substrates are well-suited to applications within III-V PV devices due to the very low dislocation densities $\leq 10^4\,\mathrm{cm}^{-2}$ that they can achieve [32].

Author contributions

MEGHAN N. BEATTIE As the lead University of Ottawa-based graduate student associated with the project, I performed the device simulations in Sentaurus and helped to develop the electrostatic model. As first author, I wrote the manuscript and prepared all of the figures.

DR. YOUCEF A. BIOUD As the lead Université de Sherbrooke graduate student associated with the project, Youcef developed the fabrication procedure for the engineered Si substrates. He also performed the electron microscopy shown in 3.15. He provided detailed feedback throughout the research process and assisted in editing the manuscript.

PROF. ABDERRAOUF BOUCHERIF As a research associate with the Institut interdisciplinaire d'innovation technologique (3IT) at the Université de Sherbrooke, Abderraouf guided Youcef in developing the engineered Si substrates. He also helped to guide my research, provided detailed feedback during analysis of my simulation results, and assisted in editing the manuscript.

DR. CHRISTOPHER E. VALDIVIA As a senior research scientist within the University of Ottawa's SUNLAB research group, Chris helped to guide my research, provided detailed feedback during analysis of my simulation results, and assisted in editing the manuscript.

PROF. DOMINIQUE DROUIN As a professor at the Université de Sherbrooke and one of Youcef's co-supervisors, Dominique oversaw Youcef's work in developing the engineered Si substrates and assisted in editing the manuscript.

PROF. RICHARD ARÈS As a professor at the Université de Sherbrooke and one of Youcef's co-supervisors, Richard oversaw Youcef's work in developing the engineered Si substrates and assisted in editing the manuscript.

PROF. KARIN HINZER As the director of the University of Ottawa's SUNLAB research group, Karin oversaw my research, provided detailed feedback during analysis of my simulation results, and assisted in editing the manuscript.

Copyright

© 2018 IEEE. Reprinted, with permission, from:

> M. N. Beattie, Y. A. Bioud, A. Boucherif, D. Drouin, R. Arès, C. E. Valdivia, and K. Hinzer, "III-V multi-junction solar cells on Si substrates with a voided Ge interface layer: A modeling study," in *2018 7th IEEE World Conference on Photovoltaic Energy Conversion (WCPEC) (A Joint Conference of 45th IEEE PVSC, 28th PVSEC & 34th EU PVSEC)*, 0180–0184, Waikoloa Village, HI, USA, 2018. DOI: 10.1109/PVSC.2018.8547836

In reference to IEEE copyrighted material which is used with permission in this thesis, the IEEE does not endorse any of the University of Ottawa's products or services. Internal or personal use of this material is permitted. If interested in reprinting/republishing IEEE copyrighted material for advertising or promotional

purposes or for creating new collective works for resale or redistribution, please go to http://www.ieee.org/publications_standards/publications/rights/rights_link.ht to learn how to obtain a License from RightsLink. If applicable, University Microfilms and/or ProQuest Library, or the Archives of Canada may supply single copies of the dissertation.

Abstract

Multi-junction solar cell efficiencies far exceed those attainable with silicon photovoltaics; however, the high cost of materials remains a barrier to their widespread use. Substantial cost reduction could be achieved by replacing the germanium substrate with a less expensive alternative: silicon. However, threading dislocations introduced by the lattice mismatch between silicon and other layers have a detrimental effect on performance. In this research, we seek to accommodate lattice mismatch by introducing a voided germanium interface layer on the silicon substrate to intercept dislocations and prevent them from reaching the active layers. We present simulation results exploring the effect of threading dislocations and substrate doping on device performance. For insufficient substrate doping, a potential barrier forms at the germanium/silicon interface, restricting current flow. This barrier becomes larger under concentration, necessitating higher doping $\sim 10^{19}$ cm^{-3} in the substrate layer. We show that for dislocation densities of 10^6 cm^{-2}, an efficiency of 28% is theoretically achievable under 100 sun concentration when the voided germanium interface and the silicon substrate are highly doped. For very low defect densities of 10^4 cm^{-2}, an efficiency of 36% could be achieved.

3.2.1 Introduction

The highest efficiency solar cells commercially available use multiple lattice-matched junctions to harness as much of the sun's energy as possible. These devices, based on III-V semiconductors, are grown on relatively expensive germanium substrates with only a fraction of the substrate being used for energy generation while the remainder serves as a mechanical support. Even under concentration, the system cost is too large to compete with standard silicon photovoltaics for many applications. Various techniques are being explored to reduce the cost of III-V semiconductor technologies by either substrate removal and reuse [147] or replacement of the substrate with a less expensive alternative, such as silicon [148].

When germanium is grown on silicon, the lattice mismatch between the materials (about 4%) causes a high density of defects at the interface. Many of these defects propagate towards the surface, resulting in

threading dislocations that inhibit minority carrier collection [148]. In this research, we are investigating the use of a voided germanium interface layer to intercept dislocations before they reach the surface, enabling epitaxial growth of high quality Ge, IV (e.g. SiGeSn), and III-V (e.g. InGaAs, InGaP) semiconductors on Si substrates.

By modelling multi-junction solar cell (MJSC) designs on Si substrates, we investigate the impact of threading dislocations on device performance. With highly doped Si, we show that it is theoretically possible to achieve device efficiency approaching 30% under 100 sun illumination with dislocation densities approaching 10^6 cm^{-2}, while for low defect densities of 10^4 cm^{-2}, we calculate efficiencies exceeding 36%.

3.2.2 Results and Discussion

3.2.2.1 Voided Germanium Interface Layer in MJSC

Mesoporous Ge, formed by bipolar electrochemical etching [33, 34], is transformed into quasi-monocrystalline voided Ge during thermal annealing, when atoms on the surface of the pores gain sufficient energy to move to more energetically favorable positions [121]. The pores in the bulk of the material enlarge while simultaneously closing off near the surface, forming cavities with dimensions on the scale of tens of nanometers beneath a cohesive crystalline surface (Figure 3.15a). The Ge material directly below the surface is highly monocrystalline (Figure 3.15b), while the crystallinity in the bulk of the voided layer is less pristine (Figure 3.15c).

When voided Ge is formed on a Si substrate, the voids act as a barrier to threading dislocations originating at the Ge/Si interface, terminating them before they reach the surface [149]. The surface dislocation density is reduced, presenting a higher quality template for epitaxial growth. Preliminary experiments have shown that the threading dislocation density can be reduced by three orders of magnitude, with the potential for further reductions through optimization of the process.

Figure 3.15d shows a schematic of the multi-junction solar cell design that we propose, using a voided Ge interface layer between the silicon substrate and the active layers of the device. A layer of voided Si near the interface forms as a consequence of the fabrication process. The void fractions in the voided Ge and Si are 0.4 and 0.7 respectively. Layer schematics for the bottom Ge subcell, the voided interface layer, and the substrate are given in Table 3.3.

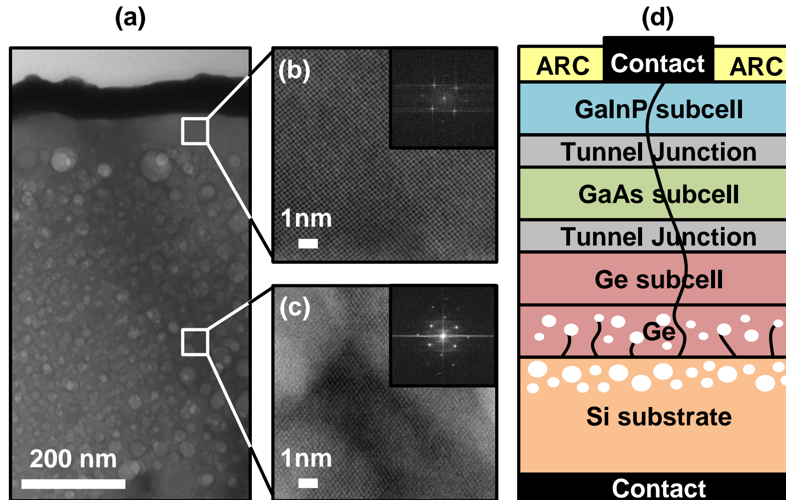

Figure 3.15: (a) Scanning electron microscopy (SEM) image of voided Ge. (b), (c) Transmission electron microscopy (TEM) images showing crystallinity of Ge near the surface and in the bulk of the voided material, respectively. The insets show the Fourier transforms of the TEM images. (d) Schematic of the proposed MJSC design.

Table 3.3: Layer schematics for bottom Ge subcell, voided interface layer, and substrate.

Layer	Material	Doping $\left(\mathrm{cm}^{-3}\right)$	Thickness (μm)
FSF	n-GaInP	7×10^{17}	0.5
Emitter	n-Ge	1×10^{18}	0.1
Base	p-Ge	5×10^{17}	2
BSF	p-Ge	1×10^{20}	0.05
Interface 1	Voided p-Ge	p-Ge N_a	1
Interface 2	Voided p-Si	p-Si N_a	1.5
Substrate	p-Si	p-Si N_a	

3.2.2.2 Electrostatic Models

Electrical transport properties of the quasi-monocrystalline Ge are estimated using electrostatic models, described in Ref. [6], inspired by the work of Banerjee et al. [128, 129]. These models of carrier concentration and mobility in p-type porous and quasi-monocrystalline Ge were found to agree within an order of magnitude to experimental resistivities [6]. The same models were used for the quasi-monocrystalline Si layer with key parameters determined based on experimental data from Dittrich [7] and Rinke [150]. The models account for the presence of surface states on the walls of the void, which trap free carriers, generating

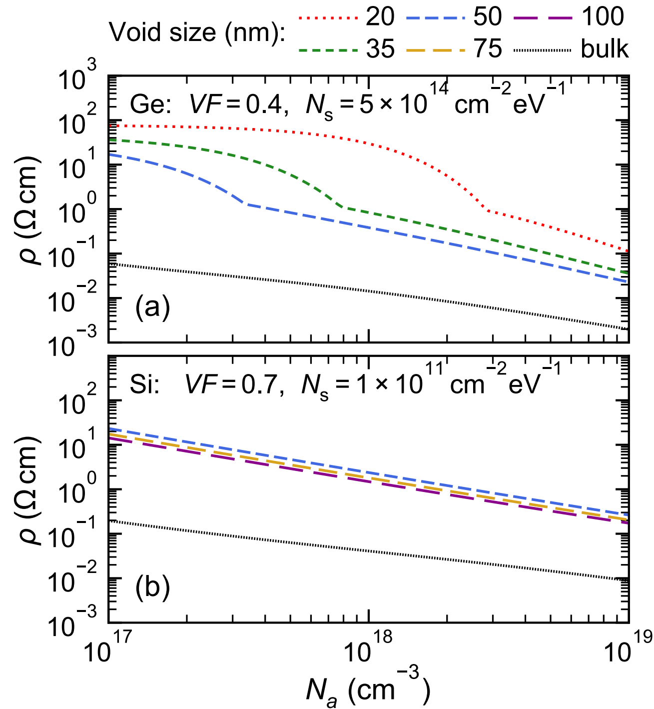

Figure 3.16: Modelled resistivities for porous Ge (a) and porous Si (b) for p-type doping concentrations ranging from 10^{17} to 10^{19} cm^{-3}. Void fractions (VF) and void sizes are chosen to correspond to what has been observed experimentally: VF = 0.4 and 20 to 50 nm for Ge, 0.7 and 50 to 100 nm for Si. The surface state densities (N_s) on the void walls are taken to be $N_s = 5 \times 10^{14}$ cm^{-2}eV^{-1} for Ge [6] and $N_s = 1 \times 10^{11}$ cm^{-2}eV^{-1} for Si [7].

a space-charge region around each cavity. Simulated electrical resistivities are plotted in Figure 3.16 as a function of doping concentration for both voided Ge and Si for realistic void fraction and size. The influence of the voids on resistivity is stronger for Ge than for Si due to the higher surface state density on the void walls. The abrupt changes in the voided Ge resistivity (Figure 3.16a) mark the transition from full to partial depletion of carriers [6].

In general, predicted electrical resistivities do not exceed 75 Ω cm in voided Ge and 23 Ω cm in voided Si for the void fractions, void sizes, and doping concentrations considered here. The maximum series resistance introduced by the voided interface layers when both are doped at 10^{17} cm^{-3} is $\sim$ 0.01 Ω cm^2, which is sufficiently low to be reasonable for concentrated solar applications.

3.2.2.3 Device Model

Detailed models of triple-junction solar cells on Si substrates using quasi-monocrystalline Ge interface layers were developed in Synopsys Sentaurus, with the basic geometry shown in Figure 3.15d. The electrostatic

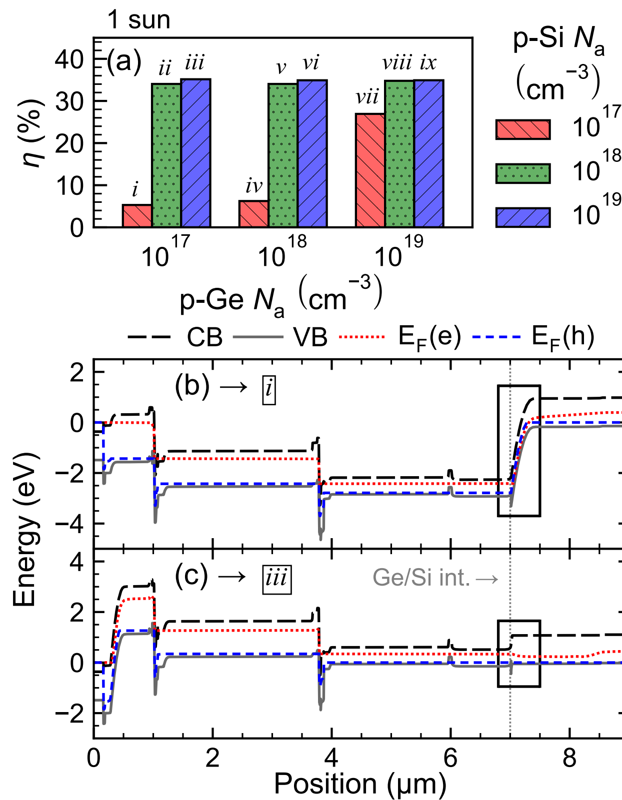

Figure 3.17: (a) MJSC efficiency (η) under 1 sun for different p-type doping concentrations N_a in the voided Ge interface layer and the Si substrate. Cell designs with different doping combinations are numbered *i* – *ix*. (b), (c) Short-circuit band diagrams for low and high doping in Si (designs *i* and *iii*). Conduction and valence bands, CB and VB, and electron and hole quasi-Fermi levels, E_F(e) and E_F(h), are indicated. The potential step at the Si/Ge interface is outlined.

model described in Section 3.2.2.2 is used to determine appropriate electrical transport properties in the voided Ge and Si layers (average void sizes of 35 and 75 nm are used for voided Ge and Si respectively). Relevant optical properties for these layers are determined using an effective medium approach [142].

We studied the impact of both doping concentration in the interface layers and the p-doped Si (p-Si) substrate was studied as well non-zero threading dislocation densities and concentrated illumination. We determined that high doping in the substrate is critical to achieving reasonable power conversion efficiencies (Figure 3.17a). This is due to the formation of a potential barrier at the Ge/Si interface, preventing efficient transport of the majority p-type carriers through the substrate. By introducing high doping levels in the Si $(> 10^{18}\ \text{cm}^{-3})$, the height of the potential barrier is reduced so that p-type carriers are able to travel freely (Figure 3.17b-c).[1]

[1]Equilibrium band diagrams are shown in Figure 3.21 in the appendix.

The impact of the threading dislocations on minority carrier lifetime is determined according to [151]:

$$\frac{1}{\tau} = \frac{1}{\tau_{\max}} + \frac{\pi^3 D \cdot TDD}{4} \tag{3.19}$$

where TDD is the threading dislocation density, D is the minority carrier diffusion constant, and $\tau_{\max}$ is the minority carrier lifetime without threading dislocations ($TDD = 0$). Efficiency drops off quickly with threading dislocation density, falling from 34.0% to 25.8% as the density increases from 0 to 10^6 cm^{-2}, for a solar cell with both Si and Ge doped at 10^{18} cm^{-3} (design *v* in Figure 3.17a). This can be marginally improved upon (by ~ 1%) by increasing the doping of the Si substrate to 10^{19} cm^{-3} (design *vi* in Figure 3.17a). The threading dislocations influence the Ge subcell more strongly than the other cells because the minority carrier lifetimes are longest here (~ 1 ms compared to 10^{-8} and 10^{-10} s for GaAs and GaInP) and so the second term in equation 3.19 is dominant. The effect is shown in the current-voltage curves in Figure 3.18, where reductions in short-circuit current and open-circuit voltage are immediately observed in the Ge subcell when threading dislocations are considered in the model. The fill-factor of the Ge subcell is improved by increasing the Si doping concentration, both with and without threading dislocations.

Low fill-factor and short-circuit current within the bottom subcell limit current flow throughout the device, reducing the power output of the entire cell. For dislocation densities approaching 10^6 cm^{-2}, the current will be limited by the bottom subcell, even at short-circuit.

In most terrestrial applications, multi-junction solar cells are used under concentrated illumination. This type of deployment requires much smaller cells (reducing material cost) while simultaneously increasing the efficiency. In the structures modelled here, we see improved cell efficiency only for very high doping concentrations in the Si $\left(10^{19}\ \text{cm}^{-3}\right)$. For Si doped at 10^{18} cm^{-3} , the potential barrier observed at the Ge/Si interface becomes substantial for the p-type carriers and current transmission through the bottom subcell is minimal. Neglecting the influence of threading dislocations, a concentration of 10 suns results in significant current limitation where short-circuit current is no longer proportional to illumination intensity and the efficiency of the device is reduced by a factor of two relative to the 1 sun case. In the case of Si doped at 10^{19} cm^{-3}, we observe an increased efficiency at 10 suns illumination. At 100 suns, the fill-factor is greatly reduced and we start to see a reduction in short-circuit current. This effect is illustrated by the current-voltage characteristic of the Ge subcell in Figure 3.19.

Increasing the doping concentration in the Ge interface layer from 10^{18} to 10^{19} cm^{-3} has minimal effect

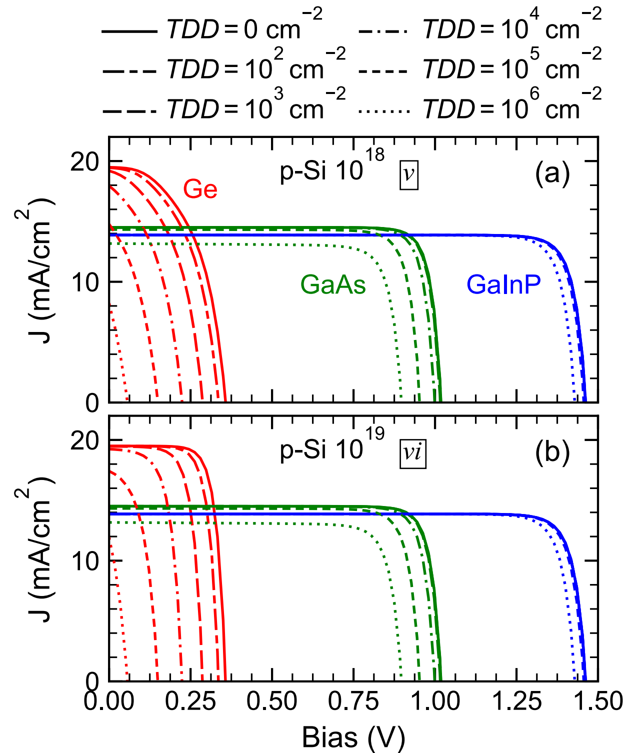

Figure 3.18: Current voltage curves of each subcell for Si doped at (a) 10^{18} cm^{-3} and (b) 10^{19} cm^{-3} (cell designs *v* and *vi*), under illumination of 1-sun AM1.5D. The Ge interface doping is 10^{18} cm^{-3} in both cases. Curves are shown for threading dislocation densities between 0 and 10^6 cm^{-2}.

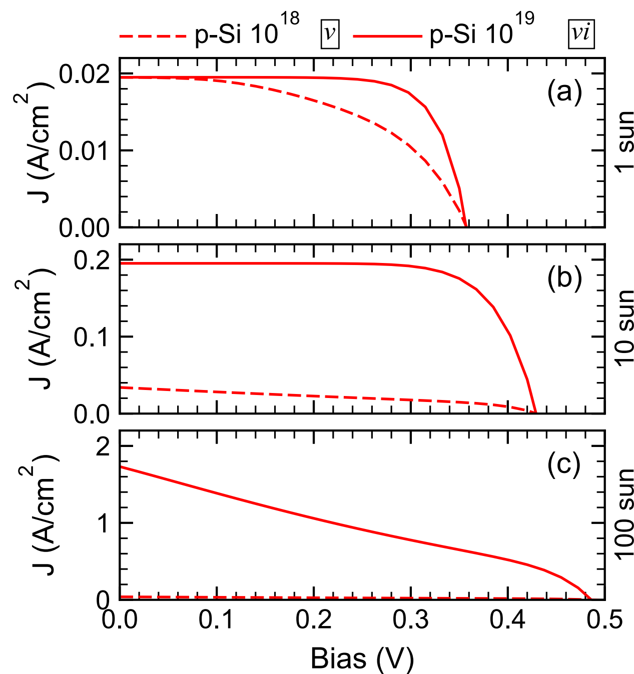

Figure 3.19: Current voltage curves in the Ge subcell for illumination at (a) 1 sun, (b) 10 suns, and (c) 100 suns. The Si doping concentrations are 10^{18} cm^{-3} (cell design *v*) and 10^{19} cm^{-3} (cell design *vi*). The Ge doping concentration is 10^{18} cm^{-3} for all cases.

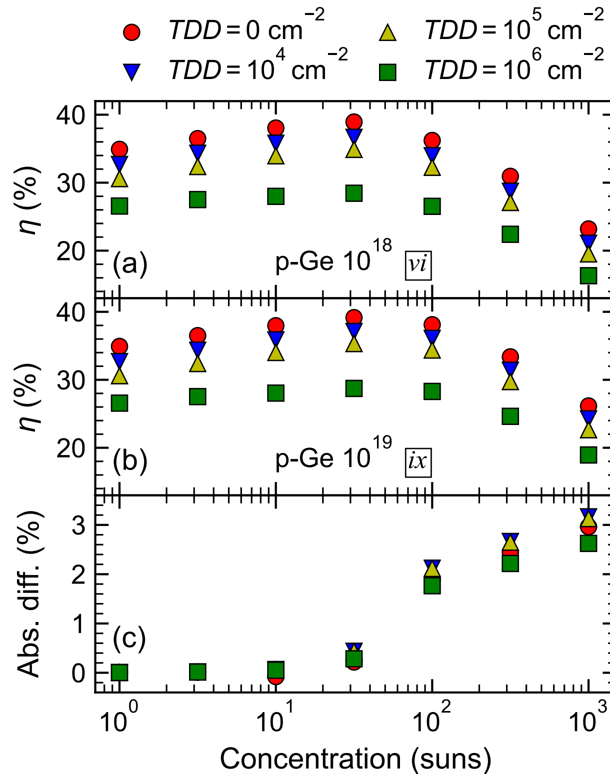

Figure 3.20: (a), (b) MJSC efficiency for concentrations ranging from 1 to 1000 suns and threading dislocation densities between 0 and 10^6 cm^{-2}. The Si doping concentration is fixed at 10^{19} cm^{-3} and the Ge interface layer doping concentration is 10^{18} cm^{-3} and 10^{19} cm^{-3} for (a) and (b) respectively (cell designs *vi* and *ix*). The absolute difference in efficiency between (a) and (b) is shown in (c).

(< 0.01% absolute) on the MJSC efficiency under 1 sun illumination; however, performance is enhanced under concentration. Substantial improvements in efficiency (8-10% absolute) are observed for increased Ge interface doping at 10 suns when the Si is doped at 10^{18} cm^{-3} ; however, there is a reduction in efficiency relative to the 1 sun case due to reduced short-circuit current in the Ge subcell (see Figure 3.19).

When the Si is highly doped at 10^{19} cm^{-3}, performance enhancements are minimal at 10 suns but become significant (> 2% absolute) at concentrations ≥ 100 suns. This is shown in Figure 3.20. At 100 suns, when both the Si substrate and the voided Ge interface layer are doped at 10^{19} cm^{-3}, efficiencies are maximized for concentrations between 10 and 100 suns for all threading dislocation densities simulated. The maximum efficiency approaches 30% for high threading dislocation density $\left(10^6 \text{ cm}^{-2}\right)$ and exceed 36% for low threading dislocation density $\left(10^4 \text{ cm}^{-2}\right)$. Potential improvements could be achieved at higher threading dislocation densities by omitting the bottom junction.

3.2.3 Conclusion

Multi-junction solar cells on silicon substrates have the potential to provide efficiencies that are much superior to standard silicon technology while leveraging silicon's low cost; however, extreme sensitivity to threading dislocation densities above $\sim 10^5$ cm^{-2} as well as the potential barrier at the Ge/Si interface present important technical challenges. Our calculations under moderate concentration between 10 and 100 suns with high doping in the Si substrate $\left(10^{19}\ \text{cm}^{-3}\right)$ yield theoretical efficiencies exceeding 36% for low threading dislocation densities $\left(\leq 10^4\ \text{cm}^{-2}\right)$ and approaching 30% for higher dislocation densities on the order of 10^6 cm^{-2}.

Acknowledgements

This work is supported by the Natural Sciences and Engineering Research Council of Canada (NSERC), the Canada Research Chair program, the Canadian Foundation for Innovation, the Fonds de recherche du Québec-Nature et technologies (FRQNT), the Ontario Research Fund, the Regroupement Quebecois sur les Matériaux de Pointe (RQMP), and CMC Microsystems.

3.2.A Appendix

3.2.A.1 Equilibrium band diagrams

Equilibrium band diagrams are shown in Figure 3.21 for cell designs *i* and *iii*. The misalignment of the valence band at the Ge/Si interface impedes the flow of free holes travelling from left to right. The barrier is reduced when the doping of the Si substrate is increased from 10^{17} cm^{-3} to 10^{19} cm^{-3}.

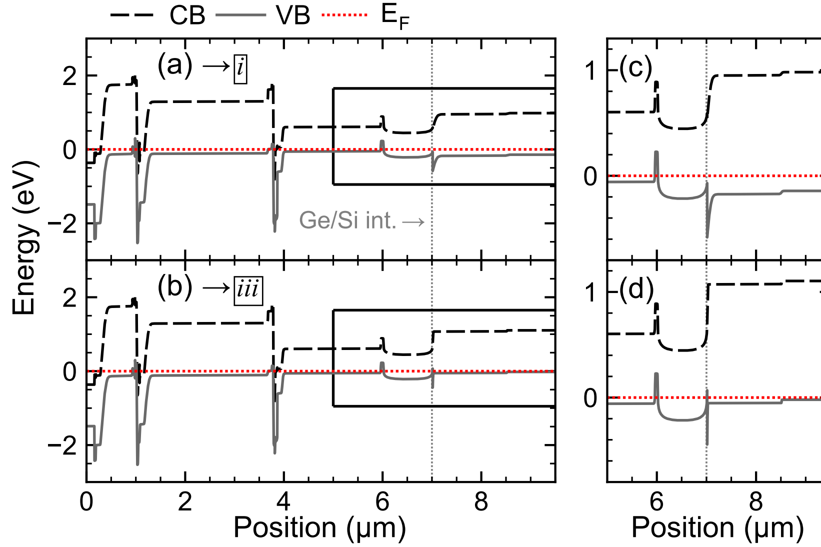

Figure 3.21: (a), (b) Equilibrium band diagrams for low and high doping in Si (designs *i* and *iii*). Conduction and valence bands, CB and VB, and the Fermi level, E_{F}, are indicated. The boxed regions in (a) and (b) are shown in more detail in (c) and (d) respectively.

3.2.A.2 Simulated device structure and material parameters

The full layer structure for the simulated triple-junction solar cell on voided Ge/Si is given in Table 3.4, based off of a standard triple-junction solar cell simulation prepared by Matthew Wilkins [63].

The material parameters used to generate the GaInP/GaAs/Ge solar cell simulations are summarized in the Tables 3.5 to 3.15.

The Masetti model is used to compute doping-dependent mobility for Si [152]

$$\mu = \mu_{\mathrm{min1}} \exp\left(\frac{-P_{\mathrm{c}}}{N_{\mathrm{d}} + N_{\mathrm{a}}}\right) + \frac{\mu_{\mathrm{max}} - \mu_{\mathrm{min2}}}{1 + \left(\frac{N_{\mathrm{d}}+N_{\mathrm{a}}}{C_{\mathrm{r}}}\right)^{\alpha_{\mathrm{M}}}} - \frac{\mu_1}{1 + \left(\frac{C_{\mathrm{s}}}{N_{\mathrm{d}}+N_{\mathrm{a}}}\right)^{\beta_{\mathrm{M}}}} \tag{3.20}$$

The Auger recombination coefficients in Si are calculated according to [153]

$$A_{\mathrm{Aug}} = A_{0,\mathrm{Aug}} \left[1 + H_{\mathrm{Aug}} \exp\left(\frac{-\{n,p\}}{N_{0,\mathrm{Aug}}}\right)\right] \tag{3.21}$$

where $\{n,p\}$ refers to either the electron density n for $A_{\mathrm{Aug,n}}$ or the hole density p for$A_{\mathrm{Aug,p}}$.

The impact of threading dislocations on minority carrier lifetime due to SRH recombination is described by equation 3.19. This relationship comes from the assumption that the dislocations are uniformly distributed with an average area per dislocation given by $\pi x_{\mathrm{c}}^2 = 1/TDD$ where x_{c} is the unit cell radius. The one-dimensional continuity equation for transport of minority carriers to the dislocations in p-type material is

$$\frac{\partial n}{\partial t} = D\frac{\partial^2 n}{\partial x^2} \tag{3.22}$$

Taking the boundary conditions to be $n = 0$ at $x = 0$ and $\partial n/\partial x = 0$ at $x = x_{\mathrm{c}}$, equation 3.22 can be satisfied by [154]

$$n(x,t) = n_0 e^{-t/\tau_{\mathrm{TDD}}} \sin\left(\frac{x\pi}{2x_{\mathrm{c}}}\right) \tag{3.23}$$

where

$$\tau_{\mathrm{TDD}} = \frac{4}{\pi^3 D \cdot TDD} \tag{3.24}$$

Electrical transport properties for the voided materials were calculated from the electrostatic model described in Section 3.1.3.4. Parameters are given in Table 3.12. Optical properties were computed using the Looyenga effective medium approximation [142], which determines the effective permittivity from the bulk semiconductor and air. Taking the relative permittivity of air to be 1, the relative effective permittivity is then

$$\varepsilon_{\mathrm{eff}} = \left[\mathcal{P} + (1-\mathcal{P})\,\varepsilon_{\mathrm{bulk}}^{1/3}\right]^3 \tag{3.25}$$

Optical parameters for the standard two-layer anti-reflection coating are given in Table 3.13. Surface recombination within the scope of MJSC simulations is described by Wilkins and Hinzer [63] and parameters are given in Table 3.14. Additional parameters, listed in Table 3.15, are required to simulate band-to-band tunneling within the tunnel diode layers of the MJSC structure, namely, the effective Richardson constants (g) and the effective tunneling masses (m_{t}). Further explanation of these parameters and an overview of the simulation of tunnel diodes is given by Walker et al. [155].

Table 3.4: Detailed epitaxial layer structure for triple-junction solar cell on voided Ge/Si.

Region	Layer	Material	Bandgap (eV)	Doping (cm^{-3})	Thickness (nm)
ARC		MgF			100
		TiO_x			60
Subcell (top)	n FSF	$Al_{0.5}In_{0.5}P$	2.382	6×10^{18}	25
	n emitter	$Ga_{0.5}In_{0.5}P$	1.88	5×10^{18}	100
	p base	$Ga_{0.5}In_{0.5}P$	1.88	8×10^{16}	650
	p BSF	$Al_{0.25}Ga_{0.25}In_{0.5}P$	1.984	3×10^{19}	50
Tunnel diode (top)	p++ TD	$Al_{0.3}Ga_{0.7}As$	1.797	2×10^{20}	30
	n++ TD	$Ga_{0.5}In_{0.5}P$	1.88	6×10^{19}	30
Subcell (middle)	n FSF	$Al_{0.8}Ga_{0.2}As$	2.05	1×10^{19}	30
	n emitter	GaAs	1.424	3×10^{18}	100
	p base	GaAs	1.424	1×10^{17}	2500
	p BSF	$Al_{0.2}Ga_{0.8}As$	1.672	1×10^{19}	80
Tunnel diode (bottom)	p++ TD	$Al_{0.3}Ga_{0.7}As$	1.797	1.2×10^{20}	30
	n++ TD	GaAs	1.424	6×10^{19}	30
Subcell (bottom)	n FSF	$Ga_{0.5}In_{0.5}P$	1.88	7×10^{17}	50
	n Emitter	Ge	0.661	1×10^{18}	100
	p Base	Ge	0.661	5×10^{17}	2000
	p BSF	Ge	0.661	1×10^{20}	50
Interface		Voided Ge	0.661	p-Ge N_a*	1000
		Voided Si	1.125	p-Si N_a*	1500
Substrate	p substrate	Si	1.125	p-Si N_a*	

* Modified in simulation.

Table 3.5: Material parameters at 300 K used for $Ga_{0.5}In_{0.5}P$ in MJSC simulations. Values for electrons and holes are separated by a comma.

Category	Parameter	Value	Ref.
Permittivity	$\varepsilon_s/\varepsilon_0$	12.005	[156]
Refractive index	n_r, κ	Tabulated	[157]
Band structure	E_g (eV)	1.88	[158]
	ΔE_g (eV)	See reference	[156]
	χ (eV)	3.924	[4]
	m_c/m_0	0.08515	[158]
	m_v/m_0	0.7125	[156]
Mobility	μ_{max} $(cm^2/V\,s)$	4300, 150	[62]
	μ_{min} $(cm^2/V\,s)$	400, 15	[62]
	N_0 (cm^{-3})	2.0×10^{16}, 1.5×10^{17}	[62]
	A^*	0.70, 0.80	[62]
Recombination	B_{rad} (cm^3/s)	1×10^{-10}	[156]
	τ_{max} (s)	2×10^{-8}, 2×10^{-8}	[63]
	τ_{min} (s)	0, 0	[63]
	N_0 (cm^{-3})	1×10^{19}, 1×10^{19}	[63]
	γ^*	1, 1	[63]
	A_{Aug}	3×10^{-30}, 3×10^{-30}	[158]

Table 3.6: Material parameters at 300 K used for GaAs in MJSC simulations. Values for electrons and holes are separated by a comma.

Category	**Parameter**	**Value**	**Ref.**
Permittivity	$\varepsilon_s/\varepsilon_0$	12.91	[156]
Refractive index	n_r, κ	Tabulated	[159]
Band structure	E_g (eV)	1.424	[4]
	ΔE_g (eV)	See reference	[160]
	χ (eV)	4.07	[4]
	m_c/m_0	0.06553	[161]
	m_v/m_0	0.5236	[161]
Mobility	μ_{max} $(\mathrm{cm^2/V\,s})$	9400, 491.5	[62]
	μ_{min} $(\mathrm{cm^2/V\,s})$	500, 20	[62]
	N_0 $(\mathrm{cm^{-3}})$	6.0×10^{16}, 1.48×10^{17}	[62]
	A^*	0.394, 0.38	[62]
Recombination	B_{rad} $(\mathrm{cm^3/s})$	1×10^{-10}	[156]
	τ_{max} (s)	1×10^{-6}, 2×10^{-8}	[63]
	τ_{min} (s)	0, 0	[63]
	N_0 $(\mathrm{cm^{-3}})$	1×10^{16}, 2×10^{18}	[63]
	γ^*	1, 3	[63]
	A_{Aug}	5×10^{-30}, 5×10^{-30}	[161]

Table 3.7: Material parameters at 300 K used for Ge in MJSC simulations. Values for electrons and holes are separated by a comma.

Category	Parameter	Value	Ref.
Permittivity	$\varepsilon_s/\varepsilon_0$	15.8	[162]
Refractive index	n_r, κ	Tabulated	[163, 164]
Band structure	E_g (eV)	0.661	[161]
	ΔE_g (eV)	See reference	[156]
	χ (eV)	3.96	[161]
	m_c/m_0	0.5438	[156]
	m_v/m_0	0.3406	[161]
Mobility	μ_{max} $\left(cm^2/V\,s\right)$	3800, 1800	[141]
	μ_{min} $\left(cm^2/V\,s\right)$	850, 300	[141]
	N_0 $\left(cm^{-3}\right)$	2.6×10^{17}, 1×10^{17}	[141]
	A^*	0.56, 1	[141]
Recombination	B_{rad} $\left(cm^3/s\right)$	6.4×10^{-14}	[161]
	τ_{max} (s)	1×10^{-3}, 1×10^{-3}	[161]
	τ_{min} (s)	0, 0	[161]
	N_0 $\left(cm^{-3}\right)$	1×10^{16}, 1×10^{16}	[161]
	γ^*	1, 1	[161]
	A_{Aug}	1×10^{-30}, 1×10^{-30}	[161]

Table 3.8: Material parameters at 300 K used for $Al_{0.5}In_{0.5}P$ in MJSC simulations. Values for electrons and holes are separated by a comma.

Category	**Parameter**	**Value**	**Ref.**
Permittivity	$\varepsilon_s/\varepsilon_0$	11.355	[156]
Refractive index	n_r, κ	Tabulated	[157]
Band structure	E_g (eV)	2.382	[165]
	ΔE_g (eV)	See reference	[156]
	χ (eV)	3.748	[165]
	m_c/m_0	0.23	[165]
	m_v/m_0	0.36	[165]
Mobility	μ_{max} $(\mathrm{cm^2/V\,s})$	150, 180	[63]
	μ_{min} $(\mathrm{cm^2/V\,s})$	0, 0	[63]
	N_0 $(\mathrm{cm^{-3}})$	5×10^{17}, 2.75×10^{17}	[63]
	A^*	0.436, 0.397	[63]
Recombination	B_{rad} $(\mathrm{cm^3/s})$	1×10^{-10}	[158]
	τ_{max} (s)	2.5×10^{-8}, 2.5×10^{-8}	[158]
	τ_{min} (s)	5×10^{-10}, 5×10^{-10}	[158]
	N_0 $(\mathrm{cm^{-3}})$	1×10^{16}, 1×10^{16}	[158]
	γ^*	1, 1	[158]
	A_{Aug}	3×10^{-30}, 3×10^{-30}	[158]

Table 3.9: Material parameters used for $Al_xGa_{1-x}As$ in MJSC simulations. Temperature is 300 K unless otherwise stated. Values apply to $In_{53}Ga_{47}As$ unless binary parameters are given, in which case interpolation is used. Values for electrons and holes are separated by a comma.

Category	**Parameter**	**Value**	**Ref.**
Permittivity	$\varepsilon_s/\varepsilon_0$	AlAs: 10.06 GaAs: 12.91	[156] [156]
Refractive index	n_r, κ	Tabulated	[166]
Band structure	E_g (eV)	$x < 0.45$: $1.422 + 1.25x$ $x \geq 0.45$: $1.947 + 0.020x + 0.143x^2$	[153] [153]
	ΔE_g (eV)	See reference	[158]
	χ (eV)	$x < 0.45$: $4.118 - 1.207x$ $x \geq 0.45$: $3.587 - 0.027x$	[153] [153]
	m_c/m_0	$x < 0.41$: $0.063 + 0.083x$ $x > 0.45$: $0.85 - 0.14x$	[158] [158]
	m_v/m_0	$0.51 + 0.25x$	[158]
Mobility	μ_{max} $(\mathrm{cm^2/V\,s})$	$x = 0.2$: 5897, 308 $x = 0.3$: 3721, 240 $x = 0.8$: 400, 133	[62]
	μ_{min} $(\mathrm{cm^2/V\,s})$	$x = 0.2$: 314, 8.86 $x = 0.3$: 195, 5 $x = 0.8$: 10, 2.86	[62]
	N_0 $(\mathrm{cm^{-3}})$	$x = 0.2$: 9.33×10^{16}, 1.07×10^{17} $x = 0.3$: 1.16×10^{17}, 1.00×10^{17} $x = 0.8$: 3.51×10^{17}, 1.89×10^{17}	[62]
	A^*	$x = 0.2$: 0.515, 0.334 $x = 0.3$: 0.576, 0.324 $x = 0.8$: 0.879, 0.399	[62]
Recombination	B_{rad} $(\mathrm{cm^3/s})$	1×10^{-10}	[158]
	τ_{max} (s)	1×10^{-6}, 1×10^{-8}	[63]
	τ_{min} (s)	0, 0	[63]
	N_0 $(\mathrm{cm^{-3}})$	1×10^{16}, 2×10^{18}	[63]
	γ^*	1, 3	[63]
	A_{Aug}	1×10^{-30}, 1×10^{-30}	[63]

Table 3.10: Material parameters at 300 K used for $Al_{0.25}Ga_{0.25}In_{0.5}P$ in MJSC simulations. Values for electrons and holes are separated by a comma.

Category	Parameter	Value	Ref.
Permittivity	$\varepsilon_s/\varepsilon_0$	11.84	[63]
Refractive index	n_r, κ	Tabulated	[157]
Band structure	E_g (eV)	1.984	[165]
	ΔE_g (eV)	See reference	[156]
	χ (eV)	3.997	[165]
	m_c/m_0	0.1214	[63]
	m_v/m_0	0.6244	[156]
Mobility	μ_{max} $(\mathrm{cm^2/V\,s})$	4300, 150	[62]
	μ_{min} $(\mathrm{cm^2/V\,s})$	400, 15	[62]
	N_0 $(\mathrm{cm^{-3}})$	2×10^{16}, 1.5×10^{17}	[62]
	A^*	0.7, 0.8	[62]
Recombination	B_{rad} $(\mathrm{cm^3/s})$	1×10^{-10}	[158]
	τ_{max} (s)	1×10^{-9}, 1×10^{-9}	[63]
	τ_{min} (s)	0, 0	[63]
	N_0 $(\mathrm{cm^{-3}})$	1×10^{19}, 1×10^{19}	[63]
	γ^*	1, 1	[63]
	A_{Aug}	3×10^{-30}, 3×10^{-30}	[158]

Table 3.11: Material parameters at 300 K used for Si in MJSC simulations. Values for electrons and holes are separated by a comma.

Category	Parameter	Value	Ref.
Permittivity	$\varepsilon_s/\varepsilon_0$	11.7	[4]
Refractive index	n_r, κ	Tabulated	[167]
Band structure	E_g (eV)	1.125	[168]
	ΔE_g (eV)	See reference	[169]
	χ (eV)	4.05	[168]
	m_c/m_0	1.090	[168]
	m_v/m_0	0.998	[168]
Mobility*	μ_{max} $(\mathrm{cm^2/V\,s})$	1417, 470.5	[152]
	μ_{min1} $(\mathrm{cm^2/V\,s})$	52.2, 44.9	[152]
	μ_{min2} $(\mathrm{cm^2/V\,s})$	52.2, 0	[152]
	μ_1 $(\mathrm{cm^2/V\,s})$	43.4, 29	[152]
	P_c $(\mathrm{cm^{-3}})$	0, 9.23×10^{16}	[152]
	C_r $(\mathrm{cm^{-3}})$	9.68×10^{16}, 2.23×10^{17}	[152]
	C_s $(\mathrm{cm^{-3}})$	3.43×10^{20}, 6.10×10^{20}	[152]
	α_M	0.68, 0.719	[152]
	β_M	2, 2	[152]
Recombination**	B_{rad} $(\mathrm{cm^3/s})$	4.73×10^{-15}	[170]
	τ_{max} (s)	1.5×10^{-3}	[170]
	τ_{min} (s)	0	[170]
	N_0 $(\mathrm{cm^{-3}})$	1×10^{18}	[170]
	γ^*	1	[170]
	$A_{0,Aug}$***	2.8×10^{-31}	[170]
	H_{Aug}***	8	[170]
	$N_{0,Aug}$***	2.5×10^{17}	[170]

* Calculated using the Masetti model (see equation 3.20).

** Only p-type Si appears in the simulation, therefore recombination parameters are listed for minority carrier electrons.

*** See equation 3.21 for expression to calculate Auger recombination coefficient.

Table 3.12: Electrical transport parameters for voided Ge and Si used in MJSC simulations.

Category	Parameter	Voided Ge		Voided Si	
		Value	**Ref.**	**Value**	**Ref.**
Permittivity	$\varepsilon_s/\varepsilon_0$	16.2	[4]	11.68	[4]
Band structure	E_g (eV)	0.661	[4]	1.12	[4]
	N_v (cm^{-3})	5×10^{18}	[4]	1.8×10^{19}	[4]
	Φ_0 (eV)	0.220	[139]	0.373	[139]
	N_s (cm^{-2})	5×10^{14}	[6]	1×10^{11}	[7]
Hole Mobility	μ_{max} $(cm^2/V\,s)$	1800	[141]	470.5	[152]
	μ_{min} $(cm^2/V\,s)$	300	[141]	44.9	[152]
	N_0 (cm^{-3})	1×10^{17}	[141]	2.23×10^{17}	[152]
	A^*	1	[141]	0.719	[152]
Recombination*	τ_{max} (s)	$\sim 10^{-10}$		$\sim 10^{-10}$	

* Minority carrier density is assumed to be negligible within the voided regions .

Table 3.13: Material parameters at 300 K used for MgF_2 and TiO_x in MJSC simulations.

Category	Parameter	MgF_2		TiO_x	
		Value	**Ref.**	**Value**	**Ref.**
Permittivity	$\varepsilon_s/\varepsilon_0$	6	[171]	6	[171]
Refractive index	n_r, κ	Tabulated	[171]	Tabulated	[171]

Table 3.14: Interface recombination parameters used for MJSC simulations. Values are the same for both electrons and holes.

Parameter	TiO_x/AlInP		AlInP/GaInP		GaAs/AlGaAs	
	Value	**Ref.**	**Value**	**Ref.**	**Value**	**Ref.**
S_0 (cm/s)	0	[63]	2×10^5	[63]	200	[63]

Table 3.15: Tunneling parameters used for MJSC simulations. Values for electrons and holes are separated by a comma.

Parameter	**GaInP**		**GaAs**		**AlGaAs**	
	Value	**Ref.**	**Value**	**Ref.**	**Value**	**Ref.**
g	0.21, 0.4	[63]	0.21, 0.4	[63]	0.21, 0.4	[63]
m_t/m_0	0.24, 0.48	[63]	0.05, 0.14		0.05, 0.14	

Chapter 4

InAlGaAs photonic power converters for O-band operation

4.1 Photonic power converter design and characterization

4.1.1 PPC device fabrication

The O-band PPCs and tunnel diodes (TD) discussed in this chapter were grown by molecular beam epitaxy (MBE) using the Veeco Gen10 system at the University of Waterloo. Quartered 3-inch InP substrates were used as the growth template, secured with a sample holder in the growth chamber using an indium-free mounting technique. For the PPC samples, Zn-doped (p-type) InP substrates were used while for the TD samples the InP substrates were S-doped (n-type). For both substrate types, the concentration of ionized dopant atoms was in the range of $(1-8)\times10^{18}\,\text{cm}^{-3}$.

The basic layer structures for a single-junction PPC, a dual-junction PPC, and a standalone TD are shown in Figure 4.1. The epi-layers, which are all ternary and quaternary arsenide alloys lattice-matched to InP, are doped with Si and Be atoms for the n- and p-type regions respectively. The first layer above the substrate is the buffer, in which high-quality epitaxial growth is established. In all structures, the top layer is the cap, a highly doped InGaAs layer that is used to establish an ohmic interface with the metal contacts that are deposited in later fabrication steps. The cap doping concentrations are $5\times10^{18}\,\text{cm}^{-3}$ for the PPCs using n-type InGaAs and $2\times10^{19}\,\text{cm}^{-3}$ for the standalone TD using p-type InGaAs. Beneath the cap is the etch stop with a 10 nm thickness, used to control the wet-chemical etching process during fabrication.

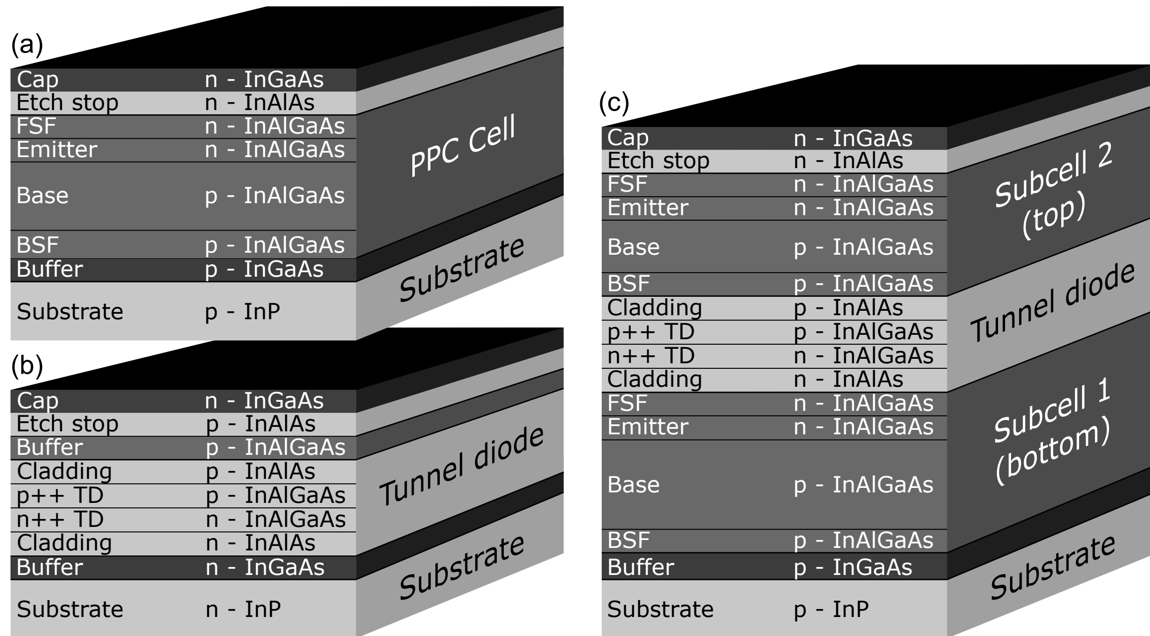

Figure 4.1: Layer schematics for (a) a single-junction PPC, (b) a standalone TD, and (c) a dual-junction PPC.

The temperature set-point was fixed at 510°C for the most of the growths, corresponding to a substrate temperature between 465°C and 480°C. For the very highly doped p-type TD layers, the temperature set-point was lowered to 490°C to reduce unwanted segregation of the Be acceptor atoms. The impact of the growth temperature on TD performance is discussed in detail in Chapter 4.4.

After epitaxy, metallization of the PPC and TD samples was performed. Two processes were used for the devices discussed in this thesis. The first process, an indium dot soldered contact method, was used for preliminary testing of some PPC devices. The second process involved a contact mask fabrication procedure to create good quality PPC devices for in-depth characterization under laser illumination. Both processes are described in this section.

4.1.1.1 Indium dot soldered contacts

Indium dot soldered contacts are advantageous for preliminary testing because the process is straightforward and takes only a few minutes to complete with very little equipment. It was found that measurements of PPC devices fabricated using this method were reliable at short-circuit current, allowing for quantum efficiency measurements to be performed on samples that had not undergone the mask fabrication process.

The first step in the quick-test contact procedure was to prepare an alumina carrier to support the sample. A gold-plated copper chuck was heated to 238°C on a hot plate. A clean alumina carrier was then placed

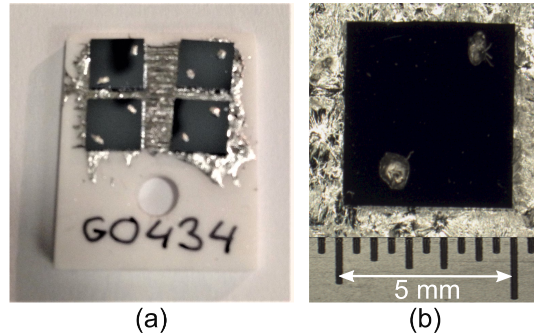

Figure 4.2: (a) Photograph and (b) microscope image of PPCs prepared using indium dot soldered contacts.

on the hot plate to heat for several minutes. After heating, the carrier was removed from the hot plate and a short length of indium wire was placed on its surface and spread using a soldering iron set to 205°C.

A rectangular piece with dimensions around 5×10 mm^2 was then cleaved from the PPC wafer. The piece was marked with a 1 mm scribe on the back side, preparing it to be cleaved in two. While still intact, a small piece of indium wire was placed on the back side and smeared into a thin layer using the soldering iron. The piece was then cleaved along the scribe line to create two 5×5 mm^2 squares. Two to four squares were arranged right-side up on the indium-coated alumina carrier.

A ½-mm length was then cut from the indium wire using a clean razor blade and divided in half to create two very small indium dots, which were placed on the surface of each PPC square. The entire carrier was then annealed on the hot plate at 238°C for 30 seconds. After annealing, the carrier was lifted off of the hotplate and allowed to cool slowly in the air for 30 seconds before being set down. Images of PPC samples prepared using indium dot soldered contacts are shown in Figure 4.2.

4.1.1.2 Contact mask fabrication

Mask-fabricated contacts were prepared primarily by the SUNLAB fabrication team, led by Marziyeh Zamiri. The process began with blanket deposition of the back contact on the substrate. A layer of photoresist was applied to the top side of the wafer using a WS-650-23 Laurell Spin Processor and baked on a hot plate to protect the epi-layers. The sample was dipped in a 10% HCl solution to remove the native oxide layer and then placed immediately into the evaporation chamber for metal deposition. Metallization for p-type InP was done at the National Research Council, Canadian Photonics Fabrication Centre. For n-type InP, the process was performed at the University of Ottawa using an Angstrom Nexdep Series thermal evaporator. The multi-layer metallization recipes are given in Table 4.1.

Table 4.1: Ohmic contact recipes and resistivities measured by TLM.

Semiconductor	**Metallization recipe**	$\boldsymbol{\rho_c}$ $(\boldsymbol{\Omega\,cm^2})$ $\boldsymbol{\pm 10^{-6}\,\Omega\,cm^2}$
p-InP	Pd (10 nm) / Zn (8 nm) / Pd (20 nm) / Au (100 nm) RTA: 400°C (2 minutes)	3×10^{-6}
n-InP	Ge (25 nm) / Ni (25 nm) / Au (50 nm)	3×10^{-6}
p-InGaAs	Pd (9 nm) / Ti (15 nm) / Pd (15 nm) / Au (50 nm)	6×10^{-6}
n-InGaAs	Pd (9 nm) / Ti (15 nm) / Pd (15 nm) / Au (50 nm)	2×10^{-6}

After metallization, the photoresist was removed. To achieve ohmic behaviour for p-type InP, rapid thermal annealing (RTA) was performed at the University of Ottawa using a Solaris 100, Surface Science Integration system. The metallized samples were annealed for 2 minutes at 400°C. No annealing was required for n-type InP. The epitaxy and back contact formation steps are depicted in Figure 4.3a-d.

After the back contact formation, the top contact was deposited and patterned at the University of Ottawa for all samples. First the samples were cleaned using a 5-minute rinse in acetone followed by isopropyl alcohol and finally deionized water. A nitrogen gun was used to dry the samples after the rinse, followed by a 5-minute bake at 180°C on a hot plate. A layer of lift-off resist with a thickness of 180 nm was deposited by spin-coating and baked followed by a ˜600 nm layer of photoresist. UV exposure through the fabrication mask was performed using a OAI Model 204IR Mask Aligner. The exposed photoresist and lift-off resist layers were then removed using the appropriate developer to create an undercut.

Following photolithography and development, a 10% HCl dip was performed to remove the native oxide from the surface of the epi-layers and the sample was loaded into the evaporator. The multi-layer metallization recipes are given in Table 4.1. After metallization, lift-off was performed by submerging the sample in PG remover, an organic solvent that dissolves the lift-off resist and photoresist layers, leaving behind the metal pattern on the surface. The top contact patterning steps are depicted in Figure 4.3e-j.

Contact resistivities were measured using the transmission line method (TLM) with a circular layout. The TLM contact configuration is shown in Figure 4.4a. For each ring, current-voltage characteristics were measured using the four-wire configuration with two probes on the outer contact pad and two probes on the circular inner pad - one probe for conducting the current and the other to measure the voltage. The total resistance (R_T) was corrected to account for the circular geometry and plotted as a function of the gap

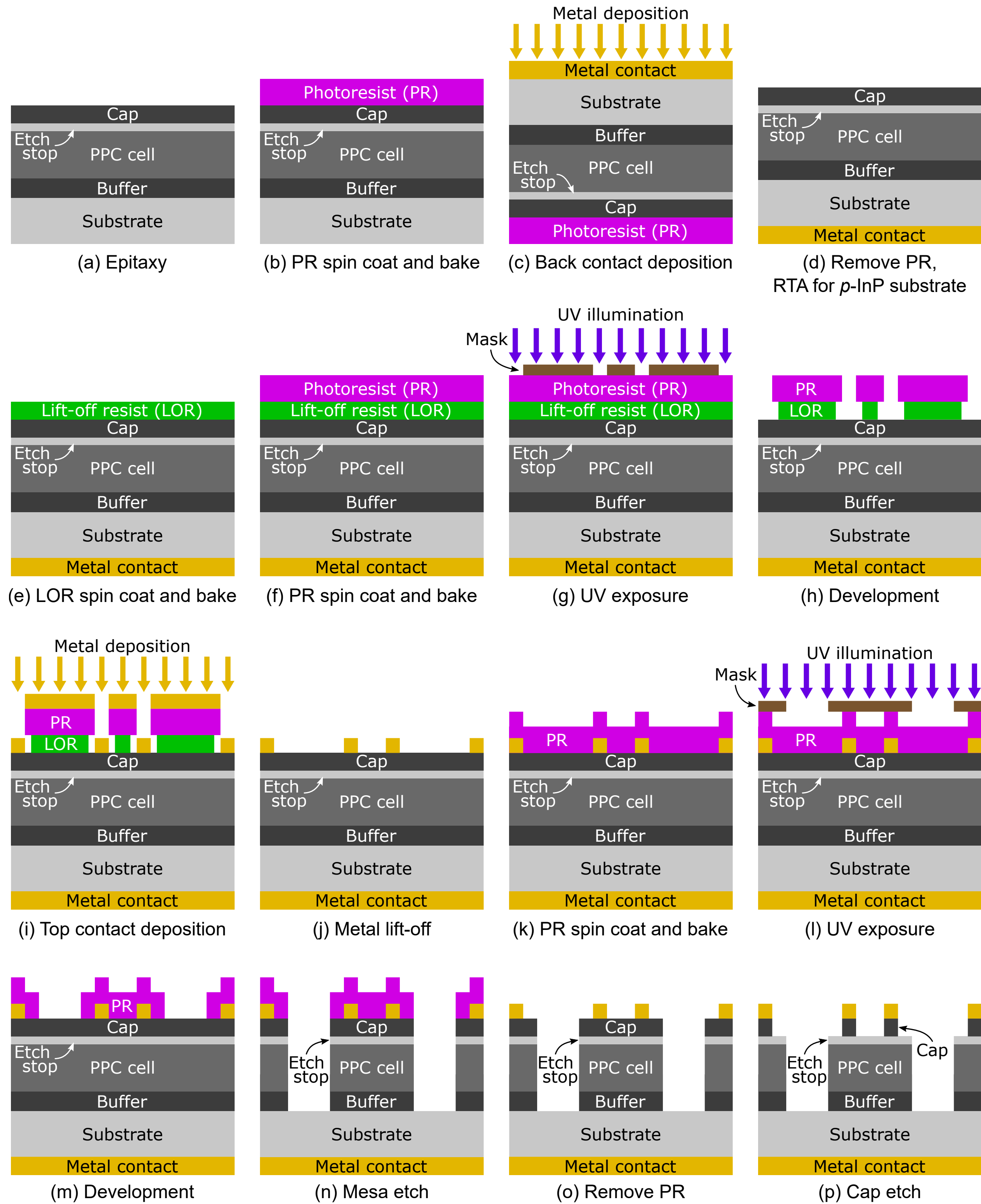

Figure 4.3: Schematic depicting the fabrication process for PPC and TD samples.

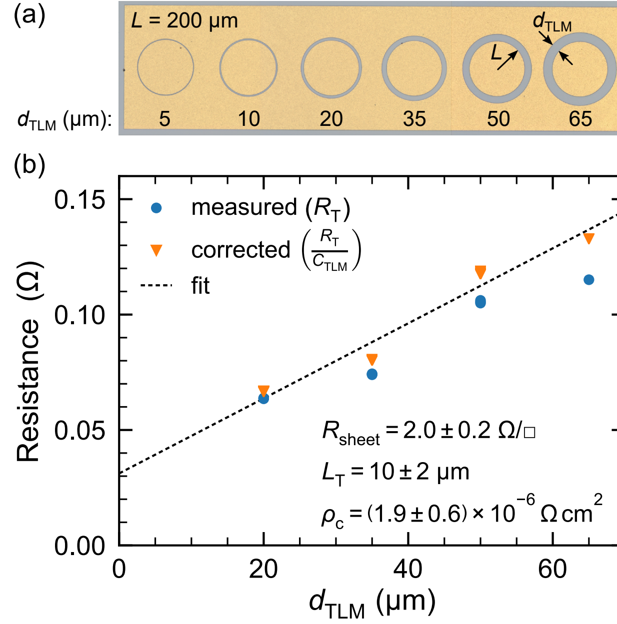

Figure 4.4: (a) Microscope image of TLM contact pads. Important dimensions are given in microns. (b) Sample TLM measurements for ohmic contact to p-InGaAs. Both measured and corrected data are shown along with the fit to (4.1).

spacing (d_{TLM}). The corrected total resistance is given by [172]

$$\frac{R_{\text{T}}}{C_{\text{TLM}}} = \frac{R_{\text{sheet}}}{2\pi L}(d_{\text{TLM}} + 2L_{\text{T}}) = \frac{R_{\text{sheet}}}{2\pi L} d_{\text{TLM}} + 2R_{\text{c}} \tag{4.1}$$

where R_{sheet} is the semiconductor sheet resistance, L is the radius of the circular pad, L_{T} is the transfer length, R_{c} is the contact resistance, and C_{TLM} is the correction factor, which is given by

$$C_{\text{TLM}} = \frac{L}{d_{\text{TLM}}} \ln\left(1 + \frac{d_{\text{TLM}}}{L}\right) \tag{4.2}$$

and the contact resistivity is given by

$$\rho_{\text{c}} = R_{\text{sheet}} L_{\text{T}}^2 \tag{4.3}$$

The correction factor C_{TLM} is required to account for the circular geometry of the contact pads. In traditional TLM, rectangular contacts are arranged in a line with varying distance between them. The advantage of the circular geometry compared to the linear pattern is that the current is confined to flow only between the central and surrounding contact pads. In the linear configuration, the potential for lateral current flow complicates the measurement.

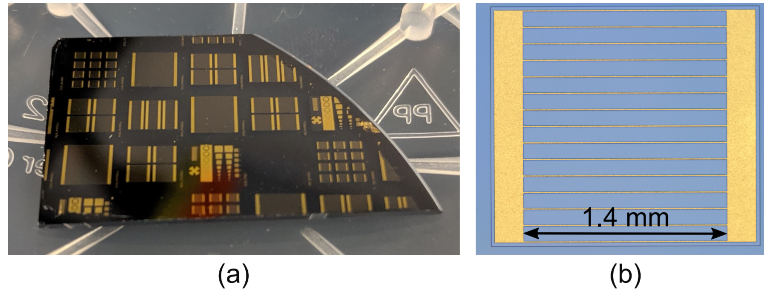

Figure 4.5: (a) Photograph and (b) microscope image of metallized and fabricated PPC wafer. The microscope image shows one of the mid-size cells in the 2×2 configuration.

Figure 4.4b shows the measured and corrected resistances as a function of d_{TLM} for a contact to p-InGaAs. In this case, the smallest gap spacings (5 μm and 10 μm) were not sufficiently well-resolved to measure the resistance and only the largest four gaps were used. The fit to equation 4.1 is indicated by the dashed line and the contact resistivity is found to be $\rho_c = (1.9 \pm 0.6) \times 10^{-6}\,\Omega\,\mathrm{cm}^2$. The same method is used to determine the values of ρ_c for contacts to n-InGaAs and to both n- and p-InP. The resulting values are summarized in Table 4.1. The uncertainties for the values of ρ_c given in the table are taken to be $10^{-6}\,\Omega\,\mathrm{cm}^2$ to account for variations across the wafer.

After metallization, the next step in the fabrication process was the mesa definition in which individual devices were separated from each other on the wafer. In this process, a layer of photoresist was deposited by spin coating and ultraviolet light exposure was performed using the appropriate fabrication mask. After development, in which the photoresist was removed in the bounding regions between devices, wet chemical etching was performed to remove the epi-layers in these regions. The etching compound H_2O:CIT:H_3PO_4:H_2O_2[220:55:3:5] preferentially etches the arsenide epi-layers so that they are removed without etching the entire InP substrate [173]. The remaining photoresist was removed after the etch. The mesa definition steps are depicted in Figure 4.3k-o.

The final step in the PPC device fabrication process was to remove the cap layer from the sample surface, except from beneath the contacts. This was done using a self-aligned wet etch in which the sample was submerged in a solution of CIT:H_2O_2[1:2]. This solution etches the cap layer very quickly (~ 80 nm/min) but for the etch stop layer, comprised of $\mathrm{In_{0.3}Al_{0.7}As}$, the etch rate is $<$ 1 nm/min and etching effectively stops when it reaches this layer and the cap can be removed without damaging the layers beneath [173]. The cap etch is depicted in Figure 4.3p. Images of a mask-fabricated wafer are shown in Figure 4.5.

4.1.2 Spectroscopic ellipsometry

Two undoped heterostructures grown by MBE with different quaternary compositions lattice matched to InP were analyzed by spectroscopic ellipsometry to measure the optical properties of the InAlGaAs layers used in the PPC designs. The layer structure consisted of 1 μm of $In_xAl_yGa_{1-x-y}As$ capped with 10 nm of $In_{0.526}Ga_{0.474}As$.

Ellipsometry measurements were performed using a Horiba Uvisel scanning spectroscopic phase modulated spectrometer with a scanning range of 255 - 2100 nm. Measurements were performed at a 70º incidence angle and with a step size of 5 nm. At each step, linearly polarized monochromatic light was incident on the sample. The component of the s-polarized light (electric field parallel to the sample surface) was reflected with a different magnitude than that of the p-polarized light (remaining component), resulting in an elliptically polarized reflection. By measuring the polarization of the reflected light, information about the sample structure was obtained. The ratio of reflectivities for s- and p-polarized light is

$$\frac{\mathcal{R}_\mathrm{p}}{\mathcal{R}_\mathrm{s}} = \tan\Psi e^{i\Delta} \tag{4.4}$$

where $\tan\Psi = \left|\mathcal{R}_\mathrm{p}\right| / |\mathcal{R}_\mathrm{s}|$ is the change in amplitude of the electric field and Δ is the phase difference between the s- and p-polarizations after reflection. The quantities measured directly by the ellipsometer are the following functions of Ψ and Δ.

$$I_\mathrm{s} = \sin 2\Psi \sin\Delta \tag{4.5}$$

$$I_\mathrm{c} = \sin 2\Psi \cos\Delta \tag{4.6}$$

By fitting an appropriate model for the sample geometry and material type to I_s and I_c, information about the layer thicknesses and refractive indices for the sample can be obtained. The Horiba DeltaPsi2 software was used to analyze the measured ellipsometry data. The layer structure was input into the software and reference index of refraction data was used for the InP substrate and the InGaAs cap layer. A thin transparent oxide layer with a fixed index of $n = 1.9$ was included on top of the of the layer stack, as per [174]. The optical properties of the quaternary layer were fit using a dispersion formula. The thicknesses of each layer in the stack were calculated during the fitting process, starting from the expected layer thicknesses summarized in Table 4.2.

Table 4.2: Starting thicknesses and refractive indices used for analysis of ellipsometry data.

Layer	**Thickness**	n_r, κ
Oxide	d_{ox} (start value: 1 nm)	$n_r = 1.9$, $\kappa = 0$
InGaAs cap	d_{cap} (start value: 10 nm)	Reference*
InAlGaAs	d_Q (start value: 1000 nm)	Fit using dispersion
InP substrate	-	Reference*

*Reference data provided in Horiba DeltaPsi2 software.

Raw ellipsometry data is shown in 4.6a for the quaternary $In_{0.532}Al_{0.097}Ga_{0.371}As$, which has a bandgap between 0.8 and 1.24 eV. This quaternary composition was used for the absorber material within the emitter and base layers of several PPC devices discussed in this chapter. The raw data was fit in this region using the Adachi new Forouhi dispersion formula [175], which is frequently used to determine the optical properties of crystalline semiconductors near the bandgap. Fitting was performed using the Horiba DeltaPsi2 commercial software. The Adachi new Forouhi dispersion can be written in terms of the complex dielectric function as

$$\tilde{\varepsilon}(E) = \tilde{\varepsilon}_0(E) + \tilde{\varepsilon}_1(E) \tag{4.7}$$

The real and imaginary components of $\tilde{\varepsilon_0}$ are given by

$$\varepsilon_{0,r}(E) = \mathrm{Re}\left[A_0\left\{\frac{f(\chi_0)}{E_g^{3/2}} + \frac{f(\chi_{so})}{2\left(E_g+\Delta_0\right)^{3/2}}\right\}\right] \tag{4.8}$$

$$\varepsilon_{0,i}(E) = \begin{cases} \mathrm{Im}\left[A_0\left\{\frac{f(\chi_0)}{E_g^{3/2}} + \frac{f(\chi_{so})}{2\left(E_g+\Delta_0\right)^{3/2}}\right\}\right] & E \geq E_g \\ \left(1+\frac{E-E_g}{3\Gamma_0}\right)\times \mathrm{Im}\left[A_0\left\{\frac{f(\chi_0)}{E_g^{3/2}} + \frac{f(\chi_{so})}{2\left(E_g+\Delta_0\right)^{3/2}}\right\}\right] & \left(E_g - 3\Gamma_0\right) < E < E_g \\ 0 & E < \left(E_g - 3\Gamma_0\right) \end{cases} \tag{4.9}$$

where

$$f(\chi_i) = \frac{2-\sqrt{1+\chi_i}-\sqrt{1-\chi_i}}{\chi_i^2}, \qquad \chi_0 = \frac{E+i\Gamma_0}{E_g}, \qquad \chi_{so} = \frac{E+i\Gamma_0}{E_g+\Delta_0}$$

E_g is the bandgap, Δ_0 is the separation of the transition energy by spin-orbit coupling, Γ_0 is the associated

broadening, and A_0 is the transition probability. The function $\tilde{\varepsilon}_1(E)$ is given by

$$\tilde{\varepsilon}_1 = [n_1(E) + i\kappa_1(E)]^2 \tag{4.10}$$

where

$$n_1(E) = n_\infty + \frac{B_1(E-\omega_j)+C_1}{(E-\omega_j)^2+\Gamma_j^2}, \qquad \kappa_1(E) = \begin{cases} \frac{f_j(E-E_g)^2}{(E-\omega_j)^2+\Gamma_j^2}, & E > E_g \\ 0, & E \le E_g \end{cases}$$

$$B_1 = \frac{f_j}{\Gamma_j}\left[\Gamma_j^2 - (\omega_j - E_g)^2\right]$$

$$C_1 = 2 f_j \Gamma_j (\omega_j - E_g)$$

n_∞ is the high frequency refractive index and f_j, ω_j , and Γ_j are respectively the strength, resonance angular frequency, and broadening of the jth oscillator.

The relationship between the complex index of refraction and the complex dielectric function is given by

$$\tilde{\varepsilon} = \varepsilon_r + i\varepsilon_i = (\tilde{n})^2 = (n_r + i\kappa)^2 \tag{4.11}$$

where ε_r and ε_i are the real and imaginary components of $\tilde{\varepsilon}$. The real and imaginary components of the refractive index are then

$$n_r = \sqrt{\frac{(\varepsilon_r^2+\varepsilon_i^2)^{1/2}+\varepsilon_r}{2}}, \qquad \kappa = \sqrt{\frac{(\varepsilon_r^2+\varepsilon_i^2)^{1/2}-\varepsilon_r}{2}} \tag{4.12}$$

The fit to the Adachi new Forouhi dispersion for $In_{0.532}Al_{0.097}Ga_{0.371}As$ is shown in Figure 4.6a and the corresponding complex refractive index is shown in Figure 4.6b. The associated fitting parameters are given in Table 4.3, as well as the goodness of fit χ^2. Fitting ellipsometry data for layered structures near the semiconductor bandgap is especially challenging, and the value of $\chi^2 = 0.409$ is acceptable in this case. Better fits with correspondingly smaller values of χ^2 can be achieved away from the bandgap, particularly for transparent materials.

Raw ellipsometry data is shown in 4.7a for the quaternary $In_{0.527}Al_{0.356}Ga_{0.117}As$, which has a bandgap > 1.24 eV and is therefore transparent within the energy range shown. This quaternary composition was

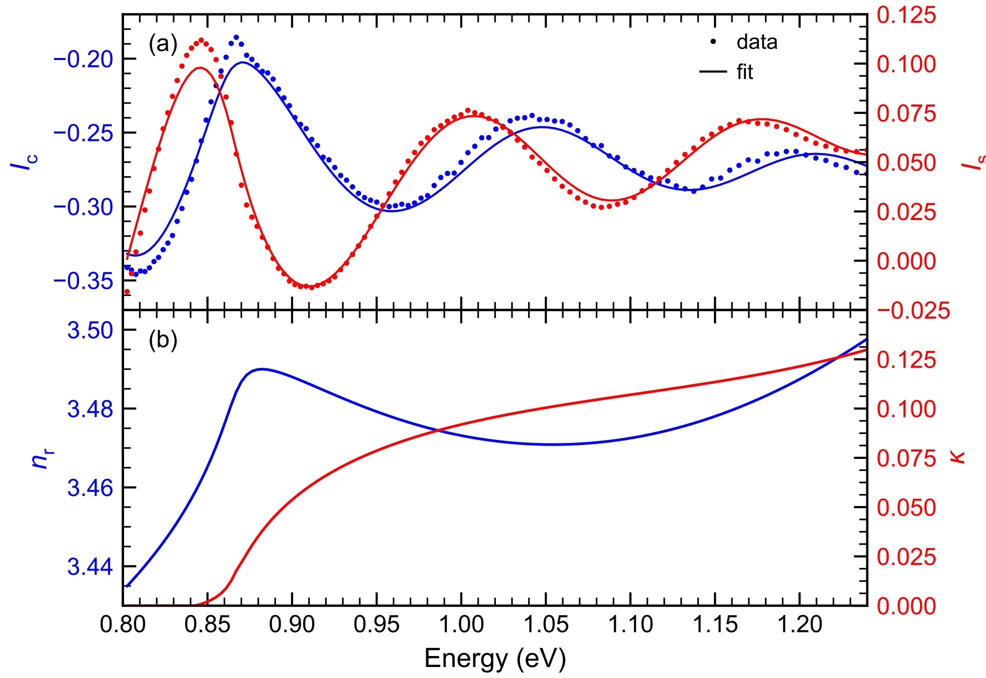

Figure 4.6: (a) Ellipsometry data and corresponding fit to the Adachi new Forouhi dispersion formula for $In_{0.532}Al_{0.097}Ga_{0.371}As$. (b) Calculated n_r, κ values.

Table 4.3: Fitting parameters and goodness of fit for $In_{0.532}Al_{0.097}Ga_{0.371}As$ heterostructure in the range from 0.8 to 1.24 eV.

Parameter	**Value**
d_{ox} $\left(\text{Å}\right)$	30 ± 3
d_{cap} $\left(\text{Å}\right)$	97 ± 14
d_Q $\left(\text{Å}\right)$	10365 ± 18
E_g (eV)	0.867 ± 0.03
n_∞	3.19 ± 0.05
f_j	0.05 ± 0.03
ω_j (eV)	1.6 ± 0.2
Γ_j (eV)	0.3 ± 0.1
Δ_0 (eV)	0.00 ± 0.09
Γ_0 (eV)	0.008 ± 0.008
A_0 $\left(\text{eV}^{3/2}\right)$	1.2 ± 0.1
χ^2	0.409

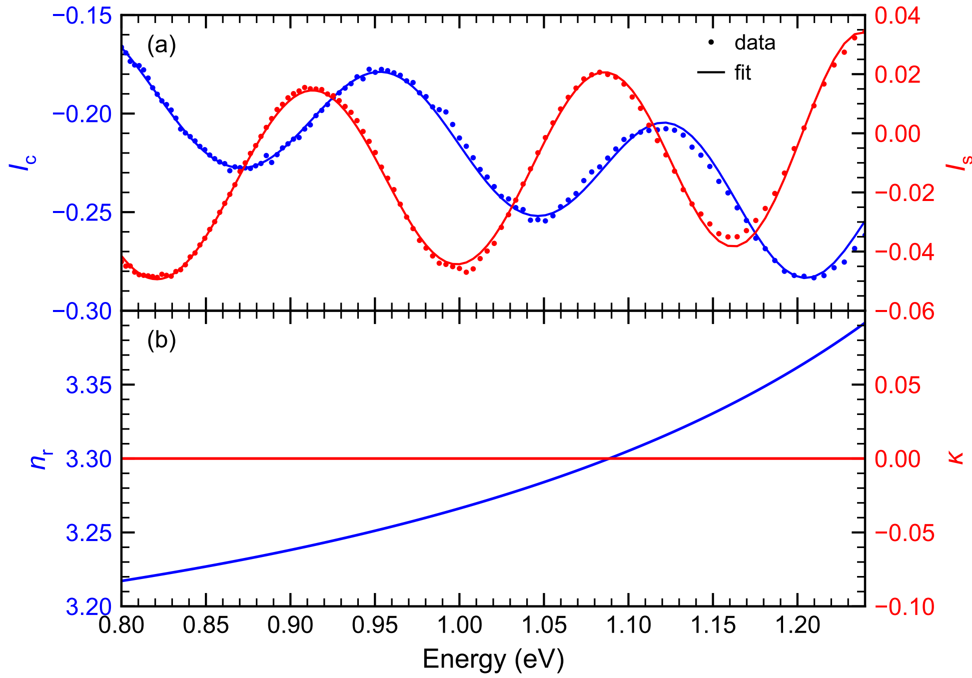

Figure 4.7: (a) Ellipsometry data and corresponding fit to the Lorentz single oscillator dispersion formula for $In_{0.527}Al_{0.356}Ga_{0.117}As$. (b) Calculated n_r, κ values.

used for the front and back surface fields of the PPCs discussed in this chapter. The raw data was fit using the Lorentz single oscillator dispersion model for non-absorbing media [176]. Under this dispersion, the real part of the dielectric function is given by

$$\varepsilon_r(E) = \varepsilon_\infty + \frac{(\varepsilon_s - \varepsilon_\infty)\omega_t^2}{\omega_t^2 - E^2} \tag{4.13}$$

where ε_∞ is the high energy dielectric constant, ε_s is the static dielectric constant at $E = 0$, and ω_t is the resonant frequency of the oscillator. In simple cases, $\varepsilon_\infty = 1$, however it is possible to have $\varepsilon_\infty > 1$ in the case where higher order oscillators are present but are not taken into account. For non-absorbing media, $\varepsilon_i = 0$ and therefore $\kappa = 0$. The real part of the refractive index is then $n_r = \sqrt{\varepsilon_r}$.

The fit to the Lorentz dispersion for $In_{0.527}Al_{0.356}Ga_{0.117}As$ is shown in 4.7a and the corresponding complex refractive index is shown in 4.7b. The associated fitting parameters are given in Table 4.4, as well as the goodness of fit χ^2.

Table 4.4: Fitting parameters and goodness of fit for $In_{0.527}Al_{0.356}Ga_{0.117}As$ heterostructure in the range from 0.8 to 1.24 eV.

Parameter	**Value**
d_{ox} (Å)	15.0 ± 0.6
d_{cap} (Å)	79 ± 1
d_{Q} (Å)	10307 ± 5
ε_{∞}	8.8 ± 0.2
ε_{s}	9.99 ± 0.03
ω_{t} (eV)	1.65 ± 0.04
χ^2	0.0501

4.1.3 Quantum efficiency

Quantum efficiency measurements were performed on all of the PPC devices discussed in this thesis to measure the absorber band edge and to evaluate the device performance. The measurements were performed using a modified commercial Newport Oriel IQE 200 measurement system. A schematic of the experimental apparatus is shown in Figure 4.8.

A 300 W xenon arc lamp is used as a broad-spectrum white light source enabling measurements in the wavelength range from 300 - 1800 nm. The white light is filtered and a specific wavelength is selected using an Oriel CS130 monochromator, which outputs nearly monochromatic light with a spectral full width at half maximum of ~ 5 nm. The monochromatic beam is divided using a beam splitter, with one path focused onto the sample and the other path collected by the reference detector, which measures the input light intensity (channel 1). Current from the device is collected in the external circuit (channel 2). Reflected light from the sample is collected by the spectral reflectivity detector (channel 3).

The three data channels are collected by a multiplexer, which passes data to a Merlin 70101 lock-in amplifier. The input light is modulated by an optical chopper, which allows the lock-in amplifier to isolate the signals. Channels 1 and 2 are used to measure the external quantum efficiency (EQE), channels 1 and 3 are used to measure the specular reflectivity ($\mathcal{R}$), and all three channels together can be used to measure the quantity $EQE/(1-\mathcal{R})$, which is equal to the internal quantum efficiency (IQE) in the case where the transmission $\mathcal{T} = 0$.

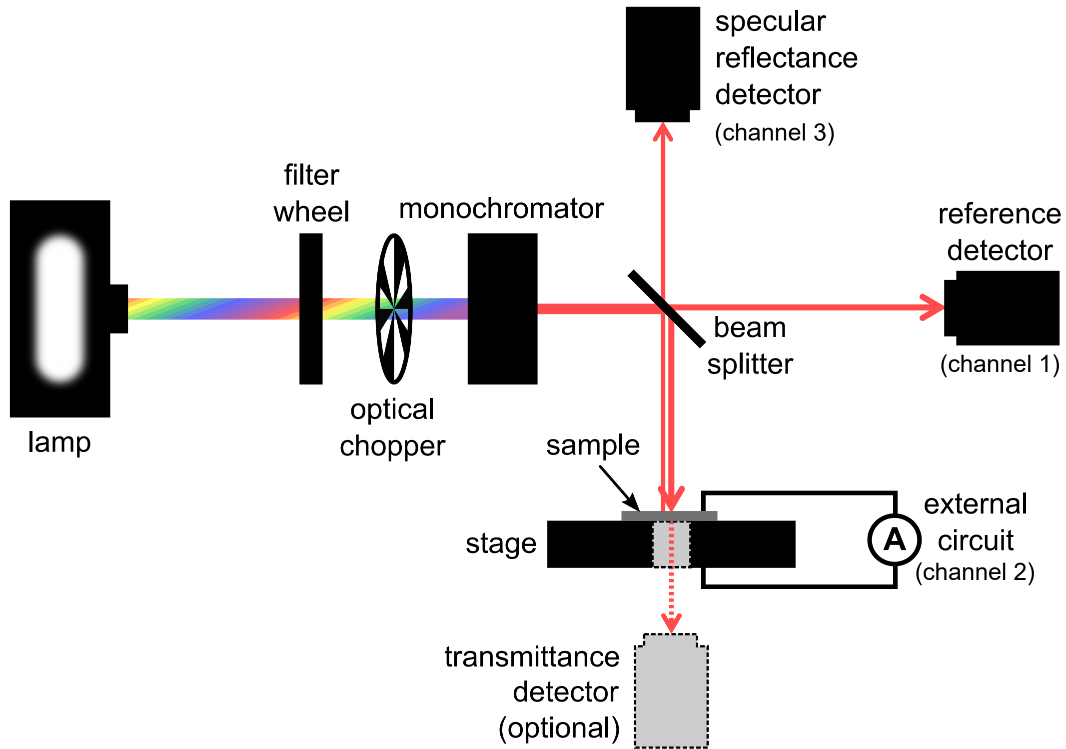

Figure 4.8: Schematic of the quantum efficiency measurement system.

The scans were performed over a wavelength range from 500 - 1500 nm with a step size of 5 nm. PPC samples prepared using either the indium dot soldered contact technique or contact mask fabrication were connected in either a two- or four-wire configuration and measured under short-circuit. Results were consistent for both wiring configurations. Measured data is shown for an optically thin PPC sample in Figure 4.9. The absorber layers have a quaternary composition of $In_{0.532}Al_{0.097}Ga_{0.371}As$ with a thickness of 0.7 μm. Curves are shown for the EQE, reflectivity $\mathcal{R}$, and $EQE/(1-\mathcal{R})$. The thickness of the absorber layers is insufficient to absorb all of the input light and therefore $EQE/(1-\mathcal{R}) \neq IQE$ because some light is transmitted through the device.

Quantum efficiency measurements are shown for optically thin PPCs with three different quaternary absorber compositions in Figure 4.10. The compositions, lattice matched to InP are defined by the compositional parameter z, which is the fraction of $In_{0.52}Al_{0.48}As$ relative to $In_{0.53}Ga_{0.47}As$. $z = 0.205$ corresponds to the quaternary composition $In_{0.532}Al_{0.097}Ga_{0.371}As$ and the quantum efficiency data shown in Figure 4.9. All three samples have an absorber thickness of 0.7 μm. The variation of the quaternary bandgap with composition is clearly observed.

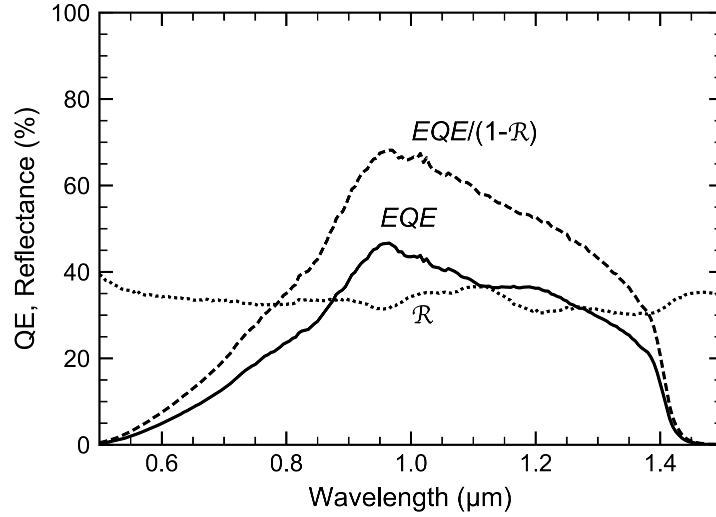

Figure 4.9: EQE, reflectance, and $EQE/(1-\mathcal{R})$ for an optically thin $In_{0.532}Al_{0.097}Ga_{0.371}As$ PPC with an absorber thickness of 0.7 µm.

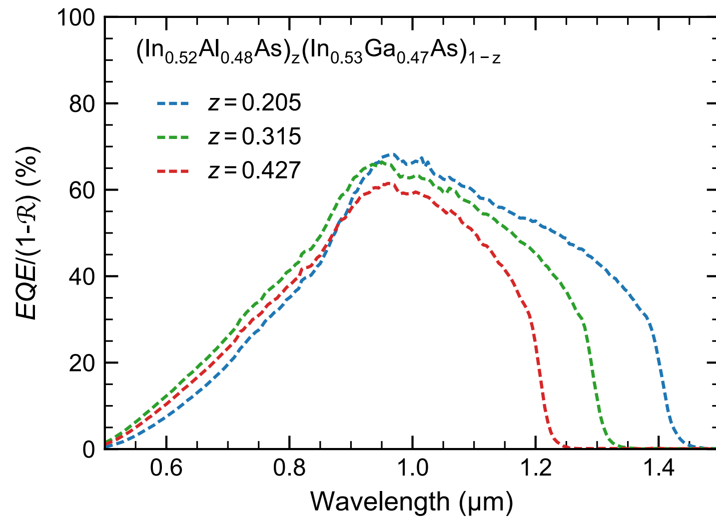

Figure 4.10: $EQE/(1-\mathcal{R})$ for optically thin $(In_{0.52}Al_{0.48}As)_z\,(In_{0.53}Ga_{0.47}As)_{1-z}$ PPCs with a 0.7 µm absorber thickness.

The optical bandgap of the absorbers was extracted from the quantum efficiency data using a Tauc plot [177]. This method relies on the assumption that the absorbance $\mathcal{A} \approx EQE/(1-\mathcal{R})$, which generally holds near the band edge. Under this assumption, the absorption coefficient was calculated according to Beer-Lambert absorption such that

$$\alpha = \frac{-\ln(1-\mathcal{A})}{t} \approx \frac{-\ln\left(1-\frac{EQE}{1-\mathcal{R}}\right)}{t} \tag{4.14}$$

where t is the absorber thickness. For a direct-gap semiconductor, the absorption coefficient varies near the

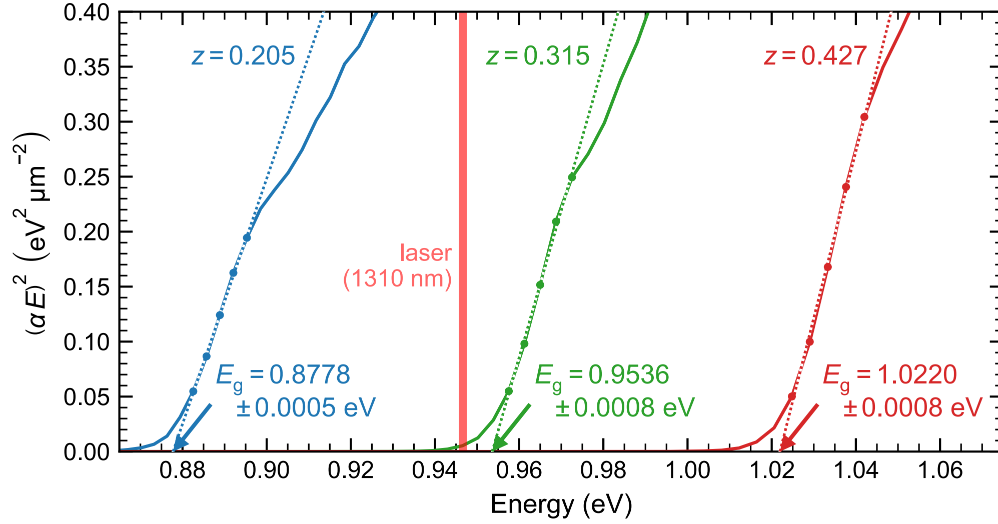

Figure 4.11: Tauc plots for optically thin $(In_{0.52}Al_{0.48}As)_z\,(In_{0.53}Ga_{0.47}As)_{1-z}$ PPCs with a 0.7 µm absorber thickness. Each curve is fit to equation 4.16 using the marked data points that display a linear trend. The dashed lines represent the fits. The compositional parameter z and the calculated E_g are indicated for each PPC. The target laser energy for PPC operation (corresponding to 1310 nm wavelength) is indicated.

bandgap according to

$$\alpha(E) \approx \beta \frac{\sqrt{E - E_g}}{E} \tag{4.15}$$

where β is an constant. This can be rearranged as [177–179]

$$(\alpha E)^2 \approx \beta^2 \left(E - E_g\right) \tag{4.16}$$

Plotting $(\alpha E)^2$ as a function of E, the bandgap can be extracted with a straightforward linear fit. This method is shown in Figure 4.11 for the three PPCs with varying quaternary compositions and an active layer thickness of 0.7 µm.

It is essential that the PPC absorber bandgap be smaller than the laser energy to absorb light and generate electricity. Given the target laser wavelength of 1310 nm for PPC operation, which corresponds to an energy of 0.947 eV, only one test device shown in Figure 4.11 had a sufficiently small bandgap (quaternary composition $z = 0.205$ or $In_{0.532}Al_{0.097}Ga_{0.371}As$). The majority of this chapter will focus on PPC devices designed using $z = 0.205$ for the target absorber composition.

Fabrication of the devices using the metallization and fabrication method rather than the indium dot soldered contacts results in some changes to the measured quantum efficiency and reflectivity. A comparison between the quantum efficiency measurements for a PPC fabricated using indium dot soldered contacts

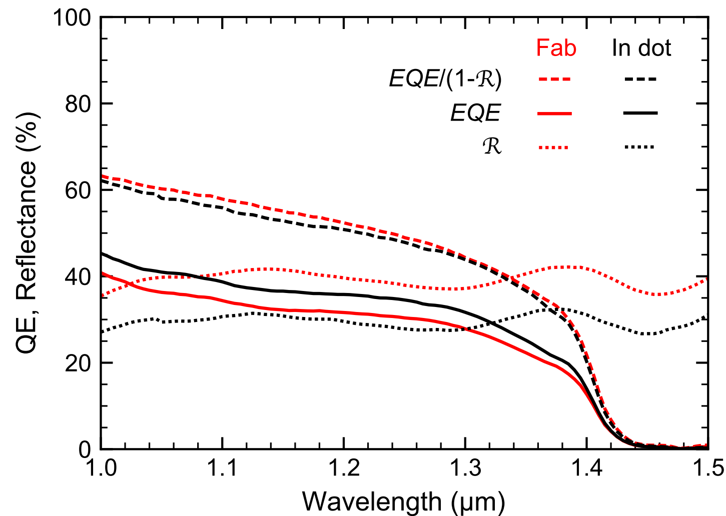

Figure 4.12: Comparison between quantum efficiency measurements for an optically thin $In_{0.532}Al_{0.097}Ga_{0.371}As$ PPC with an absorber thickness of 0.842 μm using indium dot soldered contacts (In dot) and mask-fabricated contacts (Fab), not including the cap etch. EQE, reflectance, and $EQE/(1-\mathcal{R})$ curves are shown.

and using contact mask fabrication (not including the cap etch) is shown in Figure 4.12. The quaternary composition of the absorber is $In_{0.532}Al_{0.097}Ga_{0.371}As$ ($z = 0.205$) and the absorber thickness is 0.842 μm.

The most important difference observed in Figure 4.12 when comparing the two fabrication techniques is the change in reflectivity. The fabricated PPC has a reflectivity that is ~ 9.8% (absolute) larger than that of the In dot PPC across the entire wavelength range. This is because the fabricated PPC has metal gridlines covering ~ 8% of the surface that are highly reflective. The reflectivity for the In dot PPC, on the other hand, is entirely due to reflections at the air/semiconductor interface. The discrepancy between the stated 8% metal coverage and the measured 9.8% difference in reflectivity can be attributed to the measurement system uncertainty, which is ~ 2% (absolute), related to alignment. Gridline shading may be much less significant in commercial devices with optimal contact configurations, depending on the illumination conditions for which the device is designed to operate.The quantity $EQE/(1-\mathcal{R})$, which takes into account the difference in reflectivity, is very similar across the entire wavelength range, as expected.

Further changes were observed in the fabricated PPC quantum efficiency after etching the InGaAs cap layer. A comparison of the measured curves before and after the cap etch is shown in Figure 4.13. Notable changes were observed in the reflectivity spectrum, resulting from the removal of the cap. After accounting for these changes in the quantity quantity $EQE/(1-\mathcal{R})$, we see a wavelength-dependent improvement in the

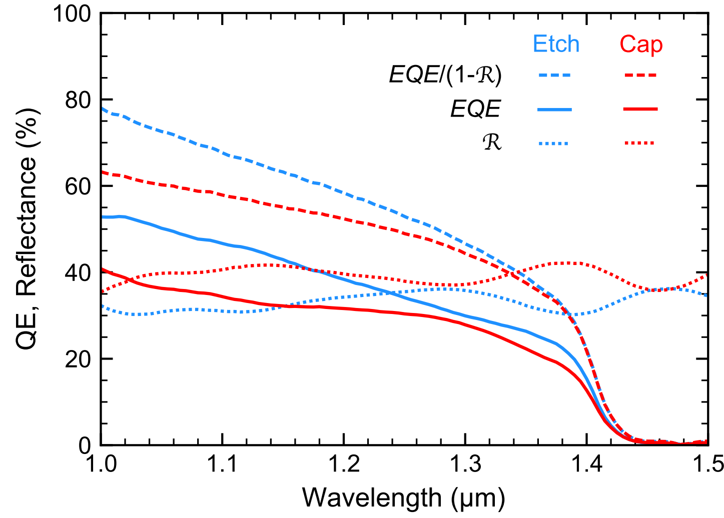

Figure 4.13: Comparison between quantum efficiency measurements for a mask-fabricated, optically thin $In_{0.532}Al_{0.097}Ga_{0.371}As$ PPC with an absorber thickness of 0.842 µm before and after etching the cap layer. EQE, reflectance, and $EQE/(1-\mathcal{R})$ curves are shown.

PPC performance for the etched device. This is due to parasitic absorption within the InGaAs cap layer, an effect that disappears when the cap is removed.

The n-type $In_{0.53}Ga_{0.47}As$ cap layer used for the PPCs had a target doping concentration of $5\times10^{18}\,cm^{-3}$ and a thickness of 100 nm. The transmittance of the cap $(\mathcal{T}_{cap})$ was determined using

$$\mathcal{T}_{cap} = \frac{EQE_{cap}/(1-\mathcal{R}_{cap})}{EQE_{etch}/(1-\mathcal{R}_{etch})} \tag{4.17}$$

where $EQE_{cap}/(1-\mathcal{R}_{cap})$ corresponds to the PPC sample with the cap layer intact and $EQE_{etch}/(1-\mathcal{R}_{etch})$ corresponds to the PPC with the cap layer removed. The absorption coefficient (α_{cap}) for the cap layer was extracted assuming Beer-Lambert absorption where $\mathcal{T} = e^{-\alpha t}$. $\mathcal{T}_{cap}$ and α_{cap} are plotted in Figure 4.14 as a function of wavelength. The transmittance data was fit using a cubic polynomial function. The expected absorption coefficient for intrinsic $In_{0.53}Ga_{0.47}As$ is shown in Figure 4.14 for reference.

A significant difference is observed between the absorption properties calculated from the data and the reference values. This is most likely caused by the very high doping concentration in the cap, which can cause a blue-shift in the optical bandgap, known as the Moss–Burstein shift [180–182]. The bandgap for intrinsic $In_{0.53}Ga_{0.47}As$ is 0.74 eV (1.675 µm) whereas the optical bandgap for the highly doped $In_{0.53}Ga_{0.47}As$ cap appears to be ~ 0.84 eV (1.47 µm). High doping concentrations can also lead to a narrowing of the electrical

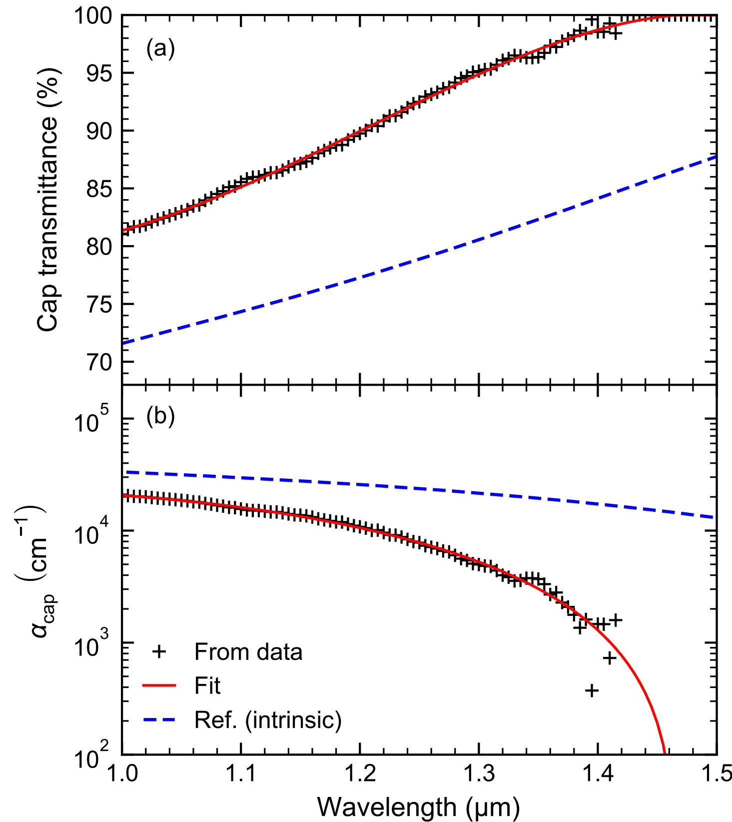

Figure 4.14: (a) Transmittance and (b) absorption coefficient of the InGaAs cap layer determined from the PPC quantum efficiency data shown in Figure 4.13. The reference data comes from the reference optical properties for intrinsic $In_{0.53}Ga_{0.47}As$ stored in the Horiba DeltaPsi2 software.

bandgap when the concentration of the impurity atoms is sufficiently high to create a continuum of donor (n-type) or acceptor (p-type) states within the bandgap, effectively reducing the gap itself [8, 183].

4.1.4 Optical absorption of p-InP substrate

All of the PPCs discussed in this chapter were grown on p-type InP substrates. The bandgap of intrinsic InP is 1.344 eV, corresponding to a wavelength of 923 nm. Incident light with wavelength > 923 nm will not have sufficient energy to promote electrons from the valence band into the conduction band in InP. Absorption of these longer wavelengths in the InP happens through free carrier absorption (FCA) when free carriers in the conduction or valence bands are promoted to higher energy states after absorbing a long-wavelength incident photon.

The strength of FCA depends on the density of free carriers within the material and is extremely weak in intrinsic semiconductors that have very low free carrier densities. FCA can be much more important in

doped semiconductors.

The importance of FCA in the p-type InP substrates used for the InAlGaAs PPCs was determined by measuring the substrate transparency using the quantum efficiency measurement system depicted in Figure 4.8. The bare substrate was positioned on a sample holder with a hole for light to pass through. A Ge photodiode detector was positioned beneath the hole to collect the transmitted light. The EQE was measured first from the detector by itself, for reference, and then again with the InP substrate between the detector and the light source. Reflectance $\mathcal{R}$ from the InP substrate was also measured to determine the amount of light absorbed in the substrate. The substrate used for the measurements came from the same batch as those used for the PPC fabrication: p-InP with a Zn doping concentration of $(1-8)\times10^{18}\,\mathrm{cm}^{-3}$ and a thickness of $\sim 625\ \mu$m. The measured thickness of the substrate used for these measurements was 616 μm.

The reference signal (EQE_{ref}) and the signal that measured from the detector beneath the InP substrate EQE_{InP} are shown in Figure 4.15a. The transmittance $\mathcal{T}$ was determined by taking the ratio $EQE_{\mathrm{InP}}/EQE_{\mathrm{ref}}$. $\mathcal{T}$ and $1-\mathcal{R}$ are plotted together in Figure 4.15b, which depicts the relative intensities of transmitted, reflected, and absorbed light. Each region of the graph is labelled accordingly.

Calculations were done using the Python transfer matrix method (TMM) package [73] to determine the absorption properties of the InP substrate. A simple geometry was used for the TMM calculations, with 616 μm of InP sandwiched between semi-infinite layers of air. The air was modelled with $n_{\mathrm{r,\,air}} = 1$, $\kappa_{\mathrm{air}} = 0$. For InP, reference data [163, 184] was used for the real part of the refractive index $n_{\mathrm{r,\,InP}}$, which is not expected to change significantly with doping. A fitting routine was used to determine α_{InP}, and by extension κ_{InP} at each data point, minimizing the difference between the measured and calculated transmittance.

After obtaining the optimal value for α_{InP} at each data point, a curve-fit was performed according to the equation

$$\alpha_{\mathrm{InP}}(E) = \alpha_{\mathrm{BB}}(E) + \alpha_{\mathrm{FCA}}(E) \tag{4.18}$$

The band-to-band component is given by [3]

$$\alpha_{\mathrm{BB}}(E) = a_1 e^{b_1 E} \tag{4.19}$$

accounting for absorption in the Urbach tail. The FCA component varies with wavelength according to [59]

$$\alpha_{\mathrm{FCA}}(\lambda) = a_2 \lambda^{b_2} \tag{4.20}$$

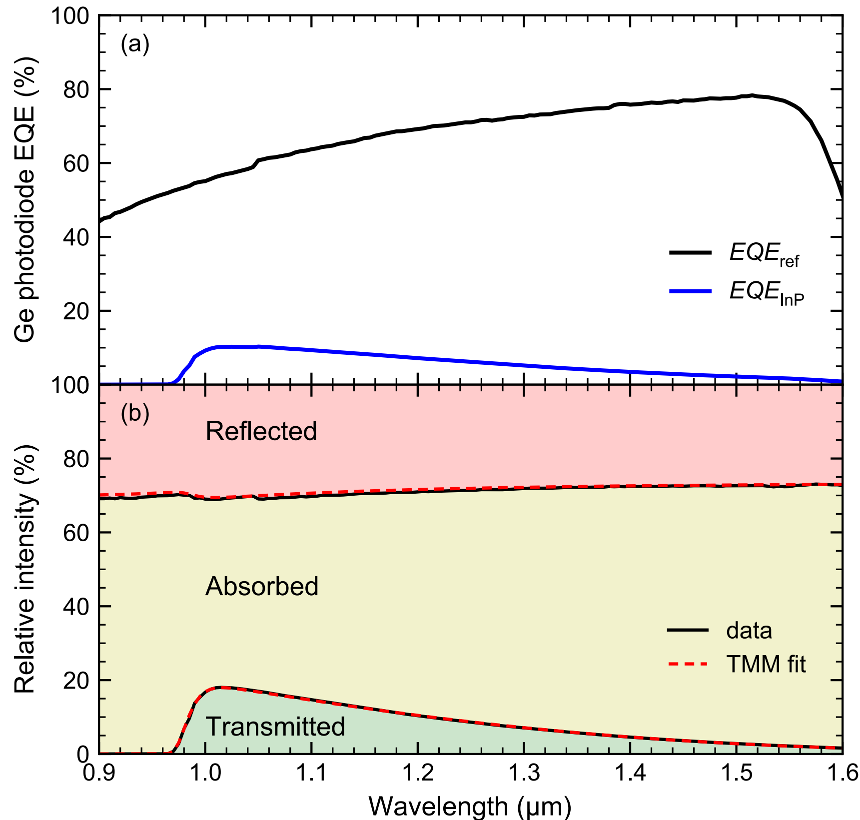

Figure 4.15: (a) EQE measured from Ge photodiode, reference signal (EQE_{ref}) and for light transmitted through InP substrate (EQE_{InP}). (b) Relative intensities of light reflected from, absorbed within, and transmitted through the InP substrate. Regions are determined by plotting $\mathcal{T}$ and $1-\mathcal{R}$. Fit to the measured data is shown.

noting that $\lambda = hc/E$ is the wavelength of light. a_1, b_1, a_2, and b_2 are fitting parameters. The resulting fits to the absorption coefficient are shown in Figure 4.16. Fitting parameters and uncertainties are given in Table 4.5.

The resultant data for the complex refractive index for the p-InP substrate, using the fit results for κ_{InP}, were used along with the TMM to calculate the reflectance and transmittance of the suspended InP substrate. These TMM calculations are represented by the dashed red lines in Figure 4.15.

At the target laser wavelength of 1310 nm, the p-InP substrate has an absorption coefficient of 33 cm^{-1} due to FCA. For a substrate with a thickness of 625 µm, 87.4% of incident 1310 nm light will be absorbed on a single pass (neglecting the reflectance). If a perfectly reflecting surface was placed at the bottom of the substrate, effectively doubling the path-length, 98.4% of the 1310 nm light would be absorbed and the back-reflector would offer little or no benefit to the PPCs presented in this chapter. For design purposes, it was assumed that any light transmitted into the substrate was lost.

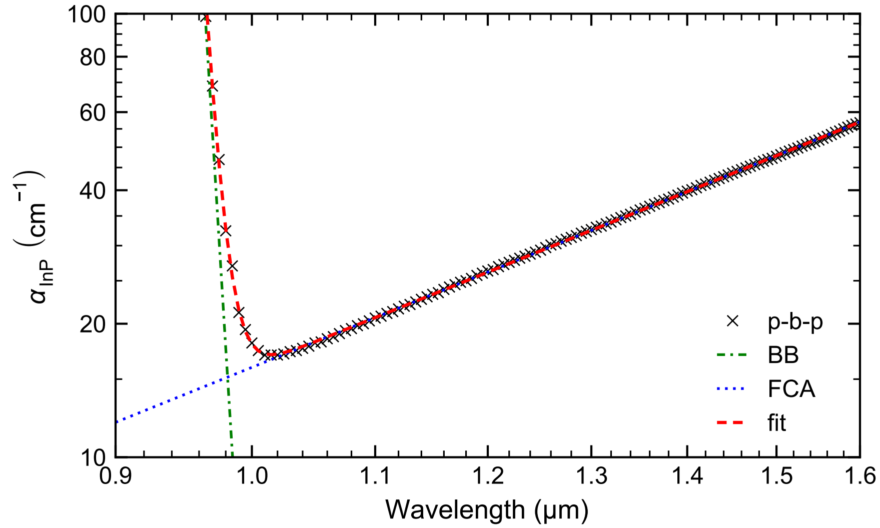

Figure 4.16: Absorption coefficient for p-InP substrate as a function wavelength on a log-log scale. α_{InP} data points were extracted point-by-point (p-b-p) from the data shown in Figure 4.15 using the TMM. Fits are shown for the band-to-band (BB) and FCA components as well as for the entire curve, fit according to equation 4.18.

Table 4.5: Fitting parameters and goodness of fit for $In_{0.527}Al_{0.356}Ga_{0.117}As$ heterostructure in the range from 0.8 to 1.24 eV.

Mechanism	**Parameter**	**Value**
Band-to-band (equation 4.19)	a_1 (cm^{-1})	2.4×10^{-46} $(2.6\times10^{-48}, 2.2\times10^{-44})$*
	b_1 (eV^{-1})	85 ± 4
FCA (equation 4.20)	a_2 (cm^{-1})	15.95 ± 0.03
	b_2	2.710 ± 0.007

* 95% confidence interval

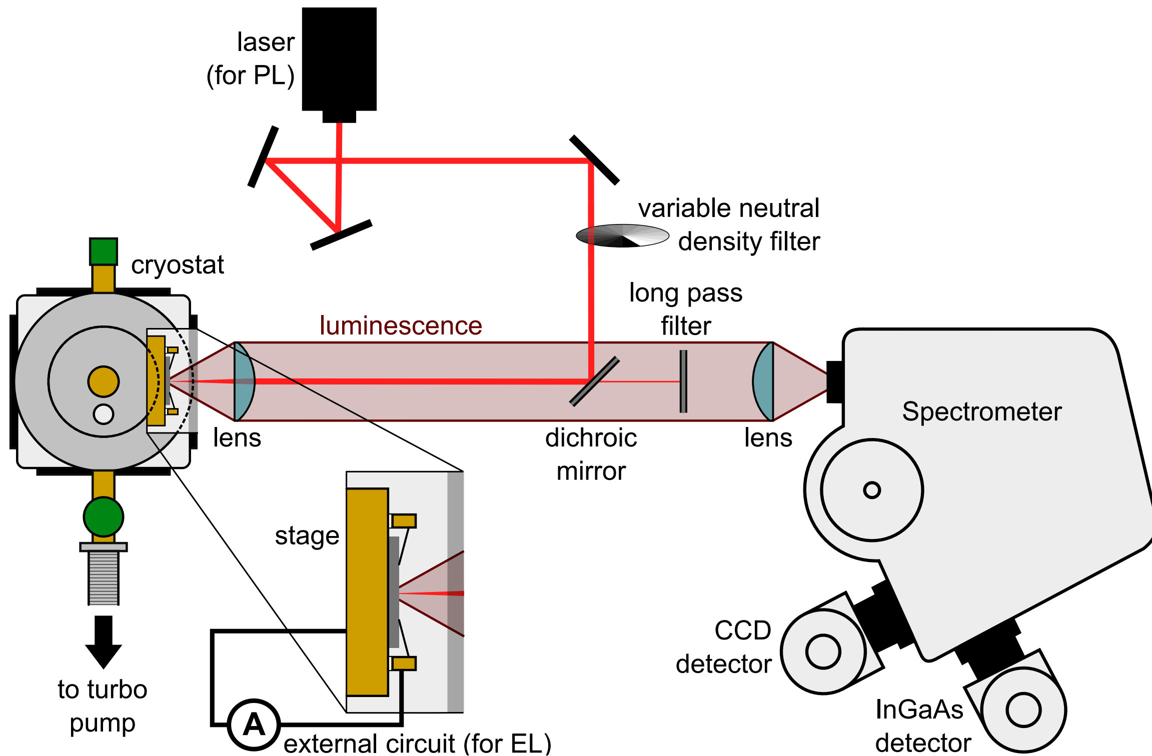

Figure 4.17: Measurement system for electroluminescence (EL) and photoluminescence (PL).

4.1.5 Luminescence measurements

Luminescence measurements were performed on several samples to verify the bandgap and to gauge the epitaxial material quality. The experimental setup, which was used for both electroluminescence (EL) and photoluminescence (PL) measurements, is shown in Figure 4.17. The system was built through the combined effort of several graduate students in the SUNLAB, including myself.

A Lasos TLD-XT 830 nm laser with a maximum output power of 220 mW was used as the excitation source for the PL experiments. The beam power was modulated using a continuously variable neutral density (ND) filter and directed toward the sample using a long-pass dichroic mirror at a 45°angle to the beam path. The sample was mounted vertically on a copper chuck affixed to a cold finger inside of a Cryo Industries of America 110-637-DND cryostat. The cryostat was cooled using liquid nitrogen and connected to a Varian roughing pump and turbo pump to maintain a vacuum level of $\sim 10^{-4}$ mbar within the sample chamber for temperature-controlled experiments. The temperature of the cold finger was regulated using a Cryocon temperature controller. For EL measurements, a sample chuck with integrated electrical probes was used to connect the sample to an external power supply. The for both PL and EL experiments, the samples were held

in place on the copper chuck using Elmers rubber cement.

A UV-fused silica lens with a focal length of 10 cm was used both to focus the beam onto the sample and to collimate the luminescence along the same trajectory. Reflected laser light was blocked using the dichroic mirror and a long-pass filter and the luminescence was focused into an iHR 320 Horiba Jobin-Yvon spectrometer using another UV-fused silica lens. Two liquid nitrogen-cooled detectors were used to measure the luminescence spectra, a Horiba Symphony CCD detector with a detection range of ~ 300-1000 nm (1.24-4.13 eV) and a Horiba Symphony InGaAs detector with a range of ~ 1000-1600 nm (0.78-1.24 eV). Two Horiba Jobin-Yvon plane ruled diffraction gratings were used within the spectrometer to perform luminescence measurements, one blazed at 1000 nm (510-15) and the other at 1500 nm (510-16), both with a groove density of 600 lines/mm.

4.1.5.1 Electroluminescence

EL measurements were performed on a PPC with active layer quaternary composition $In_{0.53}Al_{0.15}Ga_{0.32}As$ (z = 0.315). The PPC was fabricated using indium dot soldered contacts and connected to the external circuit in a two-wire configuration. Measurements were performed at cold finger temperatures ranging from 78 to 300 K. Measurements were taken at short-circuit with current densities ranging up to ~ 0.4 A/cm^2. EL spectra are shown for the sample at 78 K in Figure 4.18a and at 300 K in Figure 4.19a. Correction factors were applied to the measured data to account for the grating efficiency and to correct stitching errors caused by imperfect alignment of the InGaAs detector. The peaks were fit using a skew pseudo-Voigt distribution, which is a linear combination of a skew Lorentzian and a skew Gaussian, having the form

$$I_{\text{skew pV}}(E) = f\, I_{\text{skew L}}(E) + (1-f)\, I_{\text{skew G}}(E) \tag{4.21}$$

where f is a fitting parameter and $I_{\text{skew L}}$ and $I_{\text{skew G}}$ are the skew Lorentzian and skew Gaussian distributions respectively given by

$$I_{\text{skew L}}(E) = \left(\frac{2B_0}{\pi w_{\text{skew}}}\right) \frac{1}{1 + 4\left(\frac{E-E_{\text{peak}}}{w_{\text{skew}}}\right)^2} \tag{4.22}$$

$$I_{\text{skew G}}(E) = \frac{B_0}{w_{\text{skew}}}\sqrt{\frac{4\ln 2}{\pi}} \exp\left[-4\ln 2\left(\frac{E-E_{\text{peak}}}{w_{\text{skew}}}\right)^2\right] \tag{4.23}$$

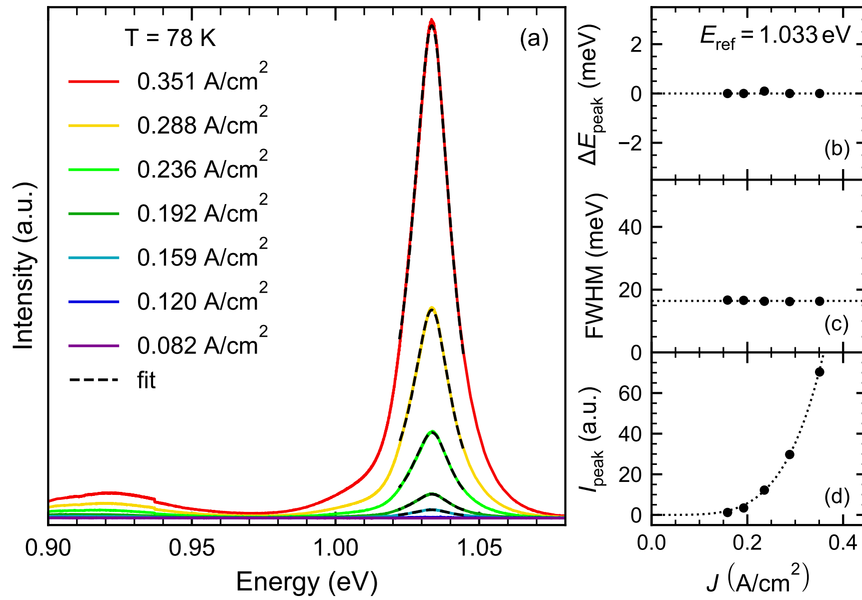

Figure 4.18: (a) EL spectra for a PPC with active layer composition $In_{0.53}Al_{0.15}Ga_{0.32}As$ ($z = 0.315$) at 78 K for various current densities. Fits to equation 4.21 are shown by the dashed lines. (b) Shift in the EL peak energy as a function of current density, calculated relative to the peak for the largest current density (E_{ref}). (c) Full width at half maximum (FWHM) values as a function of current density. The dotted line gives the average. (d) Intensity of the EL peak as a function of current density. The dotted line is the power law fit.

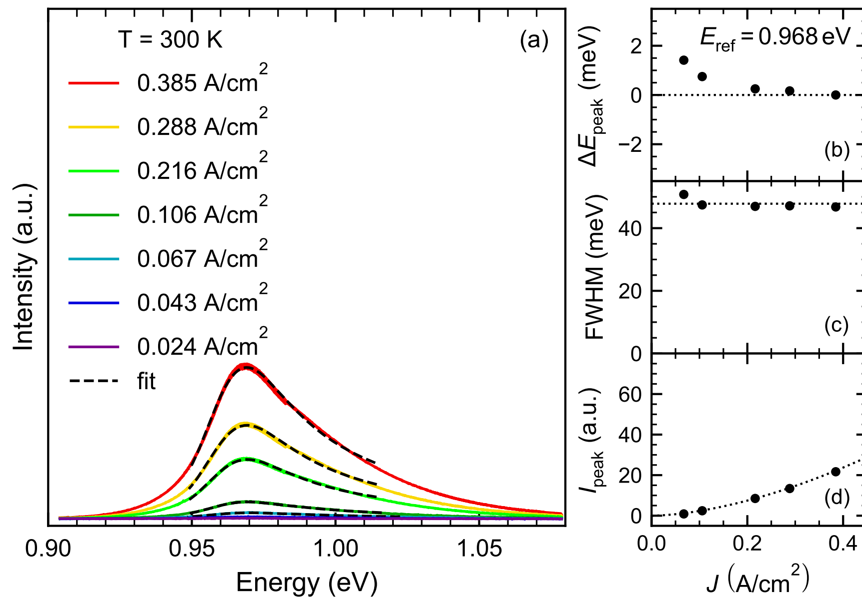

Figure 4.19: (a) EL spectra for a PPC with active layer composition $In_{0.53}Al_{0.15}Ga_{0.32}As$ ($z = 0.315$) at 300 K for various current densities. Fits to equation 4.21 are shown by the dashed lines. (b) Shift in the EL peak energy as a function of current density, calculated relative to the peak for the largest current density (E_{ref}). (c) Full width at half maximum (FWHM) values as a function of current density. The dotted line gives the average. (d) Intensity of the EL peak as a function of current density. The dotted line is the power law fit.

where B_0 is a fitting parameter, E_{peak} is the EL peak, and

$$w_{\mathrm{skew}} = \frac{2w_0}{1 + e^{s\left(E - E_{\mathrm{peak}}\right)}}$$

with fitting parameters w_0 and s. The factor of $4\ln 2$ in equation 4.23 comes about such that, for $s = 0$, the full width at half maximum (FWHM) is equal to w_0.

The small peak to the left of the main EL peak in Figure 4.18a is attributed to defect states. As the temperature increases, increasing lattice vibrations enhance the electron-phonon interaction and non-radiative recombination mechanisms become dominant, quenching the radiative transition between defect states [185].

At all measured temperatures between 78 K and 300 K, the EL peak remained constant with applied current to within ~ 3 meV or less. The shift relative to the peak at the highest measured current $\left(\Delta E_{\mathrm{peak}}\right)$ is plotted as a function of current density in Figures 4.18b and 4.19b for 78 K and 300 K respectively. The FWHM of the EL peaks is also constant with current. This is shown in Figures 4.18c and 4.19c for 78 K and 300 K respectively. The peak intensity $\left(I_{\mathrm{peak}}\right)$ varies with the current density (J) according to a power law relationship.

The ideal shape of the luminescence peak for a bulk semiconductor is given by [70]

$$I_{\mathrm{lum}}(E) \propto \sqrt{E - E_{\mathrm{g}}}\, e^{-E/k_{\mathrm{B}}T} \tag{4.24}$$

Based on this relation, the peak generally falls at an energy $E_{\mathrm{peak}} = E_{\mathrm{g}} + \frac{kT}{2}$. Comparing the measured value at 300 K, $E_{\mathrm{peak,\,300\,K}} \sim 0.968$ eV, to the bandgap obtained for this sample using the Tauc plot method, $E_{\mathrm{g,\,Tauc}} = 0.9536$ eV, the difference is 14 meV which is very close to the value $k_{\mathrm{B}}\left(300\,\mathrm{K}\right)/2 = 13$ meV, as expected.

The semiconductor bandgap varies with temperature according to the Varshni relation [186, 187]

$$E_{\mathrm{g}}(T) = E_{\mathrm{g},0} - \frac{\alpha_{\mathrm{g}} T^2}{T + \beta_{\mathrm{g}}} \tag{4.25}$$

where $E_{\mathrm{g},0}$ is the bandgap at 0 K and α_{g} and β_{g} are fitting parameters. It follows that the luminescence peak will vary according to

$$E_{\mathrm{peak}}(T) = E_{\mathrm{g},0} - \frac{\alpha_{\mathrm{g}} T^2}{T + \beta_{\mathrm{g}}} + \frac{k_{\mathrm{B}} T}{2} \tag{4.26}$$

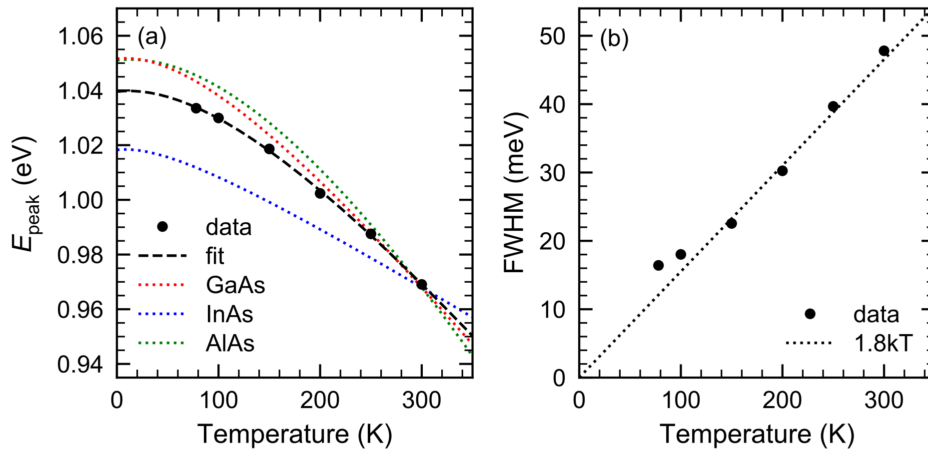

Figure 4.20: (a) EL peak as a function of temperature, fit using equation 4.26. Trends for GaAs, InAs, and AlAs are shown for reference, shifted such the the curves overlap at 300 K. (b) Full width at half maximum for the EL peaks as a function of temperature. The dotted line shows the expect trend of FMWH ~ $1.8k_BT$.

Table 4.6: Varshni parameters for $In_{0.53}Al_{0.15}Ga_{0.32}As$ and for the component binaries.

Material	$E_{g,0}$ **(eV)**	α_g **(meV/K)**	β_g **(K)**	**Reference**
$In_{0.53}Al_{0.15}Ga_{0.32}As$	1.039 ± 0.001	0.54 ± 0.07	280 ± 80	Fit
InAs	0.417	0.276	93	[165]
AlAs	3.099	0.885	530	[165]
GaAs	1.519	0.5405	204	[165]

The measured values for E_{peak} are plotted as a function of temperature in Figure 4.20a and the fit to equation 4.26 is shown. For comparison, the relevant functions for the three binary compounds InAs, AlAs, and GaAs are also plotted, with the values of $E_{g,0}$ scaled so that the curves overlap at 300 K. It can be seen that the trend for the quaternary falls between the trends for the component binaries, as expected. The calculated Varshni parameters for $In_{0.53}Al_{0.15}Ga_{0.32}As$ are shown in Table 4.6, along with the binary parameters for comparison.

Based on equation 4.24, the expected FWHM for the luminescence peak of a bulk semiconductor is $1.8k_BT$. In Figure 4.20b, the measured FWHM is plotted as a function of temperature. The data falls very close to the ideal $1.8k_BT$ trend, indicating that the quaternary material is reasonably uniform, as significant non-uniformities in the composition throughout the device would manifest as a broadening of the peak.

4.1.5.2 Photoluminescence

PL spectroscopy was performed at room temperature for undoped $In_{0.532}Al_{0.097}Ga_{0.371}As$ ($z = 0.205$) on InP capped with 10 nm of InGaAs. The PL spectrum is shown in Figure 4.21a. A correction factor was applied to the measured data to account for the grating efficiency, a background spectra measured in the dark were subtracted from the illuminated spectra, the data was smoothed using a Savitzgy-Golay filter, and stitching errors caused by imperfect alignment of the detector were eliminated by measuring spectra at different starting wavelengths and reconstructing the true spectrum from there. To the left of the $In_{0.532}Al_{0.097}Ga_{0.371}As$ peak is a PL peak generated by the InGaAs cap layer (expected bandgap 0.74 eV). The InGaAs peak was not resolved because it lies outside the range of the detector.

The PL peak occurs at 0.879 eV and the FWHM is ~ 51 meV. Assuming ideal behaviour where $FWHM = 1.8k_BT$, the estimated sample temperature is ~ 329 K, which is larger than room temperature (~ 300 K). This discrepancy can be explained by localized heating from the laser, which may have increased the sample temperature in the measurement area. Non-uniformities in the quaternary composition may also broaden the luminescence peak.

Using the measured PL peak, an estimated temperature of 329 K, and assuming ideal behaviour where $E_{peak} = E_g + \frac{k_BT}{2}$, the estimated bandgap is $E_{g,\,est.} = 0.865$ eV. This estimation is ~ 13 meV smaller than the bandgap obtained for this quaternary composition using the Tauc plot method, $E_{g,\,Tauc} = 0.8778$ eV, which

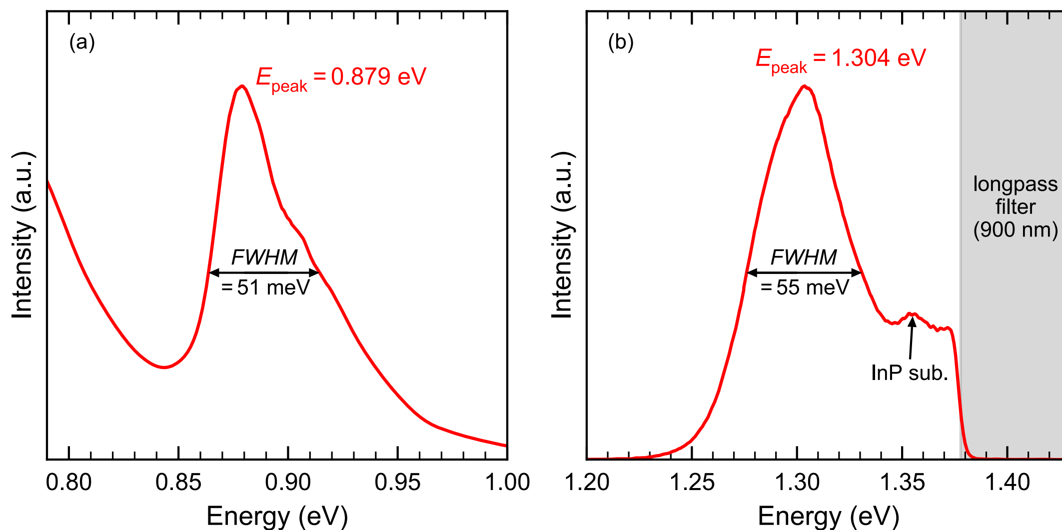

Figure 4.21: Room temperature PL spectra for undoped (a) $In_{0.532}Al_{0.097}Ga_{0.371}As$ ($z = 0.205$) and (b) $In_{0.527}Al_{0.356}Ga_{0.117}As$ ($z = 0.748$) on InP with a 10 nm InGaAs cap layer.

was measured at room temperature. Assuming similar temperature-dependent behaviour to that summarized in Figure 4.20a and Table 4.6 for $In_{0.53}Al_{0.15}Ga_{0.32}As$, the 13 meV difference between $E_{g,\,est.}$ and $E_{g,\,Tauc}$ can be explained by laser induced heating.

Additional PL spectroscopy was performed at room temperature for undoped $In_{0.527}Al_{0.356}Ga_{0.117}As$ (z = 0.748) on InP capped with 10 nm of InGaAs. This quaternary composition was used for front and back surface fields in PPC devices. The PL spectrum is shown in Figure 4.21b. The measured data was corrected to account for the grating efficiency and smoothed using a Savitzgy-Golay filter. To the right of the $In_{0.527}Al_{0.356}Ga_{0.117}As$ peak is a second peak generated by the InP substrate (expected bandgap 1.344 eV). The measurement is cut off at 900 nm (1.378 eV) by the long-pass filter that was used to prevent the 830 nm laser beam from entering the spectrometer.

The PL peak occurs at 1.304 eV, suggesting a bandgap of $\sim$ 1.29 eV. The FWHM is $\sim$ 55 meV. In addition to temperature broadening caused by localized heating from the laser, the partially overlapping InP PL peak makes it difficult to resolve the exact width of the quaternary PL signal.

4.1.6 Single- and multi-junction PPC designs

PPCs were designed with specific absorbance targets. The active layer thickness required to achieve these targets were determined by assuming simple Beer-Lambert absorption (see equation 2.34) throughout the active layer regions, neglecting reflections at layer interfaces. Assuming an absorption coefficient of 7144 cm^{-1} for $In_{0.532}Al_{0.097}Ga_{0.371}As$ (z = 0.205) at a wavelength of 1319 nm, a total absorber thickness of 5.476 μm is required to absorb 98% of the incident light. The absorption coefficient was measured by ellipsometry (see Figure 4.6 and Table 4.3) and the wavelength was chosen to match the central wavelength of the laser used for experimental measurements (see Section 4.1.7). Figure 4.22 shows how the absorbance can be portioned to create a 4-junction structure, evenly dividing the incident light between the four subcells.

Several of the single-junction PPCs discussed in this thesis were designed to be optically thin, mimicking the performance of the top junction in a multi-junction device. In all samples, an emitter thickness of 0.1 μm was maintained and the base thickness was adjusted to achieve the target subcell thickness. The detailed epitaxial layer structure for a two-junction PPC is given in Table 4.7. The n-type cap layer allows for top contact formation and the n-type etch stop allows the cap to be removed by self-aligned wet chemical etching (see Section 4.1.1). The front and back surface fields (FSF and BSF) improve carrier collection efficiency by deflecting minority carriers towards the depletion region and away from interfaces where they have a

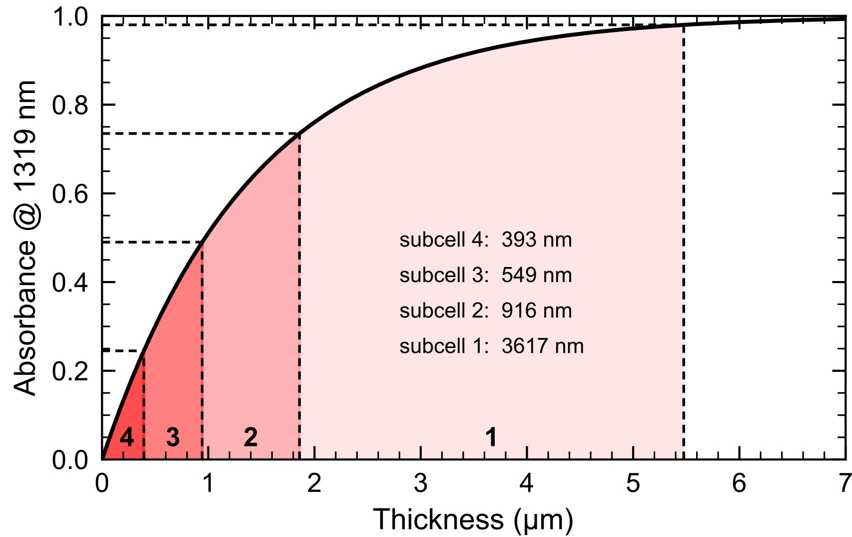

Figure 4.22: Partitioned absorbance for a 4-junction InAlGaAs PPC with an active layer absorption coefficient of 7144 cm^{-1} at 1319 nm illumination targeting a total absorbance of 98%. The thickness of each subcell is indicated.

high probability of being lost to recombination. The top FSF layer, which is much thicker than the bottom FSF, doubles as a lateral conduction layer, which helps to spread current across the PPC mesa area when illuminated by a non-uniform light source such as a laser. An extra p-type cap layer was included at the bottom of the layer stack for some samples to allow the rear-side contact to be deposited on the front side of the wafer by etching down. This functionality was not used for the PPCs presented in this thesis.

The thicknesses of the top and bottom subcells are indicated in Table 4.7 by t_{top} and t_{bottom} respectively. Using an absorption coefficient of 7144 cm^{-1}, these thicknesses would be t_{top} = 942 nm and t_{bottom} = 4533 nm. The many optically thin PPC samples discussed in this thesis followed the same layer structure outlined in Table 4.7 with the tunnel diode and bottom subcell layers removed.

4.1.7 Current-voltage characteristics

Current-voltage (I-V) characteristics were measured using a four-wire configuration and a Keithley 2420 series source-meter. Two probes were used to conduct current in the top of the mesa structure (one for each busbar) and a third probe was used as the voltage sensor. From the backside of the PPC samples, current was conducted through a gold-plated copper chuck. Two wires were connected to screws mounted in the chuck, one wire for current and the other to measure voltage.

Table 4.7: Detailed InAlGaAs/InP two-junction PPC epitaxial layer structure.

Region	**Layer**	**Material**	**Bandgap (eV)**	**Doping (cm^{-3})**	**Thickness (nm)**
	n cap	$In_{0.526}Ga_{0.474}As$	0.74	Si: 5×10^{18}	100
	n etch stop*	$In_{0.3}Al_{0.7}As$	1.93 (indirect)	Si: 2×10^{18}	10
Subcell (top)	n FSF	$In_{0.527}Al_{0.356}Ga_{0.117}As$	1.29	Si: 5×10^{18}	400
	n emitter	$In_{0.532}Al_{0.097}Ga_{0.371}As$	0.88	Si: 1×10^{18}	100
	p base	$In_{0.532}Al_{0.097}Ga_{0.371}As$	0.88	Be: 2×10^{16}	$t_{top}-100$
	p BSF	$In_{0.527}Al_{0.356}Ga_{0.117}As$	1.29	Be: 5×10^{18}	50
Tunnel diode **	p cladding	$In_{0.523}Al_{0.477}As$	1.44	Be: 5×10^{18}	30
	p++ TD	$In_{0.527}Al_{0.330}Ga_{0.143}As$	1.25	Be: 2.68×10^{19}	15
	n++ TD	$In_{0.527}Al_{0.330}Ga_{0.143}As$	1.25	Si: 5×10^{19}	15
	n cladding	$In_{0.523}Al_{0.477}As$	1.44	Si: 1×10^{18}	30
Subcell (bottom) **	n FSF	$In_{0.527}Al_{0.356}Ga_{0.117}As$	1.29	Si: 5×10^{18}	50
	n emitter	$In_{0.532}Al_{0.097}Ga_{0.371}As$	0.88	Si: 1×10^{18}	100
	p base	$In_{0.532}Al_{0.097}Ga_{0.371}As$	0.88	Be: 2×10^{16}	$t_{bottom}-100$
	p BSF	$In_{0.527}Al_{0.356}Ga_{0.117}As$	1.29	Be: 5×10^{18}	50
	p cap*	$In_{0.526}Ga_{0.474}As$	0.74	Be: 2×10^{19}	200
	p buffer	$In_{0.526}Ga_{0.474}As$	0.74	Be: 2×10^{18}	100
Substrate	p substrate	InP	1.34	Zn: $(1-8)\times10^{18}$	~ 625 μm

* Layer omitted from early devices (Figures 4.9-4.11)
** Layers omitted from single-junction devices

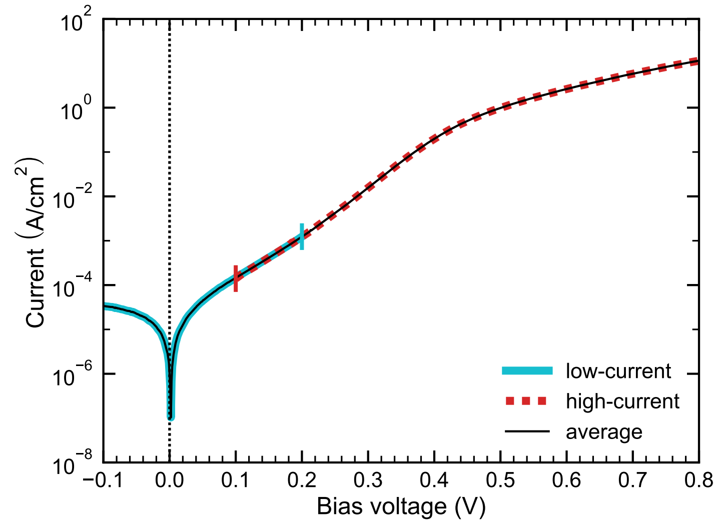

Figure 4.23: Dark *I-V* curve for InAlGaAs PPC. The low- and high-current measurement regimes are indicated as well as the resultant curve for which the currents are averaged in the overlapping region.

4.1.7.1 Dark

Dark *I-V* characteristics were measured with blackout fabric enclosing the sample stage and with lights, computer monitors, and electrical displays turned off or blocked. The *I-V* curves were collected in two voltage ranges, the first from -0.12 - 0.2 V using a current limit of 9 µA to capture the low-current regime close to 0 V and the second from 0.1 - 1 V using a current limit allowing up to 20 A/cm^2 for the corresponding mesa size. For both measurement regimes, the step size was 0.001 V. The data sets were then stitched together and averaged in the overlapping region between 0.1 and 0.2 V. A sample dark *I-V* curve indicating each measurement regime is shown in Figure 4.23. Further discussion of dark *I-V* characteristics can be found in Section 4.2.2.2.

4.1.7.2 Illuminated

I-V characteristics for O-band PPCs were measured under the illumination of a Dilas M1F4S22-1310.20-14C-SS5.2 fiber-coupled laser centred at 1319 nm with a spectral line-width of 8.9 nm. The spectrum shown in Figure 4.24 was measured by the manufacturer at 25°C for an output power of 14.0 W. The multimode optical fiber had a diameter of 400 µm and a numerical aperture of 0.22.

A schematic of the measurement apparatus, which I designed and assembled, is shown in Figure 4.25a. A photo with the beam-path overlaid is shown in Figure 4.25b. The fiber output was collimated using a

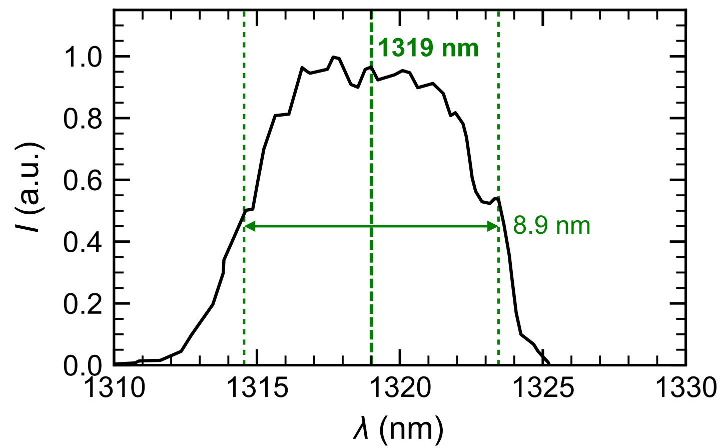

Figure 4.24: Dilas laser spectrum measured at 25°C with an output power of 14.0 W.

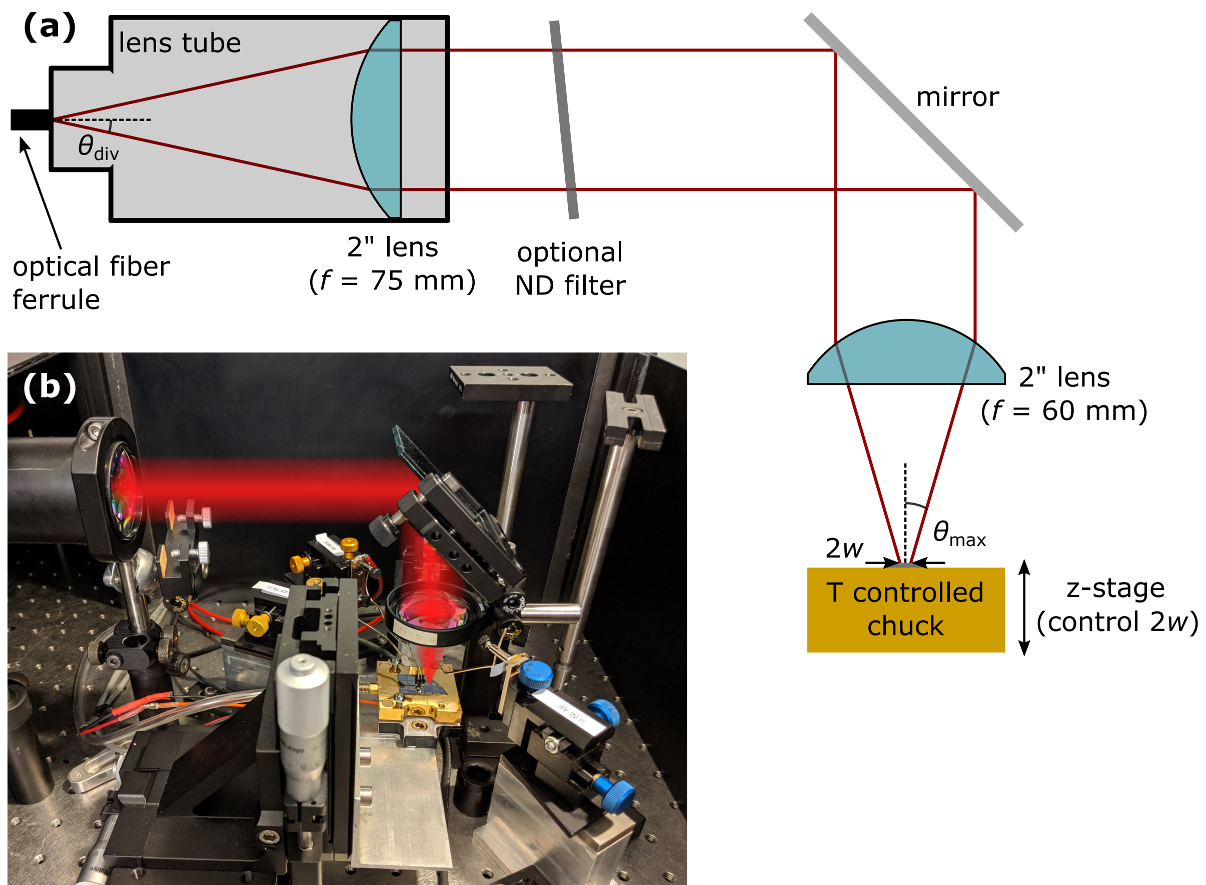

Figure 4.25: (a) Schematic of laser measurement setup showing beam path and optics. (b) Photograph of experimental setup with beam path overlaid in red. f denotes the lens focal length and $2w$ is the beam diameter.

2” lens with a focal length of 75 mm and then passed through a focusing lens with a focal length of 60 mm directly above the measurement stage. The entire apparatus was contained within a light-proof box that could be closed to fully contain the laser beam. The size of the laser beam incident on the sample was controlled by adjusting the lens-to-sample distance.

The output power of the laser was controlled by adjusting the current to the laser diode. Absorptive neutral density (ND) filters were used to attenuate the output power to achieve measurements at lower illumination powers. The output power was initially measured as a function of the laser current using a Newport 818P-020-12 thermopile detector, first without a filter and again using an ND2 filter to determine the degree of attenuation. The measurement was repeated using a calibrated Newport 918D-IR-OD2 photodiode detector with a maximum power rating of 130 mW using an ND2 filter and an ND1 filter to determine the relationship between output power and the laser current and the degree of attenuation for the ND1 filter. Both the thermopile and the photodiode detectors were paired with a Newport 842-PE optical power meter.

The measured data for each detector and filter combination is shown in Figure 4.26. The observed trends in output power are nearly linear with the laser current; however, better agreement was obtained using a quadratic fit, particularly near the threshold current of 9.6 A. A quadratic fit was performed using the ND2 data measured with the photodiode detector. Using the transmittance of the ND2 filter, which is found to be $\mathcal{T}_{\mathrm{ND2}} = 1.373 \pm 0.004\%$, the resultant equation for power as a function of laser current (I_{laser}) is

$$P_{\mathrm{Full}}\left(I_{\mathrm{laser}}\right) = \frac{P_{\mathrm{ND2}}\left(I_{\mathrm{laser}}\right)}{0.01373} = 0.0018 I_{\mathrm{laser}}^{2} + 0.255 I_{\mathrm{laser}} - 2.24\ \mathrm{W} \tag{4.27}$$

The transmittance of the ND1 filter was found to be $\mathcal{T}_{\mathrm{ND1}} = 10.05 \pm 0.04\%$ and the corresponding current-dependent power can be determined similarly. Note that the calibration of the thermopile detector was found to be 11.5% above that of the properly calibrated photodiode detector.

The uncertainty in the laser power determined from the laser current can be estimated from the standard deviation of residuals, which is calculated according to

$$\sigma_{P_{\mathrm{ND2}}} = \sqrt{\frac{\sum_{i}\left(P_{\mathrm{ND2}i} - P_{\mathrm{ND2}}\left(I_{\mathrm{laser}}\right)\right)^{2}}{N_{\mathrm{pts}} - 1}} = 0.00017\ \mathrm{W} \tag{4.28}$$

where N_{pts} is the number of data points. The corresponding uncertainty is estimated to be $2\sigma_{P_{\mathrm{ND2}}} = 0.0003$ W for the ND2 filter. For the ND1 filter and for full power, the uncertainty estimates are $2\sigma_{P_{\mathrm{ND1}}} = 0.003$ W and

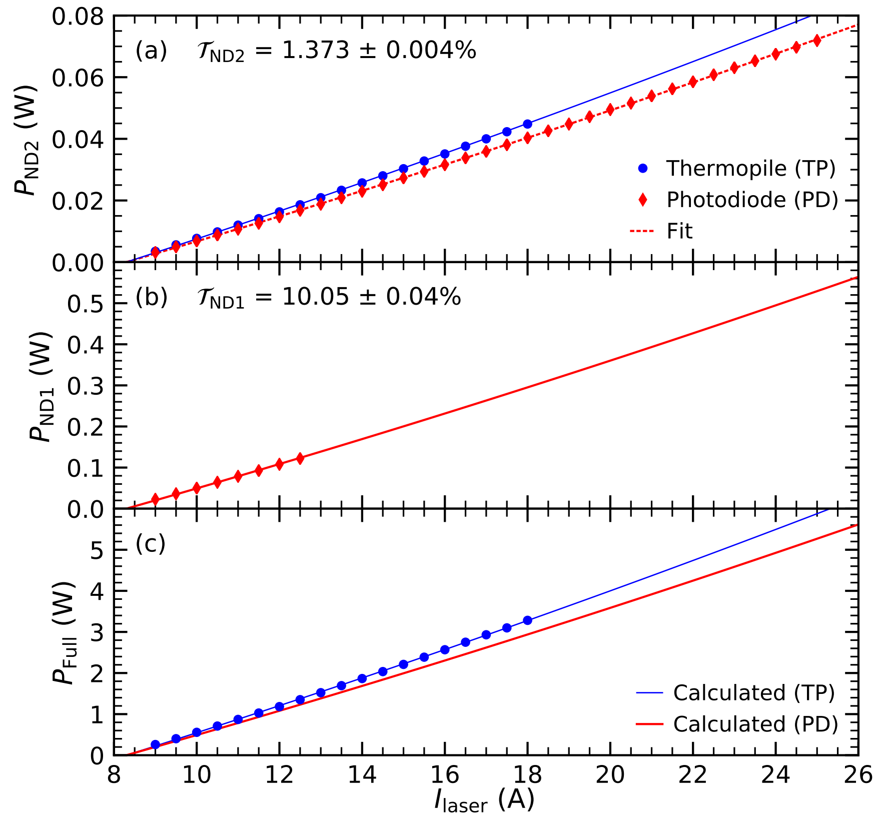

Figure 4.26: Laser power as a function of laser current for (a) the ND2 filter, (b) the ND1 filter, and (c) full power. Measurements are shown for both the thermopile and the calibrated photodiode detectors. Calculations are based off of the fit to the ND2 photodiode measurement.

$2\sigma_{P_{\mathrm{Full}}} = 0.03$ W respectively. This uncertainty analysis accounts for random error due to power fluctuations, but does not account for systematic error that may be present in the measurements. When measuring the laser power using the photodiode detector, it was difficult to ensure that the entire laser beam was captured by the photodiode. To mitigate this potential source of systematic error, the position of the detector was manually adjusted to maximize the reading on the power meter before fixing the detector position.

For small-diameter single-mode optical fibres, the output beam is typically Gaussian in shape. For a larger diameter multi-mode fiber, the beam-shape can be represented by a super-Gaussian profile [188]. The intensity of the beam as a function of position in the x-y plane is then

$$I_{\mathrm{light}}(x,y) = I_{\mathrm{peak}} e^{-2|x/w_x|^{\beta_x}} e^{-2\left|y/w_y\right|^{\beta_y}} \tag{4.29}$$

where I_{peak} is the peak intensity and w_x and w_y are the $1/e^2$ beam radii and β_x and β_y are the beam shape

parameters in the x and y directions. The total power of the output beam is found by integrating the intensity over all space

$$P_{\text{Tot}} = I_{\text{peak}} \int_{-\infty}^{\infty} e^{-2|x/w_x|^{\beta_x}} dx \int_{-\infty}^{\infty} e^{-2\left|y/w_y\right|^{\beta_y}} dy$$
$$= I_{\text{peak}} \frac{2^{(1-1/\beta_x)}\Gamma(1/\beta_x)}{\beta_x} w_x \frac{2^{\left(1-1/\beta_y\right)}\Gamma\left(1/\beta_y\right)}{\beta_y} w_y \quad (4.30)$$

Assuming a symmetrical beam where $w_x = w_y = w$ and $\beta_x = \beta_y = \beta$, the expressions simplify to the following

$$I_{\text{light}}(x,y) = I_{\text{peak}} e^{-2\left(|x|^{\beta}+|y|^{\beta}\right)/w^{\beta}} \quad (4.31)$$

$$P_{\text{Tot}} = I_{\text{peak}} \frac{4^{(1-1/\beta)}\Gamma^2(1/\beta)}{\beta^2} w^2 \quad (4.32)$$

In the case of a perfect Gaussian beam, where $\beta = 2$, the total power is $I_{\text{peak}} \frac{\pi}{2} w^2$.

The uniformity of the irradiance across the sample can be quantified using the peak-to-average ratio (PAR), which is defined as

$$PAR = \frac{I_{\text{peak}}}{I_{\text{avg}}} = \frac{I_{\text{peak}}}{0.99 P_{\text{Tot}}/\left(\pi w_{99}^2\right)} \quad (4.33)$$

where I_{avg} is the average intensity and w_{99} is the beam radius that contains 99% of the incident power. This is a metric for comparison to describe the uniformity of the laser beam and the exact values are not important.

The knife-edge profiling technique was used to measure the diameter of the laser beam incident on the samples. A razor blade was moved incrementally across the beam in the x-direction, gradually blocking it, and the power was measured at each position. The power as a function if the razor's x-position is

$$P(x) = P_{\text{Tot}} - I_{\text{peak}} \int_{-\infty}^{x} e^{-2|x/w|^{\beta}} dx \int_{-\infty}^{\infty} e^{-2|y/w|^{\beta}} dy$$
$$= \frac{P_{\text{Tot}}}{2} \left(1 - \text{sign}(x) \frac{\gamma\left(1/\beta, 2(x/w)^{\beta}\right)}{\Gamma(1/\beta)} \right) \quad (4.34)$$

The razor blade was carefully positioned to be nearly level with the height of the PPC samples that were measured on the apparatus. Knife-edge measurements and Gaussian profiles are shown in Figure 4.27 for three different stage heights, corresponding to different beam sizes.

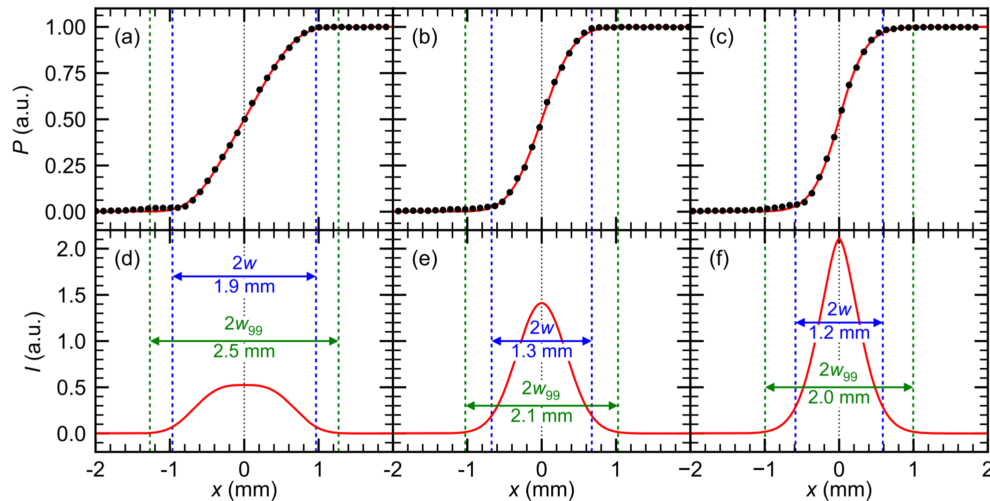

Figure 4.27: (a-c) Knife-edge beam profile measurements with the curve-fit shown in red for three spot sizes. (d-f) Super-Gaussian beam-shapes extracted from the fits. The $1/e^2$ diameter ($2w$) and the diameter containing 99% of the incident power ($2w_{99}$) are indicated. The profiles are normalized to a total power of 1.

Table 4.8: Laser beam parameters.

z (mm)	$2w$ (mm)	β	$2w_{99}$ (mm)	PAR
5	2.3 ± 0.2	3.4 ± 0.8	2.9 ± 0.4	2.5
6	1.9 ± 0.1	3.1 ± 0.5	2.5 ± 0.3	2.7
7	1.7 ± 0.1	3.0 ± 0.4	2.2 ± 0.2	2.8
8	1.35 ± 0.08	2.0 ± 0.3	2.1 ± 0.2	4.7
9	1.17 ± 0.08	1.6 ± 0.2	2.0 ± 0.3	6.6

The lens-to-sample distance was adjusted in increments of 1 mm over a range of 5 mm to generate five spot sizes used in this thesis. The micrometer position corresponding to each spot size is referred to as z. The beam parameters summarized in Table 4.8. The beam diameters $2w$ and $2w_{99}$ are plotted against z in Figure 4.28, with dashed lines indicating quadratic fits. The uncertainties in the beam diameters come from the 95% confidence limits on the fitting parameters and an estimated error of ±0.2 mm in the lens-to-sample distance. Henceforth, beam sizes will be referred to according to the $1/e^2$ diameter, $2w$.

The *I-V* characteristics for PPCs were measured under laser illumination of various powers. The voltage range was from −0.1 to 1.0 V. In general, the spot size was chosen to fit within the boundaries of the active device area. When measuring *I-V* characteristics for a single PPC, different procedures were used depending on the incident power. For powers < 0.1 W, the laser was allowed to illuminate the sample continuously and

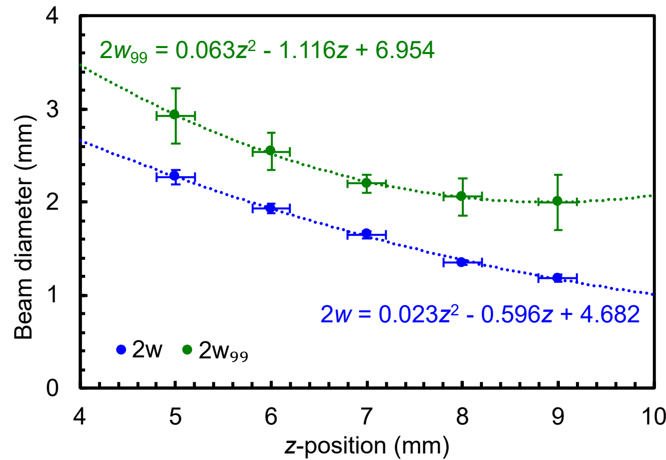

Figure 4.28: Beam diameters $2w$ and $2w_{99}$ plotted against the z-position. Error bars correspond to the 95% confidence limits on the fitting parameters on the vertical axis and to the 0.2 mm uncertainty in the lens-to-sample distance on the horizontal axis. Quadratic fits are shown and the equations given.

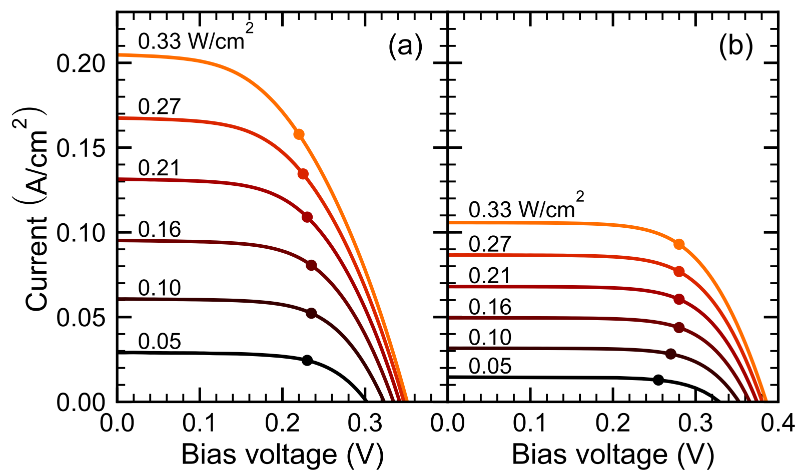

Figure 4.29: *I*-*V* characteristics for InAlGaAs PPC samples with mesa dimensions of $3.85 \times 3.85\,\mathrm{mm}^2$ and absorber thicknesses of (a) 4.1 µm and (b) 0.84 µm. The average irradiance is labelled and markers indicate the maximum power points for each curve. The beam diameter was $2w$ = 1.9 mm.

a step size of 0.005 V was used. Between each measurement, the current to the laser diode was adjusted and the laser was given a few seconds to stabilize at the new power. At incident powers $>$ 0.1 W, a step size of 0.02 V was used and a beam block was manually inserted between the ND filter and the mirror between measurements to limit device heating.

I-*V* curves for two InAlGaAs PPC samples of different absorber thicknesses measured at illumination powers ranging from 7 to 50 mW are shown in Figure 4.29. The incident intensity was determined by averaging the illumination power over the device area.

4.1.7.3 Limitations of the measurement apparatus

The most significant practical limitation of the experimental setup shown in Figure 4.25 is the fact that height of the sample stage cannot be adjusted while maintaining electrical contact to the device via the probes. For every adjustment of the vertical position to modify the beam size, it was necessary to lift the probes. This could be remedied by using an *x*-*y*-*z* stage large enough to hold both the sample chuck and electrical probers.

Another potential improvement would involve the integration of a beam block that could be accurately positioned without opening the top of the light-proof box.

4.2 Single- and dual-junction InAlGaAs photonic power converters

MEGHAN N. BEATTIE, MARZIYEH ZAMIRI, KAYDEN L. C. KALLER, MATTHEW M. WILKINS, CHRISTOPHER E. VALDIVIA, DAIXI XIA, MAN CHUN TAM, HOSUNG KIM, JACOB J. KRICH, ZBIGNIEW R. WASILEWSKI, AND KARIN HINZER

Scope and impact

The following is a reproduction of a conference proceeding that was presented virtually at the 47th IEEE Photovoltaic Specialists Conference, June 2020, with the original title: “Two-Junction III-V Photonic Power Converter Operating At Monochromatic Telecom Wavelengths” [189]. The publication describes my work designing and characterizing a two-junction InAlGaAs PPC designed for O-band operation, including analysis of two optically thin single-junction PPCs and a brief discussion of the TD design. To our knowledge, these are the first results published for a two-junction O-band PPC. The design approach for a multi-junction PPC device is described and detailed experiments and analysis are presented that demonstrate the device capabilities. Multi-junction detailed balance calculations are introduced to provide a benchmark for the experimental results. Loss mechanisms are discussed and potential areas for improvement in the design are outlined.

Author contributions

MEGHAN N. BEATTIE As the lead Ph.D. student associated with the project, I spearheaded the research process and performed all of the experiments and data analysis presented in this paper (Sections 4.2.2.2-4.2.2.4). I designed the PPCs assisted with the design of the TD. As first author, I wrote the manuscript and prepared all of the figures.

DR. MARZIYEH ZAMIRI As a postdoctoral fellow within the University of Ottawa's SUNLAB research group, Marzi developed the in-house fabrication and metallization process that was used to prepare the TD and PPC devices.

KAYDEN L. C. KALLER As a M.Sc. student within the University of Ottawa's SUNLAB research group, Kayden assisted with the in-house fabrication and metallization process that was used to prepare the TD and PPC devices.

DR. MATTHEW M. WILKINS As a postdoctoral fellow within the University of Ottawa's SUNLAB research group, Matt proposed the TD design and assisted with the PPC designs. He also provided detailed feedback during data collection and analysis.

DR. CHRISTOPHER E. VALDIVIA As a senior research scientist within the University of Ottawa's SUNLAB research group, Chris helped to guide my research, provided detailed feedback during data analysis, and assisted in editing the manuscript.

DAIXI (DAISY) XIA As a M.Sc. student at the University of Ottawa under the supervision of Jacob Krich and a SUNLAB collaborator, Daisy developed the extended detailed-balance model used to calculate theoretical efficiency limits and performed the calculations summarized in Section 4.2.2.1.

DR. MAN CHUN (ALAN) TAM As a Ph.D. student within the University of Waterloo's MBE research group, Alan performed the MBE growth for several of the samples discussed in this paper.

DR. HOSUNG KIM As a postdoctoral fellow within the University of Waterloo's MBE research group, HoSung performed the MBE growth for several of the samples discussed in this paper.

PROF. JACOB J. KRICH As a professor at the University of Ottawa and a key collaborative member of the SUNLAB research group, Jacob oversaw the development of Daisy's detailed balance model, provided detailed feedback during data analysis, and assisted in editing the manuscript.

PROF. ZBIGNIEW WASILEWSKI As the director of the University of Waterloo's MBE research group, Zbig oversaw the MBE growth of the samples discussed in this paper, provided detailed feedback during data analysis, and assisted in editing the manuscript.

PROF. KARIN HINZER As the director of the University of Ottawa's SUNLAB research group, Karin oversaw my research, provided detailed feedback during data analysis, and assisted in editing the manuscript.

Copyright

© 2020 IEEE. Reprinted, with permission, from:

> M. N. Beattie, M. Zamiri, K. L. C. Kaller, M. M. Wilkins, C. E. Valdivia, D. Xia, M. C. Tam, H.S. Kim, J. J. Krich, Z. R. Wasilewski, and K. Hinzer, "Two-junction III-V photonic power converter operating at monochromatic telecom wavelengths," in *2020 47th IEEE Photovoltaic Specialists Conference (PVSC)*, 1062–1066. Calgary, AB, Canada, June 2020, 2020.
> DOI: 10.1109/PVSC45281.2020.9300885

In reference to IEEE copyrighted material which is used with permission in this thesis, the IEEE does not endorse any of the University of Ottawa's products or services. Internal or personal use of this material is permitted. If interested in reprinting/republishing IEEE copyrighted material for advertising or promotional purposes or for creating new collective works for resale or redistribution, please go to http://www.ieee.org/publications_standards/publications/rights/rights_link.ht to learn how to obtain a License from RightsLink. If applicable, University Microfilms and/or ProQuest Library, or the Archives of Canada may supply single copies of the dissertation.

Abstract

We present a two-junction photonic power converter operating under monochromatic illumination in the telecommunications O-band. The design, which is a direct extension of multi-junction solar cell technology, incorporates InAlGaAs absorbing layers lattice-matched to InP. Multi-junction detailed balance calculations

are presented to benchmark device performance. A transparent tunnel diode with peak tunneling current near 1000 A/cm^2 provides a series connection between the subcells. Current-voltage measurements under laser illumination at 1319 nm yield ideality factors near 1, with open-circuit voltages up to 0.38 V and 0.66 V for the one- and two-junction devices, respectively, under intensities of up to 0.33 W/cm^2. Quantum efficiency measurements reveal that the two-junction device is current-matched near 1390 nm.

4.2.1 Introduction

Widespread deployment of communications equipment, sensors, and smart technology is driving a need for reliable power supplies to electrically-isolated and extreme environments. Traditional copper cabling is sensitive to electromagnetic interference and presents a risk of heating and sparking. Photonic power transmission via optical fiber is immune to electromagnetic interference and presents minimal risk in hazardous conditions. Electrical power can be converted to light using a laser or an LED, transmitted through fiber, and converted back to electrical power using a photonic power converter (PPC) that, like a solar cell, converts light to electricity through the photovoltaic effect.

Most commercially available PPCs are based on GaAs, operating in the 850 nm band. To increase the output voltage, p-n junctions can be vertically stacked using design principles that are a direct extension of multi-junction solar cell technology. Multi-junction PPCs differ from solar cells in that the absorbers in each junction all have the same bandgap and achieve current matching using optically thin subcells, which can also be used in multi-junction solar cells to improve current matching and boost voltage [190]. Monochromatic conversion efficiencies exceeding 66% and output voltages exceeding 30 V have been obtained in state-of-the-art PPC devices [50, 191]. Efficiencies of more than 50% have been demonstrated for GaAs PPCs even at very high illumination intensities exceeding 150 W/cm^2, averaged over the active area of the device [15].

Existing GaAs-based technologies are well suited to free-space power transfer, or short distances (< 1 km) over optical fiber. Light attenuation in fiber becomes a significant problem for longer distance power-over-fiber transmission, with losses near 50% per kilometer in the 850 nm band. By designing for longer wavelengths in the telecom regime where attenuation in fiber is minimized, longer-distance transmission (up to 10 km) becomes practical.

In this paper, we present a two-junction vertically stacked PPC operating at 1319 nm. The lattice-matched device, grown on InP, consists of InAlGaAs absorbing layers interconnected by a higher-bandgap InAlGaAs tunnel diode, which is fully transparent at 1319 nm. Experimental current-voltage and quantum

efficiency measurements for semi-transparent single-junction devices, high-performance tunnel diodes, and for a two-junction device are shown. Multi-junction detailed balance calculations in the radiative limit are also presented to benchmark device performance.

4.2.2 Results and discussion

4.2.2.1 Multi-junction detailed balance calculations

Detailed balance calculations, extended to include multi-junction architectures and luminescent coupling (see [192]) are used to benchmark the performance of experimental devices. The current is fixed throughout the device and in each junction is calculated by subtracting the number of photons lost from the number of absorbed photons. Photons are lost by radiative emission using a modified Planck spectrum, assuming a step function absorption coefficient with a value of 7143 cm^{-1} above the 0.867 eV bandgap, chosen to match our experimental target at the operating wavelength. The calculations presented here are done in the radiative limit, assuming an input laser spectrum centered at 1319 nm with an intensity of 1 W/cm^2.

The modelled current-voltage characteristics for one to ten junctions are shown in Figure 4.30. For a single-junction device, the open-circuit voltage (V_{OC}) in the radiative limit is 0.65 V, at 1 W/cm^2. For the 10-junction device, the V_{OC} is 6.68 V, slightly more than a 10-fold increase compared to the single-junction. Luminescent coupling leads to a slight voltage enhancement in the top subcells of a multi-junction device. This effect is described in detail in [192, 193].

Modelled efficiencies are shown as a function of the number of junctions in the inset of Figure 4.30. The

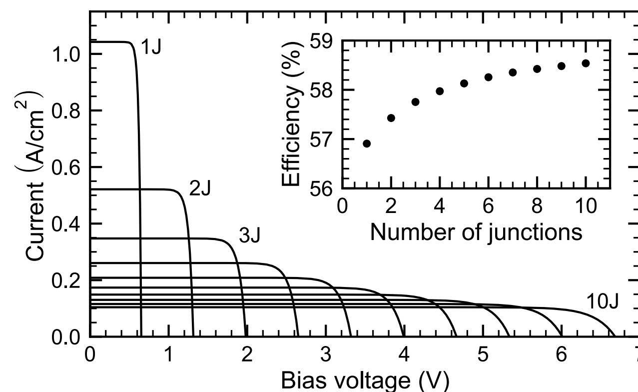

Figure 4.30: Theoretical current-voltage characteristics for PPCs with 1 to 10 junctions. The inset shows the efficiency as a function of the number of junctions. Calculations are done using an extended detailed balance model in the radiative limit. Incident illumination is centered at 1319 nm with an intensity of 1 W/cm^2. The active layer bandgap is 0.867 eV.

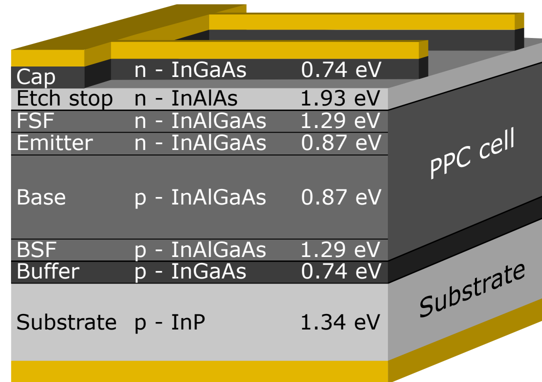

Figure 4.31: Design schematic for one-junction PPC (not to scale). Materials and target bandgaps are indicated.

slight increase in efficiency from 56.9% for the single-junction to 58.5% for the 10-junction can be explained by the voltage enhancement. Due to the logarithmic relationship between V_{OC} and the illumination intensity, the efficiency is strongly intensity-dependent. By increasing the intensity to 10 W/cm^2, the modelled efficiencies increase to 62.8% and 64.5% for one- and 10-junction PPCs respectively. At 100 W/cm^2, modelled efficiencies are 68.8% and 70.4% respectively.

4.2.2.2 Single-junction photonic power converters

Molecular beam epitaxy (MBE) is used to grow single-junction PPC test devices of various thicknesses. The quaternary material InAlGaAs, lattice-matched to InP, is used for the emitter and base absorbing layers as well as for transparent front and back surface fields (FSF, BSF) to improve carrier collection, as shown in Figure 4.31. By varying the quaternary composition, the bandgap can be tuned from 0.72 to 1.44 eV while lattice-matched to InP. The devices presented in this paper were designed to operate in the telecommunications O-band with wavelengths near 1310 nm, or photon energies near 0.95 eV. Ohmic contacts are made to the p-doped InP substrates and to a highly n-doped InGaAs cap layer, the latter of which is removed by self-aligned wet etch after fabrication of the contact gridlines.

Current-voltage (J-V) characteristics for semi-transparent single-junction PPCs under laser illumination at 1319 ± 2 nm are shown in Figure 4.32a and b. The absorber bandgap is 0.867 eV and absorber thicknesses are (a) 4.1 μm and (b) 0.84 μm. Expected absorbance values are 95% and 45% respectively, based on an absorption coefficient of 7143 cm^{-1}, determined by spectroscopic ellipsometry of undoped InAlGaAs, fit using the Adachi-New Forouhi dispersion model [175].

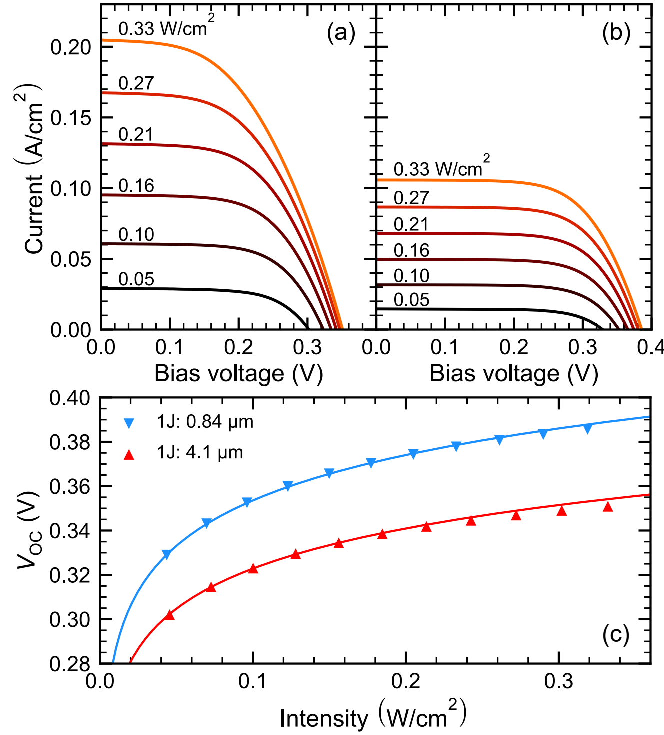

Figure 4.32: (a,b) Current-voltage characteristics for semi-transparent 1-junction PPCs under 1319 nm laser illumination at intensities between 0.05 and 0.33 W/cm^2. Absorber thicknesses are (a) 4.1 µm and (b) 0.84 µm. (c) Open-circuit voltage as a function of illumination intensity for the PPCs in (a) and (b). Solid lines show fits according to (1). See Table 4.9 for fit parameters.

Table 4.9: Figures of merit for 1-junction PPCs in Figure 4.32.

Thickness (µm)	***R* (A/W)**	n_{ideal}	J_0 (A/cm^2)
4.1	0.623	1.02	2.87×10^{-7}
0.84	0.323	1.16	2.32×10^{-7}

Open-circuit voltage (V_{OC}) scales with intensity (I_{light}) as in:

$$V_{OC} = \frac{n_{ideal}\, k_B\, T}{q} \ln\left(\frac{J_{SC}}{J_0} + 1\right) \tag{4.35}$$

$$J_{SC} = R\, I_{light}\, A \tag{4.36}$$

where n_{ideal} is the ideality factor, k is the Boltzmann constant, T is the absolute temperature (298 K), J_0 is the dark saturation current, J_{SC} is the short-circuit current, R is the responsivity at the laser wavelength and A is the active area. The V_{OC} is shown as a function of intensity for both single-junction PPCs in Figure 4.32c.

Fits are performed using equation 4.35 for the first six data points (up to 0.18 W/cm^2) and fitting parameters are given in Table 4.9. Ideality factors near 1 are obtained, suggesting that recombination outside of the depletion region dominates between 0.3 and 0.4 V. At higher intensities, deviations from the trend are likely caused by localized heating effects.

The measured V_{OC} is low compared to the limiting values determined by detailed balance calculations. At an intensity of 0.1 W/cm^2, the maximum V_{OC} for a 1-junction device in the radiative limit is 0.59 V. Measured values at 0.1 W/cm^2 are 0.32 V and 0.35 V for the thick and thin PPCs respectively. A reduction in non-radiative recombination may lead to a significant improvement in the V_{OC} .

Measured external quantum efficiency (EQE) and specular reflectance $(\mathcal{R}_{spec})$ for the 1-junction PPCs are shown in Figure 4.33. $\mathcal{R}_{spec}$ is close to 35% at the laser wavelength for both PPCs. This loss will be virtually eliminated by the application of an anti-reflection coating on future devices. In an ideal device with only specular reflection and transmission losses, the $\mathcal{R}_{spec}$ adjusted QE, corresponding to the dashed lines in Figure 4.33, would be equivalent to absorbance. Table 4.10 shows a comparison between the expected absorbance and the $\mathcal{R}_{spec}$-adjusted QE at the laser wavelength for each device. For the 4.1 µm PPC, the ~ 6% (abs.) difference between the expected absorbance and the $\mathcal{R}_{spec}$ adjusted QE indicates that the minority carrier diffusion length is insufficient for complete carrier collection in such a thick device. For the 0.84 µm

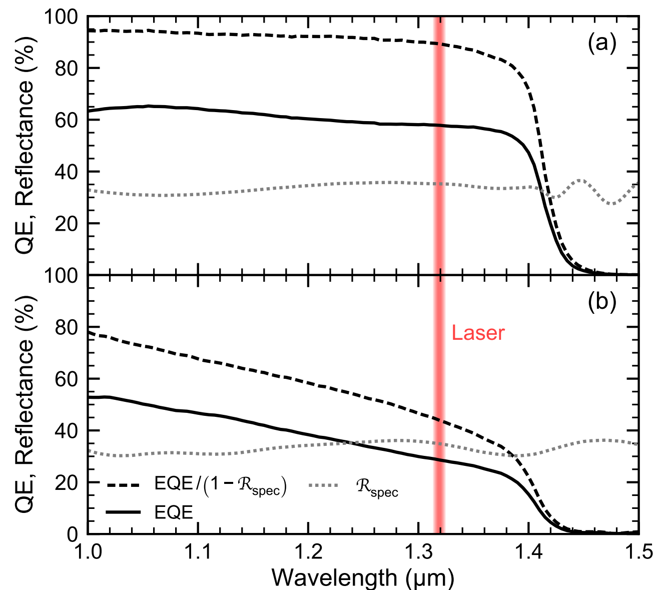

Figure 4.33: Quantum efficiency and specular reflectance for semi-transparent 1-junction PPCs. The laser wavelength used for the *J*-*V* measurements is indicated. Absorber thicknesses are (a) 4.1 µm and (b) 0.84 µm.

Table 4.10: Expected absorbance and $\mathcal{R}_{spec}$-adjusted QE at laser wavelength for 1-junction PPCs in Figure 4.33.

Thickness (μm)	**Expected absorbance**	**$\mathcal{R}_{spec}$-adjusted QE**
4.1	95%	$89 \pm 2\%$
0.84	45%	$44 \pm 2\%$

PPC, the expected absorbance and the $\mathcal{R}_{spec}$-adjusted QE fall within uncertainty of each other, indicating that the minority carrier diffusion length is sufficiently long to have minimal impact on carrier collection for devices of this thickness. These results suggest that a multi-junction PPC with several thinner absorbing subcells is likely to perform better than a single-junction PPC of the same total absorber thickness due to improved carrier collection within the subcells.

Dark J-V curves were measured for a series of square diodes of varying sizes fabricated on the thick single-junction PPC with a 4.1 μm absorber. The top contact for these diodes consisted of a single square pad covering the active area of the device, set back 25 μm from the mesa edge. The measurements are shown in Figure 4.34. The J-V curves corresponding to the smallest two diodes are set apart from the three larger diodes, which very nearly overlap. This near overlap signifies that edge effects such as reduced shunt resistance at the perimeter strongly impact only very small diodes with side length < 250 μm. Edge effects are negligible in square diodes larger than 250 μm.

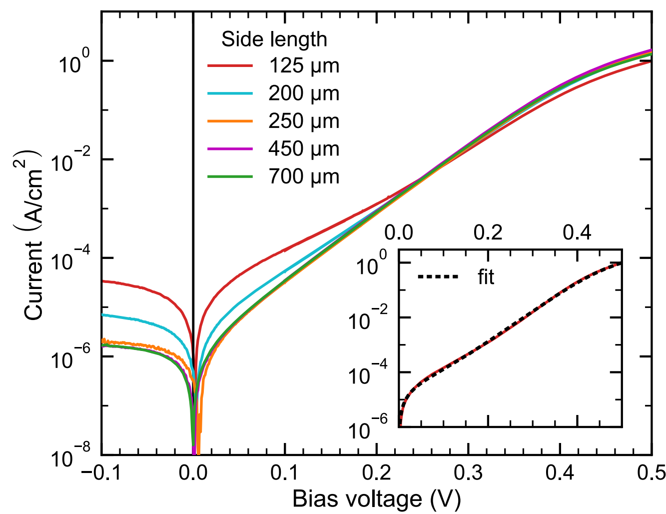

Figure 4.34: Dark current-voltage characteristics for 1-junction PPC square diodes with 4.1 μm. absorber thickness. The side length for each square diode is shown in the legend. The inset shows the non-ideal diode equation 4.37 fit to the 125 μm. diode dark $J-V$ curve. See Table 4.11 for fit parameters.

Table 4.11: Fitting parameters for dark $J-V$ curves in Figure 4.34.

Side length (μm)	**P/A ratio (cm^{-1})**	**n_{ideal}**	**J_0 (A/cm^2)**	**R_s $(\Omega\,cm^2)$**	**R_{sh} $(\Omega\,cm^2)$**
125	320	1.5	6.61×10^{-6}	4.42×10^{-2}	2.24×10^{3}
200	200	1.35	2.90×10^{-6}	3.32×10^{-2}	5.19×10^{4}
250	160	1.24	1.29×10^{-6}	3.82×10^{-2}	8.47×10^{10}
450	89	1.24	1.51×10^{-6}	3.53×10^{-2}	9.91×10^{10}
700	57	1.26	1.64×10^{-6}	4.48×10^{-2}	8.54×10^{10}

The curves in Figure 4.34 are fit with the non-ideal diode equation:

$$J = J_0\left\{\exp\left[\frac{q(V-J\,R_s)}{n_{ideal}\,k_B\,T}\right]-1\right\}+\frac{V-J\,R_s}{R_{sh}} \tag{4.37}$$

where R_s is the series resistance and R_{sh} is the shunt resistance. The fit for the smallest diode can be seen in the Figure 4.34 inset. The fitting parameters for each of the curves are shown in Table 4.11. We see a clear increase in shunt resistance with decreasing perimeter to area ratio (P/A). For the largest three diodes with $P/A \leq 160$ cm^{-1}, shunt resistance has a negligible impact on the fit. Both ideality factor, n_{ideal}, and dark saturation current J_0 initially decrease with increasing side length before levelling off.

The PPCs for which illuminated measurements are presented in Figure 4.32 and Figure 4.33 have a side length of 3.85 mm, corresponding to a P/A ratio of 10.4 cm^{-1}, which is much less than the 160 cm^{-1} threshold. We conclude that edge effects have negligible impact on their performance.

The difference between the ideality factors and dark saturation currents presented in Table 4.11 and the analysis presented in Table 4.9 can be attributed to a change in ideality factor that occurs between 0.3 and 0.4 V, which is masked by the series resistance in the square diodes.

4.2.2.3 Tunnel diodes

To develop a multi-junction device, tunnel diodes are required to create series connections between adjacent p-n junctions. To this end, fully transparent tunnel diodes are grown by MBE. The structure is similar to a design proposed by Lumb et al. [194, 195] and consists of highly doped InAlGaAs layers with a bandgap near 1.25 eV surrounded by wide-bandgap InAlAs cladding, as shown in Figure 4.35. Peak tunneling currents (J_{pk}) on the order of 1000 A/cm^2 are measured, which is more than sufficient for operating a multi-junction

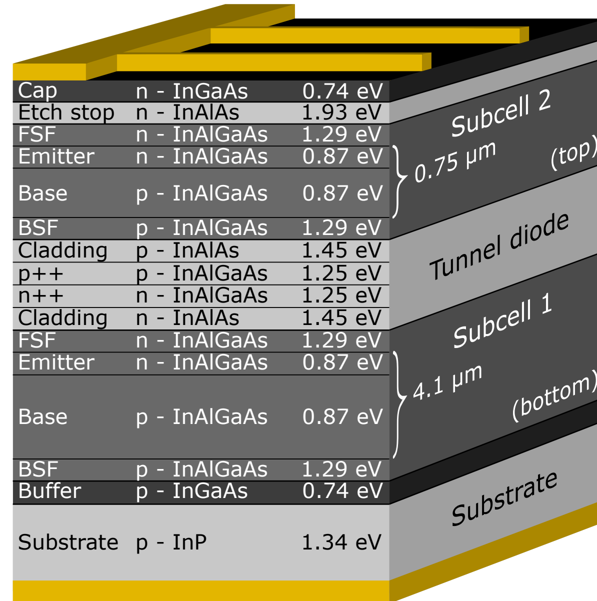

Figure 4.35: Design schematic for two-junction PPC (not to scale). Materials and target bandgaps are indicated. The cap is not etched for this work.

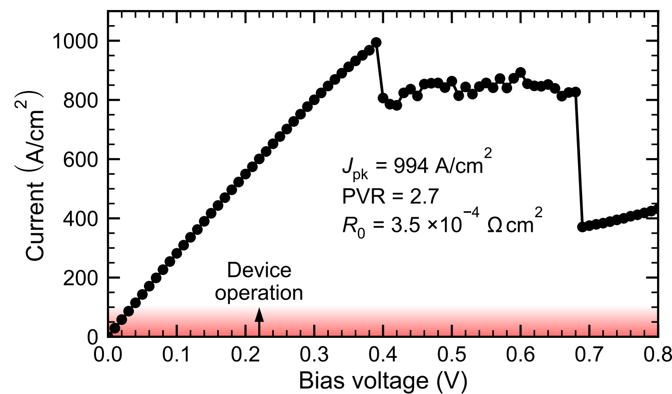

Figure 4.36: *J*-*V* behaviour for InAlGaAs tunnel diode lattice-matched to InP, fully transparent up to 1.2 eV (including telecommunications O-band and C-band). The device operation range (currents up to 100 A/cm^2) is indicated.

PPC at currents up to 100 A/cm^2. A sample *J*-*V* curve is shown in Figure 4.36. The peak-to-valley ratio (PVR) is 2.7 and the resistance at 0 V (R_0) is $3.5 \times 10^{-4}\ \Omega\,\text{cm}^2$.

4.2.2.4 Two-junction photonic power converter

A two-junction PPC is grown by MBE following the design in Figure 4.35. The bottom subcell has an absorber thickness of 4.1 μm while the top absorber thickness is 0.75 μm. The thickness of the top subcell was chosen for 49% absorption at 1319 nm, assuming an absorption coefficient of 9000 cm^{-1}. Subsequent

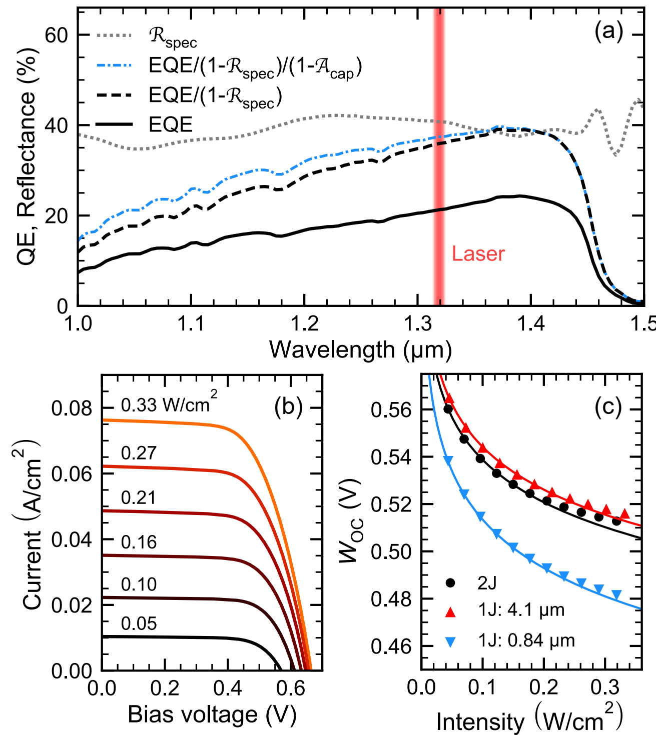

Figure 4.37: (a) Measured EQE and $\mathcal{R}_{spec}$ for the 2-junction PPC. Adjusted QEs account for $\mathcal{R}_{spec}$ and for absorbance in the InGaAs cap ($\mathcal{A}_{cap}$). (b) *J-V* characteristics for the 2-junction PPC under 1319 nm illumination (not current-matched). (c) W_{OC} for 1-junction PPCs and average W_{OC} for the 2-junction PPC. Intensities are adjusted for the 2-junction and 0.84 μm PPCs to account for 4% absorption in the cap. Solid lines show fits done using (1) and (4) for 1- and 2-junction PPCs respectively.

analysis of the single-junction PPCs revealed this was an over-estimate. Future multi-junction devices will be designed using an absorption coefficient of 7143 cm^{-1}.

Measured quantum efficiency and specular reflectance for the two-junction device are shown in Figure 4.37a. In addition to the $\mathcal{R}_{spec}$-adjusted QE, a second adjusted curve is shown that accounts for a small amount of absorption in the InGaAs cap ($\mathcal{A}_{cap}$), which has not been etched. Comparing Figure 4.37a to Figure 4.33, a shift in the absorber bandgap is observed from 0.867 eV to 0.845 eV for the 2-junction device. Analysis of X-ray diffraction spectra and Nomarski images indicate compressive strain and partial relaxation in the epitaxial layers, suggesting that the In composition is slightly higher than expected in the quaternary layers, resulting in the reduced bandgap.

At short wavelengths, most incident light is absorbed in the top subcell and the current is limited by the bottom subcell, leading to a low QE. Moving to longer wavelengths, a larger portion of light is transmitted through the top subcell to the bottom and the QE increases. At the target wavelength of 1319 nm, the top

subcell is still over-producing while the bottom is limiting, resulting in slight current mismatch. The QE is maximized near 1390 nm, where the absorption in each subcell is equal. The adjusted QE of 40% at the peak is less than the ideal 49%, suggesting that minority carrier recombination is impacting carrier collection. This can be explained by the above-target In composition that induces strain and relaxation via generation of misfit and threading dislocations with high density of recombination centers.

J-V measurements for the two-junction device are shown in Figure 4.37b under illumination at 1319 nm, yielding a responsivity $R = 0.231$ A/W. V_{OC} scales with intensity as in [68]:

$$V_{OC} = V_{OC_{ref}} + n_{sum} \frac{k_B T}{q} \ln\left(\frac{I_{light}}{I_{ref}}\right) \tag{4.38}$$

where $I_{ref} = 0.05\ \mathrm{W/cm^2}$ and $V_{OC_{ref}}$ is the V_{OC} when illuminated by I_{ref}. n_{sum} is the sum of the ideality factors for each subcell. Fitting to the V_{OC} values up to an intensity of 0.18 W/cm^2 yields $n_{sum} = 2.04$.

Due to the difference in bandgap, V_{OC} cannot be directly compared for the 1- and 2-junction devices. Instead, we compare the bandgap-voltage offset, $W_{OC} = (E_g/q) - V_{OC}$. For the 2 junction device, we use the average V_{OC} per subcell. The results are plotted in Figure 4.37c as a function of power. W_{OC} for the 2-junction device agrees very well with the 4.1 μm 1 junction device. W_{OC} is smaller for the 0.84 μm device, but still substantial when compared to the theoretical W_{OC} in the radiative limit, which is 0.275 V at 0.1 W/cm^2 for a 1-junction PPC. The large W_{OC} values observed are likely the result of significant non-radiative recombination outside of the depletion regions. Bandgap narrowing due to doping in the active layers may be another contributing factor. Design optimization will bring the V_{OC} closer to the bandgap.

4.2.3 Conclusion

Experimental measurements for 1-junction PPCs operating in the telecom wavelength regime demonstrate V_{OC} up to 0.38 V and ideality factors near 1. A tunnel diode with peak tunneling current near 1000 A/cm^2 is presented, which is fully transparent in the O-band. First results for a fully functioning 2-junction device are shown, with V_{OC} up to 0.66 V. Further optimization of the 2-junction design is underway. This design approach is applicable to higher numbers of junctions for the generation of higher voltages suitable to power electronic devices directly.

4.3 Analysis of loss mechanisms

4.3.1 TCAD Sentaurus simulations

Loss mechanisms for the InAlGaAs O-band PPCs were analyzed by comparing experimental results for the 4.1 μm thick PPC to a comparable device simulated using TCAD Sentaurus. A comparison between the experimental and simulated quantum efficiency curves is shown in Figure 4.38. To achieve agreement in the reflectance spectrum, it was necessary to reduce the thickness of the FSF used in the simulation from the target thickness of 0.4 μm to 0.388 μm. The material parameters used to generate the simulation are given in Section 4.3.2. The one-dimensional nature of the TCAD simulation does not natively account for shading from gridlines. As such, the simulated EQE and reflectance were modified to include perfect reflectivity across 8% of the surface, which agrees with the 8% metal coverage for the experimental PPC sample.

Agreement is found between the simulation and experiment, except for the region near the band edge. This discrepancy is attributed to the complex index of refraction data used for the simulation, which was obtained by spectroscopic ellipsometry and is less reliable close to the band edge (see Section 4.1.2). Agreement between simulation and experiment at the laser wavelength of 1319 nm is very good. Accounting for reflection and transmission losses, recombination processes were found to be responsible for $\sim 4\%$ absolute loss in quantum efficiency for wavelengths ranging from $1.0-1.36$ μm. The losses are shown in Figure 4.39.

In Figure 4.40, simulated $J-V$ curves for the 4.1 μm PPC are compared to one measured experimentally

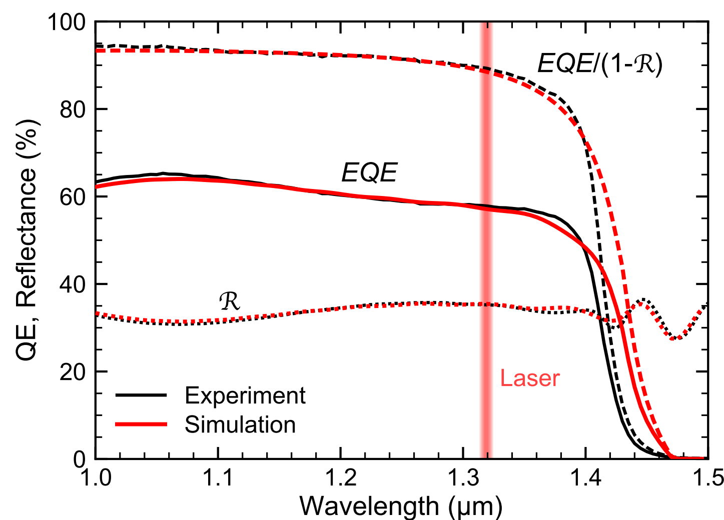

Figure 4.38: Comparison between experimentally measured and simulated QE and reflectivity for the 4.1 μm thick PPC.

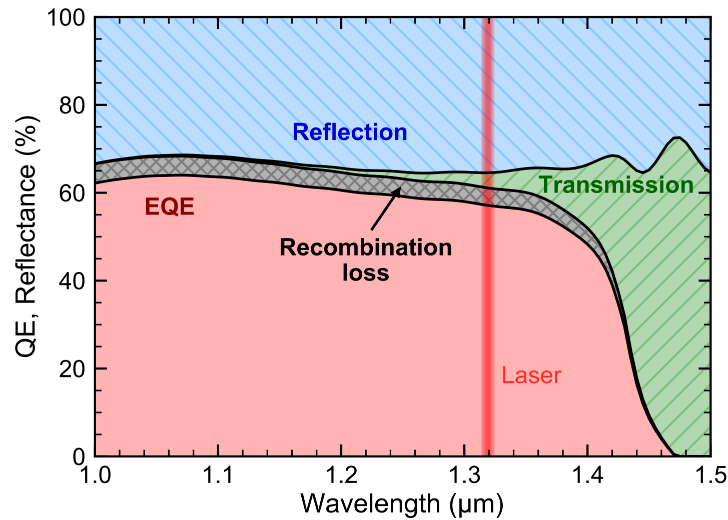

Figure 4.39: Breakdown of simulated EQE and loss mechanisms for the 4.1 µm thick PPC.

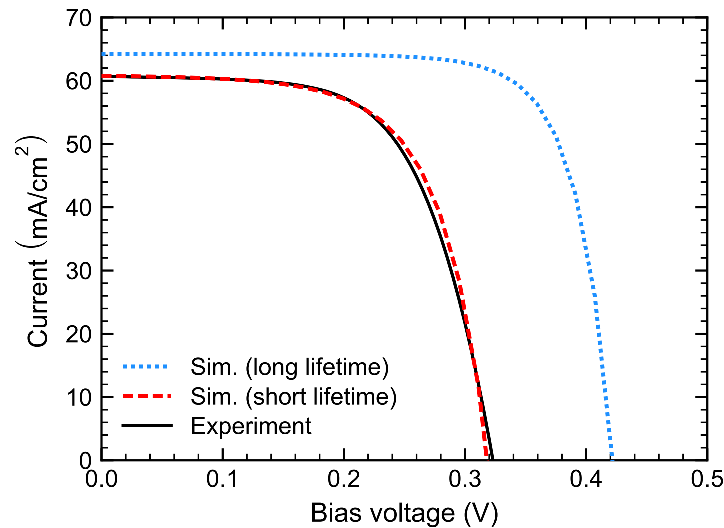

Figure 4.40: Simulated and experimentally measured $J-V$ curves for PPC with 4.1 µm absorber thickness under 1319 nm illumination with an intensity of 100 mW/cm^2.

under 1319 nm laser illumination at an incident power of 100 mW/cm^2. To reproduce the experimental V_{OC} of ~ 0.32 V, it was necessary to include the effects of bandgap narrowing as well as very short SRH lifetimes in the emitter and the base (5×10^{-11} s and 2.5×10^{-9} s). This simulation result corresponds to the "short lifetime" case shown in Figure 4.40. Bandgap narrowing was approximated using the Bennet-Wilson formulation [196]:

$$\Delta E_g(N_a+N_d)=\begin{cases}E_{ref}\left[\ln\left(\frac{N_a+N_d}{N_0}\right)\right]^2 & N\geq N_0\\ 0 & N<N_0\end{cases} \tag{4.39}$$

where E_{ref} and N_0 are empirical fitting parameters. For this simulation, the model was applied to the InAlGaAs material using the parameters $E_{ref} = 4.5$ meV and $N_0 = 10^{15}$ cm^{-3}. These parameters were selected by trial and error in combination with adjustments to the SRH lifetimes in an attempt to recreate the measured data.The bandgap narrowing is show in Figure 4.41 as a function of doping concentration. The simulated bandgap narrowing values corresponding to the emitter and the base are indicated. For comparison, bandgap narrowing trends are shown for n- and p-type GaAs, calculated using the Jain and Roulson model [8]. The simulated values for InAlGaAs are larger than those for both n- and p-type GaAs at doping concentrations $< 10^{19}$ cm^{-3}, suggesting that the quaternary bandgap narrowing is likely overestimated in this simulation.

The short SRH lifetimes of 5×10^{-11} s and 2.5×10^{-9} s for the emitter and the base indicate that non-radiative processes dominate the recombination behaviour and limit the V_{OC} of the PPC devices. This suggests that significant performance improvements may be achievable with improved minority carrier lifetimes in the absorber material. For comparison, the simulation was repeated with longer SRH lifetimes of 1×10^{-8} s for both emitter and base. The result was a significant improvement in the simulated PPC performance with a $\sim 30\%$ increase in the V_{OC}.

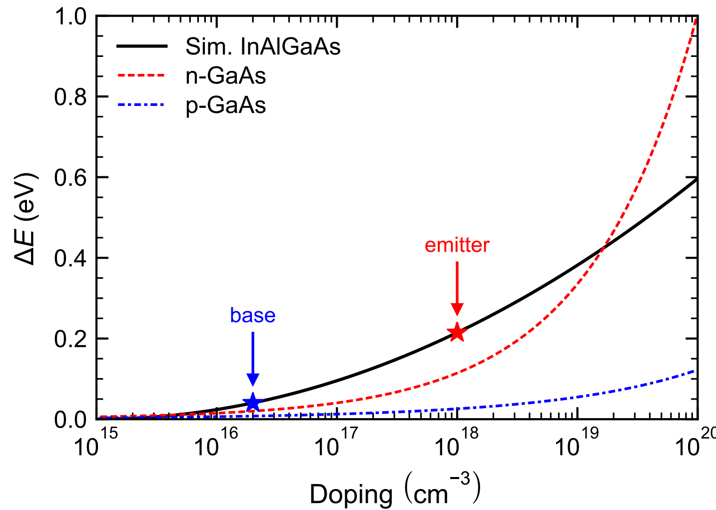

Figure 4.41: Simulated bandgap narrowing as a function of doping concentration for InAlGaAs according to equation 4.39. Values for GaAs are shown for comparison [8].

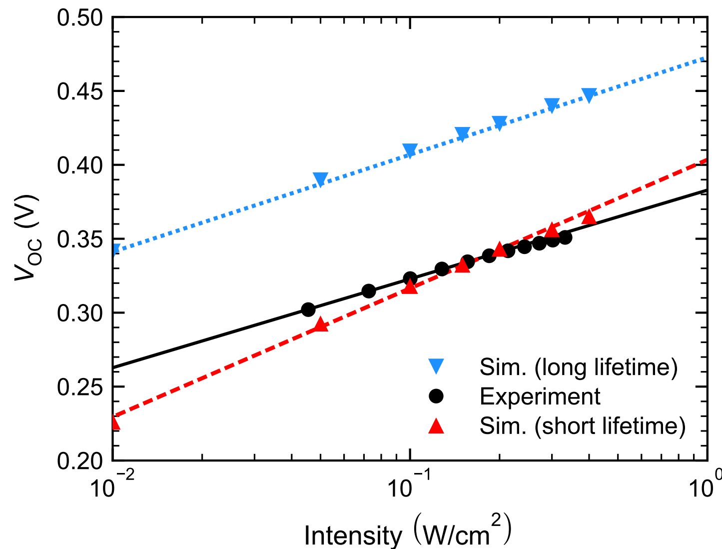

Figure 4.42: Simulated and experimentally measured V_{OC} as a function of input intensity averaged over the entire PPC.

Table 4.12: Figures of merit obtained from fitting V_{OC} for 4.1 μm PPC simulation and experiment.

Source	n_{ideal}	J_0 (A/cm^2)
Experiment	1.02	2.59×10^{-7}
Simulation (short lifetime)	1.47	1.42×10^{-5}
Simulation (long lifetime)	1.11	4.03×10^{-8}

Figure 4.42 shows the simulated and measured V_{OC} as a function of the illumination intensity, averaged over the device area. Table 4.12 lists the parameters extracted by fitting the V_{OC} to equation 4.35. A significantly different trend is observed for simulation and experiment. The ideality factor obtained experimentally is close to 1, signifying that the PPC behaviour is dominated be recombination outside of the space-charge region. In contrast, the ideality factor extracted from the short lifetime simulation results is closer to 1.5, indicating that recombination within the space-charge region is predicted to be more significant. The dark saturation current, J_0, on the other hand, is larger than the experimental value for the short lifetime simulation. For the long lifetime simulation, the ideality factor is closer to 1; however, J_0 is much smaller than the experimental value. From this comparison, it is clear that the simulation does not fully capture the physics

happening within the PPC. Other effects that may be contributing to the device performance include surface recombination, dopant diffusion, and measurement effects including spreading and contact resistance. This should be the object of further study.

4.3.2 Material parameters used for PPC simulations

The material parameters used to generate the InAlGaAs PPC simulations in this thesis are summarized in Tables 4.13 to 4.16.

Table 4.13: Material parameters at 300 K used for InP in PPC simulations. Values for electrons and holes are separated by a comma.

Category	**Parameter**	**Value**	**Ref.**
Permittivity	$\varepsilon_s/\varepsilon_0$	12.5	[161]
Refractive index	n_r, κ	Tabulated	[163, 184]
Band structure	E_g (eV)	1.344	[161]
	χ (eV)	4.38	[161]
	m_c/m_0	0.079	[156]
	m_v/m_0	0.56	[156]
Mobility	μ_{max} $(\mathrm{cm^2/V\,s})$	5200, 170	[62]
	μ_{min} $(\mathrm{cm^2/V\,s})$	400, 10	[62]
	N_0 $(\mathrm{cm^{-3}})$	3.0×10^{17}, 4.97×10^{17}	[62]
	A^*	0.47, 0.62	[62]
Recombination	B_{rad} $(\mathrm{cm^3/s})$	1×10^{-10}	[156]
	τ_{max} (s)	2×10^{-9}, 3×10^{-6}	[161]
	τ_{min} (s)	0, 0	[161]
	N_0 $(\mathrm{cm^{-3}})$	1×10^{15}, 1×10^{14}	[161]
	γ^*	1, 1	[161]
	A_{Aug}	9×10^{-31}, 9×10^{-31}	[161]

Table 4.14: Material parameters used for $In_xGa_{1-x}As$ in PPC simulations. Temperature is 300 K unless otherwise stated. Values apply to $In_{53}Ga_{47}As$ unless binary parameters are given, in which case interpolation is used. Values for electrons and holes are separated by a comma.

Category	**Parameter**	**Value**	**Ref.**
Permittivity	$\varepsilon_s/\varepsilon_0$	13.9	[4]
Refractive index	n_r, κ	Tabulated	[197]
Band structure	$E_{g,0}$ (eV)	InAs: 0.417 GaAs: 1.519	[156] [156]
	$K_{E_{g,0}}$ (eV)	0.477	[156]
	α $\left(\mathrm{eV\,K^{-1}}\right)$	InAs: 2.76×10^{-4} GaAs: 5.405×10^{-4}	[156] [156]
	β (K)	InAs: 93.0 GaAs: 204.0	[156] [156]
	χ (eV)	InAs: 4.9 GaAs: 4.07	[156] [156]
	m_c/m_0	0.041	[4]
	m_v/m_0	0.45	[4]
Mobility	μ_{max} $\left(\mathrm{cm^2/V\,s}\right)$	14000, 320	[62]
	μ_{min} $\left(\mathrm{cm^2/V\,s}\right)$	300, 10	[62]
	N_0 $\left(\mathrm{cm^{-3}}\right)$	1.3×10^{17}, 4.9×10^{17}	[62]
	A^*	0.48, 0.403	[62]
Recombination	B_{rad} $\left(\mathrm{cm^3/s}\right)$	1×10^{-10}	[156]
	τ_{max} (s)	1×10^{-7}, 1×10^{-8}	[158]
	τ_{min} (s)	0, 0	[158]
	N_0 $\left(\mathrm{cm^{-3}}\right)$	1×10^{18}, 1×10^{18}	[158]
	γ^*	1, 1	[158]
	A_{Aug}	7×10^{-29}, 7×10^{-29}	[158]

Table 4.15: Material parameters used for $In_xAl_{1-x}As$ in PPC simulations. Temperature is 300 K unless otherwise stated. Values apply to $In_{52}Al_{48}As$ unless binary parameters are given, in which case interpolation is used. Values for electrons and holes are separated by a comma.

Category	**Parameter**	**Value**	**Ref.**
Permittivity	$\varepsilon_s/\varepsilon_0$	12.3	[5]
Refractive index	n_r, κ	Tabulated	[174]
Band structure	$x \geq 0.37$ (direct): $E_{g,\Gamma}$ (eV)	InAs: 0.359 AlAs: 3.01	[65] [65]
	$x \geq 0.37$ (direct): $K_{E_{g,\Gamma}}$ (eV)	0.720	[65]
	$x < 0.37$ (indirect): $E_{g,X}$ (eV)	InAs: 1.37 AlAs: 2.15	[65] [65]
	$x < 0.37$ (indirect): $K_{E_{g,X}}$ (eV)	0	[65]
	χ (eV)	InAs: 4.9 AlAs: 2.97	[156] [4]
	m_c/m_0	0.071	[65]
	m_v/m_0	0.607	[4]
Mobility	μ_{max} $(\mathrm{cm^2/V\,s})$	1532, 39.8	[181]
	μ_{min} $(\mathrm{cm^2/V\,s})$	0, 0	[181]
	N_0 $(\mathrm{cm^{-3}})$	$9.9\times10^{17}, 1.6\times10^{18}$	[181]
	A^*	0.38, 0.16	[181]
Recombination	B_{rad} $(\mathrm{cm^3/s})$	1×10^{-10}	-
	τ_{max} (s)	1×10^{-8}, 1×10^{-8}	-
	τ_{min} (s)	0, 0	-
	N_0 $(\mathrm{cm^{-3}})$	1×10^{18}, 1×10^{18}	-
	γ^*	1, 1	-
	A_{Aug}	1×10^{-30}, 1×10^{-30}	-

Table 4.16: Material parameters at 300 K used for $(In_{0.52}Al_{0.48})_z(In_{0.53}Ga_{0.47})_{1-z}As$ in PPC simulations. Values for electrons and holes are separated by a comma. Interpolations are between $In_{0.53}Ga_{0.47}As$ and $In_{0.52}Al_{0.48}As$.

Category	**Parameter**	**Value**	**Ref.**
Permittivity	$\varepsilon_s/\varepsilon_0$	Linear interpolation	-
Refractive index	n_r, κ	Experimentally measured	Section 4.1.2
Band structure	E_g (eV)	$z = 0.205$: 0.878 $z = 0.748$: 1.29	Section 4.1.3 Section 4.1.5.2
	E_{ref} (eV)	4.5×10^{-3}	-
	N_0 $\left(cm^{-3}\right)$	1×10^{15}	-
	χ (eV)	$In_{0.53}Ga_{0.47}As$: 4.51 $In_{0.52}Al_{0.48}As$: 3.98	[4] [4]
	m_c/m_0	Linear interpolation	-
	m_v/m_0	Linear interpolation	-
Mobility	$\mu(N)$ $\left(cm^2/V\,s\right)$	Linear interpolation	-
Recombination	B_{rad} $\left(cm^3/s\right)$	1×10^{-10}	-
	τ_{SRH} (s)	Optimistic: 1×10^{-8}, 1×10^{-8} Realistic: 2.5×10^{-9}, 5×10^{-11}	- -
	A_{Aug}	1×10^{-30}, 1×10^{-30}	-

4.4 High current density tunnel diodes

MEGHAN N. BEATTIE, CHRISTOPHER E. VALDIVIA, MATTHEW M. WILKINS, MARZIYEH ZAMIRI, KAYDEN L. C. KALLER, MAN CHUN TAM, HOSUNG KIM, JACOB J. KRICH, ZBIGNIEW R. WASILEWSKI, AND KARIN HINZER

Scope and impact

The following is a reproduction of an article that was published in *Applied Physics Letters* in 2021, with the original title: "High current density tunnel diodes for multi-junction photovoltaic devices on InP substrates" [198]. The publication describes my work developing and characterizing a high-performance tunnel diode for use within a multi-junction InAlGaAs PPC designed for O-band operation. A comprehensive analysis of tunnel diode current-voltage characteristics at a range of positions across the growth substrate is provided. The discussion highlights the advantages of the proposed design, namely a very high tunneling current density, and the associated challenges including acute sensitivity to the MBE growth temperature.

With tunneling current densities exceeding 1200 A/cm^2, the best tunnel diodes presented in our paper have achieved tunneling current densities an order of magnitude higher than what has previously been demonstrated in similar devices [194, 199]. Our work represents an important step forward in the development of InP-based multi-junction photovoltaics for very high illumination intensities in the near-infrared and highlights the importance of minimizing unwanted dopant segregation, illustrating a path toward significant performance improvements through optimization of the growth temperature.

Author contributions

MEGHAN N. BEATTIE As the lead Ph.D. student associated with the project, I spearheaded the research process for this work and performed the vast majority of the experiments and data analysis presented in this paper, excepting the secondary ion mass spectrometry (SIMS), which was performed by EAG Laboratories. I assisted with the design of the tunnel diodes and designed the PPCs. As first author, I wrote the manuscript and prepared all of the figures.

DR. CHRISTOPHER E. VALDIVIA As a senior research scientist within the University of Ottawa's SUNLAB research group, Chris helped to guide my research, provided detailed feedback during data analysis, and assisted in editing the manuscript.

Dr. Matthew M. Wilkins As a postdoctoral fellow within the University of Ottawa's SUNLAB research group, Matt proposed the tunnel diode design and assisted with the PPC designs. He also provided detailed feedback during data collection and analysis.

Dr. Marziyeh Zamiri As a postdoctoral fellow within the University of Ottawa's SUNLAB research group, Marzi developed the in-house fabrication and metallization process that was used to prepare the tunnel diode and PPC devices. Marzi also measured the back contact resistivity.

Kayden L. C. Kaller As a M.Sc. student within the University of Ottawa's SUNLAB research group, Kayden assisted with the in-house fabrication and metallization process that was used to prepare the tunnel diode and PPC devices.

Dr. Man Chun (Alan) Tam As a Ph.D. student within the University of Waterloo's MBE research group, Alan performed the MBE growth for several of the samples discussed in this paper.

Dr. HoSung Kim As a postdoctoral fellow within the University of Waterloo's MBE research group, HoSung performed the MBE growth for several of the samples discussed in this paper.

Prof. Jacob J. Krich As a key collaborative member of the University of Ottawa's SUNLAB research group, Jacob provided detailed feedback during data analysis, and assisted in editing the manuscript.

Prof. Zbigniew Wasilewski As the director of the University of Waterloo's MBE research group, Zbig oversaw the MBE growth of the samples discussed in this paper, provided detailed feedback during data analysis, and assisted in editing the manuscript.

Prof. Karin Hinzer As the director of the University of Ottawa's SUNLAB research group, Karin oversaw my research, provided detailed feedback during data analysis, and assisted in editing the manuscript.

Copyright

This is the Accepted Manuscript version of an article accepted for publication in Applied Physics Letters. Reproduced from:

M. N. Beattie, C. E. Valdivia, M. M. Wilkins, M. Zamiri, K. L. C. Kaller, M. C. Tam, H.S. Kim, J. J. Krich, Z. R. Wasilewski, and K. Hinzer, "High current density tunnel diodes for multi-junction photovoltaic devices on InP substrates," *Applied Physics Letters* **118**(6), 062101, 2021.

DOI: 10.1063/5.0036053

with the permission of AIP Publishing.

Abstract

InAlGaAs tunnel diodes, lattice-matched to InP and grown by molecular beam epitaxy, are demonstrated with peak tunnelling current densities exceeding 1200 A/cm^2. This was achieved by a 20°C reduction in growth temperature for the p-type tunnel diode layers resulting in up to two orders of magnitude improvement in the peak tunneling current density. Secondary ion mass spectrometry measurements reveal that the lower growth temperature reduces unwanted segregation of p-type Be dopants, improving dopant incorporation within the active tunnel diode layers. The diodes are transparent to wavelengths above 1000 nm and are compatible with the bottom junctions of InP-based multi-junction solar cells and with InP-based photonic power converters operating in the telecommunications O- and C-bands. When incorporated into a dual-junction photonic power converter test structure, measurements under 1319-nm laser illumination demonstrate successful tunnel diode operation, enabling a halving of the short-circuit current and doubling of the open-circuit voltage as compared to a single junction reference device.

Main text

Multi-junction (MJ) photovoltaic (PV) devices offer many advantages over single-junction designs, from record-setting efficiencies in MJ solar cells (MJSCs) [200, 201] to high output voltages in MJ photonic power converters (PPCs) [50] that convert monochromatic light from a laser or an LED to electricity (also called optical or laser power converters). MJ PV devices vertically stack multiple epitaxial layers of absorbing series-connected p-n junctions which require interconnection via transparent tunnel diodes (TDs). These TDs must provide high peak tunneling current and low differential resistance without introducing parasitic absorption or impeding current flow between adjacent junctions.

The open-circuit voltage of a PV device is related to the bandgap of the absorbing material. In a MJ device, the total voltage is the sum of the voltages of each absorbing junction. For a typical MJSC, each junction is made from a different material that absorbs a different portion of the solar spectrum [201, 202]. In con-

trast, the absorbing junctions of a MJ PPC are all made from the same material [50, 71]. The PPC operating voltage scales linearly with the number of junctions while the current drops proportionally. Given the series-connection of the MJ design, the same current flows through each junction. To prevent any one junction from limiting current flow through the entire MJ structure, the thickness of each junction can be optimized to absorb an equal number of photons. PPC junctions are grown optically thin to partition monochromatic illumination.

Under concentrated solar illumination or high intensity input from a laser or LED, irradiance of 100 W/cm^2 generates current densities in the tens of A/cm^2 range in both MJSCs and PPCs [201, 203–205]. To operate at such high current densities, TDs must have peak tunneling current densities $\left(J_{pk}\right)$ that are even higher to avoid limitation of the current flow and minimize resistive power losses and reduced voltage output. TDs with J_{pk} on the order of 1000 A/cm^2 are routinely used in PV devices based on Ge and GaAs substrates [203, 205, 206]. TD designs for emerging MJ photovoltaics based on InP substrates are still under development, with an emphasis on arsenide and antimonide semiconductor alloys in the tunneling layers [194, 195, 199, 207–210].

MJSCs based on InP substrates show great promise as a high efficiency alternative to GaAs-based devices due to the availability of lattice-matched materials with ideal bandgaps for a triple-junction structure [195, 201, 211–213]. Several TD designs have been proposed by Lumb et al. for this structure [194, 195, 199, 207]. TDs designed to link the bottom two junctions (bandgaps of 1.18 eV and 0.74 eV respectively) have been demonstrated with J_{pk} exceeding 100 A/cm^2. They are also compatible with MJ PPCs based on InP substrates designed for operation in the telecommunications O- and C-bands (near 1310 nm and 1550 nm respectively) [48, 55, 57, 189].

In this work, we investigate the effect of growth temperature during molecular beam epitaxy (MBE) on the performance of an InAlGaAs TD grown on InP. We demonstrate a 10- to 100-fold improvement in J_{pk} resulting from a 20°C reduction in growth temperature, achieving current densities in excess of 1200 A/cm^2. We also present a dual-junction PPC designed for operation in the telecommunications O-band, showing that the TD can survive the growth of subsequent junctions.

The TDs developed in our experimental work are composed of InAlGaAs lattice-matched to InP, grown by MBE using a Veeco Gen10 system on quarter InP 3”-wafers. An indium-free mounting technique was used. The TDs are designed for full transparency at wavelengths exceeding 1000 nm and for integration between the lower junctions of InP-based MJSCs [195, 199, 201] or into InP-based PPCs operating in the

telecommunications O-band or C-band (demonstrated in this work). The design, shown in Figure 4.43a and adapted from work by Lumb et al. [194, 195], uses a p^{++}/n^{++} junction architecture that enables vertical interconnection of multiple n/p absorbing junctions on a p-type InP substrate. Lattice-matched InAlAs cladding layers on both sides of the TD improve carrier confinement and reduce unwanted dopant diffusion [195]. The TD test structures were grown on n-type InP wafers to maintain the layer growth order in the absence of the absorbing n/p junctions.

The TD structures were grown at different MBE temperatures. For the first device, referred to as HT for “high temperature”, the substrate heater was fixed at 510°C throughout the growth corresponding to

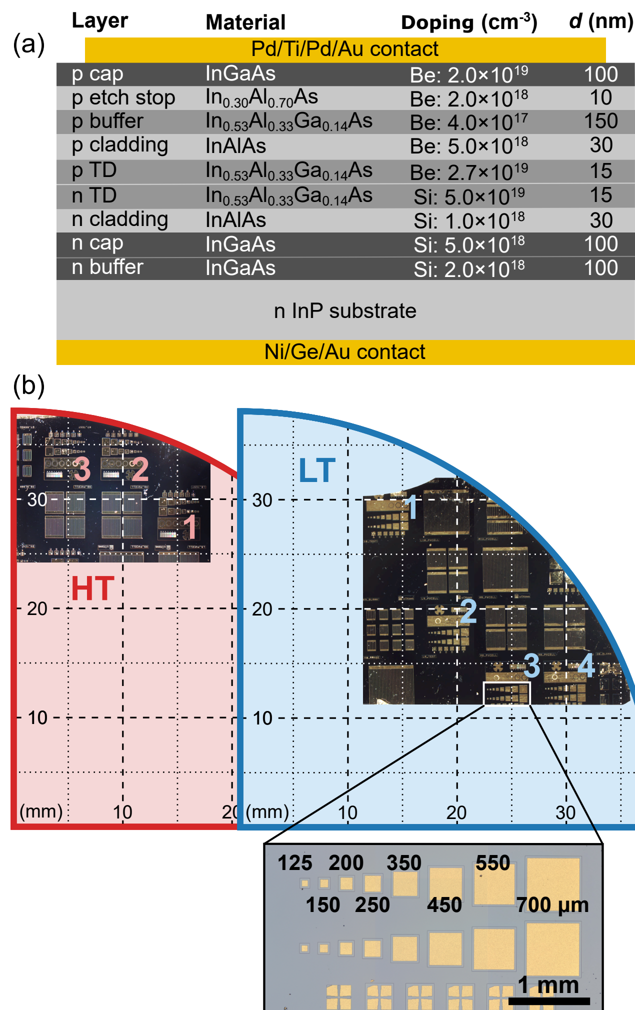

Figure 4.43: (a) TD target structure schematics (d represents the layer thickness). InGaAs and InAlAs layers, except for the etch stop, are lattice-matched to InP. (b) Top view microscope images of tunnel diode samples HT and LT respectively. Relative positions on InP quarter 3”-wafers are shown. The magnified image shows the square diode test pads used for measurements. Side lengths for each diode are given in microns. Note: The orientation of the test pads is upside-down for HT compared to LT.

an estimated substrate temperature between 465°C and 480°C, as measured by pyrometer and band edge thermometry systems, respectively. For the second device, referred to as LT for "low temperature", the substrate heater was initially set to 510°C for the entire n-type region. Before starting growth of the first p-type layer, the substrate heater was ramped down to 490°C and then held constant for the entire p-type region. This corresponded to an estimated substrate temperature between 445°C and 460°C, which was an equivalent 20°C reduction in substrate temperature for the p-type epi-layers in sample LT compared to HT.

Epitaxial wafers were processed with a blanket Ni/Ge/Au contact to the n-InP substrate back surface. On the front p-InGaAs cap, lithography and wet chemical etching were used to fabricate square mesas with Pd/Ti/Pd/Au contact pads set back 25 μm from the mesa edge. Figure 4.43b shows the metallized TD samples and their positions on the quarter 3"-wafer on which they were processed. The side lengths of the square mesas shown in the inset of Figure 4.43b range from 125 to 700 μm. Current-voltage (J-V) characteristics were measured using the four-point probe method, with the sample held in place by vacuum on a gold-plated copper chuck. The top contact pads were probed directly while current at the rear side was conducted through the chuck.

Measured J-V characteristics are shown for several of the TDs in Figure 4.44. The operational region of a typical TD J-V curve is characterized by a quasi-linear relationship between the tunneling current density and voltage passing through the origin, exhibiting a small differential resistance (R_0). At higher voltage, the current density reaches a maximum known as the peak tunneling current density $\left(J_{\text{pk}}\right)$ which limits the highest practical operational intensity. Beyond the peak, the curve enters the negative resistance region where the current density decreases with increasing bias voltage creating a valley before the thermal diffusion current, responsible for conventional diode behaviour, dominates and the current density again increases with bias voltage. The negative resistance region of the graph is typically unresolved in time-averaged experimental measurements such as those in Figure 4.44.

Figure 4.44a shows the J-V characteristics for TDs with a side length of 200 μm on a semi-logarithmic scale. Two curves are shown for each nominal growth temperature, corresponding to J-V measurements performed at different positions on their respective quarter wafers, to show the range of performance for each sample. LT significantly outperforms HT, with J_{pk} 1-2 orders of magnitude larger.

Figure 4.44b and c show the J-V characteristics on a linear scale for the LT-4 and HT-1 diodes. For diode HT-1, J_{pk} consistently increases with increasing diode size, suggesting that edge effects such as perimeter recombination may have an impact on the device performance. A similar effect is observed for LT-4, although

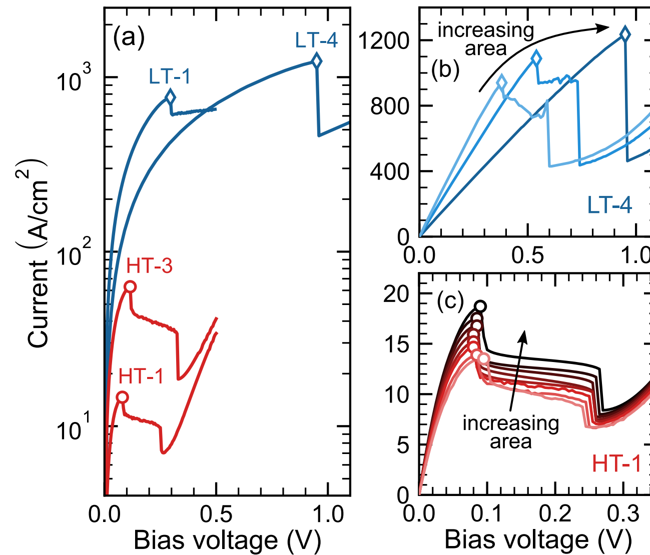

Figure 4.44: (a) TD J-V curves are compared on a semi-logarithmic scale for diodes with a 200 μm side length. The position on the wafer is indicated for each curve. (b), (c) J-V curves on a linear scale for the LT-4 and HT-1 diodes respectively. All diodes shown are from the bottom row. Diodes with side lengths of up to 200 μm are shown for LT-4 in (b) and all sizes are shown for HT-1 in (c). See Figure 4.43b for diode locations. A marker indicates J_{pk} in all sub-figures.

the peak current density is less well resolved due to series resistance effects that impact the shape of the curve [203, 206]. The larger diodes were not measured for sample LT because the high measurement currents exceeded the damage threshold of our fabricated devices.

J_{pk} is shown as a function of diode side length for HT and LT in Figure 4.45a and b, respectively. For sample HT, the diodes closest to the wafer edge have higher J_{pk}, increasing by a factor of 4 from HT-1 to HT-3. Considering the larger J_{pk} for the lower temperature growth, LT, the positional dependence for sample HT indicates a temperature gradient across the wafer during growth, with lower temperature near the substrate edges resulting in higher tunneling currents. A similar trend is observed for LT, with the notable exception of the LT-1 diodes, which have the lowest J_{pk} values despite being closer to the wafer edge than LT-2 and LT-3. This implies that the substrate temperature profile may be influenced by multiple factors [214].

The results in Figure 4.45a and b also confirm that J_{pk} generally increases with diode size. This trend is observed for all of the measured diodes, including HT-1 and HT-2. Mesa edge effects including trap states or fixed charges that counteract tunneling near the perimeter may be impacting the device performance, changing the effective area for current flow through the mesa structure. Another important factor is the spatial variation that results from non-uniform substrate temperature during growth. This positional effect

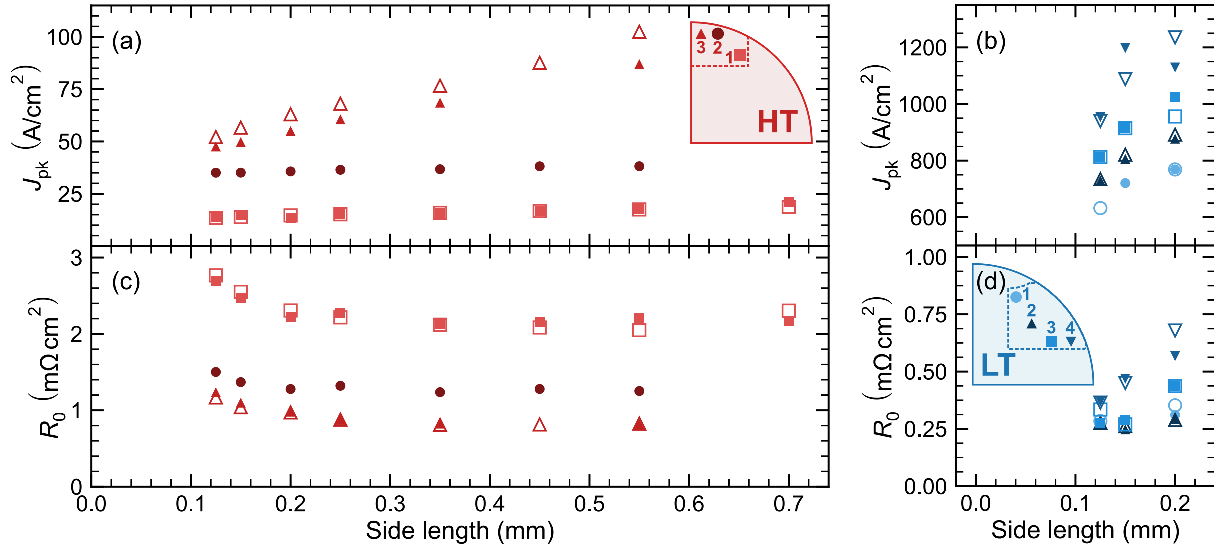

Figure 4.45: (a), (b) J_{pk} as a function of diode side length for HT and LT respectively. (c), (d) differential resistance R_0 as a function of diode side length for HT and LT respectively. The diode positions on each wafer are indicated. Solid symbols correspond to the top row of diodes and open symbols to the bottom row (see Figure 4.43b).

influences the electrical response of diodes along a single row (see Figure 4.43b), likely enhancing the observed increase in current density with diode size due to the spatial orientation of the diodes on each wafer in some cases.

R_0 is shown as a function of diode side length for both samples in Figure 4.45c and d. For sample HT, the resistance ranges from 0.8 to 2.8 mΩ cm^2 and is smallest for the diodes closest to the wafer edge, where we expect that the growth temperature is lower. R_0 is a factor of 4 smaller for sample LT, ranging from 0.2 to 0.7 mΩ cm^2 for all diode sizes and positions.

The top contact resistivity for sample LT was measured as ~ 0.002 mΩ cm^2. For HT, a much larger top contact resistivity of ~ 0.36 mΩ cm^2 was found. Given the 25 µm gap between the contact pad and the mesa edge, the contribution of the top contact to $R_0 = J/V$ is proportional to $L_{mesa}^2/(L_{mesa} - 25\,\mu\text{m})^2$ where L_{mesa} is the mesa side length. We therefore expect a decrease in R_0 with diode size, as observed in Figure 4.45c. R_0 begins to stabilize as the ratio $L_{mesa}^2/(L_{mesa} - 25\,\mu\text{m})^2 \rightarrow 1$. The contribution of the top contact to R_0 is clearly observed for sample HT. For sample LT, the top contact resistivity is small enough that its contribution to R_0 is negligible.

High doping concentrations $\left(> 10^{19}\ \text{cm}^{-3}\right)$ in a thin, abrupt junction are essential characteristics of a high-performance tunnel diode, but this is challenging to achieve due to unwanted dopant diffusion and

segregation during growth. Precise placement of very high Be doping levels can be particularly challenging to achieve [215]. Therefore, secondary ion mass spectrometry (SIMS) was performed on unprocessed wafers by EAG Laboratories using a Dynamic-SIMS PHI ADEPT-1010 system to measure the Si and Be doping profiles through the active layers of the TDs.

Comparisons between the Si and Be doping profiles for HT and LT measured by SIMS are shown in Figure 4.46a. Positions are measured relative to the centre of the TD, with the substrate towards the positive side of the position axis. The target doping profile is indicated by the shaded region and refers to the desired active dopant concentration, whereas SIMS measures the total dopant atomic concentration, both active and inactive. Si incorporation is consistent between the two samples as the substrate heater temperature was 510°C for both samples in the n-doped region. Be, on the other hand, tends to segregate during growth leading to the dopant distributing through subsequent growth layers rather than fully incorporating in the region where it was deposited. The 20°C lower growth temperature reduces the unwanted Be segregation, thereby improving the Be incorporation in the TD layers of the LT sample. The striking difference in Be segregation for the two samples coupled with the observed variability in tunnelling performance between the two samples and across a single substrate highlight the sensitivity of these Be-containing TDs to the growth temperature.

Figure 4.46b applies a linear scale for the doping profiles in the immediate vicinity of the active layers, highlighting the difference in the Be doping concentration within the TD for the two samples. Due to the resolution of the SIMS measurements across the narrow Be peaks, direct comparison of the Be peaks is somewhat uncertain. Per the SIMS measurements, the maximum Be concentrations are $\sim 5 \times 10^{19}$ and $\sim 7 \times 10^{19}$ cm^{-3} for HT and LT, respectively. Integrating the Be concentration within the central p TD and n TD layers yields integrated Be concentrations of $\sim 5.0 \times 10^{13}$ and $\sim 6.7 \times 10^{13}$ cm^{-2} for HT and LT respectively. Higher p-type doping will result in a more abrupt junction with a narrower depletion region, increasing J_{pk}.

To demonstrate the functionality of the LT TDs within a functional device, we compared single- and dual-junction PPCs, the latter of which required one TD to interconnect each absorbing junction. The $In_{0.53}Al_{0.33}Ga_{0.14}As$ absorbing layers with a 0.88 eV bandgap were grown by MBE on p-type InP wafers. The PPCs were designed for monochromatic power conversion from a laser source in the telecommunications O-band. The single-junction PPC has an absorber thickness of 4.1 µm, while the dual-junction PPC consists of a 0.76-µm absorber atop a TD and a 4.1-µm absorber (schematic shown in Figure 4.47a). For the

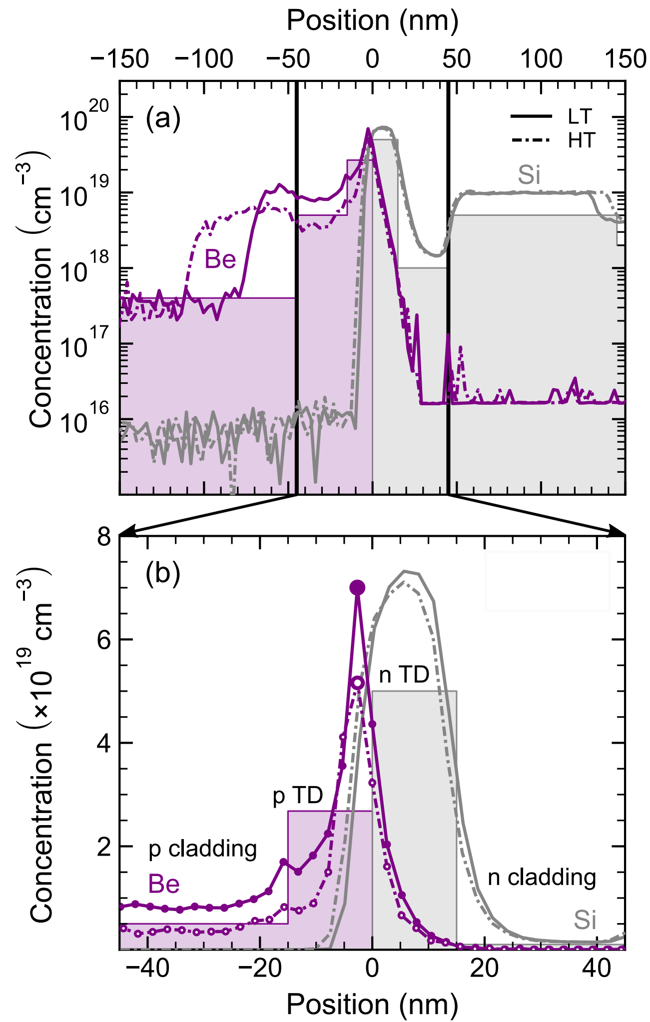

Figure 4.46: SIMS measurements of Be and Si concentrations in HT and LT. Position zero aligns with the centre of the tunnel diode. Doping concentrations are shown on a logarithmic scale across a 300 nm range surrounding the TD in (a), where the active TD and InAlAs cladding region is bounded by the solid black lines. In (b), the central TD region is shown with concentrations on a linear scale. Target doping concentrations are indicated by the shaded regions. Peak Be concentrations are indicated by the large markers in (b).

single-junction PPC, the substrate heater was held at 510°C for the entire growth. For the dual-junction PPC, the heater temperature was ramped down from 510°C to 490°C between the highly doped tunneling layers, as for the LT TDs, and held at the lower temperature for the remainder of the epitaxy.

PPC devices were processed with a blanket Pd/Zn/Pd/Au contact to p-InP on the rear face, followed by rapid thermal annealing at 400°C for 2 minutes to achieve ohmic behaviour. Pd/Ti/Pd/Au contacts were patterned on the top face and wet chemical etching was used to define mesas with dimensions of of 1.65 mm × 1.85 mm. Two 200-μm wide busbars are connected by 6-μm wide gridlines on a 114-μm pitch, resulting

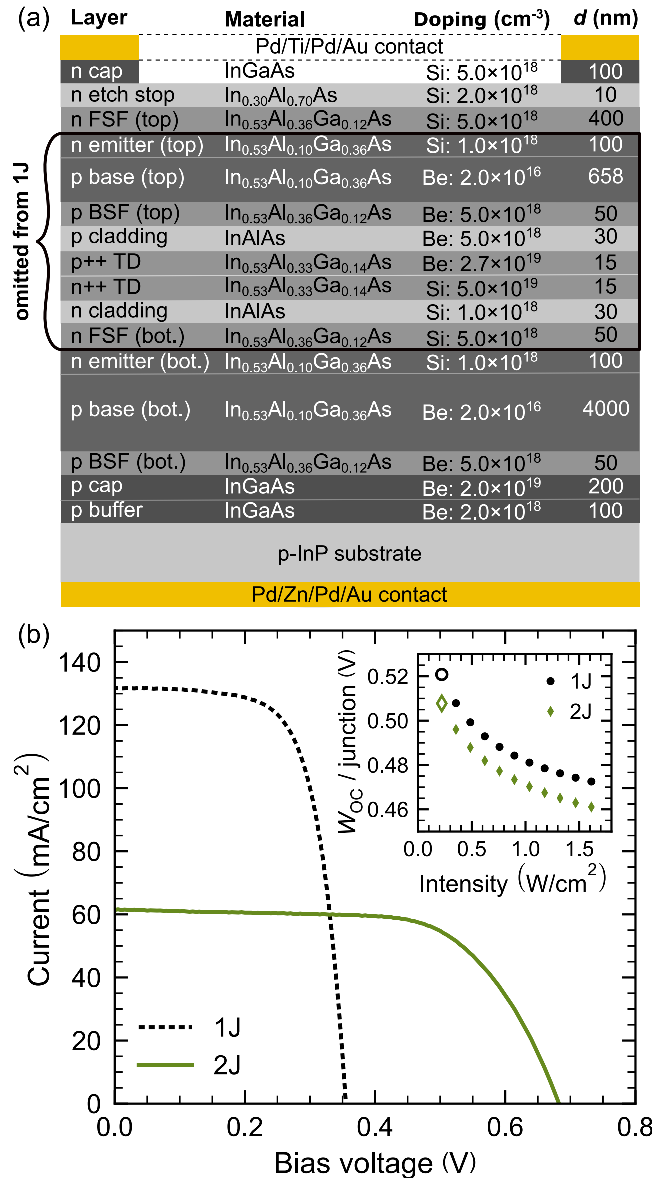

Figure 4.47: (a) PPC target structure schematic (d represents the layer thickness). InGaAs and InAlAs layers, except for the etch stop, are lattice-matched to InP. (b) 1- and 2-junction InAlGaAs operating J-V characteristics under 1319 nm laser illumination at an intensity of 0.22 W/cm^2. The inset shows the average W_{OC} per junction as a function of illumination intensity, up to 1.6 W/cm^2. The open symbols correspond to the J-V curves shown.

in a shading factor of 5%. The metallization is set back by 25 μm from the mesa edge. The n-type InGaAs cap was removed between the contacts using a wet chemical etch.

PPC J-V characteristics were measured under 1319-nm illumination from a Dilas conduction-cooled single bar fiber-coupled laser. Two probes were used to conduct current from the top busbars with the rear-side current being conducted through a gold-plated copper chuck maintained at 25°C using a thermoelectric cooler. The J-V characteristics are shown in Figure 4.47b for both devices measured under monochromatic 1319 nm illumination with an intensity of 0.22 W/cm^2, averaged over the 0.0305 cm^2 mesa area. As expected, the dual-junction V_{OC} is nearly double the single-junction V_{OC} due to the successful series-connection of two junctions, each producing similar voltage. The single-junction device was designed to absorb 95% of the incident light. When current-matched, a dual-junction device should produce close to half the short-circuit current density of the single-junction at the laser wavelength [189].

Due to a slightly In-rich quaternary composition in the dual-junction device, its bandgap energy was red-shifted by ~ 30 meV compared to the perfectly lattice-matched single-junction structure. Therefore, rather than a direct comparison of the V_{OC}, we can instead compare the bandgap-voltage offset, $W_{OC} = (E_g/q) - V_{OC}$, where the bandgap energies (E_g) are 0.88 eV and 0.85 eV for the single- and dual-junction PPCs, respectively. The average W_{OC} per junction is shown as a function of illumination intensity up to 1.6 W/cm^2 in the Figure 4.47b inset. The W_{OC} values are similar for both devices across the intensity range indicating that the TD is providing an effective series connection between the junctions with minimal voltage loss. The W_{OC}/junction is slightly lower for the dual-junction device because the thinner top junction is expected to have a larger V_{OC} compared to the thick bottom junction and the single-junction PPC, as discussed in Ref. [189], due to its higher photo-generated carrier concentration.

In summary, we have developed an InP-based TD composed of lattice-matched InAlGaAs that is transparent for wavelengths >1000 nm. The peak tunneling current density >1200 A/cm^2 makes it suitable for MJ device operation at illumination intensities up to and exceeding 100 W/cm^2. We show a one to two order of magnitude improvement in the peak tunneling current density following a 20°C reduction in nominal growth temperature during Be incorporation due to reduced Be segregation. The results demonstrate that this TD design is viable for use and is a worthwhile platform for further study. Finally, we demonstrate the functionality of the TD embedded in a dual-junction PPC, generating the expected doubling of V_{OC} compared to a single-junction reference device. The sensitivity of the Be-containing tunnel diodes to growth temperature that we observe in this work highlights the importance of keeping tight tolerances for temperature-uniformity

across the wafer during growth to achieve device reproducibility.

Acknowledgements

The authors acknowledge financial support from the Natural Sciences and Engineering Research Council of Canada (NSERC) STPGP 494090-16 research grant, the NSERC Discovery grant RGPIN-05345-2018, the NSERC PGS-D scholarship program, the NSERC CREATE TOP-SET program (award number 497981), the Canadian Foundation for Innovation, the Government of Ontario, and the Optical SatCom Consortium (OSC). The authors would also like to thank Reza Dowlatshahi and Philip Waldron at the National Research Council of Canada for assistance with contact fabrication.

Chapter 5

InGaAsP and GaInAs PPCs for O-band operation

In addition to the quaternary compound InAlGaAs that was discussed in Chapter 4, several alternative material systems exist that are compatible with the development of a PPC for O-band operation around 1310 nm. Two such examples will be discussed in this chapter, namely InGaAsP lattice matched to InP and lattice-mismatched GaInAs grown on GaAs using a metamorphic (MM) compositionally graded buffer.

The bandgaps of the ternary alloys comprising the quaternary InGaAsP are shown as a function of lattice constant in Figure 5.1. Using an InP substrate, lattice-matched InGaAsP can be used to access bandgaps that absorb O-band wavelengths of light. Alternatively, it's possible to design an O-band PPC using a GaAs substrate when lattice-mismatched GaInAs is used for the absorber. Compared to InP, GaAs is less expensive, less brittle, and available in larger wafer sizes [55]. On the other hand, lattice-mismatched materials present considerable challenges for achieving high-quality epitaxial growth.

The PPCs discussed in this chapter were designed and fabricated at the Fraunhofer Institute for Solar Energy Systems (ISE) in Freiburg, Germany. For both designs, the layer structure was grown by metal-organic vapour phase epitaxy (MOVPE) using an Aixtron G4 2800TM reactor. InGaAsP with a bandgap of 0.890 eV was used for the absorber material in the lattice-matched design, grown on a 4" p-type InP substrate. The thickness of the InGaAsP absorber was 2.625 μm. For the lattice-mismatched design, GaInAs with a bandgap of 0.855 eV was used for the absorber, grown on a 4" n-type GaAs substrate using an n-type GaInP-based step-graded metamorphic buffer [20, 55, 69]. The thickness of the GaInAs absorber was 2.8 μm. A

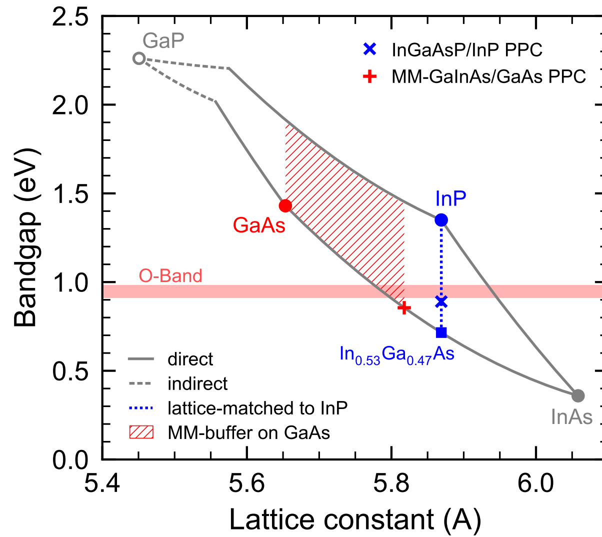

Figure 5.1: Bandgap as a function of lattice constant for ternaries making up InGaAsP. Binary and bowing parameters are taken from [5]. The absorber materials used for the InGaAsP/InP and MM-GaInAs/GaAs PPCs are indicated by the × and + symbols respectively. The O-band is highlighted for reference.

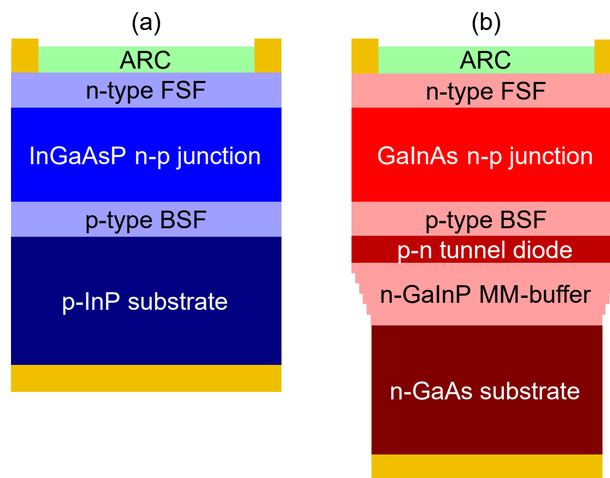

Figure 5.2: Layer schematics for (a) InGaAsP/InP and (b) MM-GaInAs/GaAs PPCs.

tunnel diode (TD) was incorporated beneath the active layers to connect the n-type buffer layers with the p-type base. For both PPCs, the n-p junction that forms the active region of the device was sandwiched between wider-bandgap front and back surface fields. Ohmic contact formation and anti-reflection coating deposition followed epitaxial growth, and wet-chemical mesa etching was used to separate individual PPC devices, each with an active area of 2.2×2.2 mm^2 between the busbars and a nominal designated area of 0.054 cm^2, calculated by subtracting the area of the busbars from the total device area. Schematics of the layer structure are shown in Figure 5.2.

5.1 Quantum efficiency analysis

The quantum efficiencies and reflectivities for the InGaAsP/InP and MM-GaInAs/GaAs PPCs, measured at the University of Ottawa, are shown as a function of wavelength in Figure 5.3. Unlike the InAlGaAs PPCs discussed in Chapter 4, these PPCs were both processed with an anti-reflection coating, reducing the reflectance at the laser wavelength to $< 1\%$.

The absorber bandgap was extracted from the QE measurements using the Tauc method described in Section 4.1.3. The resulting plot is shown in Figure 5.4. The Tauc method, which is derived from the joint density of states for direct-gap transitions, predicts that the absorption coefficient near the band edge varies according to

$$\alpha(E) \approx \beta \frac{\sqrt{E - E_g}}{E} \tag{5.1}$$

for constant β, and requires that $\alpha = 0$ for $E < E_g$.

In real semiconductor materials, phonon-assisted absorption and potential fluctuations caused by randomly distributed dopant atoms and local compositional variations result in sub-gap absorption [3, 67, 216]. This results in the formation of an Urbach tail, with can be described by the relation [3, 66, 67, 216]

$$\alpha(E) = \alpha_{E_g} \exp\left[\frac{s_{\text{Urb.}}}{k_B T}(E - E_g)\right] \tag{5.2}$$

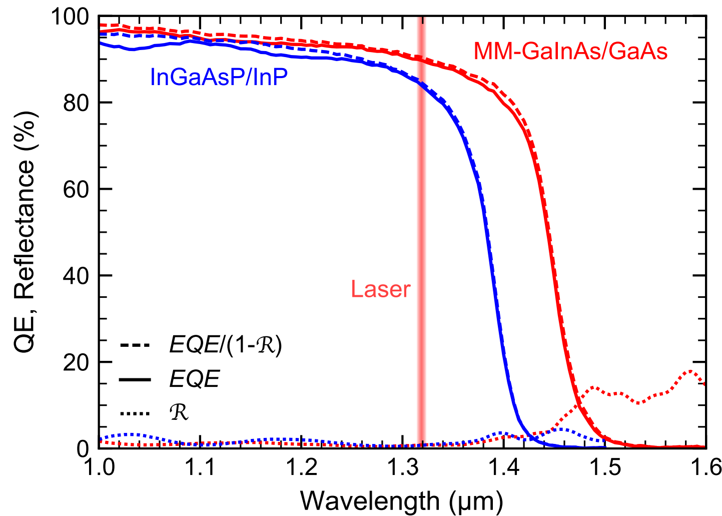

Figure 5.3: EQE, reflectance, and $EQE/(1-\mathcal{R})$ for InGaAsP/InP and MM-GaInAs/GaAs PPCs. The 1319 nm laser wavelength is highlighted for reference.

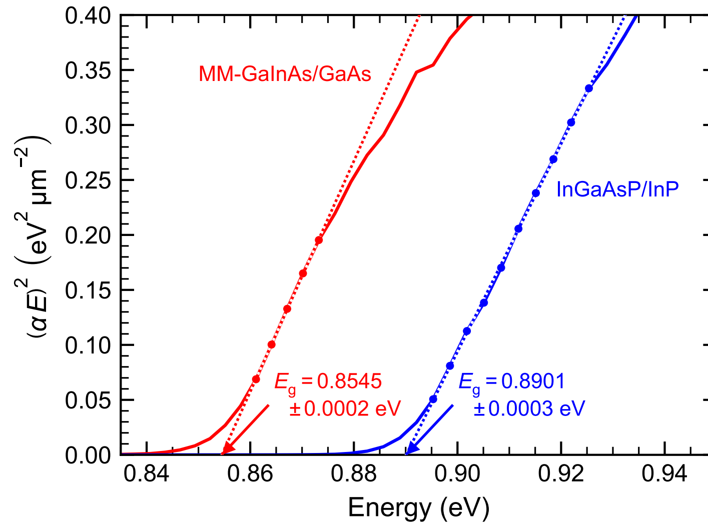

Figure 5.4: Tauc plots for InGaAsP/InP and MM-GaInAs/GaAs PPCs. Each curve is fit to equation 5.1 using the marked data points that display a linear trend. The dashed lines represent the fits and the calculated E_g is indicated for each PPC.

where α_{E_g} is the absorption coefficient at E_g and $s_{Urb.}$ is a dimensionless steepness parameter. At room temperature, $k_BT \sim 25.7$ meV. When $s_{Urb.} \sim 1$, the sub-gap absorption behaviour is primarily driven by phonon interactions. Values of $s_{Urb.} > 1$ signify the importance of impurity and alloy effects [67].

Figure 5.5 shows the absorption coefficient as a function of photon energy for the two PPCs with fits to equations 5.1 and 5.2. The value for E_g obtained using the Tauc plot method is used in equation 5.2 to fit the Urbach tail. Fitting parameters for both regions are given in Table 5.1 as well as the energy corresponding the the point of closest approach between the two fits (E_{CA}), which corresponds to the energy below which the Urbach tail dominates the absorption behaviour.

Several alternative methods have been proposed in the literature to determine the bandgap from quantum efficiency measurements. In 2013, Helmers et al. proposed a strategy that defines the bandgap as the energy at which the QE transitions from exponential growth in the Urbach tail region to saturation near unity [9]. This technique relies on the assumptions that $QE \propto \alpha$ near the band edge and that $QE \rightarrow 1$ for $E > E_g$, which holds true for devices that have thick enough absorber layers to absorb most of the incident light and that are not diffusion-limited. Fits are performed on the QE within the Urbach tail and within the saturation regime to the equation

$$QE(E) = ae^{bE} \tag{5.3}$$

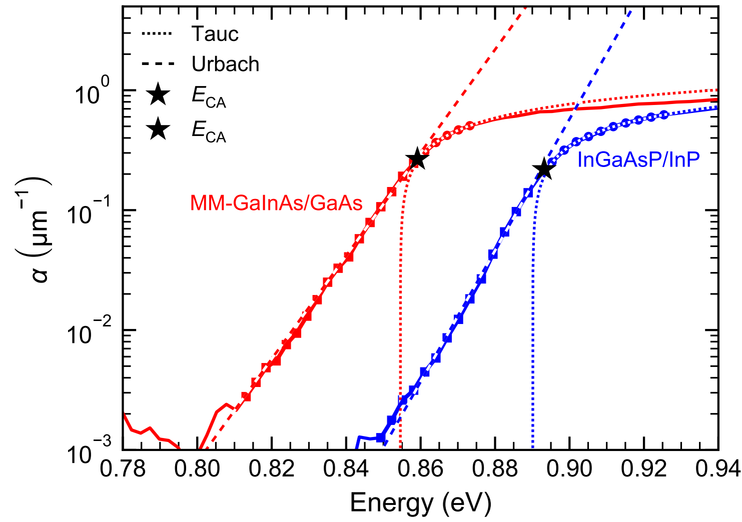

Figure 5.5: Absorption coefficient as a function of energy for InGaAsP/InP and MM-GaInAs/GaAs PPCs. Fits to equation 5.1 (Tauc) and equation 5.2 (Urbach) are shown as well as the point of closest approach between the fits (E_{CA}).

Table 5.1: Tauc and Urbach fitting parameters for InGaAsP/InP and MM-GaInAs/GaAs PPCs.

PPC	**Tauc**		**Urbach**		E_{CA} **(eV)**
	E_g **(eV)**	$\beta\ (\mu m^{-1})$	$\alpha_{E_g}\ (\mu m^{-1})$	$s_{\text{Urb.}}$	
InGaAsP/InP	0.890	3.08	0.165	3.24	0.893
MM-GaInAs/GaAs	0.855	3.24	0.097	2.54	0.859

where a and b are fitting parameters. The bandgap is taken to be the intersection between the two exponential fits. The procedure is shown in Figure 5.6 along with the resultant bandgap values for the two PPCs.

In 2017, Rau et al. proposed a detailed-balance-based approach that allows the bandgap to be determined from the derivative of the quantum efficiency graph [10]. They define the photovoltaic bandgap to be the mean peak energy at the band edge for the QE derivative $QE'(E)$, defined according to

$$E_g = \frac{\int_{E_1}^{E_2} E \times QE'(E)\, dE}{\int_{E_1}^{E_2} QE'(E)\, dE} \tag{5.4}$$

where E_1 and E_2 correspond to the upper and lower energy bounds between which $QE'(E) \geq \max[QE'(E)]/2$. Rau et al. emphasize that their proposed approach "aims at a consistent analysis of losses for a solar cell entirely from its external properties," rather than "internal semiconductor properties" [10]. The EQE and its

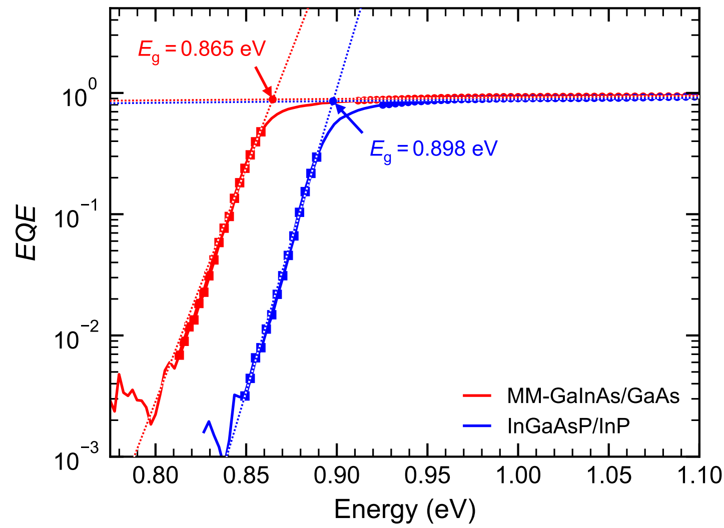

Figure 5.6: Fitting procedure to extract E_g for InGaAsP/InP and MM-GaInAs/GaAs PPCs according the method proposed by Helmers et al. [9]. Fits to equation 5.3 are represented by the dashed lines. The resultant value of E_g is indicated for each PPC.

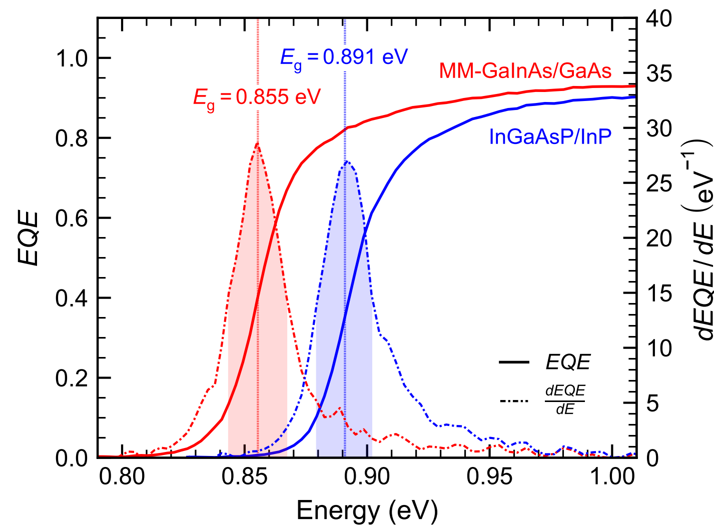

Figure 5.7: Procedure to extract E_g for InGaAsP/InP and MM-GaInAs/GaAs PPCs according the method proposed by Rau et al. [10]. The EQE is shown as a function of energy near the band edge along with its derivative. The integration region for which $QE'(E) \geq \max[QE'(E)]/2$ is shaded and the resultant value of E_g is indicated for each PPC.

Table 5.2: Bandgaps obtained using Tauc, Helmers, and Rau methods for InGaAsP/InP and MM-GaInAs/GaAs PPCs.

PPC	**Tauc E_g (eV)**	**Helmers E_g (eV)**	**Rau E_g (eV)**
InGaAsP/InP	0.890	0.898	0.891
MM-GaInAs/GaAs	0.855	0.865	0.855

derivative is shown in Figure 5.7 for both PPCs along with the bandgaps calculated from equation 5.4.

A summary of the bandgaps calculated using each of the methods described above is given in Table 5.2. Given that each method relies on different physical phenomena, it is expected that the resultant bandgap values will vary to a certain extent [10]. We see that the values obtained using the Tauc and Rau methods are very similar, which isn't unexpected for direct-gap semiconductors [10]. Those obtained using the Helmers method are larger by $\sim$ 10 meV. For the remainder of this thesis, the bandgap will be defined according to the values obtained using the Tauc method.

5.2 Current-voltage characteristics and beam size dependence

Current-voltage characteristics for the PPCs were measured under 1319 nm laser illumination at a variety of incident powers and laser spot sizes. An example of the laser beam profile overlaid on a PPC cell is shown in Figure 5.8a and b with the $1/e^2$ beam diameter ($2w$) and the diameter containing 99% of the incident light ($2w_{99}$) indicated. The beam diameters corresponding to $I-V$ measurements presented in this section are listed in Figure 5.8c along with the peak-to-average ratios (PAR), which is a measure of the beam uniformity. PAR is used as a means to quantify the spatial uniformity of the beam on the PPC device. The beam profile depends on the configuration of the system and can be adjusted through beam shaping techniques [188]. A perfectly uniform illumination profile will have a PAR of 1 whereas increasing PAR signifies declining uniformity. A photograph of the red pointer laser illuminating a PPC sample is shown in Figure 5.8d.

The short-circuit current is shown as a function of incident laser power in Figure 5.9a for the InGaAsP/InP and MM-GaInAs/GaAs PPCs, measured using a $1/e^2$ beam diameter of $2w$ = 1.3 mm. For this beam size, > 99% of the laser power is contained within the active area of the PPC ($2w_{99}$ = 2.1 mm). The responsivity

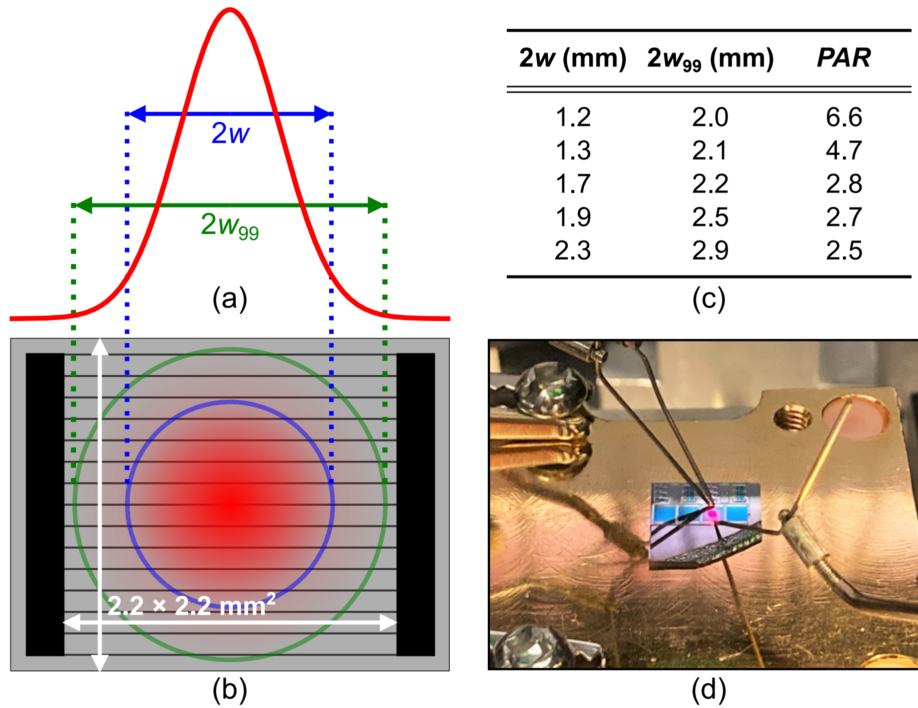

2w (mm)	2w99 (mm)	PAR
1.2	2.0	6.6
1.3	2.1	4.7
1.7	2.2	2.8
1.9	2.5	2.7
2.3	2.9	2.5

Figure 5.8: (a) Sample beam profile with $2w$ = 1.3 mm. (b) Schematic showing beam profile overlaid on PPC chip with diameters $2w$ and $2w_{99}$ indicated. (c) Relevant beam diameters and peak-to-average ratios (PAR). (d) Photograph of pointer laser illuminating PPC chip.

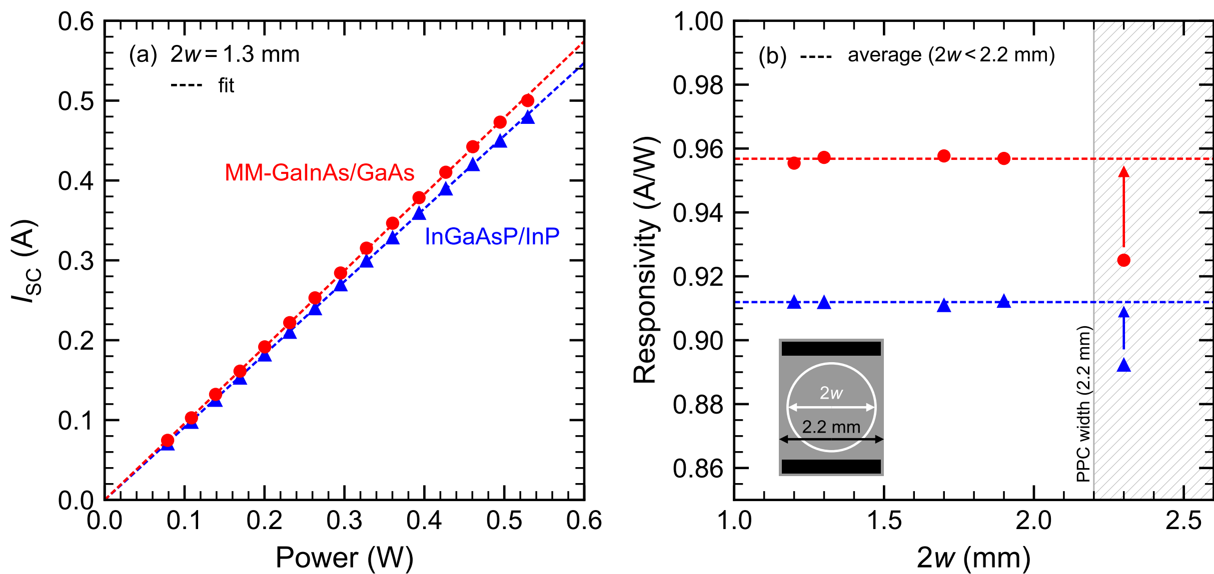

Figure 5.9: (a) I_{SC} as a function of incident 1319 nm laser power for InGaAsP/InP and MM-GaInAs/GaAs PPCs measured with a $1/e^2$ beam size of $2w$ = 1.3 mm. Dashed lines are linear fits to equation 5.5. (b) Responsivity as a function of $1/e^2$ beam size. The PPC width (2.2 mm) is indicated and the hatched region shows where the $1/e^2$ beam size will begin to spill over the PPC edges. The dashed lines indicate the average responsivity, calculated for $2w < 2.2$ mm. Arrows indicate the required correction for $2w$ = 2.3 mm.

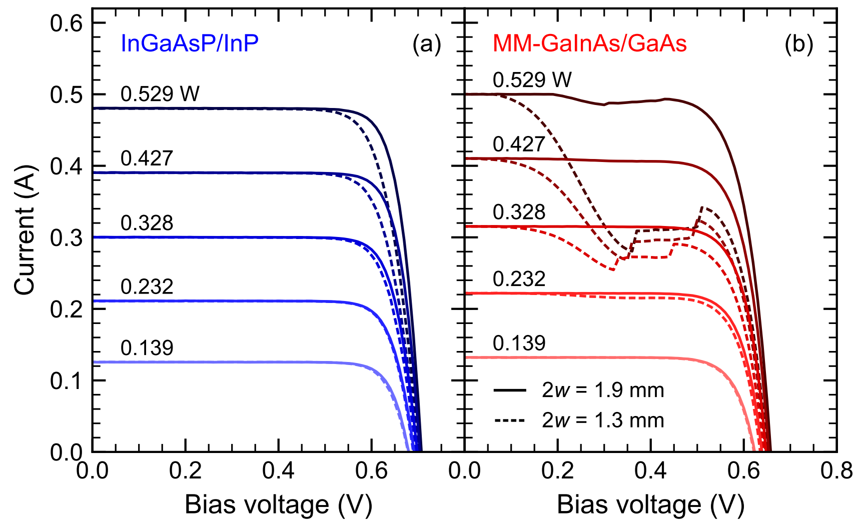

Figure 5.10: $I-V$ characteristics measured at various incident powers under 1319 nm laser illumination for (a) InGaAsP/InP and (b) MM-GaInAs/GaAs PPCs. Curves are shown for $1/e^2$ beam diameters of 1.9 and 1.3 mm. The incident power is given in W for each curve.

(R) is extracted from the data in Figure 5.9a by fitting to the equation

$$I_{SC}(P) = R \times P \tag{5.5}$$

where P is the laser power. The extracted responsivities, shown as a function of $2w$ in Figure 5.9b, deviate from each other by < 3 mA/W except for the value at $2w = 2.3$ mm, where $2w$ exceeds the width of the PPC active area. In this case, there is sufficient spillover of the laser light to impact the measured short-circuit current, and by extension the calculated responsivity. To correct for the spillover, a correction factor is applied to the effective incident power for the $2w = 2.3$ mm case going forward such that its responsivity is equal to the average responsivity calculated from the values with $2w < 2.2$ mm. The calculated averages are 0.912 and 0.957 A/W respectively for the InGaAsP/InP and MM-GaInAs/GaAs PPCs. Note that the devices have identical contact configurations.

Current-voltage characteristics for the two PPCs are shown in Figure 5.10 measured with $1/e^2$ beam diameters of $2w = 1.9$ mm and $2w = 1.3$ mm for a variety of incident laser powers ranging up to 0.529 W. For the lattice-matched InGaAsP-InP PPC (Figure 5.10a), a reduction in the fill factor is observed when the spot size is reduced from 1.9 mm to 1.3 mm. This effect becomes more significant with increasing incident power. The impact of the spot size on the shape of the $I-V$ curve is more pronounced for the lattice-mismatched

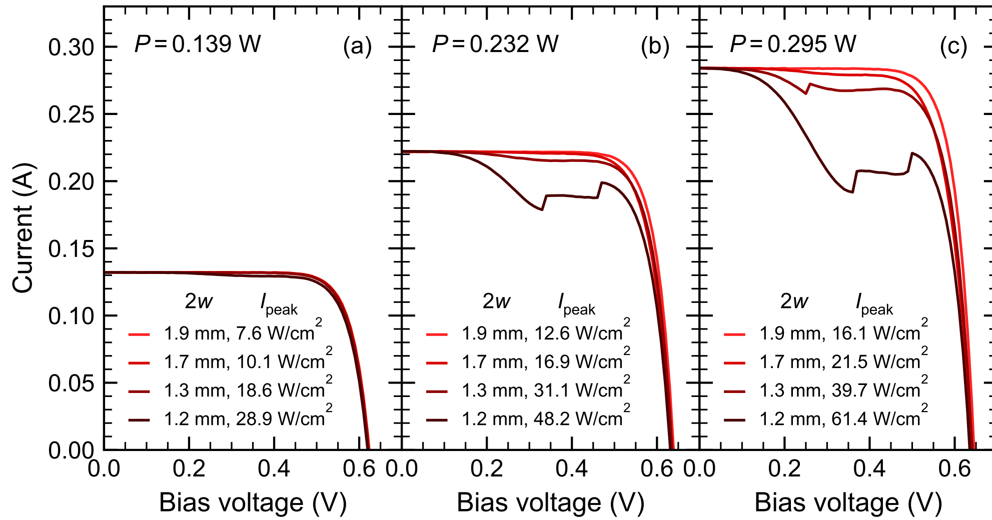

Figure 5.11: $I-V$ characteristics measured at incident powers of (a) 0.169 W, (b) 0.232 W, and (c) 0.295 W under 1319 nm laser illumination for the MM-GaInAs/GaAs PPC. Curves are shown for $1/e^2$ beam diameters from 1.2 to 1.9 mm. The peak irradiance at the centre of the illumination profile is indicated for each curve.

MM-GaInAs/GaAs PPC. A dip in the total current is observed for bias voltages > 0.1 V at higher incident powers, an effect that is much more significant for the smaller spot size. This effect occurs when the local current density exceeds the peak tunneling current density of the tunnel diode embedded beneath the active layers of the PPC. When this happens, the electrical transport mechanism within the tunnel diode switches from tunneling to thermal diffusion, which is associated with a much larger resistance [217–220].

The influence of the illumination profile on the tunnel diode is shown more clearly in Figure 5.11, where $I-V$ curves are shown for spot sizes ranging from 1.2 to 1.9 mm at three different incident powers. As the spot size decreases, the peak-to-average ratio associated with the illumination profile increases, meaning that the peak irradiance $\left(I_{\text{peak}}\right)$ also increases for the same total power (P). The values for I_{peak} are shown for each curve in Figure 5.11, calculated according to the expression

$$I_{\text{peak}} = \frac{PAR}{\pi w_{99}^2}(0.99P) \tag{5.6}$$

Table 5.3 lists the maximum incident power and corresponding peak irradiance that were measured for each spot size before the tunnel diode's peak tunneling current density was exceeded. This maximum value was defined as the largest incident power for which the difference between the short-circuit current and the current measured at $V = 0.3$ V was < 0.5%. In general, the current started to drop when $I_{\text{peak}} \gtrsim$

Table 5.3: Maximum illumination power and irradiance before TD peak tunneling current density was exceeded for MM-GaInAs/GaAs PPC.

$2w$ (mm)	PAR	$P_{\mathrm{max,TD}}$ (W)	$I_{\mathrm{peak,max,TD}}$ $(\mathrm{A/cm^2})$
1.2	6.6	0.109	22.6
1.3	4.7	0.139	18.6
1.7	2.8	0.232	16.9
1.9	2.7	0.360	19.6
2.3	2.5	-	-

20 $\mathrm{W/cm^2}$, indicating that the tunnel diode switched from tunneling to thermal diffusion near this irradiance. Some variation was observed due to the changes in the shape of the illumination profile for each spot size. The PPC's tolerance for non-uniform illumination profiles could be improved through optimization of the tunnel diode design to increase its peak tunneling current density. Improved lateral conductivity within the device could also improve the tolerance by reducing the local current density at the centre of the beam [217, 219]. This could be achieved by adjusting doping concentrations within the device or by introducing lateral conduction layers above and below the tunnel diode to spread the current.

The bandgap-voltage offset $\left(W_{\mathrm{OC}} = E_{\mathrm{g}}/q - V_{\mathrm{OC}}\right)$ is plotted in Figure 5.12 as a function of the short-circuit current density, using bandgap values calculated with the Tauc method. Data sets are shown for all beam sizes and fits are performed for data with $I_{\mathrm{SC}} < 0.1$ A using the non-ideal diode equation:

$$V_{\mathrm{OC}}\left(I_{\mathrm{SC}}\right) = \frac{n_{\mathrm{ideal}} k_{\mathrm{B}} T}{q} \ln\left(\frac{I_{\mathrm{SC}}}{I_0} + 1\right) \tag{5.7}$$

where T = 298 K. Associated fitting parameters are given in Table 5.4. The InGaAsP/InP PPC exhibits behaviour that is very close to ideal, with an average ideality factor of 1.03. The corresponding average dark saturation current is 8.9×10^{-13} A. Using the nominal sample area of 0.054 $\mathrm{cm^2}$, this corresponds to a dark saturation current density of 1.7×10^{-11} $\mathrm{A/cm^2}$. Less ideal behaviour is observed for the MM-GaInAs/GaAs PPC, with an average ideality factor of 1.34. The average dark saturation current is 1.8×10^{-9} A, or nominally 3.3×10^{-8} $\mathrm{A/cm^2}$, more than three orders of magnitude larger than the lattice-matched device, indicating that non-radiative recombination processes are significant for the metamorphic PPC.

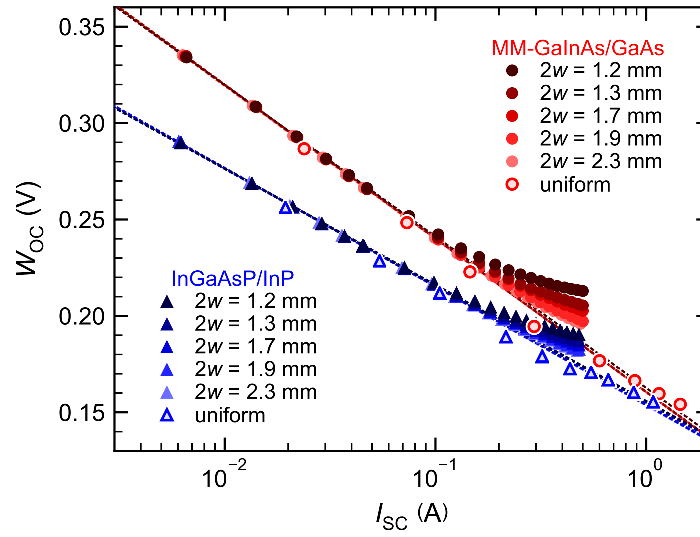

Figure 5.12: Bandgap-voltage offset as a function of short-circuit current density for InGaAsP/InP and MM-GaInAs/GaAs PPCs measured under various illumination profiles. The $1/e^2$ beam diameters are indicated for each data set measured under 1319 laser light. The uniform illumination data was measured under the AM1.5d solar spectrum. Dashed lines are fits to equation 5.7.

Table 5.4: Non-ideal diode equation parameters from fits to equation 5.7.

	InGaAsP/InP		**MM-GaInAs/GaAs**	
2w (mm)	n_{ideal}	I_0 **(A)**	n_{ideal}	I_0 **(A)**
1.2	1.02	6.66×10^{-13}	1.33	1.53×10^{-9}
1.3	1.02	7.23×10^{-13}	1.35	1.89×10^{-9}
1.7	1.04	1.05×10^{-12}	1.35	1.99×10^{-9}
1.9	1.04	9.52×10^{-13}	1.34	1.84×10^{-9}
2.3	1.04	1.06×10^{-12}	1.34	1.79×10^{-9}
Average	**1.03**	$\mathbf{8.9\times10^{-13}}$	**1.34**	$\mathbf{1.8\times10^{-9}}$

For reference, data measured at Fraunhofer ISE under uniform AM1.5d illumination is included in Figure 5.12, measured for the same lattice-matched InGaAsP/InP chip and for a substantially similar MM-GaInAs/GaAs chip. The uniform illumination data tends to follow the logarithmic trends, whereas values for W_{OC} measured under non-uniform laser illumination begin to deviate from the trend for short-circuit currents > 0.1 A. The amount of deviation increases with decreasing spot size as the beam profile becomes less uniform, which increases the PAR.

This trend is shown clearly in Figure 5.13, where the reduction in V_{OC} relative to the expected value at 298 K from the non-ideal diode equation is plotted for increasing beam size at an incident power of 0.232 W. As the beam uniformity improves, the reduction in V_{OC} declines.

There are two physical processes responsible for the observed reduction in V_{OC} induced by non-uniform illumination. First, despite the appearance from equation 5.7, V_{OC} decreases linearly with increasing temperature as the temperature-dependent parameter I_0 increases [221, 222]. As such, localized heating in the PPC devices, which becomes more significant with increasing non-uniformity in the illumination, causes a reduction in the V_{OC}.

The second mechanism responsible for the reduced V_{OC} under non-uniform illumination relates to series resistance within the PPC. Although there is no external current flow under open-circuit conditions, lateral current flow from regions of high irradiance to those of lower irradiance can cause a voltage drop at open-circuit, reducing the V_{OC} [223, 224]. Given that series resistance losses scale with current, this effect is more significant for larger incident laser power and PAR. In Figure 5.13, we see that the MM-GaInAs/GaAs

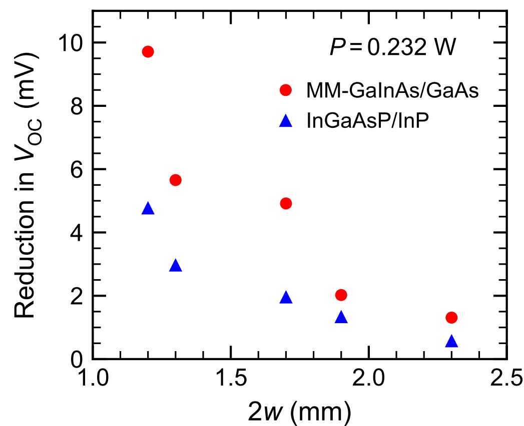

Figure 5.13: Reduction in the V_{OC} relative to expected logarithmic trend as a function of $2w$ for InGaAsP/InP and MM-GaInAs/GaAs PPCs. Incident illumination power is 0.232 W,

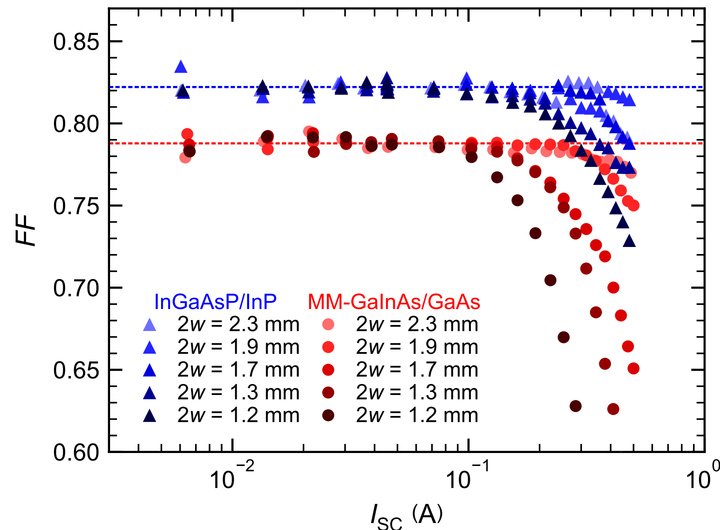

Figure 5.14: Fill-factor as a function of short-circuit current density for InGaAsP/InP and MM-GaInAs/GaAs PPCs measured under various illumination profiles. The $1/e^2$ beam diameters are indicated for each data set. Dashed lines indicate the average fill-factor calculated for $I_{SC} < 0.1$ A.

PPC is more sensitive to the spot size than the lattice-matched InGaAsP/InP PPC, with a larger reduction in V_{OC}. This suggests that the metamorphic sample has a higher series resistance than the lattice-matched device, with correspondingly larger resistive losses. Improved lateral conductivity within the PV device could significantly mitigate the voltage loss [224].

The fill-factor is plotted as a function of short-circuit current in Figure 5.14. Its value is relatively constant for $I_{SC} < 0.1$ A, with average values of 0.822 and 0.788 for the InGaAsP/InP and MM-GaInAs/GaAs PPCs respectively. At higher currents, the fill factor begins to drop off. The combined effects of localized heating within the device and series resistance losses are responsible, with larger reductions observed for the smaller, less uniform spot sizes. The roll-off is much more pronounced for the metamorphic PPC for which the performance is limited by the embedded tunnel diode.

The efficiency is plotted as a function of incident 1319 nm laser power in Figure 5.15 for all $1/e^2$ beam sizes. The maximum efficiency for the InGaAsP/InP PPC was 52.9%, measured at $P = 0.353$ W. For the MM-GaInAs/GaAs PPC, the maximum was 48.8%, measured at $P = 0.413$ W. For both PPCs, the maximum efficiency was obtained with the largest beam size of $2w = 2.3$ mm.

The reported trends indicate that better efficiencies could be obtained under laser illumination by engineering a more uniform illumination profile across the active device area. Further performance improvements could be realized through enhanced lateral conductivities, which could potentially be achieved through the

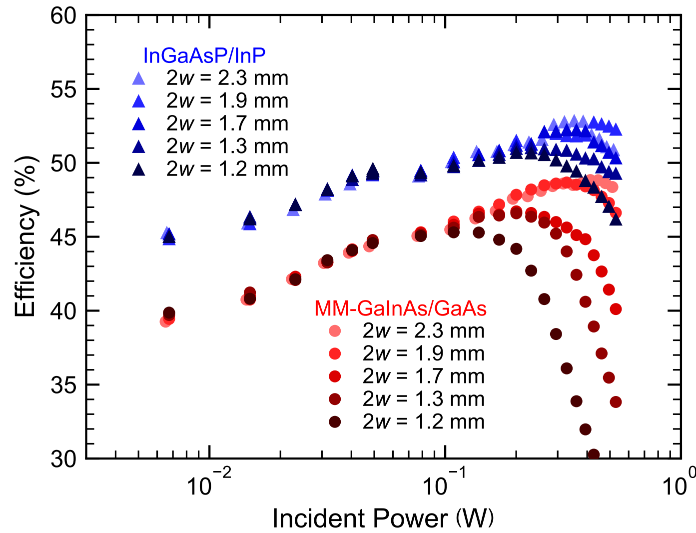

Figure 5.15: Efficiency as a function of incident 1319 nm laser power for InGaAsP/InP and MM-GaInAs/GaAs PPCs measured under various illumination profiles. The $1/e^2$ beam diameters are indicated for each data set.

inclusion of lateral conduction layers [217]. Finally, the adoption of a multi-junction architecture for the PPC devices described in this chapter would reduce the current flow through the device, enhancing the output voltage while diminishing the impact of series-resistance losses and improving the device tolerance for non-uniform illumination at higher input powers.

Chapter 6

Summary and outlook

Advanced photovoltaic devices including high-efficiency multi-junction solar cells and photonic power converters have considerable potential to supply energy in remote locations and extreme environments. For multi-junction solar cells, a key barrier to widespread implementation is the high cost and limited production capacity for state-of-the-art high devices. In the case of photonic power converters, which are suited to more niche power transmission applications, one key area for improvement is the practical transmission distance over optical fiber. The work presented in this thesis moves toward addressing the above issues through the exploration of innovative semiconductor materials and device design.

Chapter 3 investigated the possibility of growing high-performance MJSCs on silicon substrates using a voided Ge/Si compliant interface layer to accommodate the lattice-mismatch, which could reduce the threading dislocation density within the devices from 10^8 cm^{-2} for native GaAs on silicon to 10^4 cm^{-2}. Integration of MJSCs on silicon would reduce the cost associated with the substrate material and help to scale up production volume by using larger substrates and by making use of the silicon-PV supply chain. To predict the impact of the compliant interface on MJSC performance, the conductivity of mesoporous germanium was measured experimentally and found to vary between 0.6 and 33 $\left(\times 10^{-3}\right)$ $\Omega^{-1}\,\text{cm}^{-1}$ depending on the thermal annealing temperature and associated morphology. An electrostatic model was developed to relate the carrier concentrations and mobility in the porous material to its nanostructure, predicting electrical conductivity that could be tuned over four orders of magnitude.

Applying the electrostatic model to the relevant morphologies voided germanium and silicon layers, it was estimated that the compliant interface would add $\sim 0.01\ \Omega\,\text{cm}^2$ to the total series resistance of a lattice-mismatched III-V triple-junction solar cell on a silicon substrate. This additional resistance is small enough

to be suitable for concentrated illumination. Optoelectronic modeling revealed that triple-junction solar cells grown on voided Ge/Si compliant interfaces with a threading dislocation density of 10^4 cm^{-2} could achieve 93% of the efficiency of comparable defect-free devices. Given that the majority of the losses were predicted to come from the Ge subcell, alternative designs neglecting the Ge subcell could improve the performance. It's also possible that the theoretical model used to predict the influence of threading dislocations on the minority carrier lifetimes is overestimating the impact on Ge. Further experimental investigation of the impacts of threading dislocations on various semiconductor materials should be undertaken.

The sensitivity of the voided morphology to elevated temperatures presents a potential challenge for the realization of III-V epitaxy on these substrates, given that epitaxial processes usually involve temperatures exceeding 400ºC. Differences in thermal expansion coefficients between Ge and Si could pose an additional challenge. As such, the integration of III-V PV devices on Si substrates using voided Ge and Si materials is the subject of ongoing work at the Université de Sherbrooke.

Chapters 4 and 5 investigated PPCs optimized for O-band operation that will enable photonic power transmission over extended distances through optical fiber, up to several kilometres. Three potential material systems were explored in this thesis to access the O-band: lattice-matched InAlGaAs and InGaAsP on InP substrates and lattice-mismatched GaInAs grown on GaAs using a metamorphic buffer layer.

Chapter 4 explored the design and characterization of lattice-matched InAlGaAs/InP PPCs grown by molecular beam epitaxy. Quaternary materials with various compositions were analyzed and an alloy with a bandgap of $\sim$ 0.88 eV was selected for the O-band device. Single- and dual-junction devices were measured under 1319-nm laser illumination with an intensity of 0.33 W/cm^2 and found to have output voltages of 0.38 V and 0.66 V respectively. Devices were found to have relatively large bandgap-voltage offsets of $\sim$ 0.5 V/junction, indicating that non-radiative recombination was limiting the output voltage. The open-circuit voltage of a thinner PPC with 0.84 μm absorber thickness was observed to be $\sim$ 30 mV larger compared to a single-junction PPC with an absorber thickness of 4.1 μm, suggesting that thinner devices are less impacted by non-radiative recombination.

The PPC output voltages may be improved by increasing the minority carrier lifetimes through the optimization of molecular beam epitaxy growth conditions. From a design perspective, the adoption of ultra-thin device architectures employing textured back reflectors to increase the effective optical path length could reduce the impact of diffusion limiting by reducing layer thicknesses without sacrificing the amount of absorption.

Measurements of InAlGaAs tunnel diode $J-V$ characteristics revealed the sensitivity of tunnel diode performance to the MBE growth temperature, brought about by unwanted segregation of the Be dopants. A 20°C reduction in the growth temperature caused up to two order of magnitude improvement in the peak tunneling current. The best tunneling current exceeded 1200 $\mathrm{A/cm^2}$, which would be more than sufficient for operation within a multi-junction PPC under high irradiance $\left(\text{up to } 100\ \mathrm{W/cm^2}\right)$. Considerable variation in tunnel diode performance across a single wafer demonstrated the importance of minimizing temperature fluctuations across the wafer during growth. Optimization of the growth conditions could potentially result in further improvements to the tunneling current densities. Additionally, transitioning from Be doping to a less-mobile p-type dopant such as carbon may reduce unwanted dopant segregation and improve the performance variations induced by temperature non-uniformities across a single substrate.

Chapter 5 studied the performance of InGaAsP/InP and MM-GaInAs/GaAs PPCs grown by MOVPE, which is a more commercially viable epitaxial process compared to research-focussed MBE. Fabricated using well-established methods developed for high-concentration photovoltaic cells in the state-of-the-art clean room facilities at Fraunhofer ISE, these devices were well suited to investigating the impact of non-uniform illumination profiles at higher 1319-nm laser irradiance (exceeding 10 $\mathrm{W/cm^2}$ over the nominal device area). The detrimental impact of non-uniform illumination on the performance became apparent at a short-circuit current density of ~ 0.1 A for both devices. The impact was most significant for the MM-GaInAs/GaAs device when the device current exceeded the peak tunneling current of the buried tunnel diode at peak illumination intensities of $\sim 20\ \mathrm{W/cm^2}$. Illumination with a flat top laser beam, which can be achieved through beam-shaping, would produce the best performance at high illumination powers compared to more standard super-Gaussian beams. Distributed circuit modelling would be a particularly useful next step to develop a more detailed understanding of the impacts of non-uniform illumination profiles, lateral current flow, and series resistance throughout the devices.

Overall peak efficiencies were measured to be 52.9% and 48.8% respectively for the InGaAsP/InP and MM-GaInAs/GaAs PPCs. Performance enhancements could be achieved in three ways. These are by improving the uniformity of the illumination profile, by increasing lateral conductivities within the device to distribute current more evenly, or by adopting a multi-junction architecture that would reduce the total current flowing through the device and associated series resistance losses. Considering that the peak efficiency of the lattice-mismatched MM-GaInAs/GaAs PPC fell only $\sim 4\%$ short of the lattice-matched device, it represents an attractive lower-cost alternative. Further cost reductions could potentially be achieved for this PPC by

replacing the GaAs substrate with silicon using a voided Ge/Si compliant interface, although the significant number of fabrication steps involved with integrating both the voided Ge/Si interface and the MM graded buffer may reduce the cost-benefits associated with the less expensive substrate.

Further research into the design of PPCs for extended-reach power-over-fiber systems will involve transitioning to operation in the telecommunications C-band near 1550 nm, where attenuation in optical fiber is minimized. 1550 nm is also considered to be "eye-safe," meaning that C-band PPCs could also be used for free-space power transmission.

Bibliography

[1] National Renewable Energy Laboratory (NREL), "Reference air mass 1.5 spectra", url: https://www.nrel.gov/grid/solar-resource/spectra-am1.5.html.

[2] M. N. Beattie and K. Hinzer, "Extending the reach of photonic power", *Compound Semiconductor*, **25**(7), 56–63, 2019, url: https://compoundsemiconductor.net/article/108934/Extending_The_Reach_Of_Photonic_Power/feature.

[3] E. F. Schubert, *Light-Emitting Diodes*, Cambridge University Press, Cambridge, 2nd edition, 2006.

[4] Ioffe Institute, "NSM Archive: Physical properties of semiconductors", url: http://www.ioffe.ru/SVA/NSM/Semicond/.

[5] S. Adachi, "III-V Ternary and Quaternary Compounds", in S. Kasap and P. Capper (eds.), *Springer Handbook of Electronic and Photonic Materials*, chapter 30, 725–741, Springer International Publishing, 2017.

[6] M. N. Beattie, Y. A. Bioud, D. G. Hobson, A. Boucherif, C. E. Valdivia, D. Drouin, R. Arès, and K. Hinzer, "Tunable conductivity in mesoporous germanium", *Nanotechnology*, **29**, 215701, 2018, doi:10.1088/1361-6528/aab3f7.

[7] T. Dittrich, K. Kliefoth, I. Sieber, J. Rappich, S. Rauscher, and V. Y. Timoshenko, "Electronic properties of thin Au/nanoporous-Si/n-Si structures", *Thin Solid Films*, **276**(1-2), 183–186, 1996, doi:10.1016/0040-6090(95)08087-2.

[8] S. C. Jain and D. J. Roulston, "A simple expression for band gap narrowing (BGN) in heavily doped Si, Ge, GaAs and Ge_xSi_{1-x} strained layers", *Solid State Electronics*, **34**(5), 453–465, 1991, doi:10.1016/0038-1101(91)90149-S.

[9] H. Helmers, C. Karcher, and A. W. Bett, "Bandgap determination based on electrical quantum efficiency", *Applied Physics Letters*, **103**(3), 032108, 2013, doi:10.1063/1.4816079.

[10] U. Rau, B. Blank, T. C. Müller, and T. Kirchartz, "Efficiency potential of photovoltaic materials and devices unveiled by detailed-balance analysis", *Physical Review Applied*, **7**(4), 044016, 2017, doi:10.1103/PhysRevApplied.7.044016.

[11] G. L. Araújo and A. Martí, "Absolute limiting efficiencies for photovoltaic energy conversion", *Solar Energy Materials and Solar Cells*, **33**(2), 213–240, 1994, doi:10.1016/0927-0248(94)90209-7.

[12] J. Nelson, *The Physics of Solar Cells*, Imperial College Press, London, 2003.

[13] J. F. Geisz, R. M. France, K. L. Schulte, M. A. Steiner, A. G. Norman, H. L. Guthrey, M. R. Young, T. Song, and T. Moriarty, "Six-junction III–V solar cells with 47.1% conversion efficiency under 143 Suns concentration", *Nature Energy*, **5**(4), 326–335, 2020, doi:10.1038/s41560-020-0598-5.

[14] M. A. Green, "Limiting photovoltaic monochromatic light conversion efficiency", *Progress in Photovoltaics: Research and Applications*, **9**(4), 257–261, 2001, doi:10.1002/pip.375.

[15] S. Fafard, M. C. A. York, F. Proulx, C. E. Valdivia, M. M. Wilkins, R. Arès, V. Aimez, K. Hinzer, and D. P. Masson, "Ultrahigh efficiencies in vertical epitaxial heterostructure architectures", *Applied Physics Letters*, **108**(7), 071101, 2016, doi:10.1063/1.4941240.

[16] M. A. Green, E. D. Dunlop, J. Hohl-Ebinger, M. Yoshita, N. Kopidakis, and X. Hao, "Solar cell efficiency tables (version 56)", *Progress in Photovoltaics: Research and Applications*, **28**(7), 629–638, 2020, doi:10.1002/pip.3303.

[17] K. Yamamoto, K. Yoshikawa, H. Uzu, and D. Adachi, "High-efficiency heterojunction crystalline Si solar cells", *Japanese Journal of Applied Physics*, **57**(8), 08RB20, 2018, doi:10.7567/JJAP.57.08RB20.

[18] S. Philipps and W. Warmuth, "Photovoltaics Report", Technical report, Fraunhofer ISE, 2020, url: https://www.ise.fraunhofer.de/conte%0Ant/dam/ise/de/documents/publications/studies/Photovoltaics-Report.pdf.

[19] K. A. W. Horowitz, T. Remo, B. Smith, and A. Ptak, "A techno-economic analysis and cost reduction roadmap for III-V solar cells", Technical Report NREL/TP-6A20-72103, National Renewable Energy Laboratory, 2018.

[20] R. M. France, F. Dimroth, T. J. Grassman, and R. R. King, "Metamorphic epitaxy for multijunction solar cells", *MRS Bulletin*, **41**(3), 202–209, 2016, doi:10.1557/mrs.2016.25.

[21] B. Kunert, Y. Mols, M. Baryshniskova, N. Waldron, A. Schulze, and R. Langer, "How to control defect formation in monolithic III/V hetero-epitaxy on (100) Si? A critical review on current approaches", *Semiconductor Science and Technology*, **33**(9), 093002, 2018, doi:10.1088/1361-6641/aad655.

[22] S. A. Ringel, J. A. Carlin, C. L. Andre, M. K. Hudait, M. Gonzalez, D. M. Wilt, E. B. Clark, P. Jenkins, D. Scheiman, A. Allerman, E. A. Fitzgerald, and C. W. Leitz, "Single-junction InGaP/GaAs solar cells grown on Si substrates with SiGe buffer layers", *Progress in Photovoltaics: Research and Applications*, **10**(6), 417–426, 2002, doi:10.1002/pip.448.

[23] Y. B. Bolkhovityanov and O. Pchelyakov, "GaAs epitaxy on Si substrates: modern status of research and engineering", *Physics - Uspekhi*, **51**(5), 437 – 456, 2008, doi:10.1070/PU2008v051n05ABEH006529.

[24] M. E. Groenert, C. W. Leitz, A. J. Pitera, V. Yang, H. Lee, R. J. Ram, and E. A. Fitzgerald, "Monolithic integration of room-temperature cw GaAs/AlGaAs lasers on Si substrates via relaxed graded GeSi buffer layers", *Journal of Applied Physics*, **93**(1), 362–367, 2003, doi:10.1063/1.1525865.

[25] R. M. Sieg, J. A. Carlin, J. J. Boeckl, S. A. Ringel, M. T. Currie, S. M. Ting, T. A. Langdo, G. Taraschi, E. A. Fitzgerald, and B. M. Keyes, "High minority-carrier lifetimes in GaAs grown on low-defect-density Ge/GeSi/Si substrates", *Applied Physics Letters*, **73**(21), 3111–3113, 1998, doi:10.1063/1.122689.

[26] M. Yamaguchi, M. Tachikawa, Y. Itoh, M. Sugo, and S. Kondo, "Thermal annealing effects of defect reduction in GaAs on Si substrates", *Journal of Applied Physics*, **68**(9), 4518–4522, 1990, doi:10.1063/1.346156.

[27] Y. Yamamoto, G. Kozlowski, P. Zaumseil, and B. Tillack, "Low threading dislocation Ge on Si by combining deposition and etching", *Thin Solid Films*, **520**(8), 3216–3221, 2012, doi:10.1016/j.tsf.2011.10.095.

[28] Y. S. Chang, S. Naritsuka, and T. Nishinaga, "Optimization of growth condition for wide dislocation-free GaAs on Si substrate by microchannel epitaxy", *Journal of Crystal Growth*, **192**(1-2), 18–22, 1998, doi:10.1016/S0022-0248(98)00407-2.

[29] J. Z. Li, J. Bai, J. S. Park, B. Adekore, K. Fox, M. Carroll, A. Lochtefeld, and Z. Shellenbarger, "Defect reduction of GaAs epitaxy on Si (001) using selective aspect ratio trapping", *Applied Physics Letters*, **91**(2), 021114, 2007, doi:10.1063/1.2756165.

[30] J. S. Park, J. Bai, M. Curtin, B. Adekore, M. Carroll, and A. Lochtefeld, "Defect reduction of selective Ge epitaxy in trenches on Si(001) substrates using aspect ratio trapping", *Applied Physics Letters*, **90**(5), 052113, 2007, doi:10.1063/1.2435603.

[31] C. V. Falub, H. Von Känel, F. Isa, R. Bergamaschini, A. Marzegalli, D. Chrastina, G. Isella, E. Müller, P. Niedermann, and L. Miglio, "Scaling hetero-epitaxy from layers to three-dimensional crystals", *Science*, **335**(6074), 1330–1334, 2012, doi:10.1126/science.1217666.

[32] Y. A. Bioud, A. Boucherif, M. Myronov, A. Soltani, G. Patriarche, N. Braidy, M. Jellite, D. Drouin, and R. Arès, "Uprooting defects to enable high-performance III–V optoelectronic devices on silicon", *Nature Communications*, **10**, 4322, 2019, doi:10.1038/s41467-019-12353-9.

[33] S. Tutashkonko, A. Boucherif, T. Nychyporuk, A. Kaminski-Cachopo, R. Arès, M. Lemiti, and V. Aimez, "Mesoporous germanium formed by bipolar electrochemical etching", *Electrochimica Acta*, **88**, 256–262, 2013, doi:10.1016/j.electacta.2012.10.031.

[34] Y. A. Bioud, A. Boucherif, A. Belarouci, E. Paradis, S. Fafard, V. Aimez, D. Drouin, and R. Arès, "Fast growth synthesis of mesoporous germanium films by high frequency bipolar electrochemical etching", *Electrochimica Acta*, **232**, 422–430, 2017, doi:10.1016/j.electacta.2017.02.115.

[35] M. Röger, G. Böttger, M. Dreschmann, C. Klamouris, M. Huebner, A. W. Bett, J. Becker, W. Freude, and J. Leuthold, "Optically powered networks", *Optics Express*, **16**(26), 21821–21834, 2008, doi:10.1364/fio.2008.jwc2.

[36] H. Helmers, C. Armbruster, M. Von Ravenstein, D. Derix, and C. Schoner, "6-W optical power link with integrated optical data transmission", *IEEE Transactions on Power Electronics*, **35**(8), 7904–7909, 2020, doi:10.1109/TPEL.2020.2967475.

[37] A. Basanskaya, "Electricity over glass", *IEEE Spectrum*, **42**(10), 18, 2005.

[38] A. Andersson, D. Destefan, J. D. Ramboz, S. Weiss, and J. M. DeHaan, "Unique EHV current probe for calibration and monitoring", in *2001 IEEE/PES Transmission and Distribution Conference and Exposition: Developing New Perspectives*, 379–384, Atlanta, GA, USA, 2001, doi:10.1109/TDC.2001.971264.

[39] F. V. De Nazaré and M. M. Werneck, "Development of a monitoring system to improve ampacity in 138kV transmission lines using photonic technology", in *2010 IEEE PES Transmission and Distribution Conference and Exposition: Smart Solutions for a Changing World*, 1–6, New Orleans, LA, USA, 2010, doi:10.1109/TDC.2010.5484461.

[40] J.-G. Werthen and M. Cohen, "The power of light: photonic power innovations in medical, energy and wireless applications", *Photonics Specta*, 2006, url: https://www.photonics.com/Articles/The_Power_of_Light_Photonic_Power_Innovations_in/p5/vo20/i129/a25278.

[41] L. Wagner, A. W. Bett, and H. Helmers, "On the alignment tolerance of photovoltaic laser power converters", *Optik*, **131**, 287–291, 2017, doi:10.1016/j.ijleo.2016.11.072.

[42] R. Rieske, S. Sohr, K. Nieweglowski, and K. J. Wolter, "Assembly tolerance requirements for photonics packaging of multi-cell laser power converters", in *2012 4th Electronic System-Integration Technology Conference (ESTC)*, 1–6, Amsterdam, Netherlands, 2012, doi:10.1109/ESTC.2012.6542174.

[43] H. Helmers, L. Wagner, C. E. Garza, S. K. Reichmuth, E. Oliva, S. P. Philipps, D. Lackner, and A. W. Bett, "Photovoltaic cells with increased voltage output for optical power supply of sensor electronics", in *SENSOR 2015 - 17th International Conference on Sensors and Measurement Technology*, 519–524, 2015, doi:10.5162/sensor2015/D1.4.

[44] Azur Space, "Products Optoelectronics", url: http://www.azurspace.com/index.php/en/products/products-optoelectronics.

[45] V. P. Khvostikov, N. A. Kalyuzhnyy, S. A. Mintairov, S. V. Sorokina, N. S. Potapovich, V. M. Emelyanov, N. K. Timoshina, and V. M. Andreev, "Photovoltaic laser-power converter based on AlGaAs/GaAs heterostructures", *Semiconductors*, **50**(9), 1220–1224, 2016, doi:10.1134/S1063782616090128.

[46] Spectrolab, "Sensors: Infrared sensor products for power conversion and detection", url: https://www.spectrolab.com/sensors.html.

[47] A. L. Fahrenbruch, A. Lopez-aero, J. G. Werthen, and T.-c. Wu, "GaAs- and InAlGaAs-based concentrator-type cells for conversion of power transmitted by optical fibers", in *1196 IEEE 25th Photovoltaics Specialists Conference (PVSC)*, 117–120, Washington, DC, USA, 1996, doi:10.1109/PVSC.1996.563961.

[48] S. Wojtczuk, "Long-wavelength laser power converters for optical fibers", in *1997 IEEE 26th Photovoltaic Specialists Conference (PVSC)*, 971–974, Anaheim, CA, 1997, doi:10.1109/pvsc.1997.654250.

[49] V. Andreev, V. Khvostikov, V. Kalinovsky, V. Lantratov, V. Grilikhes, V. Rumyantsev, M. Shvarts, V. Fokanov, and A. Pavlov, "High current density GaAs and GaSb photovoltaic cells for laser power beaming", in *3rd World Conference onPhotovoltaic Energy Conversion*, 761–764, Osaka, Japan, 2003.

[50] S. Fafard, F. Proulx, M. C. York, L. S. Richard, P. O. Provost, R. Arès, V. Aimez, and D. P. Masson, "High-photovoltage GaAs vertical epitaxial monolithic heterostructures with 20 thin p/n junctions and a conversion efficiency of 60%", *Applied Physics Letters*, **109**(13), 131107, 2016, doi:10.1063/1.4964120.

[51] MH GoPower, "MIH VMJ PV cell", url: http://www.mhgopower.com/cell_description.html.

[52] V. P. Khvostikov, S. V. Sorokina, N. S. Potapovich, R. V. Levin, A. E. Marichev, N. K. Timoshina, and B. V. Pushnyi, "GaInAsP/InP-based laser power converters (λ = 1064 nm)", *Semiconductors*, **52**(13), 1748–1753, 2018, doi:10.1134/s1063782618130079.

[53] N. A. Kalyuzhnyy, S. A. Mintairov, A. M. Nadtochiy, V. N. Nevedomskiy, D. V. Rybalchenko, and M. Z. Shvarts, "InGaAs metamorphic laser (1064 nm) power converters with over 40% efficiency", *Electronics Letters*, **53**(3), 173–175, 2017, doi:10.1049/el.2016.4308.

[54] N. Singh, C. Kin Fai Ho, Y. Nelvin Leong, K. E. K. Lee, and H. Wang, "InAlGaAs/InP-based laser photovoltaic converter at ~1070 nm", *IEEE Electron Device Letters*, **37**(9), 1154–1157, 2016, doi:10.1109/LED.2016.2591015.

[55] H. Helmers, A. Franke, D. Lackner, O. Höhn, F. Predan, and F. Dimroth, "51% efficient photonic power converters for O-band wavelengths around 1310 nm", in *2020 47th IEEE Photovoltaic Specialists Conference (PVSC)*, 2471 – 2474, Calgary, AB, 2020, doi:10.1109/PVSC45281.2020.9300717.

[56] V. P. Khvostikov, S. V. Sorokina, O. A. Khvostikova, R. V. Levin, B. V. Pushnyi, N. K. Timoshina, and V. M. Andreev, “GaSb laser-power (λ = 1550 nm) converters: Fabrication method and characteristics”, *Semiconductors*, **50**(10), 1338–1343, 2016, doi:10.1134/s1063782616100146.

[57] J. Mukherjee, S. Jarvis, M. Perren, and S. J. Sweeney, “Efficiency limits of laser power converters for optical power transfer applications”, *Journal of Physics D: Applied Physics*, **46**(26), 2013, doi:10.1088/0022-3727/46/26/264006.

[58] C. J. Richardson and M. L. Lee, “Metamorphic epitaxial materials”, *MRS Bulletin*, **41**(03), 193–198, 2016, doi:10.1557/mrs.2016.7.

[59] P. Y. Yu and M. Cardona, *Fundamentals of Semiconductors*, Heidelberg, 4th edition, 2010, doi:10.1017/CBO9781107415324.004.

[60] J. R. Arthur, “Molecular beam epitaxy”, *Surface Science*, **500**, 189–217, 2002, doi:10.1016/0039-6028(94)90699-8.

[61] R. Pelzel, “A comparison of MOVPE and MBE growth technologies for III-V epitaxial structures”, in *2013 International Conference on Compound Semiconductor Manufacturing Technology (CS MANTECH 2013)*, 105–108, New Orleans, LA, USA, 2013.

[62] M. Sotoodeh, A. H. Khalid, and A. A. Rezazadeh, “Empirical low-field mobility model for III-V compounds applicable in device simulation codes”, *Journal of Applied Physics*, **87**(6), 2890–2900, 2000, doi:10.1063/1.372274.

[63] M. Wilkins and K. Hinzer, “Multijunction Solar Cells”, in J. Piprek (ed.), *Handbook of Optoelectronic Device Modeling and Simulation*, volume 2, chapter 40, 415–440, CRC Press, Taylor and Francis Group, Boca Raton, FL, 2017.

[64] M. Wilkins, *Multi-Junction Solar Cells and Photovoltaic Power Converters: High-Efficiency Designs and Effects of Luminescent Coupling*, Ph.D. thesis, University of Ottawa, 2017.

[65] S. Adachi, *Properties of Semiconductor Alloys: Group-IV, III-V, and II-VI Semiconductors*, John Wiley & Sons, 2009.

[66] F. Urbach, “The long-wavelength edge of photographic sensitivity and of the electronic Absorption of Solids”, *Physical Review*, **92**(5), 1324, 1953, doi:10.1103/PhysRev.92.1324.

[67] M. V. Kurik, “Urbach Rule”, *Phys. Status Solidi A*, **8**, 9–45, 1971.

[68] R. R. King, D. Bhusari, A. Boca, D. Larrabee, X.-Q. Liu, W. Hong, C. M. Fetzer, D. C. Law, and N. H. Karam, “Band gap-voltage offset and energy production in next-generation multijunction solar cells”, *Progress in Photovoltaics: Research and Applications*, **19**, 797–812, 2011.

[69] R. M. France, J. F. Geisz, I. Garcia, M. A. Steiner, W. E. McMahon, D. J. Friedman, T. E. Moriarty, C. Osterwald, J. S. Ward, A. Duda, M. Young, and W. J. Olavarria, “Design flexibility of ultra-high

efficiency 4-junction inverted metamorphic solar cells", *IEEE Journal of Photovoltaics*, **6**(2), 578–583, 2015, doi:10.1109/PVSC.2015.7356439.

[70] S. M. Sze and K. K. Ng, *Physics of Semiconductor Devices*, Wiley Interscience, John Wilkey & Sons, Hoboken, New Jersey, 3rd edition, 2007.

[71] M. Wilkins, C. E. Valdivia, A. M. Gabr, D. Masson, S. Fafard, and K. Hinzer, "Luminescent coupling in planar opto-electronic devices", *Journal of Applied Physics*, **118**, 143102, 2015, doi:10.1063/1.4932660.

[72] A. W. Walker, *Bandgap engineering of multi-junction solar cells using nanostructures for enhanced performance under concentrated illumination*, Ph.D. thesis, 2013.

[73] S. J. Byrnes, "Multilayer optical calculations", 2020, url: http://arxiv.org/abs/1603.02720.

[74] A. F. Franz, G. A. Franz, S. Selberherr, C. Ringhofer, and P. Markowich, "Finite Boxes—A Generalization of the Finite-Difference Method Suitable for Semiconductor Device Simulation", *IEEE Transactions on Electron Devices*, **30**(9), 1070–1082, 1983, doi:10.1109/T-ED.1983.21261.

[75] R. E. Bank, D. J. Rose, and W. Fichtner, "Numerical methods for semiconductor device simulation", *IEEE Transactions on Electron Devices*, **30**, 1031–1041, 1983.

[76] Synopsys, *Sentaurus Device User Guide (Version P-2019.03)*, Synposys Inc., 2019.

[77] G. S. Armatas and M. G. Kanatzidis, "Size dependence in hexagonal mesoporous germanium: Pore wall thickness versus energy gap and photoluminescence", *Nano Letters*, **10**(9), 3330–3336, 2010, doi:10.1021/nl101004q.

[78] D. A. Ruddy, J. C. Johnson, E. R. Smith, and N. R. Neale, "Size and bandgap control in the solution-phase synthesis of near-infrared-emitting germanium nanocrystals", *ACS Nano*, **4**(12), 7459–7466, 2010, doi:10.1021/nn102728u.

[79] N. Shirahata, D. Hirakawa, Y. Masuda, and Y. Sakka, "Size-dependent color tuning of efficiently luminescent germanium nanoparticles", *Langmuir*, **29**(24), 7401–7410, 2013, doi:10.1021/la303482s.

[80] Y. M. Niquet, G. Allan, C. Delerue, and M. Lannoo, "Quantum confinement in germanium nanocrystals", *Applied Physics Letters*, **77**(8), 1182–1184, 2000, doi:10.1063/1.1289659.

[81] X. Li, G. Meng, Q. Xu, M. Kong, X. Zhu, Z. Chu, and A. P. Li, "Controlled synthesis of germanium nanowires and nanotubes with variable morphologies and sizes", *Nano Letters*, **11**(4), 1704–1709, 2011, doi:10.1021/nl200229p.

[82] G. Kartopu, A. V. Sapelkin, V. A. Karavanskii, U. Serincan, and R. Turan, "Structural and optical properties of porous nanocrystalline Ge", *Journal of Applied Physics*, **103**, 113518, 2008, doi:10.1063/1.2924417.

[83] P. W. Loscutoff and S. F. Bent, "Reactivity of the germanium surface: chemical passivation and functionalization", *Annual Review of Physical Chemistry*, **57**, 467–495, 2006, doi:10.1146/annurev.physchem.56.092503.141307.

[84] F. W. Yuan, H. J. Yang, and H. Y. Tuan, "Alkanethiol-passivated Ge nanowires as high-performance anode materials for lithium-ion batteries: The role of chemical surface functionalization", *ACS Nano*, **6**(11), 9932–9942, 2012, doi:10.1021/nn303519g.

[85] S. Choi, J. Kim, N. S. Choi, M. G. Kim, and S. Park, "Cost-effective scalable synthesis of mesoporous germanium particles via a redox-transmetalation reaction for high-performance energy storage devices", *ACS Nano*, **9**(2), 2203–2212, 2015, doi:10.1021/acsnano.5b00389.

[86] S. Choi, Y.-G. Cho, J. Kim, N.-S. Choi, H.-K. Song, G. Wang, and S. Park, "Mesoporous germanium anode materials for lithium-ion battery with exceptional cycling stability in wide temperature range", *Small*, **13**, 1603045, 2017, doi:10.1002/smll.201603045.

[87] J. Hwang, C. Jo, M. G. Kim, J. Chun, E. Lim, S. Kim, S. Jeong, Y. Kim, and J. Lee, "Mesoporous Ge/GeO_2/carbon lithium-ion battery anodes with high capacity and high reversibility", *ACS Nano*, **9**(5), 5299–5309, 2015, doi:10.1021/acsnano.5b00817.

[88] X. Xiao, X. Li, S. Zheng, J. Shao, H. Xue, and H. Pang, "Nanostructured germanium anode materials for advanced rechargeable batteries", *Advanced Materials Interfaces*, **4**(6), 1600798, 2017, doi:10.1002/admi.201600798.

[89] S. Wu, C. Han, J. Iocozzia, M. Lu, R. Ge, R. Xu, and Z. Lin, "Germanium-based nanomaterials for rechargeable batteries", *Angewandte Chemie - International Edition*, **55**(28), 7898–7922, 2016, doi:10.1002/anie.201509651.

[90] T. Kennedy, E. Mullane, H. Geaney, M. Osiak, C. O'Dwyer, and K. M. Ryan, "High-performance germanium nanowire-based lithium-ion battery anodes extending over 1000 cycles through in situ formation of a continuous porous network", *Nano Letters*, **14**(2), 716–723, 2014, doi:10.1021/nl403979s.

[91] X. H. Liu, S. Huang, S. T. Picraux, J. Li, T. Zhu, and J. Y. Huang, "Reversible nanopore formation in Ge nanowires during lithiation- delithiation cycling: An in situ transmission electron microscopy study", *Nano Letters*, **11**(9), 3991–3997, 2011, doi:10.1021/nl2024118.

[92] M. H. Park, K. Kim, J. Kim, and J. Cho, "Flexible dimensional control of high-capacity Li-Ion-battery anodes: from 0D hollow to 3D porous germanium nanoparticle assemblies", *Advanced Materials*, **22**(3), 415–418, 2010, doi:10.1002/adma.200901846.

[93] D. T. Ngo, H. T. T. Le, C. Kim, J.-Y. Lee, J. G. Fisher, I.-D. Kim, and C.-J. Park, "Mass-scalable synthesis of 3D porous germanium–carbon composite particles as an ultra-high rate anode for lithium ion batteries", *Energy Environ. Sci.*, **8**(12), 3577–3588, 2015, doi:10.1039/C5EE02183A.

[94] H. C. Choi and J. M. Buriak, “Preparation and functionalization of hydride terminated porous germanium”, *Chemical Communications*, **17**, 1669–1670, 2000, doi:10.1039/B004011H.

[95] S. Tutashkonko, S. Alekseev, and T. Nychyporuk, “Nanoscale morphology tuning of mesoporous Ge: Electrochemical mechanisms”, *Electrochimica Acta*, **180**, 545–554, 2015, doi:10.1016/j.electacta.2015.08.112.

[96] E. Garralaga Rojas, H. Plagwitz, B. Terheiden, J. Hensen, C. Baur, G. La Roche, G. F. X. Strobl, and R. Brendel, “Mesoporous germanium formation by electrochemical etching”, *Journal of The Electrochemical Society*, **156**, D310, 2009, doi:10.1149/1.3147271.

[97] E. Garralaga Rojas, B. Terheiden, H. Plagwitz, J. Hensen, C. Baur, G. F. X. Strobl, and R. Brendel, “Formation of mesoporous germanium double layers by electrochemical etching for layer transfer processes”, *Electrochemistry Communications*, **12**(2), 231–233, 2010, doi:10.1016/j.elecom.2009.11.033.

[98] D. Sun, A. E. Riley, A. J. Cadby, E. K. Richman, S. D. Korlann, and S. H. Tolbert, “Hexagonal nanoporous germanium through surfactant-driven self-assembly of Zintl clusters”, *Nature*, **441**(7097), 1126–1130, 2006, doi:10.1038/nature04891.

[99] G. S. Armatas and M. G. Kanatzidis, “Mesostructured germanium with cubic pore symmetry.”, *Nature*, **441**(June), 1122–1125, 2006, doi:10.1038/nature04833.

[100] G. S. Armatas and M. G. Kanatzidis, “Hexagonal Mesoporous Germanium”, *Science*, **313**, 817–820, 2006.

[101] J. Shieh, H. L. Chen, T. S. Ko, H. C. Cheng, and T. C. Chu, “Nanoparticle-assisted growth of porous germanium thin films”, *Advanced Materials*, **16**(13), 1121–1124, 2004, doi:10.1002/adma.200306541.

[102] A. Boucherif, A. Korinek, V. Aimez, and R. Arès, “Near-infrared emission from mesoporous crystalline germanium”, *AIP Advances*, **4**, 107128, 2014, doi:10.1063/1.4898643.

[103] S. Miyazaki, K. Sakamoto, K. Shiba, and M. Hirose, “Photoluminescence from anodized and thermally oxidized porous germanium”, *Thin Solid Films*, **255**(1-2), 99–102, 1995, doi:10.1016/0040-6090(94)05630-V.

[104] T. S. Ko, J. Shieh, M. C. Yang, T. C. Lu, H. C. Kuo, and S. C. Wang, “Phase transformation and optical characteristics of porous germanium thin film”, *Thin Solid Films*, **516**(10), 2934–2938, 2008, doi:10.1016/j.tsf.2007.06.023.

[105] C. Jing, C. Zhang, X. Zang, W. Zhou, W. Bai, T. Lin, and J. Chu, “Fabrication and characteristics of porous germanium films”, *Science and Technology of Advanced Materials*, **10**(6), 065001, 2009, doi:10.1088/1468-6996/10/6/065001.

[106] A. Boucherif, G. Beaudin, V. Aimez, and R. Arès, "Mesoporous germanium morphology transformation for lift-off process and substrate re-use", *Applied Physics Letters*, **102**, 011915, 2013, doi:10.1063/1.4775357.

[107] F. Blaffart, A. Boucherif, V. Aimez, and R. Arès, "Control of mesoporous silicon initiation by cathodic passivation", *Electrochemistry Communications*, **36**, 84–87, 2013, doi:10.1016/j.elecom.2013.09.015.

[108] V. Lehmann, *Electrochemistry of Silicon: Instrumentation, Science, Materials and Applications*, Wiley-VCH Verlag GmbH, Weinheim, 2002.

[109] V. Lehmann, F. Hofmann, F. Möller, and U. Grüning, "Resistivity of porous silicon: a surface effect", *Thin Solid Films*, **255**, 20–22, 1995, doi:10.1016/0040-6090(94)05624-M.

[110] V. Timoshenko, T. Dittrich, V. Lysenko, M. Lisachenko, and F. Koch, "Free charge carriers in mesoporous silicon", *Physical Review B*, **64**(8), 085314, 2001, doi:10.1103/PhysRevB.64.085314.

[111] A. J. Simons, T. I. Cox, M. J. Uren, and P. D. J. Calcott, "The electrical properties of porous silicon produced from n+ silicon substrates", *Thin Solid Films*, **255**, 12–15, 1995, doi:10.1016/0040-6090(94)05622-K.

[112] M. Hajji, M. Khardani, N. Khedher, H. Rahmouni, B. Bessaïs, H. Ezzaouia, and H. Bouchriha, "Structural, optical and electrical properties of quasi-monocrystalline silicon thin films obtained by rapid thermal annealing of porous silicon layers", *Thin Solid Films*, **511-512**, 235–237, 2006, doi:10.1016/j.tsf.2005.12.044.

[113] L. A. Balagurov, D. G. Yarkin, and E. A. Petrova, "Electronic transport in porous silicon of low porosity made on a p+ substrate", *Materials Science and Engineering B: Solid-State Materials for Advanced Technology*, **69**, 127–131, 2000, doi:10.1016/S0921-5107(99)00230-5.

[114] R. Schwarz, F. Wang, M. Ben-Chorin, S. Grebner, A. Nikolov, and F. Koch, "Photocarrier grating technique in mesoporous silicon", *Thin Solid Films*, **255**(1-2), 23–26, 1995, doi:10.1016/0040-6090(94)05677-6.

[115] M. Ben-Chorin, A. Kux, and I. Schechter, "Adsorbate effects on photoluminescence and electrical conductivity of porous silicon", *Appl. Phys. Lett.*, **64**(24), 481–483, 1994, doi:10.1063/1.111136.

[116] I. Schechter, M. Ben-Chorin, and A. Kux, "Gas sensing properties of porous silicon", *Analytical Chemistry*, **67**(20), 3727–3732, 1995, doi:10.1021/ac00116a018.

[117] D. Stievenard and D. Deresmes, "Are electrical properties of an aluminum-porous silicon junction governed by dangling bonds?", *Appl. Phys. Lett.*, **67**, 1570–1572, 1995, doi:10.1063/1.114942.

[118] C. Fang, H. Föll, and J. Carstensen, "Electrochemical pore etching in germanium", *Journal of Electroanalytical Chemistry*, **589**(2), 259–288, 2006, doi:10.1016/j.jelechem.2006.02.021.

[119] G. Flamand, J. Poortmans, and K. Dessein, “Formation of porous Ge using HF-based electrolytes”, *Physica Status Solidi C: Conferences*, **2**(9), 3243–3247, 2005, doi:10.1002/pssc.200461130.

[120] N. Ott, M. Nerding, G. Müller, R. Brendel, and H. P. Strunk, “Evolution of the microstructure during annealing of porous silicon multilayers”, *Journal of Applied Physics*, **95**(2), 497–503, 2004, doi:10.1063/1.1633657.

[121] S. Tutashkonko, T. Nychyporuk, V. Lysenko, and M. Lemiti, “Thermally induced Ostwald ripening of mesoporous Ge nanostructures”, *Journal of Applied Physics*, **113**(2), 023517, 2013, doi:10.1063/1.4775576.

[122] G. Müller, M. Nerding, N. Ott, H. P. Strunk, and R. Brendel, “Sintering of porous silicon”, *Physica Status Solidi (A) Applied Research*, **197**(1), 83–87, 2003, doi:10.1002/pssa.200306472.

[123] P. Handler, “Electrical properties of a clean Ge surface”, in R. H. Kingston (ed.), *Semiconductor Surface Physics, Conference on the Physics of Semiconductor Surfaces*, 23–51, Philadelphia University of Pennsylvania Press, Philadelphia, PA, USA, 1956.

[124] D. Wang, Y. L. Chang, Q. Wang, J. Cao, D. B. Farmer, R. G. Gordon, and H. Dai, “Surface chemistry and electrical properties of germanium nanowires”, *Journal of the American Chemical Society*, **126**(37), 11602–11611, 2004, doi:10.1021/ja047435x.

[125] D. Wang and H. Dai, “Germanium nanowires: From synthesis, surface chemistry, and assembly to devices”, *Applied Physics A: Materials Science and Processing*, **85**(3), 217–225, 2006, doi:10.1007/s00339-006-3704-z.

[126] S. Davison and J. Levine, “Surface states”, *Solid State Physics*, **25**, 1–149, 1970, doi:10.1016/S0081-1947(08)60008-9.

[127] M. Ben-Chorin, F. Moller, and F. Koch, “Nonlinear electrical-transport in porous silicon”, *Physical Review B*, **49**(4), 2981–2984, 1994, doi:10.1103/PhysRevB.49.2981.

[128] M. Banerjee, S. K. Datta, and H. Saha, “Carrier density in a thin silicon layer with nanovoids”, *Nanotechnology*, **17**, 163–169, 2006, doi:10.1088/0957-4484/17/1/026.

[129] M. Banerjee, S. K. Dutta, U. Gangopadhyay, D. Majumdar, and H. Saha, “Modeling and simulation of layer-transferred thin silicon solar cell with quasi monocrystalline porous silicon as active layer”, *Solid-State Electronics*, **49**, 1282–1291, 2005, doi:10.1016/j.sse.2005.06.019.

[130] C. Salm, J. G. E. Klappe, J. Holleman, J. B. Rem, and H. Pierre, “XRD texture and morphology analysis of polycrystalline LPCVD germanium silicon”, in *MRS Proceedings*, volume 343, 721–726, 1994.

[131] B. P. Tyagi and K. Sen, “On the resistivity of polycrystalline silicon”, *Physica Status Solidi (a)*, **80**(2), 679–684, 1983, doi:10.1002/pssa.2210800233.

[132] D. Bellet and G. Dolino, "X-ray diffraction studies of porous silicon", *Thin Solid Films*, **276**, 1–6, 1996, doi:10.1016/0040-6090(95)08035-X.

[133] S. Tutashkonko and T. Nychyporuk, "Crystalline/amorphous porous Ge nanostructures by electrochemical etching", in K. Termentzidis (ed.), *Nanostructured Semiconductors: Amorphization and Thermal Properties*, 297–314, CRC Press, Boca Raton, FL, 2017.

[134] J. M. Buriak, "Organometallic chemistry on silicon and germanium surfaces", *Chemical Reviews*, **102**(5), 1271–1308, 2002, doi:10.1021/cr000064s.

[135] S. Rivillon, Y. J. Chabal, F. Amy, and A. Kahn, "Hydrogen passivation of germanium (100) surface using wet chemical preparation", *Applied Physics Letters*, **87**, 253101, 2005, doi:10.1063/1.2142084.

[136] Y. Lee, K. Park, Y. S. Cho, and S. Lim, "Effect of Ge surface termination on oxidation behavior", *Applied Surface Science*, **254**, 7544–7548, 2008, doi:10.1016/j.apsusc.2008.01.022.

[137] M. B. Robinson, A. C. Dillon, and S. M. George, "Porous silicon photoluminescence versus HF etching: No correlation with surface hydrogen species", *Applied Physics Letters*, **62**(13), 1493–1495, 1993, doi:10.1063/1.108669.

[138] A. Halimaoui, "Porous silicon: material processing, properties and applications", in J. C. Vial and J. Derrien (eds.), *Porous Silicon Science and Technology. Centre de Physique des Houches, vol 1*, 33–52, Springer Berlin Heidelberg, Berlin, Heidelberg, 1995, doi:10.1007/978-3-662-03120-9_3.

[139] E. H. Rhoderick, "The physics of Schottky barriers", *J. Phys. D: Appl. Phys.*, **3**(8), 1153, 1970, doi:10.1088/0022-3727/3/8/203.

[140] D. B. M. Klaassen, "A unified mobility model for device simulation I. Model equations and concentration dependence", *Solid State Electronics*, **35**(7), 953–959, 1992, doi:10.1016/0038-1101(92)90325-7.

[141] V. Palankovski and R. Quay, "Physical Models", in *Analysis and Simulation of Heterostructure Devices*, 26–140, Springer Vienna, Vienna, 2004, doi:10.1007/978-3-7091-0560-3_3.

[142] H. Looyenga, "Dielectric constants of heterogeneous mixtures", *Physica*, **31**, 401–406, 1965, doi:10.1016/0031-8914(65)90045-5.

[143] J. Salonen, E. Mäkilä, J. Riikonen, T. Heikkilä, and V. P. Lehto, "Controlled enlargement of pores by annealing of porous silicon", *Physica Status Solidi (A) Applications and Materials Science*, **206**(6), 1313–1317, 2009, doi:10.1002/pssa.200881023.

[144] C. H. Lee, T. Tabata, T. Nishimura, K. Nagashio, K. Kita, and A. Toriumi, "Ge/GeO2 interface control with high-pressure oxidation for improving electrical characteristics", *Applied Physics Express*, **2**, 071404, 2009, doi:10.1143/APEX.2.071404.

[145] Y. Fukuda, H. Okamoto, T. Iwasaki, Y. Otani, and T. Ono, “Surface passivation of p-type Ge substrate with high-quality GeNxlayer formed by electron-cyclotron-resonance plasma nitridation at low temperature”, *Applied Physics Letters*, **99**, 132907, 2011, doi:10.1063/1.3647621.

[146] M. N. Beattie, Y. A. Bioud, A. Boucherif, D. Drouin, R. Arès, C. E. Valdivia, and K. Hinzer, “III-V multi-junction solar cells on Si substrates with a voided Ge interface layer: A modeling study”, in *2018 IEEE 7th World Conference on Photovoltaic Energy Conversion (WCPEC) (A Joint Conference of 45th IEEE PVSC, 28th PVSEC & 34th EU PVSEC)*, 180–184, Waikoloa, HI, USA, 2018, doi:10.1109/PVSC.2018.8547836.

[147] J. S. Ward, T. Remo, K. Horowitz, M. Woodhouse, B. Sopori, K. VanSant, and P. Basore, “Techno-economic analysis of three different substrate removal and reuse strategies for III-V solar cells”, *Progress in Photovoltaics: Research and Applications*, **24**, 1284–1292, 2016.

[148] H. Ye and J. Yu, “Germanium epitaxy on silicon”, *Science and Technology of Advanced Materials*, **15**, 024601, 2014, doi:10.1088/1468-6996/15/2/024601.

[149] Y. A. Bioud, A. Boucherif, D. Drouin, and R. Arès, “Low cost Ge/Si virtual substrate engineering for III-V multijunction solar cell”, in *13th International Conference on Concentrator Photovoltaic Systems*, Ottawa, ON, Canada, 2017.

[150] T. Rinke, R. Bergmann, R. Brüggemann, and J. Werner, “Ultrathin Quasi-Monocrystalline Silicon Films for Electronic Devices”, *Solid State Phenomena*, **67-68**, 229–236, 1999, doi:10.4028/www.scientific.net/SSP.67-68.229.

[151] C. Andre, A. Khan, M. Gonzalez, M. Hudait, E. Fitzgerald, J. Carlin, M. Currie, C. Leitz, T. Langdo, E. Clark, D. Wilt, and S. Ringel, “Impact of threading dislocations on both n/p and p/n single junction GaAs cells grown on Ge/SiGe/Si substrates”, in *Conference Record of the Twenty-Ninth IEEE Photovoltaic Specialists Conference, 2002.*, 1043–1046, 2002, doi:10.1109/PVSC.2002.1190784.

[152] G. Masetti, M. Severi, and S. Solmi, “Modeling of carrier mobility against carrier concentration in arsenic-, phosphorus-, and boron-doped silicon”, *IEEE Transactions on Electron Devices*, **30**(7), 764–769, 1983, doi:10.1109/T-ED.1983.21207.

[153] Synopsys, “SDevice Material Database”, 2018.

[154] J. Zolper and A. M. Barnett, “The effect of dislocations on the open-circuit voltage of gallium arsenide solar cells”, *IEEE Transactions on Electron Devices*, **37**(2), 478–484, 1990, doi:10.1109/16.46386.

[155] A. W. Walker, O. Thériault, M. M. Wilkins, J. F. Wheeldon, and K. Hinzer, “Tunnel-junction-limited multijunction solar cell performance over concentration”, *IEEE Journal on Selected Topics in Quantum Electronics*, **19**(5), 0–7, 2013, doi:10.1109/JSTQE.2013.2258140.

[156] J. Piprek, *Semiconductor Optoelectronic Devices: Introduction to Physics and Simulation*, Academic Press, San Diego, CA, USA, 2003.

[157] M. Schubert, J. A. Woollam, G. Leibiger, B. Rheinländer, I. Pietzonka, T. Saß, and V. Gottschalch, "Isotropic dielectric functions of highly disordered $Al_xGa_{1-x}InP$ ($0 \leq x \leq 1$) lattice matched to GaAs", *Journal of Applied Physics*, **86**(4), 2025–2033, 1999, doi:10.1063/1.371003.

[158] M. Levinshtein, S. Rumyantsev, and M. Shur (eds.), *Handbook series on Semiconductor Parameters*, volume 2, World Scientific, London, 1999.

[159] S. Adachi, *Optical Constants of Crystalline and Amorphous Semiconductors: Numerical Data and Graphical Information*, Springer, Boston, MA, 1999.

[160] E. F. Schubert, *Physical Foundations of Solid-State Devices*, Rensselaer Polytechnic Institute, 2006.

[161] M. Levinshtein, S. Rumyantsev, and M. Shur (eds.), *Handbook series on Semiconductor Parameters*, volume 1, World Scientific, London, 1996.

[162] W. C. Dunlap, Jr. and R. L. Watters, "Direct Measurement of the Dielectric Constants of Silicon and Germanium", *Physical Review*, **92**(6), 1396–1397, 1953.

[163] E. D. Palik (ed.), *The Handbook of Optical Constants of Semiconductors*, Academic Press, 1997.

[164] S. Adachi, *The Handbook on Optical Constants of Semiconductors: In Tables and Figures*, World Scientific, 2012.

[165] I. Vurgaftman, J. R. Meyer, and L. R. Ram-Mohan, "Band parameters for III-V compound semiconductors and their alloys", *Journal of Applied Physics*, **89**(11), 5815–5875, 2001, doi:10.1063/1.1368156.

[166] A. B. Djurišić, A. D. Rakić, P. C. Kwok, E. H. Li, M. L. Majewski, and J. M. Elazar, "Modeling the optical constants of AlxGa1-xAs alloys", *Journal of Applied Physics*, **86**(1), 445–451, 1999, doi:10.1063/1.370750.

[167] M. A. Green and M. J. Keevers, "Optical properties of intrinsic silicon at 300 K", *Progress in Photovoltaics: Research and Applications*, **3**, 189–192, 1995, doi:10.1002/pip.4670030303.

[168] M. A. Green, "Intrinsic concentration, effective densities of states, and effective mass in silicon", *Journal of Applied Physics*, **67**(6), 2944–2954, 1990, doi:10.1063/1.345414.

[169] A. Schenk, "Finite-temperature full random-phase approximation model of band gap narrowing for silicon device simulation", *Journal of Applied Physics*, **84**(7), 3684–3695, 1998, doi:10.1063/1.368545.

[170] P. P. Altermatt, "Models for numerical device simulations of crystalline silicon solar cells - A review", *Journal of Computational Electronics*, **10**(3), 314–330, 2011, doi:10.1007/s10825-011-0367-6.

[171] M. Breselge, *Simulation von III-V Kaskadensolarzellen und Charakterisierung optischer Materialparameter*, Ph.D. thesis, Albert-Ludwigs-Universität und Fraunhofer ISE Freiburg, 2003.

[172] D. K. Schroder, *Semiconductor Material and Device Characterization (Third Edition)*, 2006, doi:10.1063/1.2810086.

[173] M. F. Bennett, M. Gonzalez, M. P. Lumb, M. K. Yakes, K. J. Schmieder, S. Tomasulo, J. Abell, J. R. Meyer, and R. J. Walters, "Development of wet etch processing for $In_xAl_{1-x}As_ySb_{1-y}$ solar cells grown on InP", in *2015 IEEE 42nd Photovoltaic Specialist Conference (PVSC)*, 53–56, 2015, doi:10.1109/PVSC.2015.7356353.

[174] H. W. Dinges, H. Burkhard, R. Lösch, H. Nickel, and W. Schlapp, "Refractive indices of InAlAs and InGaAs/InP from 250 to 1900 nm determined by spectroscopic ellipsometry", *Applied Surface Science*, **54**(C), 477–481, 1992, doi:10.1016/0169-4332(92)90090-K.

[175] M.-I. Kang, S. W. Kim, Y.-G. Kim, and J. W. Ryu, "Dependence of optical anisotropy of ZnO thin films on the structural properties", *Journal of the Korean Physical Society*, **57**(2), 389–394, 2010, doi:10.3938/jkps.57.389.

[176] Horiba Jobin Yvon, "Spectroscopic Ellipsometry: Lorentz Dispersion Model", Technical Report TN08, Horiba, 2006, url: https://www.horiba.com/fileadmin/uploads/Scientific/Downloads/OpticalSchool_CN/TN/ellipsometer/Lorentz_Dispersion_Model.pdf.

[177] J. Tauc, "Optical properties and electronic structure of amorphous Ge and Si", *Materials Research Bulletin*, **3**(1), 37–46, 1968, doi:10.1016/0025-5408(68)90023-8.

[178] G. Zoppi, I. Forbes, R. W. Miles, P. J. Dale, J. J. Scragg, and L. M. Peter, "$Cu_2ZnSnSe_4$ thin film solar cells produced by selenisation of magnetron sputtered precursors", *Progress in Photovoltaics: Research and Applications*, **17**, 315–319, 2009, doi:10.1002/pip.886.

[179] S. Ahn, S. Jung, J. Gwak, A. Cho, K. Shin, K. Yoon, D. Park, H. Cheong, and J. H. Yun, "Determination of band gap energy (E_g) of $Cu_2ZnSnSe_4$ thin films: On the discrepancies of reported band gap values", *Applied Physics Letters*, **97**(2), 2010, doi:10.1063/1.3457172.

[180] J. H. Neave, P. J. Dobson, J. J. Harris, P. Dawson, and B. A. Joyce, "Silicon doping of MBE-grown GaAs films", *Applied Physics A Solids and Surfaces*, **32**(4), 195–200, 1983, doi:10.1007/BF00820260.

[181] M. P. Lumb, M. K. Yakes, M. González, J. G. Tischler, and R. J. Walters, "Optical properties of Si-doped and Be-doped InAlAs lattice-matched to InP grown by molecular beam epitaxy", *Journal of Applied Physics*, **114**(10), 103504, 2013, doi:10.1063/1.4820519.

[182] G. W. Charache, D. M. Depoy, J. E. Raynolds, P. F. Baldasaro, K. E. Miyano, T. Holden, F. H. Pollak, P. R. Sharps, M. L. Timmons, C. B. Geller, W. Mannstadt, R. Asahi, A. J. Freeman, W. Wolf, and I. Introduction, "Moss–Burstein and plasma reflection characteristics of heavily doped", *Journal of Applied Physics*, **86**(1), 452–458, 1999.

[183] B. P. Yan, J. S. Luo, and Q. L. Zhang, "Study of band-gap narrowing effect and nonradiative recombination centers for heavily C-doped GaAs by photoluminescence spectroscopy", *Journal of Applied Physics*, **77**(9), 4822–4824, 1995, doi:10.1063/1.359406.

[184] D. E. Aspnes and A. A. Studna, "Dielectric functions and optical parameters of Si, Ge, GaP, GaAs, GaSb, InP, InAs, and InSb from 1.5 to 6.0 eV", *Physical Review B*, **27**(2), 985–1009, 1983, doi:10.1103/PhysRevB.27.985.

[185] J. Y. Huang, L. Shang, S. F. Ma, B. Han, G. D. Wei, Q. M. Liu, X. D. Hao, H. S. Shan, and B. S. Xu, "Low temperature photoluminescence study of GaAs defect states", *Chinese Physics B*, **29**(1), 2020, doi:10.1088/1674-1056/ab5fb8.

[186] Y. P. Varshni, "Band-to-band radiative recombination in groups IV, VI, and III-V semiconductors (I)", *Phys. Stat. Sol.*, **19**, 459–512, 1967, doi:10.1002/pssb.19670190202.

[187] Y. P. Varshni, "Band-to-band radiative recombination in groups IV, VI, and III-V semiconductors (II)", *Phys. Stat. Sol.*, **20**, 9–36, 1967, doi:10.1002/pssb.19670200102.

[188] Thorlabs, "Multimode Fiber Beam Profiles Lab Facts", url: https://www.thorlabs.com/newgrouppage9.cfm?objectgroup_id=11993.

[189] M. N. Beattie, M. Zamiri, K. L. C. Kaller, M. M. Wilkins, C. E. Valdivia, D. Xia, M. C. Tam, H. Kim, J. J. Krich, Z. Wasilewski, and K. Hinzer, "Two-junction III-V photonic power converter operating at monochromatic telecom wavelengths", in *2020 47th IEEE Photovoltaic Specialists Conference (PVSC)*, 1062–1066, Calgary, AB, 2020, doi:10.1109/PVSC45281.2020.9300885.

[190] C. E. Valdivia and K. Hinzer, "Segmented multi-junction solar cells : A new opportunity for cell design & optimization", in *2019 IEEE 46th Photovoltaic Specialists Conference (PVSC)*, 45–48, 2019, doi:10.1109/PVSC40753.2019.8980689.

[191] S. Fafard, "Ultrahigh efficiency optical power converters based on the Vertical Epitaxial HeteroStructure Architecture (VEHSA) design", in *Optics & Photonics International Congress, 1st Optical Wireless and Fiber Power Transmission Conference*, 2019.

[192] D. Xia and J. J. Krich, "Efficiency increase in multijunction monochromatic photovoltaic devices due to luminescent coupling", *Journal of Applied Physics*, **128**, 013101, 2020, doi:10.1063/5.0009870.

[193] D. Xia, M. N. Beattie, M. C. Tam, M. M. Wilkins, C. E. Valdivia, Z. R. Wasilewski, K. Hinzer, and J. J. Krich, "Opportunities for high efficiency monochromatic photovoltaic power conversion at 1310 nm", in *2019 IEEE 46th Photovoltaic Specialists Conference (PVSC)*, 2303–2306, 2019, doi:10.1109/PVSC40753.2019.8980470.

[194] M. P. Lumb, M. González, M. K. Yakes, C. A. Affouda, C. G. Bailey, and R. J. Walters, "High temperature current–voltage characteristics of InP-based tunnel junctions", *Progress in Photovoltaics: Research and Applications*, **23**, 773–782, 2015, doi:10.1002/pip.

[195] M. P. Lumb, M. K. Yakes, M. Gonzalez, R. Hoheisel, C. G. Bailey, W. Yoon, and R. J. Walters, “Development of tunnel junctions with high peak tunneling currents for InP-based multijunction solar cells”, in *2012 IEEE 38th Photovoltaic Specialists Conference (PVSC)*, 949–953, 2012, doi:10.1109/PVSC.2012.6317759.

[196] H. S. Bennett and C. L. Wilson, “Statistical comparisons of data on band-gap narrowing in heavily doped silicon: Electrical and optical measurements”, *Journal of Applied Physics*, **55**(10), 3582–3587, 1984, doi:10.1063/1.332950.

[197] Horiba, “DeltaPsi2: Application Library”, 2016.

[198] M. N. Beattie, C. E. Valdivia, M. M. Wilkins, M. Zamiri, K. L. C. Kaller, M. C. Tam, H. S. Kim, J. J. Krich, Z. R. Wasilewski, and K. Hinzer, “High current density tunnel diodes for multijunction photovoltaic devices on InP substrates”, *Applied Physics Letters*, **118**(6), 062101, 2021, doi:10.1063/5.0036053.

[199] M. P. Lumb, M. K. Yakes, M. González, I. Vurgaftman, C. G. Bailey, R. Hoheisel, and R. J. Walters, “Double quantum-well tunnel junctions with high peak tunnel currents and low absorption for InP multi-junction solar cells”, *Applied Physics Letters*, **100**(21), 213907, 2012, doi:10.1063/1.4722890.

[200] M. A. Green, E. D. Dunlop, J. Hohl-Ebinger, M. Yoshita, N. Kopidakis, and A. W. Ho-Baillie, “Solar cell efficiency tables (Version 55)”, *Progress in Photovoltaics: Research and Applications*, **28**(1), 3–15, 2020, doi:10.1002/pip.3228.

[201] M. González, N. Chan, N. J. Ekins-daukes, J. G. J. Adams, P. Stavrinou, I. Vurgaftman, J. R. Meyer, J. Abell, J. Robert, C. D. Cress, and P. P. Jenkins, “Modeling and analysis of multijunction solar cells”, in *Proceedings of SPIE, Physics and Simulation of Optoelectronic Devices XIX*, 79330R, San Fransisco, 2011, doi:10.1117/12.875757.

[202] J. F. Geisz, M. A. Steiner, N. Jain, K. L. Schulte, R. M. France, W. E. Mcmahon, E. E. Perl, and D. J. Friedman, “Building a six-junction inverted metamorphic concentrator solar cell”, *IEEE Journal of Photovoltaics*, **8**(2), 626–632, 2018.

[203] J. F. Wheeldon, C. E. Valdivia, A. W. Walker, G. Kolhatkar, A. Jaouad, A. Turala, B. Riel, D. Masson, N. Puetz, S. Fafard, R. Arès, V. Aimez, T. J. Hall, and K. Hinzer, “Performance comparison of AlGaAs, GaAs and InGaP tunnel junctions for concentrated multijunction solar cells”, *Progress in Photovoltaics: Research and Applications*, **19**, 442–452, 2011, doi:10.1002/pip.1056.

[204] F. Dimroth, “High-efficiency solar cells from III-V compound semiconductors”, *Physica Status Solidi C: Conferences*, **3**(3), 373–379, 2006, doi:10.1002/pssc.200564172.

[205] D. Masson, F. Proulx, and S. Fafard, “Pushing the limits of concentrated photovoltaic solar cell tunnel junctions in novel high-efficiency GaAs phototransducers based on a vertical epitaxial heterostructure architecture”, *Progress in Photovoltaics: Research and Applications*, **23**, 1687–1696, 2015.

[206] G. Kolhatkar, J. F. Wheeldon, C. E. Valdivia, A. W. Walker, S. Fafard, A. Turala, A. Jaouad, R. Arès, V. Aimez, and K. Hinzer, "Current-voltage measurements within the negative differential resistance region of AlGaAs/AlGaAs tunnel junctions for high concentration photovoltaics", *International Journal of Nanoscience*, **11**(4), 1240014, 2012, doi:10.1142/S0219581X12400145.

[207] M. P. Lumb, M. K. Yakes, M. González, M. F. Bennett, K. J. Schmieder, C. A. Affouda, M. Herrera, F. J. Delgado, S. I. Molina, and R. J. Walters, "Wide bandgap, strain-balanced quantum well tunnel junctions on InP substrates", *Journal of Applied Physics*, **119**, 194503, 2016, doi:10.1063/1.4948958.

[208] B. Romanczyk, P. Thomas, D. Pawlik, S. L. Rommel, W. Y. Loh, M. H. Wong, K. Majumdar, W. E. Wang, and P. D. Kirsch, "Benchmarking current density in staggered gap $In_0.53Ga_0.47As/GaAs_0.5Sb_0.5$ heterojunction Esaki tunnel diodes", *Applied Physics Letters*, **102**, 213504, 2013, doi:10.1063/1.4808362.

[209] I. García, J. F. Geisz, R. M. France, J. Kang, S. H. Wei, M. Ochoa, and D. J. Friedman, "Metamorphic $Ga_0.76In_0.24As/GaAs_0.75Sb_0.25$ tunnel junctions grown on GaAs substrates", *Journal of Applied Physics*, **116**(7), 074508, 2014, doi:10.1063/1.4892773.

[210] P. Thomas, M. Filmer, A. Gaur, D. J. Pawlik, B. Romanczyk, E. Marini, S. L. Rommel, K. Majumdar, W. Y. Loh, M. H. Wong, C. Hobbs, K. Bhatnagar, R. Contreras-Guerrero, and R. Droopad, "Performance evaluation of $In_0.53Ga_0.47As$ Esaki tunnel diodes on silicon and InP substrates", *IEEE Transactions on Electron Devices*, **62**(8), 2450–2456, 2015, doi:10.1109/TED.2015.2445731.

[211] M. P. Lumb, M. González, C. G. Bailey, I. Vurgaftman, J. R. Meyer, J. Abell, M. Yakes, R. Hoheisel, J. G. Tischler, P. N. Stavrinou, M. Fuhrer, N. J. Ekins-Daukes, and R. J. Walters, "Drift-diffusion modeling of InP-based triple junction solar cells", in *Proc. SPIE 8620, Physics, Simulation, and Photonic Engineering of Photovoltaic Devices II*, 86201G, San Fransisco, CA, USA, 2013, doi:10.1117/12.2005332.

[212] S. Tomasulo, M. Gonzalez, M. P. Lumb, M. E. Twigg, I. Vurgaftman, J. R. Meyer, R. J. Walters, and M. K. Yakes, "Molecular beam epitaxy of wide-bandgap InAlAsSb on InP substrates for an all lattice-matched triple-junction solar cell", in *2019 IEEE 46th Photovoltaic Specialists Conference (PVSC)*, 3187–3190, Chicago, IL, USA, 2019, doi:10.1109/PVSC40753.2019.8980506.

[213] R. L. Woo, W. D. Hong, S. Mesropian, M. S. Leite, H. A. Atwater, and D. C. Law, "First demonstration of monolithic InP-based InAlAs/InGaAsP/InGaAs triple junction solar cells", in *2011 IEEE 37th Photovoltaic Specialists Conference (PVSC)*, 295–298, IEEE, Seattle, WA, 2011, 2011, doi:10.1109/PVSC.2011.6185903.

[214] A. W. Jackson and A. C. Gossard, "Thermal imaging of wafer temperature in MBE using a digital camera", *Journal of Crystal Growth*, **301-302**, 105–108, 2007, doi:10.1016/j.jcrysgro.2006.12.020.

[215] R. A. Metzger, M. Hafizi, W. E. Stanchina, T. Liu, R. G. Wilson, and L. G. McCray, "Confinement of high Be doping levels in AlInAs/GaInAs npn heterojunction bipolar transistors by low

temperature molecular-beam epitaxial growth", *Applied Physics Letters*, **63**(10), 1360–1362, 1993, doi:10.1063/1.109677.

[216] J. D. Dow and D. Redfield, "Toward a unified theory of Urbach's rule and exponential absorption edges", *Physical Review B*, **5**(2), 594–610, 1972, doi:10.1103/PhysRevB.5.594.

[217] M. Steiner, W. Guter, G. Peharz, S. P. Philipps, F. Dimroth, and A. W. Bett, "A validated SPICE network simulation study on improving tunnel diodes by introducing lateral conduction layers", *Progress in Photovoltaics: Research and Applications*, **20**, 274–283, 2012, doi:10.1002/pip.

[218] W. Guter and A. W. Bett, "I-V characterization of tunnel diodes and multijunction solar cells", *IEEE Transactions on Electron Devices*, **53**(9), 2216–2222, 2006, doi:10.1109/TED.2006.881051.

[219] P. Espinet, I. García, I. Rey-Stolle, C. Algora, and M. Baudrit, "Distributed simulation of real tunnel junction effects in multi-junction solar cells", in *Proceedings of the 6th International Conference on Concentrating Photovoltaic Systems (CPV-6)*, 24–27, 2010, doi:10.1063/1.3509203.

[220] A. Braun, B. Hirsch, E. A. Katz, J. M. Gordon, W. Guter, and A. W. Bett, "Localized irradiation effects on tunnel diode transitions in multi-junction concentrator solar cells", *Solar Energy Materials and Solar Cells*, **93**(9), 1692–1695, 2009, doi:10.1016/j.solmat.2009.04.022.

[221] H. Helmers, M. Schachtner, and A. W. Bett, "Influence of temperature and irradiance on triple-junction solar subcells", *Solar Energy Materials and Solar Cells*, **116**, 144–152, 2013, doi:10.1016/j.solmat.2013.03.039.

[222] K. Nishioka, T. Takamoto, T. Agui, M. Kaneiwa, Y. Uraoka, and T. Fuyuki, "Annual output estimation of concentrator photovoltaic systems using high-efficiency InGaP/InGaAs/Ge triple-junction solar cells based on experimental solar cell's characteristics and field-test meteorological data", *Solar Energy Materials and Solar Cells*, **90**(1), 57–67, 2006, doi:10.1016/j.solmat.2005.01.011.

[223] A. Cuevas and S. López-Romero, "The combined effect of non-uniform illumination and series resistance on the open-circuit voltage of solar cells", *Solar Cells*, **11**(2), 163–173, 1984, doi:10.1016/0379-6787(84)90024-3.

[224] P. Sharma, M. M. Wilkins, H. P. Schriemer, and K. Hinzer, "Concentrating optical system optimization for 3- and 4-junction solar cells: impact of illumination profiles", *Journal of Photonics for Energy*, **7**(1), 014501, 2017, doi:10.1117/1.jpe.7.014501.